

AD646351

FINAL REPORT

VOLUME II

CONTRACT NO. ARDS-598

PROJECT NO. 232-001-02C

DEVELOPMENT AND TESTING
OF
HF WIRE-GRID LENS ANTENNA

JUNE 1966

This report has been approved for general availability

PREPARED FOR

FEDERAL AVIATION AGENCY
SYSTEMS RESEARCH AND DEVELOPMENT SERVICE

BY

TRG, INCORPORATED
A SUBSIDIARY OF CONTROL DATA CORPORATION
130 CONSTITUTION DRIVE, MENLO PARK, CALIFORNIA 94025

DDC
FEB 8 1967
A

ARCHIVE COPY

Final Report

Volume II

Contract ARDS-598

Project No. 232-001-02C

Report No. RD-66-20

DEVELOPMENT AND TESTING

OF

HF WIRE-GRID LENS ANTENNA

by

E. M. T. Jones

R. L. Tanner

M. G. Andreasen

F. B. Harris, Jr.

E. D. Sharp

June 1966

TRG-West Project W102

This report has been prepared by TRG, Incorporated for the Systems Research and Development Service, Federal Aviation Agency, under Contract ARDS-598. The contents of this report reflect the views of the contractor, who is responsible for the facts and the accuracy of the data presented herein, and do not necessarily reflect the official views or policy of the FAA. This report does not constitute a standard, specification or regulation.

TRG, Incorporated

a Subsidiary of Control Data Corporation

130 Constitution Drive, Menlo Park, California 94025


TRG, Incorporated, a Subsidiary of Control Data Corporation,
Menlo Park, California 94025
DEVELOPMENT AND TESTING OF HF WIRE-GRID LENS ANTENNA,
Volume II, E. M. T. Jones, R. L. Tanner, M. G. Andreasen,
F. B. Harris, Jr., E. D. Sharp, June 1966
269 pages, 208 illustrations, 7 tables, 15 references, (3 appendices)
Contract ARDS-598, Report No. RD-66-20, Project No. 232-001-02C

ABSTRACT

This report describes the results of a Joint Services Evaluation conducted in the Spring and Summer of 1964 on the first full-scale model of the Wire-Grid Lens HF Antenna, constructed by TRG for the FAA at their International Flight Service Receiver Station at Molokai, Hawaii. The evaluation was carried out by TRG and their subcontractor, SRI, in cooperation with NRL personnel working under the overall supervision of the FAA. Representatives from the Army, Navy, Air Force, and the FAA both witnessed the tests and participated in their planning. The results of a previous, more limited evaluation are described in the previously issued Final Report, Volume I.

The lens employs a novel focusing medium consisting of two wire grids, one above the other, whose wave slowing or refractive characteristics are to first order independent of frequency. This property makes the lens inherently capable of operation over very wide bandwidths. The basic refractive profile and circularly symmetric form of the lens are similar to the well known Luneburg lens. As a consequence, the Wire-Grid HF Lens is in focus with waves arriving from any azimuth direction. By locating feeds at many different points on the lens circumference, it becomes equivalent to many highly directive broad-band antennas pointed in many different directions.

During the evaluation SRI and NRL made an extensive series of airborne pattern measurements on the lens, the FAA station rhombics, and several reference antennas using the SRI airborne pattern measuring equipment. These data were later reduced by SRI with aid of a computer to the form presented in this report. These patterns demonstrate the predicted directivity and beam forming properties of the lens at all azimuth angles over its 3 to 30 Mc design frequency band, which are comparable to those of the station rhombics over the 5 to 25 Mc band each of which operates over a more restricted frequency band.



Error-count measurements were also made on received messages by NRL over a period of five months using both FAA and NRL developed equipment. These measurements showed that the lens and the rhombics both had low bit error counts and were essentially equivalent in their ability to receive operational traffic.

TABLE OF CONTENTS

Abstract	iii
List of Illustrations	ix
List of Tables	xxiii
1. INTRODUCTION	1
1.1 Preliminary Evaluation	1
1.2 Joint Services Evaluation	1
1.3 Design Performance Characteristics	2
1.4 Optimized Feeds	3
2. PHYSICAL DESCRIPTION AND PRINCIPLES OF OPERATION OF THE WIRE-GRID LENS	5
3. CONSTRUCTION OF WIRE-GRID LENS	9
4. DESCRIPTION OF ANTENNA SITE AND LOCATION OF TEST ANTENNAS	17
5. LENS FEEDS AND THEORETICAL AZIMUTH PATTERNS	23
6. MEASUREMENT OF RADIATION PATTERNS	29
6.1 Introduction	29
6.2 Flight Tests	29
6.2.1 Xeledop Transmitter	29
6.2.2 Aircraft Guidance and Tracking	30
6.2.3 Receiving and Recording Technique	32
6.3 Data Reduction	34
6.4 Pattern Data Display	38
6.5 Accuracy Considerations - General	40
6.5.1 Forward and Reverse Orbits	41
6.5.2 Whip Antenna Above Lens	48
6.6 Measured Radiation Patterns	50
7. LENS GAIN	55
7.1 Measured Relative Lens Gain Using the Xeledop Transmitter	55
7.2 Measured Relative Lens Gain Using Arriving Skywave Signals	57
7.3 Absolute Gain	58

TABLE OF CONTENTS (continued)

- 8. COMMUNICATION TRAFFIC ERROR RATES
 - 8.1 Operational Traffic Error Count Evaluation Using FAA Developed Equipment
 - 8.1.1 Introduction
 - 8.1.2 FAA Error Measuring Equipment
 - 8.1.3 Analysis of FAA Error Measuring Equipment
 - 8.1.4 Measured Error Rates Using the FAA Technique
 - 8.2 Error-Count Evaluation Using NRL Developed Techniques
 - 8.2.1 NRL Error-Count Measuring Technique
 - 8.2.2 NRL Signal and Noise Amplitude Data Measurement Technique
 - 8.2.3 NRL Radio Teletype Test Results
 - 8.3 Noise Levels at Molokai
 - 8.4 Discussion of FAA and NRL Error-Count Tests
- 9. CONCLUSIONS
- 10. RECOMMENDATIONS

References

**APPENDIX A - An Analysis of the Error Counting System
Developed by the FAA for Testing the
Molokai Wire-Grid Lens Antenna**

APPENDIX B - Measured Radiation Patterns

- B.1 General
- B.2 In-Band Patterns
 - B.2.1 Principal Polarization Contour Plots of In-Band Patterns
 - B.2.2 Cross Polarization Contour Plots of In-Band Patterns
 - B.2.3 Principal Polarization In-Band Polar Plots
 - B.2.4 Horizontal Polarization In-Band Polar Patterns for the Lens

TABLE OF CONTENTS (continued)

APPENDIX B - Measured Radiation Patterns (continued)

B.3	Out-of-Band Patterns	B-5
B.3.1	Principal Polarization Out-of-Band Contour Plots	B-5
B.3.2	Principal Polarization Out-of-Band Polar Plots	B-6

APPENDIX C - Optimized Feeds C-1

	Introduction	C-1
C.1	Design	C-3
C.2	Measured Performance	C-5
C.2.1	Absolute Feed Efficiency	C-7
C.2.2	Feed Response to the Zero Order Mode	C-9
C.2.3	Measured Gain Increase of Optimized Feeds	C-11
C.2.4	Input Impedance of Optimized Feeds	C-13
C.3	Areas in Which Installation of Optimized Feeds Would Modify Results of the Joint Services Evaluation	C-13
C.4	Conclusions	C-18

ILLUSTRATIONS

Fig. 2.1	Gathering and Focusing of Wave Power by Wire-Grid Lens Antenna	6
Fig. 2.2	Focusing Action Due to Wave Slowing in Luneburg Lens	8
Fig. 3.1	Aerial View of Lens, Receiver Building to Left	10
Fig. 3.2	Aerial View of Lens	11
Fig. 3.3	View from Under Lens Showing Construction of Truss and Lens Grids with Satellite Wires	12
Fig. 3.4	View Across Lens Showing Lens Grids and Grid Spacers	13
Fig. 3.5	Portion of Upper Horn Surface Showing Workman Preparing to Attach it to Lens	14
Fig. 3.6	View of Completed Portion of Horn	15
Fig. 4.1	Antenna Locations at FAA International Flight Service Receiver Station, Molokai, Hawaii	19/20
Fig. 4.2	Feed Locations in the Lens Antenna	21
Fig. 5.1	Plan View of Typical Feed in Molokai Wire-Grid Lens Antenna	24
Fig. 5.2	Idea lized Currents on Feeds Consisting of a Ramp and End Dipole Elements	24
Fig. 5.3	Physical Configuration of Ramp Used in Feeds	24
Fig. 5.4	Equivalent Circuits of Inboard and Outboard Phasing Networks on Feeds	26
Fig. 5.5	Calculated Azimuth Voltage Patterns of Wire-Grid Lens Antenna at the Elevation Angle, θ , Corresponding to the Peak of the Main Beam	27

ILLUSTRATIONS (continued)

Fig. 5.6	Theoretical Efficiency of the Feeds	2
Fig. 6.1	Xeledop Configurations for Vertical and Horizontal Polarizations	3
Fig. 6.2	Block Diagram of Measuring System Used by Stanford Research Institute	3
Fig. 6.3	Block Diagram of Data Processing System	3
Fig. 6.4	A Contour Plot as a Map of a Hemisphere	3
Fig. 6.5	Anchorage Feed at 4.1 Mc	4
Fig. 6.6	Anchorage Feed at 5.6 Mc	4
Fig. 6.7	Anchorage Feed at 9.1 Mc	4
Fig. 6.8	Anchorage Feed at 15.3 Mc	4
Fig. 6.9	Sydney Feed at 4.1 Mc	4
Fig. 6.10	Sydney Feed at 5.6 Mc	4
Fig. 6.11	Sydney Feed at 9.1 Mc	4
Fig. 6.12	Sydney Feed at 15.3 Mc	4
Fig. 6.13	Nandi-Canton Feed at 4.1 Mc	4
Fig. 6.14	Nandi-Canton Feed at 5.6 Mc	4
Fig. 6.15	Nandi-Canton Feed at 9.1 Mc	4
Fig. 6.16	Nandi-Canton Feed at 15.3 Mc	4
Fig. 6.17	Variation in Elevation Angle During Reverse-orbit Test	4
Fig. 6.18	Effect of Whip Antenna on Anchorage Feed Pattern at 11.8 Mc	4

ILLUSTRATIONS (Continued)

Fig. 6.19	Effect of Whip Antenna on Sydney Feed Pattern at 11.8 Mc	49
Fig. 6.20	Comparison of Calculated and Measured 3-db Azimuth Beamwidth of Wire-Grid Lens Antenna	51
Fig. 6.21	Comparison of Calculated Maximum Minor Lobe Level at Peak of Main Beam and Maximum Measured Minor Lobe Level for Wire-Grid Lens Antenna	51
Fig. 6.22	Comparison of Calculated and Measured Elevation -3 db Beam Contours for the Wire-Grid Lens Antenna	53
Fig. 6.23	Measured Elevation Pattern Coverage of Wire-Grid Lens Antenna and Expected Distribution of Arrival Angles for HF Point-to-Point Communications	53
Fig. 6.24	Measured 3-db Azimuth Beamwidths of San Francisco Rhombics 4A, 4B, and 4C	54
Fig. 6.25	Measured Elevation 3-db Beam Points of San Francisco Rhombics 4A, 4B, and 4C	54
Fig. 6.26	Measured Minor Lobe Level of San Francisco Rhombics 4A, 4B, and 4C	54
Fig. 7.1	Maximum Relative Principally Polarized Signals Received from Xeledop at Antenna Terminals of Various Test Antennas (Calculated From Data Measured at Multicoupler Terminals)	56
Fig. 7.2	Ratio of Median Signal Levels on Rhombics to That on Lens	59
Fig. 7.3	Double-Dipole Gain Standard Antenna	60
Fig. 7.4	Impedance Vertically Oriented of Double-Dipole Measured at Antenna Terminals (Chart Impedance = 100 ohms)	63
Fig. 7.5	Directivity and Gain of Wire-Grid Lens Antenna	66

ILLUSTRATIONS (Continued)

Fig. 8.1	FAA Binary Error Recording System	
Fig. 8.2	Binary Error Rates for Rhombics and Wire-Grid Lens at Molokai When Receiving San Francisco Signals at 5 Mc	
Fig. 8.3	Binary Error Rates for Rhombics and Wire-Grid Lens at Molokai When Receiving San Francisco Signals at 6 Mc	
Fig. 8.4	Binary Error Rates for Rhombics and Wire-Grid Lens at Molokai When Receiving San Francisco Signals at 8 - 13 Mc	
Fig. 8.5	Binary Error Rates for Rhombics and Wire-Grid Lens at Molokai When Receiving San Francisco Signals at 16 - 24 Mc	
Fig. 8.6	Binary Error Rates for Rhombics and Wire-Grid Lens at Molokai When Receiving San Francisco Signals at 5 - 24 Mc	7
Fig. 8.7	NRL Teletype Test Recording System	8
Fig. 8.8	Character Error Rates for Rhombic and Wire-Grid Lens at Molokai When Receiving 600 character-per-minute R Y Test Signals from Washington at 8 Mc	8
Fig. 8.9	Character Error Rates for Rhombic and Wire-Grid Lens at Molokai When Receiving 600 character-per-minute R Y Test Signals from Washington at 10.7 Mc	8
Fig. 8.10	Character Error Rates for Rhombic and Wire-Grid Lens at Molokai When Receiving 600 character-per-minute R Y Test Signals from Washington in the 12 - 13.6 Mc Band	8
Fig. 8.11	Character Error Rates for Rhombic and Wire-Grid Lens at Molokai When Receiving 600 character-per-minute R Y Test Signals from Washington at 17.5 Mc	8

ILLUSTRATIONS (Continued)

Fig. 8. 12	Character Error Rates for Rhombic and Wire-Grid Lens at Molokai When Receiving 600 character-per-minute R Y Test Signals from Washington at 20 Mc	86
Fig. 8. 13	Character Error Rates for Rhombic and Wire-Grid Lens at Molokai When Receiving 600 character-per-minute R Y Test Signals from Washington in the 8 - 20 Mc Band	87
Fig. 8. 14	NRL Signal and Noise Test Receiving System	88
Fig. 8. 15	Summary of the NRL Signal-to-Noise Ratio Data at the Antenna Terminals Obtained at Five Different Test Frequencies Ranging from 8 - 20 Mc	89
Fig. A. 1	Test Set-up to Measure "Binary Errors" on the Lens and a Rhombic Using a Pair of Rhombics as the Diversity Standard	A-2
Fig. A. 2	Test Set-up to Measure "Binary Errors" on the Lens and a Rhombic Using the Lens and a Rhombic as the Diversity Standard	A-3
IN-BAND (3-30Mc) PRINCIPAL POLARIZATION CONTOUR PLOTS:		
Fig. B. 1	Anchorage Feed at 3.0 Mc, E_{θ}	B-7
Fig. B. 2	Anchorage Feed at 4.1 Mc, E_{θ}	B-8
Fig. B. 3	Anchorage Feed at 5.6 Mc, E_{θ}	B-9
Fig. B. 4	Anchorage Feed at 9.1 Mc, E_{θ}	B-10
Fig. B. 5	Anchorage Feed at 11.8 Mc, E_{θ}	B-11
Fig. B. 6	Anchorage Feed at 15.3 Mc, E_{θ}	B-12

ILLUSTRATIONS (Continued)

Fig. B. 7	Anchorage Feed at 21.5 Mc, E_{θ}	B-
Fig. B. 8	Anchorage Feed at 25.3 Mc, E_{θ}	B-
Fig. B. 9	Anchorage Feed at 30.0 Mc, E_{θ}	B-
Fig. B. 10	Nandi-Canton Feed at 3.0 Mc, E_{θ}	B-
Fig. B. 11	Nandi-Canton Feed at 4.1 Mc, E_{θ}	B-
Fig. B. 12	Nandi-Canton Feed at 5.6 Mc, E_{θ}	B-
Fig. B. 13	Nandi-Canton Feed at 9.1 Mc, E_{θ}	B-
Fig. B. 14	Nandi-Canton Feed at 11.8 Mc, E_{θ}	B-
Fig. B. 15	Nandi-Canton Feed at 15.3 Mc, E_{θ}	B-
Fig. B. 16	Nandi-Canton Feed at 21.5 Mc, E_{θ}	B-
Fig. B. 17	Nandi-Canton Feed at 25.3 Mc, E_{θ}	B-
Fig. B. 18	Nandi-Canton Feed at 30.0 Mc, E_{θ}	B-
Fig. B. 19	Sydney Feed at 3.0 Mc, E_{θ}	B-
Fig. B. 20	Sydney Feed at 4.1 Mc, E_{θ}	B-
Fig. B. 21	Sydney Feed at 5.6 Mc, E_{θ}	B-
Fig. B. 22	Sydney Feed at 9.1 Mc, E_{θ}	B-
Fig. B. 23	Sydney Feed at 11.8 Mc, E_{θ}	B-
Fig. B. 24	Sydney Feed at 15.3 Mc, E_{θ}	B-
Fig. B. 25	Sydney Feed at 21.5 Mc, E_{θ}	B-
Fig. B. 26	Sydney Feed at 25.3 Mc, E_{θ}	B-
Fig. B. 27	Sydney Feed at 30.0 Mc, E_{θ}	B-

ILLUSTRATIONS (continued)

Fig. B. 28	San Francisco Feed at 3.0 Mc, E_{θ}	B-34
Fig. B. 29	San Francisco Feed at 4.1 Mc, E_{θ}	B-35
Fig. B. 30	San Francisco Feed at 5.6 Mc, E_{θ}	B-36
Fig. B. 31	San Francisco Feed at 9.1 Mc, E_{θ}	B-37
Fig. B. 32	San Francisco Feed at 11.8 Mc, E_{θ}	B-38
Fig. B. 33	San Francisco Feed at 15.3 Mc, E_{θ}	B-39
Fig. B. 34	San Francisco Feed at 21.5 Mc, E_{θ}	B-40
Fig. B. 35	San Francisco Feed at 25.3 Mc, E_{θ}	B-41
Fig. B. 36	San Francisco Feed at 30.0 Mc, E_{θ}	B-42
Fig. B. 37	Lens Excited as Biconical Antenna at 3.0 Mc, E_{θ}	B-43
Fig. B. 38	Lens Excited as Biconical Antenna at 5.6 Mc, E_{θ}	B-44
Fig. B. 39	Lens Excited as Biconical Antenna at 9.1 Mc, E_{θ}	B-45
Fig. B. 40	Lens Excited as Biconical Antenna at 11.8 Mc, E_{θ}	B-46
Fig. B. 41	Lens Excited as Biconical Antenna at 15.3 Mc, E_{θ}	B-47
Fig. B. 42	Lens Excited as Biconical Antenna at 21.5 Mc, E_{θ}	B-48
Fig. B. 43	Lens Excited as Biconical Antenna at 25.3 Mc, E_{θ}	B-49
Fig. B. 44	Lens Excited as Biconical Antenna at 30 Mc, E_{θ}	B-50
Fig. B. 45	NRL Monopole at 4.1 Mc, E_{θ}	B-51
Fig. B. 46	NRL Monopole at 5.6 Mc, E_{θ}	B-52
Fig. B. 47	NRL Monopole at 9.1 Mc, E_{θ}	B-53
Fig. B. 48	NRL Monopole at 15.3 Mc, E_{θ}	B-54

ILLUSTRATIONS (continued)

Fig. B. 49	NRL Monopole at 21.5 Mc, E_{θ}
Fig. B. 50	NRL Monopole at 25.3 Mc, E_{θ}
Fig. B. 51	NRL Monopole at 30.0 Mc, E_{θ}
Fig. B. 52	Rhombic 4A at 4.1 Mc, E_{ϕ}
Fig. B. 53	Rhombic 4A at 5.6 Mc, E_{ϕ}
Fig. B. 54	Rhombic 4B at 5.6 Mc, E_{ϕ}
Fig. B. 55	Rhombic 4B at 9.1 Mc, E_{ϕ}
Fig. B. 56	Rhombic 4B at 15.3 Mc, E_{ϕ}
Fig. B. 57	Rhombic 4C at 9.1 Mc, E_{ϕ}
Fig. B. 58	Rhombic 4C at 15.3 Mc, E_{ϕ}
Fig. B. 59	Rhombic 4C at 21.5 Mc, E_{ϕ}
Fig. B. 60	Rhombic 4C at 25.3 Mc, E_{ϕ}
Fig. B. 61	Rhombic 4C at 30.0 Mc, E_{ϕ}
Fig. B. 62	Double-Dipole Array at 5.6 Mc, E_{θ}
Fig. B. 63	Double-Dipole Array at 9.1 Mc, E_{θ}
Fig. B. 64	Double-Dipole Array at 11.8 Mc, E_{θ}
Fig. B. 65	Double-Dipole Array at 15.3 Mc, E_{θ}
Fig. B. 66	Double-Dipole Array at 21.5 Mc, E_{θ}
Fig. B. 67	Double-Dipole Array at 25.3 Mc, E_{θ}
Fig. B. 68	Double-Dipole Array at 30.0 Mc, E_{θ}
Fig. B. 69	Double-Dipole Array at 5.6 Mc, E_{ϕ}
Fig. B. 70	Double-Dipole Array at 9.1 Mc, E_{ϕ}

ILLUSTRATIONS (continued)

Fig. B. 71	Double-Dipole Array at 15.3 Mc, E_{ϕ}	B-77
Fig. B. 72	Double-Dipole Array at 21.5 Mc, E_{ϕ}	B-78
Fig. B. 73	Double-Dipole Array at 25.3 Mc, E_{ϕ}	B-79
Fig. B. 74	Double-Dipole Array at 30.0 Mc, E_{ϕ}	B-80

IN-BAND (3-30Mc) CROSS-POLARIZATION CONTOUR PLOTS:

Fig. B. 75	Anchorage Feed at 3.0 Mc, E_{ϕ} (E_{ϕ} peak 15 db below E_{θ} peak) ^{ϕ}	B-81
Fig. B. 76	Anchorage Feed at 4.1 Mc, E_{ϕ} (E_{ϕ} peak 9 db below E_{θ} peak) ^{ϕ}	B-82
Fig. B. 77	Anchorage Feed at 5.6 Mc, E_{ϕ} (E_{ϕ} peak 8.5 db below E_{θ} peak) ^{ϕ}	B-83
Fig. B. 78	Anchorage Feed at 9.1 Mc, E_{ϕ} (E_{ϕ} peak 11.5 db below E_{θ} peak) ^{ϕ}	B-84
Fig. B. 79	Anchorage Feed at 15.3 Mc, E_{ϕ} (E_{ϕ} peak 11 db below E_{θ} peak) ^{ϕ}	B-85
Fig. B. 80	Anchorage Feed at 21.5 Mc, E_{ϕ} (E_{ϕ} peak 5.5 db below E_{θ} peak) ^{ϕ}	B-86
Fig. B. 81	Anchorage Feed at 25.3 Mc, E_{ϕ} (E_{ϕ} peak 5.5 db below E_{θ} peak) ^{ϕ}	B-87
Fig. B. 82	Anchorage Feed at 30.0 Mc, E_{ϕ} (E_{ϕ} peak 5 db below E_{θ} peak) ^{ϕ}	B-88
Fig. B. 83	San Francisco Feed at 4.1 Mc, E_{ϕ} (E_{ϕ} peak 10 db below E_{θ} peak) ^{ϕ}	B-89
Fig. B. 84	San Francisco Feed at 5.6 Mc, E_{ϕ} (E_{ϕ} peak 10.5 db below E_{θ} peak) ^{ϕ}	B-90
Fig. B. 85	San Francisco Feed at 9.1 Mc, E_{ϕ} (E_{ϕ} peak 9 db below E_{θ} peak) ^{ϕ}	B-91
Fig. B. 86	San Francisco Feed at 15.3 Mc, E_{ϕ} (E_{ϕ} peak 9.5 db below E_{θ} peak) ^{ϕ}	B-92

ILLUSTRATIONS (continued)

-
- Fig. B. 87 San Francisco Feed at 25.3 Mc, E_{ϕ}
(E_{ϕ} peak 9 db below E_{θ} peak)
- Fig. B. 88 San Francisco Feed at 30.0 Mc, E_{ϕ}
(E_{ϕ} peak 10.5 db below E_{θ} peak)
- Fig. B. 89 NRL Monopole at 25.3 Mc, E_{ϕ}

IN-BAND (3-30Mc) PRINCIPAL-POLARIZATION FOLAR PLOTS:

- Fig. B. 90 Anchorage Feed at 3 Mc, E_{θ}
- Fig. B. 91 Anchorage Feeds at 11.8 Mc, E_{θ}
- Fig. B. 92 Anchorage Feed at 30.0 Mc, E_{θ}
- Fig. B. 93 Sydney Feed at 3.0 Mc, E_{θ}
- Fig. B. 94 Sydney Feed at 11.8 Mc, E_{θ}
- Fig. B. 95 Sydney Feed at 30.0 Mc, E_{θ}
- Fig. B. 96 San Francisco Feed at 3.0 Mc, E_{θ}
- Fig. B. 97 San Francisco Feed at 4.1 Mc, E_{θ}
- Fig. B. 98 San Francisco Feed at 5.6 Mc, E_{θ}
- Fig. B. 99 San Francisco Feed at 9.1 Mc, E_{θ}
- Fig. B. 100 San Francisco Feed at 11.8 Mc, E_{θ}
- Fig. B. 101 San Francisco Feed at 15.3 Mc, E_{θ}
- Fig. B. 102 San Francisco Feed at 21.5 Mc, E_{θ}
- Fig. B. 103 San Francisco Feed at 25.3 Mc, E_{θ}
- Fig. B. 104 San Francisco Feed at 30.0 Mc, E_{θ}
- Fig. B. 105 Rhombic 4A at 4.1 Mc, E_{ϕ}
- Fig. B. 106 Rhombic 4A at 5.6 Mc, E_{ϕ}
- Fig. B. 107 Rhombic 4B at 9.1 Mc, E_{ϕ}

ILLUSTRATIONS (continued)

Fig. B.108	Rhombic 4B at 15.3 Mc, E_{ϕ}	B-114
Fig. B.109	Rhombic 4C at 9.1 Mc, E_{ϕ}	B-115
Fig. B.110	Rhombic 4C at 15.3 Mc, E_{ϕ}	B-116
Fig. B.111	Rhombic 4C at 21.5 Mc, E_{ϕ}	B-117
Fig. B.112	Rhombic 4C at 25.3 Mc, E_{ϕ}	B-118
Fig. B.113	Rhombic 4C at 30.0 Mc, E_{ϕ}	B-119

IN-BAND (3-30 Mc) CROSS-POLARIZATION POLAR PLOTS:

Fig. B.114a	Anchorage Feed at 3 Mc, E_{ϕ} (E_{ϕ} peak 15 db below E_{θ} peak)	B-120
Fig. B.114b	Anchorage Feed at 9.1 Mc, E_{ϕ} (E_{ϕ} peak 12 db below E_{θ} peak)	B-120
Fig. B.114c	Anchorage Feed at 30.0 Mc, E_{ϕ} (E_{ϕ} peak 5 db below E_{θ} peak)	B-120
Fig. B.115	San Francisco Feed at 4.1 Mc, E_{ϕ} (E_{ϕ} peak 10 db below E_{θ} peak)	B-121
Fig. B.116	San Francisco Feed at 5.6 Mc, E_{ϕ} (E_{ϕ} peak 10.5 db below E_{θ} peak)	B-122
Fig. B.117	San Francisco Feed at 9.1 Mc, E_{ϕ} (E_{ϕ} peak 9 db below E_{θ} peak)	B-123
Fig. B.118	San Francisco Feed at 15.3 Mc, E_{ϕ} (E_{ϕ} peak 9 db below E_{θ} peak)	B-124
Fig. B.119a	San Francisco Feed at 25.3 Mc, E_{ϕ} (E_{ϕ} peak 9 db below E_{θ} peak)	B-125
Fig. B.119b	San Francisco Feed at 30.0 Mc, E_{ϕ} (E_{ϕ} peak 11 db below E_{θ} peak)	B-125

ILLUSTRATIONS (continued)

OUT-OF-BAND PRINCIPAL POLARIZATION CONTOUR PLOTS:

Fig. B. 120	Anchorage Feed at 2.25 Mc, E_θ	E
Fig. B. 121	Anchorage Feed at 2.6 Mc, E_θ	B.
Fig. B. 122	Nandi-Canton Feed at 2.25 Mc, E_θ	B.
Fig. B. 123	Nandi-Canton Feed at 2.6 Mc, E_θ	B.
Fig. B. 124	Sydney Feed at 2.25 Mc, E_θ	B-
Fig. B. 125	Sydney Feed at 2.6 Mc, E_θ	B.
Fig. B. 126	San Francisco Feed at 2.25 Mc, E_θ	B
Fig. B. 127	San Francisco Feed at 2.6 Mc, E_θ	B
Fig. B. 128	San Francisco Feed at 35.0 Mc, E_θ	B.
Fig. B. 129	Lens Excited as Biconical Antenna at 2.6 Mc, E_θ	B
Fig. B. 130	NRL Monopole at 2.6 Mc, E_θ	B-

OUT-OF-BAND PRINCIPAL POLARIZATION POLAR PLOTS:

Fig. B. 131	Anchorage Feed at 2.0 Mc, E_θ	B
Fig. B. 132	Nandi-Canton Feed at 2.0 Mc, E_θ	B-
Fig. B. 133	Sydney Feed at 2.0 Mc, E_θ	B-
Fig. C. 1	Equivalent Circuit of Optimized Two-Hop Ramps for Molokai Wire-Grid Lens Antenna	C-
Fig. C. 2	Calculated Azimuth Voltage Patterns of Wire-Grid Lens Antenna Equipped with Optimized Feeds at the Elevation Angle, θ , Corresponding to the Peak of the Main Beam	C-

ILLUSTRATIONS (continued)

Fig. C. 3	Efficiency of Optimized and Original Feeds in Molokai Wire-Grid Lens Antenna	C-8
Fig. C. 4	Difference in Response to the Zero Order Mode of Optimized and Original Samoa and Nandi-Canton Feeds Together with the Difference in Response of the Original Wake, Sydney, Tokyo, and San Francisco Feeds when Optimized and Original Feeds are Installed	C-10
Fig. C. 5	Measured Relative Gain of Molokai Wire-Grid Lens Antenna Using Optimized and Original Samoa Feeds	C-12
Fig. C. 6	Measured Relative Gain of Molokai Wire-Grid Lens Antenna Using Optimized and Original Nandi-Canton feeds	C-14
Fig. C. 7	Decibel Difference Between Median Signal Levels Received on Rhombics and on Lens (Equipped with Optimized Feeds). Positive Values Correspond to Stronger Rhombic Signals Negative Values to Stronger Lens Signals. (Calculations based on use of coaxial transmission lines to rhombics.)	C-16
Fig. C. 8	Directivity and Gain of Wire-Grid Lens Antenna Equipped with Optimized Feeds	C-17

TABLES

Table 7.1	Double Dipole Calculated Directivity and Radiation Resistance	6
Table 7.2	Measured Values of Lens Gain	11
Table 8.1	Measured Error Rates for the Wire-Grid Lens Antenna Receiving Operational Traffic Determined Using the FAA Measuring Techniques	
Table 8.2	Antennas Used During the FAA Error-Count Evaluation	7
Table 8.3	Summary of Antennas Arranged According to Frequency Bands Used in the FAA Error-Count Tests	2
Table 8.4	Summary of NRL Wire-Grid Lens Antenna Evaluation Measurements	
Table C.1	Input Impedance of Optimized Feeds	C-

1. INTRODUCTION

1.1 Preliminary Evaluation

The Wire-Grid Lens Antenna at the FAA Receiver Station on the Island of Molokai, Hawaii, was completed in the Summer of 1963, and is the first full-scale antenna of this type ever built. Shortly after completion in the Fall of 1963, a preliminary evaluation of the lens was conducted by TRG. The results of this evaluation are described in Volume I of the Final Report on this project¹ and in FAA Report No. RD-64-38.² During this evaluation, its radiation patterns were measured by recording the signals received at the lens from a transmitter mounted in a jeep which was located at various azimuth positions in the far field of the lens. These patterns were somewhat perturbed by the varying (with azimuth) ground-wave propagation characteristics between the lens and the jeep. Nevertheless, the measurements demonstrated the predicted beam-forming properties of the lens over a major part of the 3 to 30 Mc design band.

The utility of the lens as a direction finder was also investigated by recording the signals received on a pair of adjacent feeds, spaced approximately ten degrees apart, as the ground-based transmitter was located in the far zone at various known azimuth bearings between these feeds. It was found that both the amplitude ratio (measured in decibels) and the phase difference in the signals received on the feeds were linear functions of the transmitter position. This property of the lens^{3, 4} has subsequently been utilized by the Air Force to construct a direction-finding version which is located at the RADC Clark Hill test site near Rome, New York. A detailed evaluation of this direction-finding installation is now being carried out by the Air Force.

A limited number of measurements were also made of the communications traffic error rates on the lens and station rhombics when receiving the same operational frequency signals from a transmitter keyed in a known repetitive pattern. It was found that with operational traffic in the 11 to 23 Mc band the measured error rates for the lens were essentially the same as for the rhombics.

1.2 Joint Services Evaluation

Because of the potential utility of the Molokai Wire-Grid Lens HF Antenna as an HF receiving and direction-finding antenna, a Joint Services Evaluation was conducted in the Spring and Summer

of 1964 to more precisely determine its radiation patterns and to compare, over an extended period of time, the traffic error rates on the lens with those of the station rhombics. The results of this evaluation are presented in this report.

This evaluation was carried out under the overall supervision of representatives from the Systems Research and Development Section of the Federal Aviation Agency, with technical assistance being provided by TRG. The planning of the evaluation was done by representatives from a number of government agencies including not only the FAA, also NRL, Bureau of Ships, Headquarters Naval Communications, Army Electronics Command, and the U. S. Air Force (RADC). Representatives from NRL provided on-site supervision and direction during the evaluation. The radiation patterns were measured by Stanford Research Institute using an airborne transmitter circling the lens, later reduced by SRI with the aid of high-speed digital computers to the form shown in this report. The NRL team assisted in the recording of the pattern data. In addition, they also made numerous measurements of the traffic error rates over an extended time period using techniques developed by the FAA and NRL.

1.3 Design Performance Characteristics

The principal design performance characteristics for the W Grid Lens Antenna specified in the contract executed with TRG on July 1962 are as follows:

Frequency Range	3 to 30 Mc
Polarization	Vertical
VSWR	2.5:1 maximum
Directive Gain (over Isotropic)	3 Mc - 8 db minimum 10 to 30 Mc - 16 db minimum
Azimuthal Main Beamwidth (half power points)	3 Mc - 30 degrees minimum 10 Mc - 15 degrees minimum 30 Mc - 10 degrees minimum
Vertical Main Beamwidth (half power points)	50 degree maximum at 3 Mc 25 degree nominal at 10 Mc
Vertical Uptilt of Main Beam	Between 0 and 10 degrees nominal
Minor Lobes	Above 10 Mc at least - 15 db
Impedance Level	70 ohms nominal
Transmission Lines	Low-loss coaxial cable

Power Handling Capability	Receiving application
Operational Environment	100 mph wind, without ice.

1.4 Optimized Feeds

Subsequent to the Joint Services Evaluation, a program was initiated to develop optimized feeds for the Molokai Wire-Grid Lens Antenna. The results of this program, which has been completed, are reported in Appendix C and in Reference 5.

2. PHYSICAL DESCRIPTION AND PRINCIPLES OF OPERATION OF THE WIRE-GRID LENS

The Wire-Grid Lens consists of a pair of circular grids of wire, 600 feet in diameter, suspended one above the other. Surrounding the lens is a concentric structure, also made of wire and supported by means of cables and tall poles, known as an electromagnetic horn. The purpose of the horn, which increases the diameter of the total structure to 850 feet, is analogous to that of an old-fashioned ear trumpet. It intercepts the power contained in a broad area of the wave front of the arriving radio wave, concentrates it in the vertical direction, and channels it into the lens--the space between the two grids. As the wave travels through this space, a focusing action takes place that causes the wave, initially a plane wave, to converge on a focal point at the perimeter of the lens opposite the side from which the wave entered. This process is illustrated schematically in Fig. 2.1. At this focal point, where the power concentration is approximately 100 times greater than in the free space arriving wave, a signal output coupler is placed and connected by coaxial cable to the receiver.

As an antenna, the Wire-Grid Lens has the unique feature that it can concentrate many waves from many different directions and at many different frequencies simultaneously. Thus, an output coupler placed at the West point of the lens circle will respond strongly to signals arriving from the East and discriminate against signals arriving from other directions, while at the same time a coupler at the South point of the lens circle will detect signals from the North and discriminate against other signals. The FAA lens at Molokai has been equipped initially with seven output couplers to receive signals from San Francisco, Anchorage, Tokyo, Wake Island, Sydney, the Fiji Islands, and Samoa. As many as thirty-six couplers could be installed if required. Each would have its own highly directive receiving pattern and all could operate simultaneously. However, this report covers performance data recorded for a seven-feed configuration.

Operation of the Wire-Grid Lens Antenna depends strongly on two principles of relatively recent invention. The first of these is due to the late Dr. R. K. Luneburg who was professor of optics at Brown University. Professor Luneburg invented the general concept of the lens, known subsequently as the Luneburg lens, which has a circular cross-section (rather than the more familiar lenticular cross-section found in the lenses of eye-glasses, cameras, telescopes, and other optical devices) and which will bring to a focus waves falling on it from any direction.

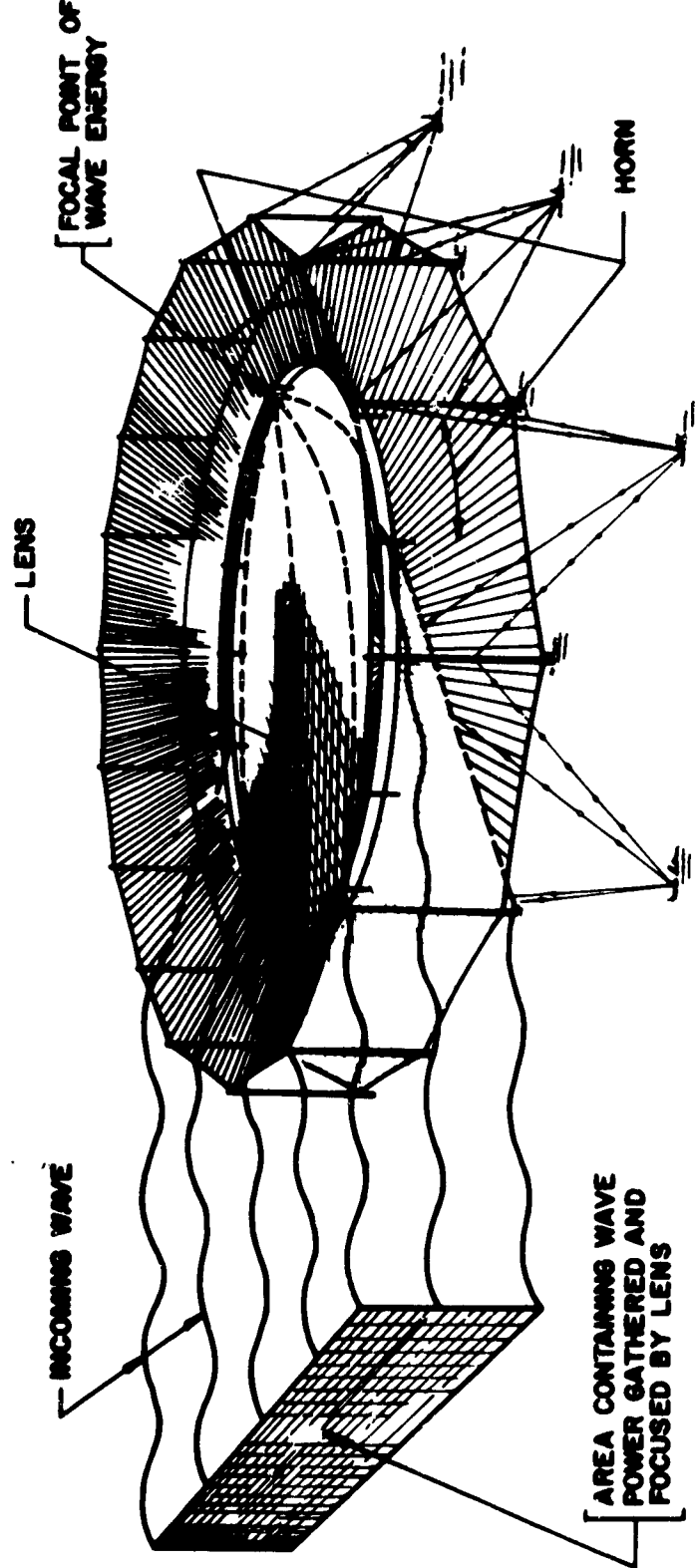


Fig. 2.1 Gathering and Focusing of Wave Power by Wire-Girid Lens Antenna

The second important invention is due to Dr. R. L. Tanner of TRG-West. Dr. Tanner showed that a radio wave traveling between two wire grids can be refracted or bent in a manner analogous to the bending of light waves traveling through glass. Reducing the spacing between the grids causes a slowing of the speed of travel of the radio waves in a manner completely analogous to the slowing of light waves produced by increasing the optical density of the glass. Invention of the wire-grid refractive medium enabled the realization of the Luneburg lens at radio communication frequencies.

Refraction or bending of a wave occurs because of the slowing of the wave in the refractive medium. The manner in which wave slowing is utilized to produce the focusing effect of the Luneburg lens is illustrated in Fig. 2.2. The dotted circle outlines the periphery of the lens. The plane wave, approaching the lens from the top, is characterized by wave fronts which are straight lines external to the lens and perpendicular to the direction of travel. As the wave enters the lens, that portion of the wave traveling in the lens is slowed, with the part of the wave passing through the center being slowed most. Those parts of the wave front which experience most slowing lag behind the rest, producing a curvature in the wave front. This curvature increases as the wave progresses through the lens so that by the time the wave has traversed the entire lens the wave fronts have been transformed from straight lines into circles converging on the focal point. All the wave energy contained in a channel equal in width to the entire lens is now concentrated in the small area at the focus.

To achieve its all-angle focusing characteristic, the Luneburg lens requires maximum wave slowing at the center where the wave travels only 70 percent as fast as in free space. The slowing diminishes smoothly in all directions from the center, so that at the edges the wave velocity is the same as in free space.

In the Wire-Grid Lens this varying wave slowing characteristic is achieved by adjustment of the spacing between the grids. At the center of the lens circle the grids, which have a mesh size of five feet, are only seven inches apart. Moving out from the center, the spacing is increased gradually so that at the edges of the lens the two grids are separated by twelve feet.

The low-frequency limit of operation of the lens occurs (1) when its diameter measured in terms of wavelength becomes less than approximately two wavelengths so that significant focusing action cannot occur, and (2) when the horn height, also measured in terms of wavelength, becomes less than approximately one-third wavelength so that it is no longer well matched to space. The high-frequency limit occurs when the size (in this case five feet) of the square mesh comprising the lens becomes greater than about one-sixth wavelength.

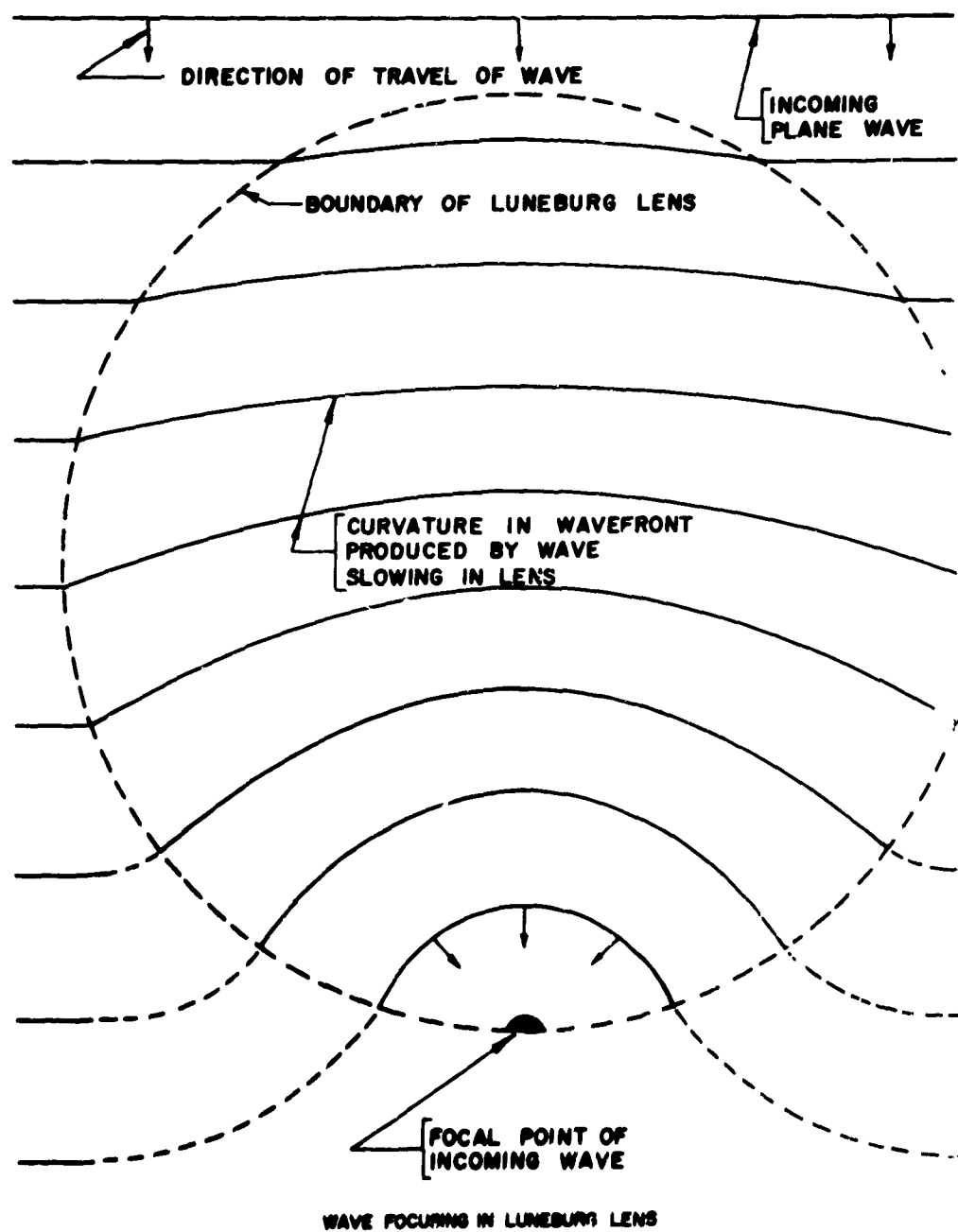


Fig. 2.2 Focusing Action Due to Wave Slowing in Luneburg L.

3. CONSTRUCTION OF WIRE-GRID LENS

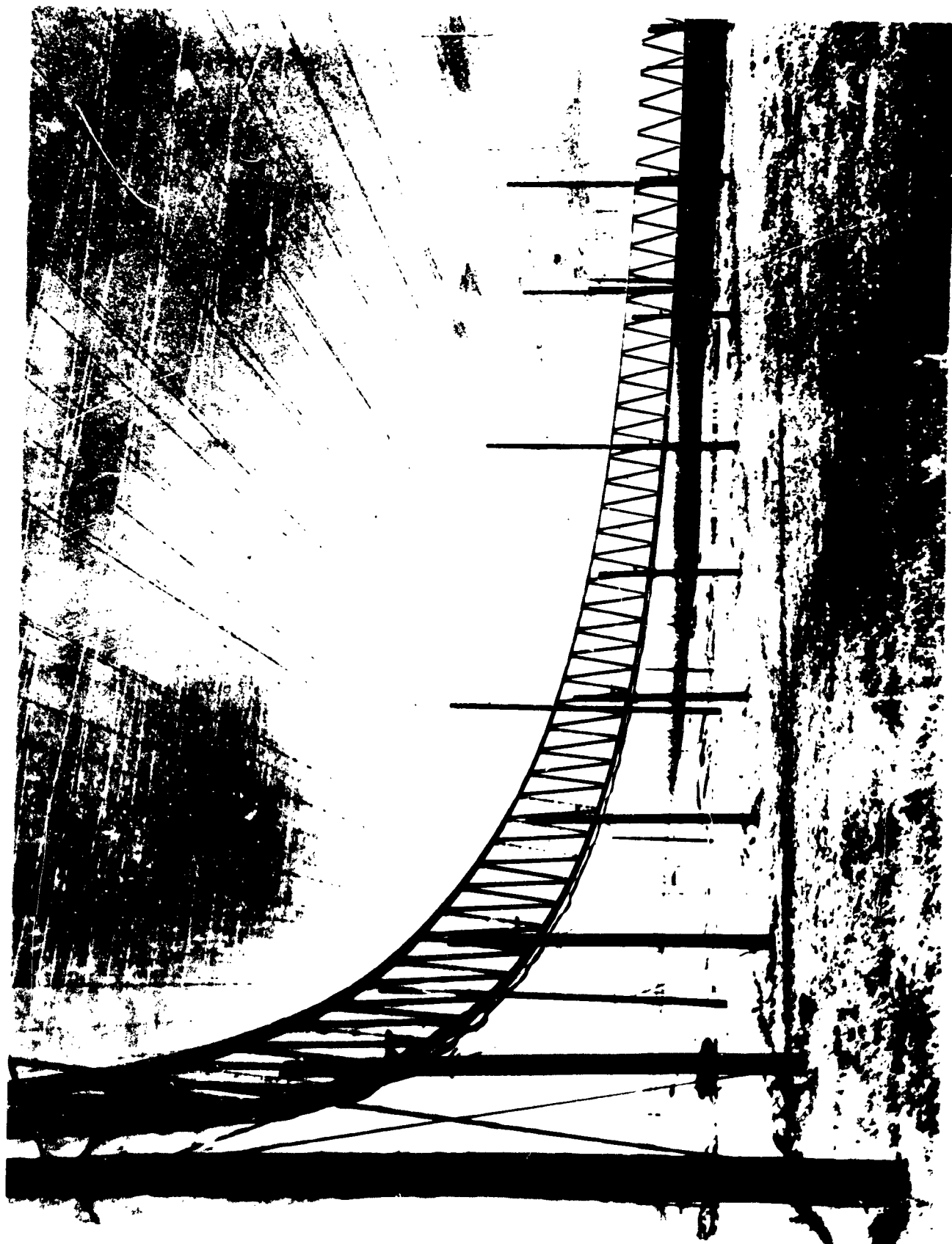
Figures 3.1 through 3.6 are photographs of the Wire-Grid Lens in Molokai which permit a visualization of its construction. Figure 3.1 is an aerial view showing the lens to the right and the station receiver building to the left. Also visible in the photograph are the poles of a few of the rhombic antennas installed at the station. Figure 3.2 is another aerial view from a lower altitude. On close examination, the wire grids composing the lens can be discerned.

Figure 3.3 is a view of the lens from underneath and near one edge. The construction and support of the compression ring truss which, in turn, supports the grids of the lens, can be seen in this photograph. The truss is composed of upper and lower chord rings, fabricated from special aluminum extrusions, tied together by diagonal web members of impregnated timber. The upper grid of the lens is carried by the upper chord ring and the lower grid by the lower chord ring. The depth of the truss, which determines the spacing of the grids at the edge of the lens, is twelve feet. Another feature of the lens, visible in the photograph of Fig. 3.3, is the satellite wires of the grids. For electrical reasons, it would be desirable to have the grids at the edge of the lens spaced a distance even greater than twelve feet. A greater spacing than this cannot easily be accommodated structurally, but the equivalent electrical effect is achieved by paralleling each of the principal wires of the grids by a satellite wire. These satellite wires are installed only in the outer forty feet of each grid. The distance between the main grid wires and their satellite wires varies in this region from zero at the inner edge of the region, where the satellite is connected to the principal wire, to two and one-half feet--or half the mesh size--at the outer edge of the lens.

Figure 3.4 is a view across the lens in which the wires of both the upper and lower grids are clearly distinguishable. Also visible are several of the impregnated wood spacers which maintain the proper spacing between the grids.

Figure 3.5 shows a portion of the upper horn surface which consists of radial wires attached to a cable stretched between the tops of the tall outer poles. Joining the radial wires are short lengths of transverse, or circumferential, wires. These provide required paths for circumferential currents, and are installed only in the inner thirty percent of the horn. Installing the circumferential wires in staggered rows as shown imparts a flexibility and elasticity to the completed panel which facilitates handling and installation. Figure 3.6 shows a





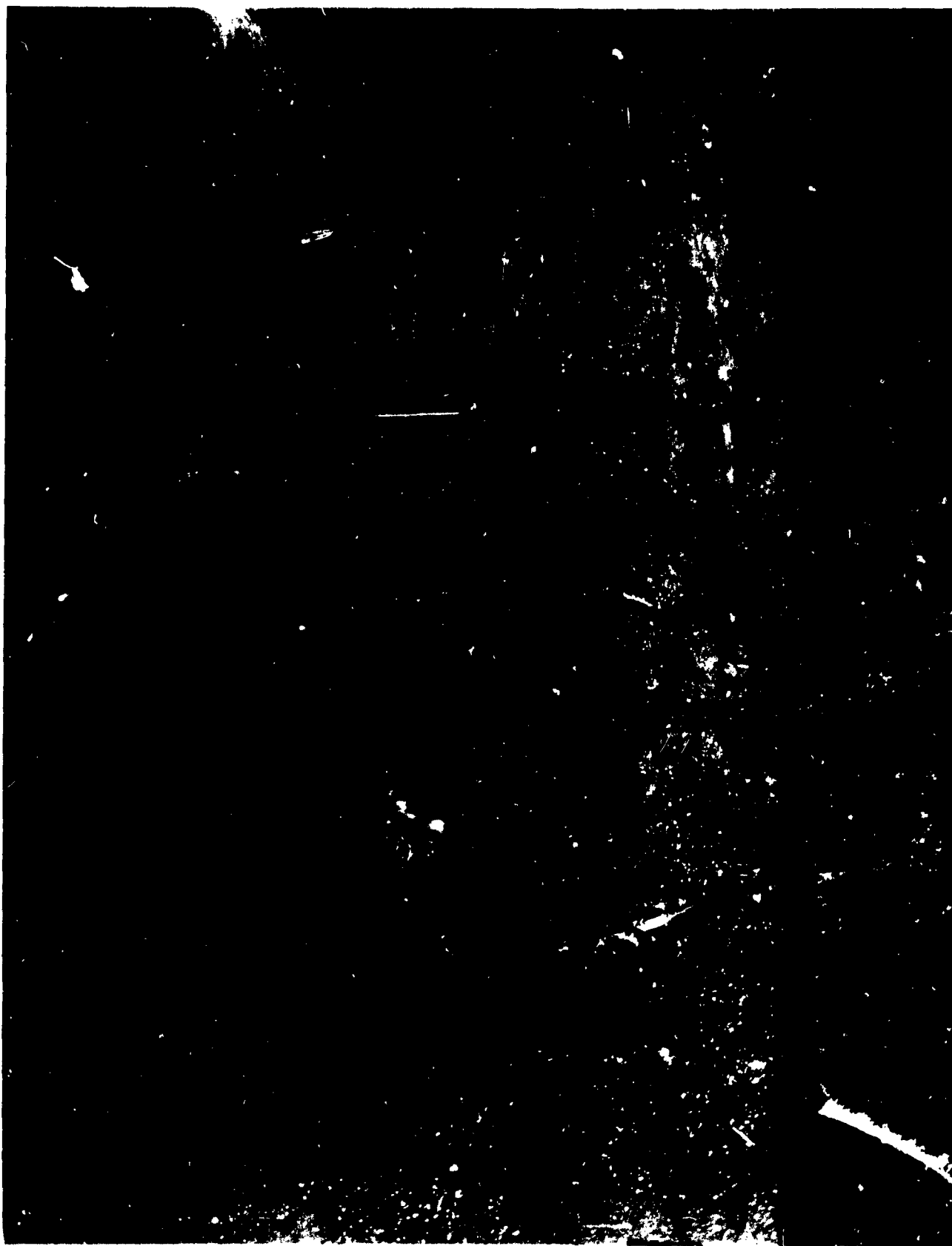
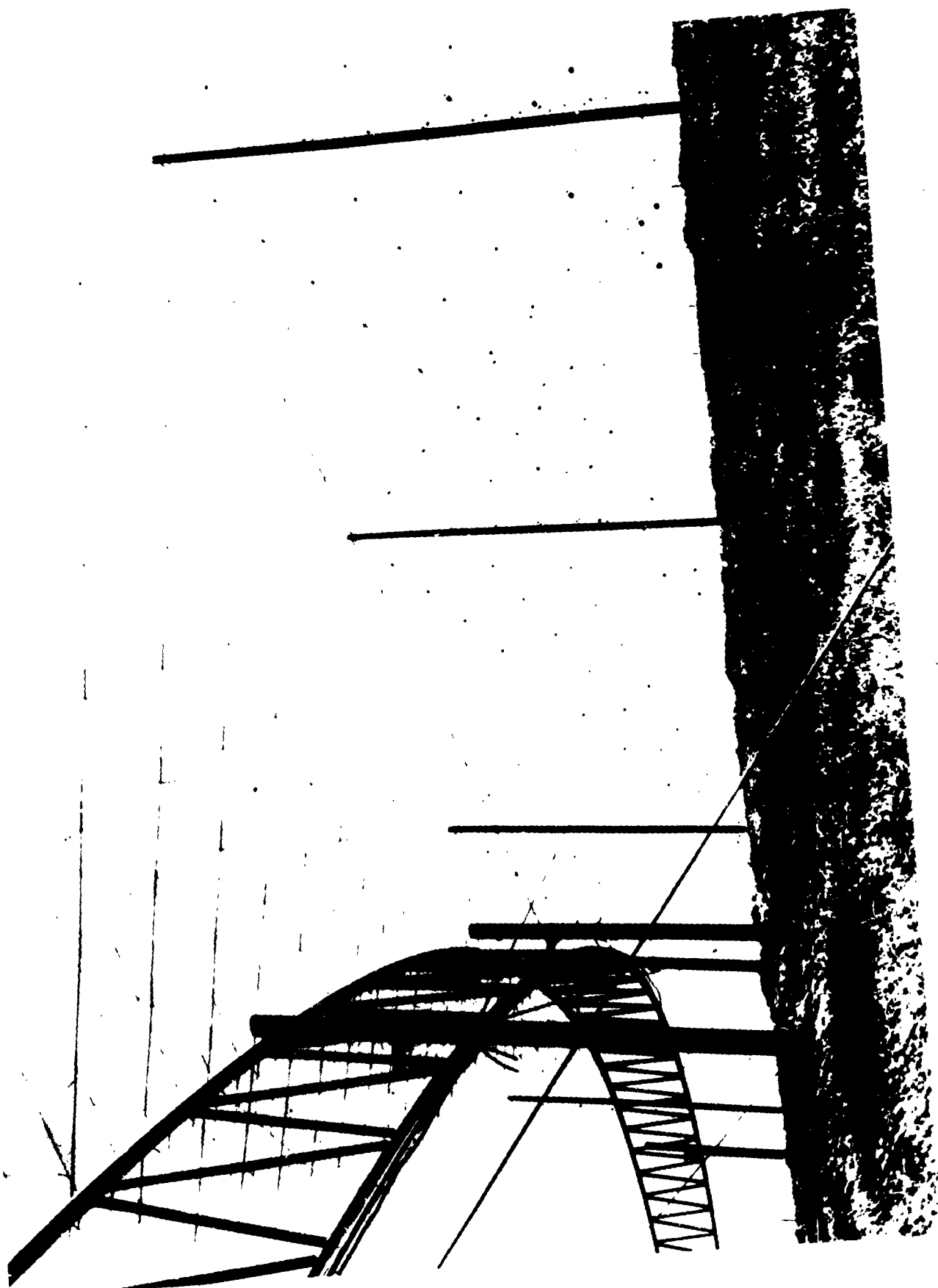


Fig. 3.4 View Across Lens Showing Lens Grains and Grain Spacers





portion of the completed horn, in which both the upper and lower horn surfaces are visible. As indicated previously, the upper horn surface extends between the upper chord ring of the truss and a support cable stretched between the tops of the outer poles. The lower horn surface extends between the lower chord ring and a similar cable stretched between the outer poles at points seven feet above the ground.

4. DESCRIPTION OF ANTENNA SITE AND LOCATION OF TEST ANTENNAS

The FAA Receiver Station on the Island of Molokai, Hawaii, is located on the North side of the Island as shown in Fig. 4.1. The site is generally gently rolling red soil covered with grass on which cattle graze. The rhombic antennas on the site are mounted parallel to the ground so that most of them are tipped slightly from the horizontal. The lens is also mounted parallel to the ground and is tipped approximately three degrees from the horizontal.

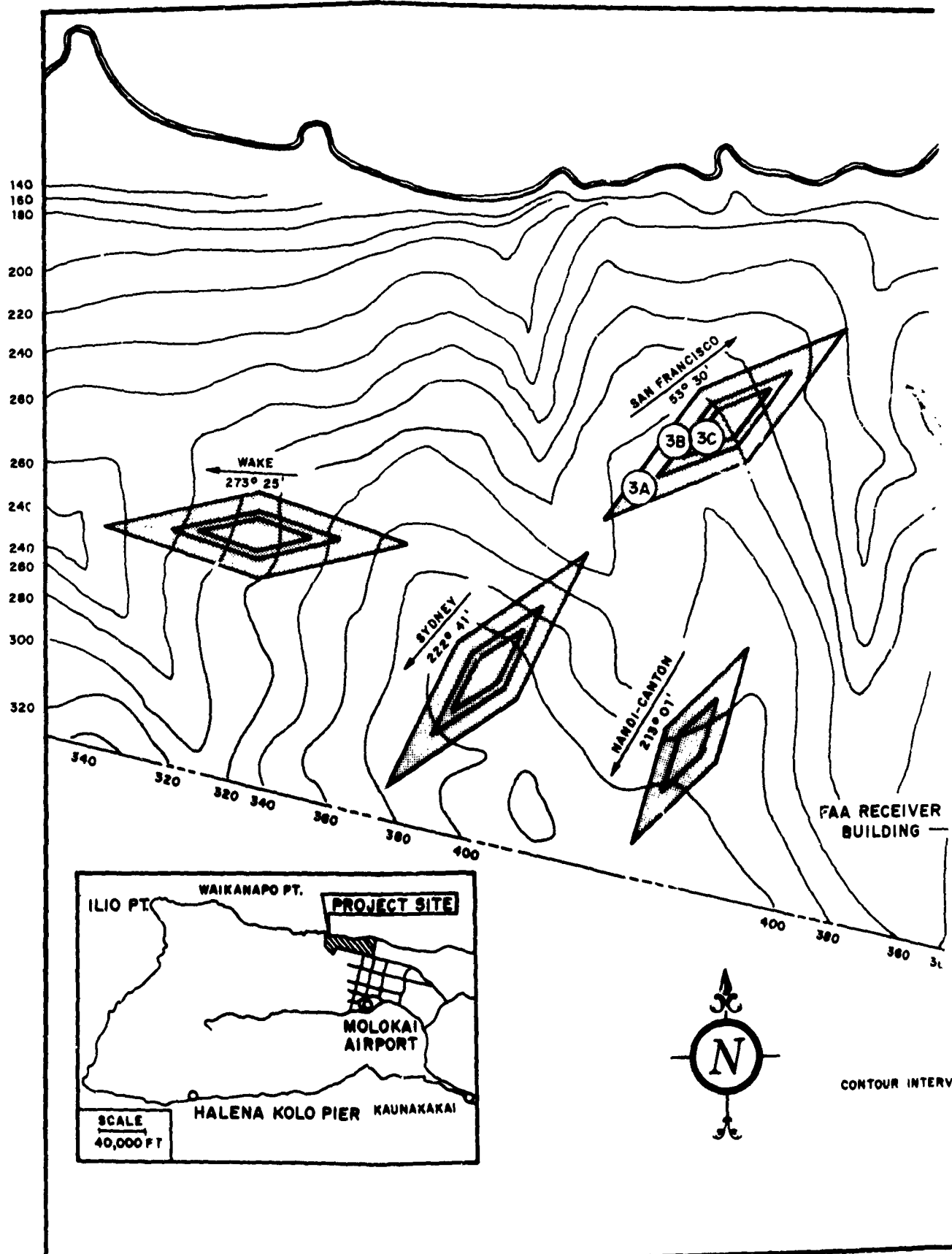
The land beneath the lens and immediately adjacent to it is quite smooth. However, at a distance of approximately one mile to the North, the land drops precipitously nearly 400 feet to the ocean. To the East the ground rises smoothly to a large knoll, while to the West and Southwest, at a distance of about one-half mile, there is a deep gully. These variations in ground elevation have an appreciable effect on the patterns, as can be seen from an inspection of the patterns of the various lens feeds in Appendix B and the summary pattern data in Sec. 6.6. Another perturbing influence on the patterns is the presence of the approximately 100-foot long vertical counterweight cables of the nearby Sydney and Samoa rhombics which are parallel to the incident vertically polarized electric field received by the lens.

Besides the station rhombics, several auxiliary antennas were used at the receiver site during the evaluation, and their locations are also shown on the map. One of these is the Rawin AN/GMD-13 Weather Balloon Tracker, which was used to track the airplane towing the Xeledop transmitter during the pattern tests (see Sec. 6.2.2). Another was the double dipole array (see Sec. 7.3) which was used as a gain standard antenna. A third was an approximately 15-foot high NRL-furnished monopole, mounted over a radial ground which was used as a reference antenna. The fourth was a monopole mounted above the upper grid in the lens center. This monopole, which was used as a reference antenna during the preliminary evaluation, was not used in this Joint Services Evaluation.

The fifth antenna used during the evaluation was the Wire-Grid Lens Antenna operated as an omniazimuthal biconical antenna. For this mode of operation, connection was made to the center of the lens by means of a coaxial line. The outer shield of the coaxial line was connected to the lower lens grid. The extended center of the coaxial line was connected to the upper lens grid through a 1,000-ohm isolating resistor which decoupled the omniazimuthal feed from the other directive feeds, thus preventing their patterns from being distorted by the omniazimuthal feed.

Each of the seven operational traffic circuits at the FAA Receiver Station has two rhombics spaced several thousand feet apart to service it in space diversity. The rhombics on the San Francisco, Sydney, and Wake circuits consist of nests of three rhombics. The outside member of each nest is mounted on 120-foot poles, while the poles of the smaller members are proportionally shorter. Each of the rhombics in a nest can be operated separately to cover a 3/1 bandwidth. Using the three rhombics, the HF frequency range is covered in three overlapping bands. In each nest, the A rhombic operates over the 3 to 10 Mc frequency band, the B rhombic over the 6 to 18 Mc frequency band and the C rhombic over the 9 to 27 Mc frequency band. The maximum length of the A rhombics is 1,550 feet, while their maximum width is 430 feet. The rhombics on the Samoa, Anchorage, Tokyo and Nandi-Canton circuits consist of nests of two rhombics and cover a more limited frequency range. The maximum length of the lowest frequency rhombics in these nests is 1,125 feet and their maximum width is 320 feet. These rhombics are mounted on 90-foot poles.

Seven feeds were installed in the Wire-Grid Lens HF Antenna so that it could receive from the same directions as the station rhombics. The azimuthal positions of these feeds within the lens are shown in Fig. 4.2 together with the bearings of the various transmitting stations.



A

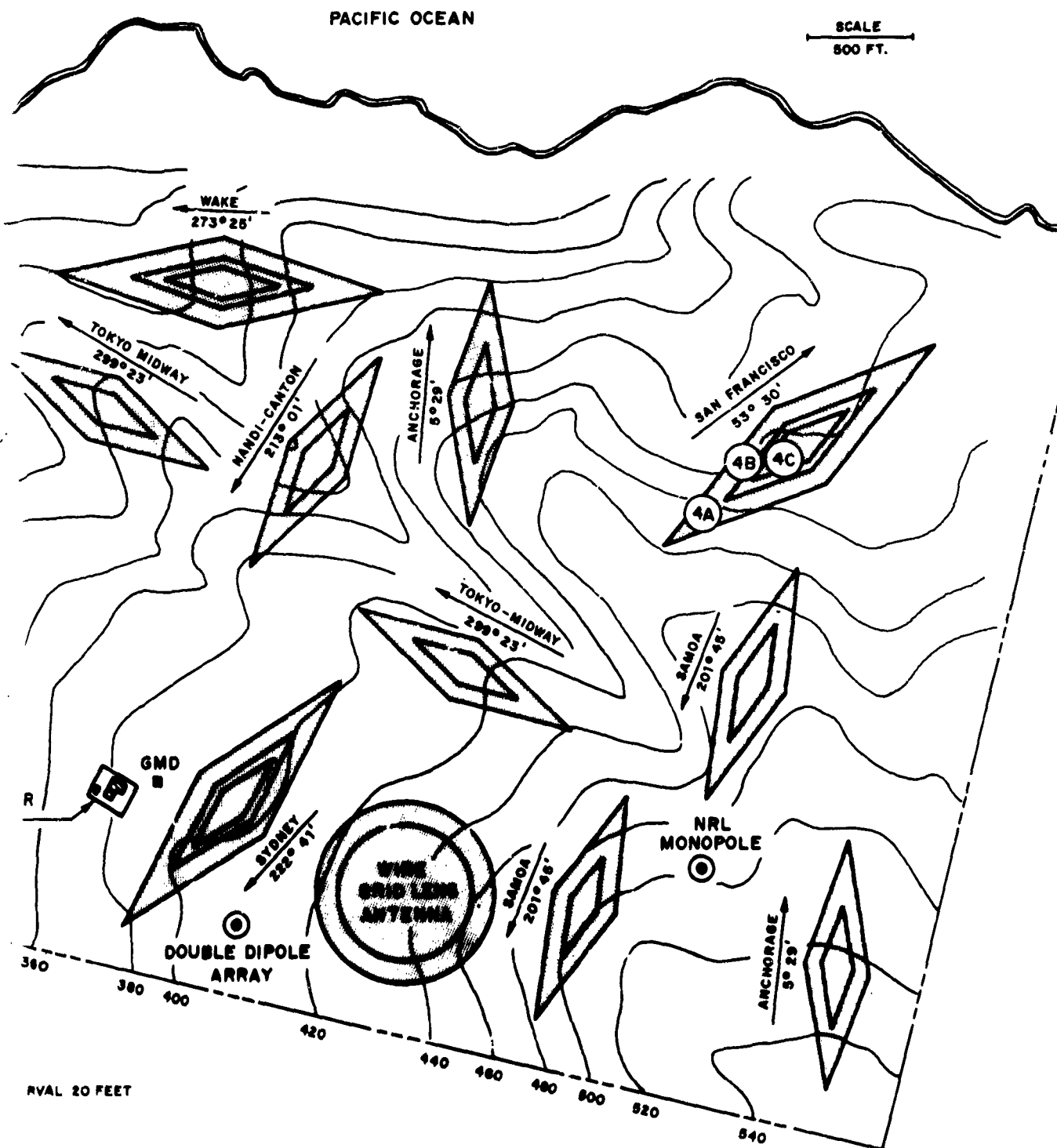


FIG. 4.1 ANTENNA LOCATIONS AT FAA INTERNATIONAL
FLIGHT SERVICE RECEIVER STATION MOLOKAI,
HAWAII

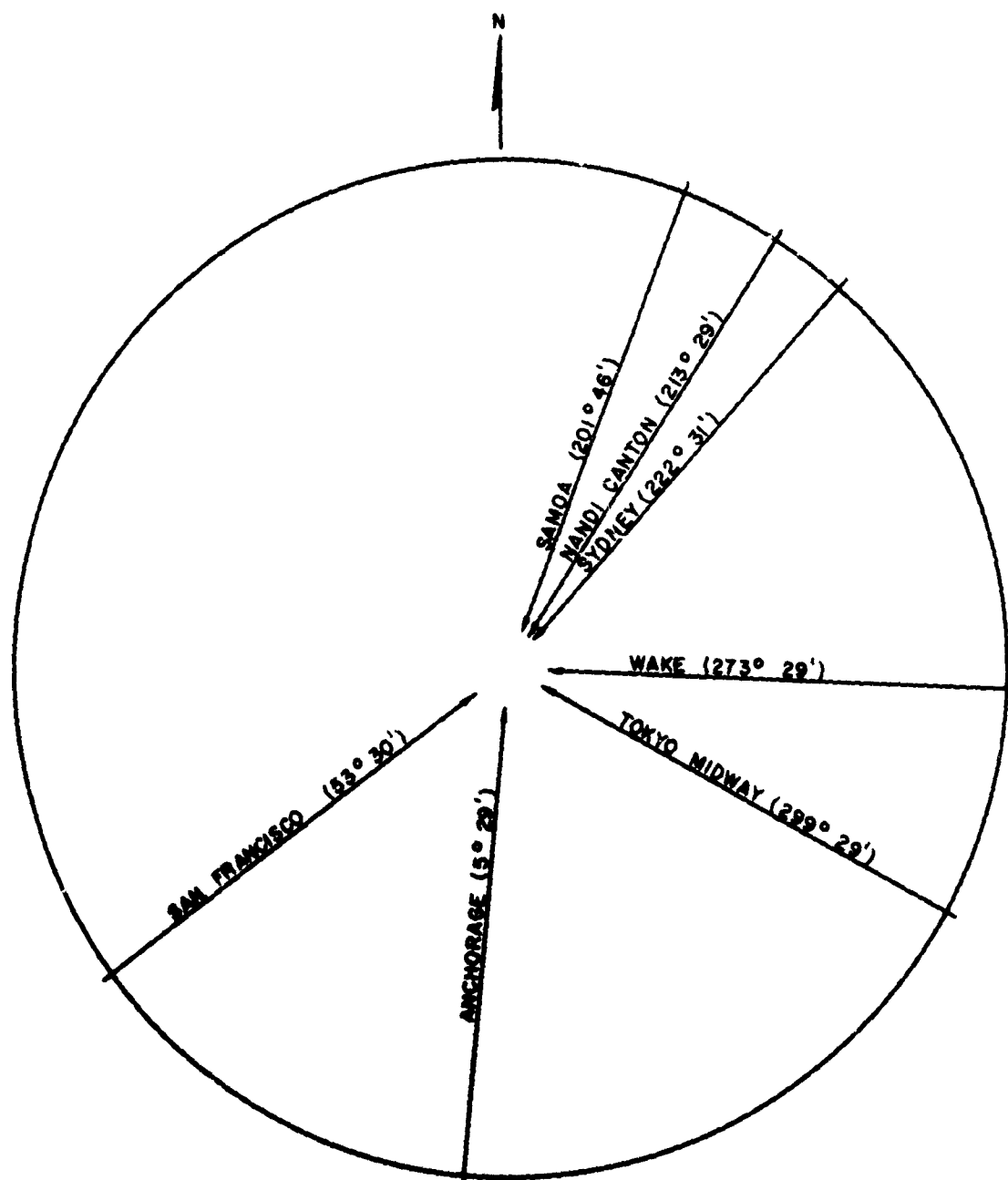


Fig. 4.2 Feed Locations in the Lens Antenna

5. LENS FEEDS AND THEORETICAL AZIMUTH PATTERNS

The theory of operation of the initially installed feeds in the Molokai Wire-Grid Lens Antenna which were used during the Joint Services Evaluation has been described in detail in References 1 and 2. Briefly, each feed consists of two end-fire arrays connected in parallel. Each extends from the edge of the lens towards the center, a distance equal to one-fourth the lens radius, or 75 feet, as illustrated in Fig. 5.1. The particular end-fire array used in these feeds is illustrated schematically in Fig. 5.2 and consists of a transmission line, commonly called a ramp, running diagonally from the outer edge of the lens at the lower grid to the three-fourths radius point on the upper grid. Dipoles running vertically from the upper to the lower grids at each end of the ramp are excited through the networks indicated at either end of the ramp to carry currents having the magnitude and phase indicated in the figure. As shown in References 1 and 2, this array is equivalent to a traveling wave array of magnetic dipoles or loops and has a null at right angles to the plane of the array. This feature of the array is particularly advantageous because it minimizes the excitation of the higher order circulating azimuthal modes within the lens, thus minimizing the side lobes of the radiation pattern, particularly at the low-frequency end of the band.

At the low-frequency end of the band, the spacing between the two arrays in a feed is so small in terms of wavelength that it is electrically equivalent to a single array located halfway between them. However, at the high-frequency end of the band the spacing between the arrays is an appreciable fraction of a wavelength and the pair of arrays in the feeds has a much narrower azimuth beamwidth (within the lens) than a single array located halfway between the two arrays would have. Therefore, thinking of the antenna as a transmitter for the moment, the aperture of the lens is illuminated only over its central region by this feed at the high end of the band. Thus, the azimuth beamwidth, which by reciprocity is the same for transmission and reception, is greatly increased over the value it would have if the feed consisted only of a single array. This increase in azimuth beamwidth at the high end of the band enables the lens to be receptive to sky-wave signals deviating from the great circle path, by more than would be possible from the use of a single array feed.

The ramp used in these feeds consists of a pair of wires having a varying center-to-center spacing that are capacitively loaded by metal strips attached to the ramp wires and wooden struts used to position the ramp wires. The center-to-center spacing of the wires in the ramp and the size of the capacitive loading elements are adjusted to maintain the characteristic impedance of the ramp constant at 190 ohms and the average propagation velocity of a wave on the ramp

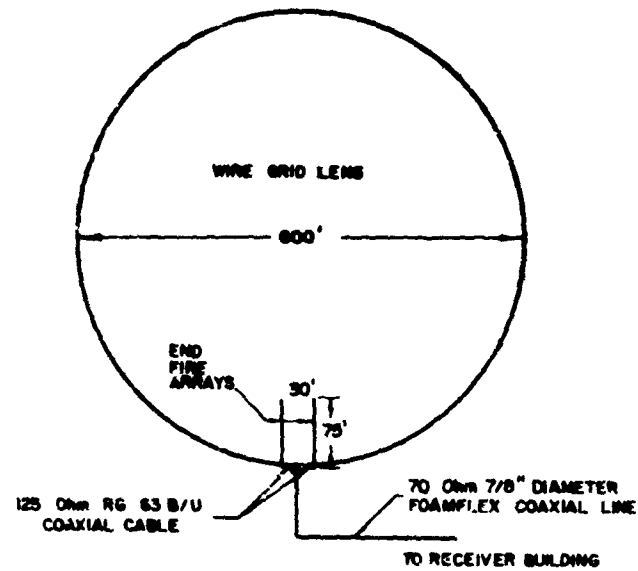


Fig. 5.1 Plan View of Typical Feed in Molokai Wire-Grid Lens Antenna

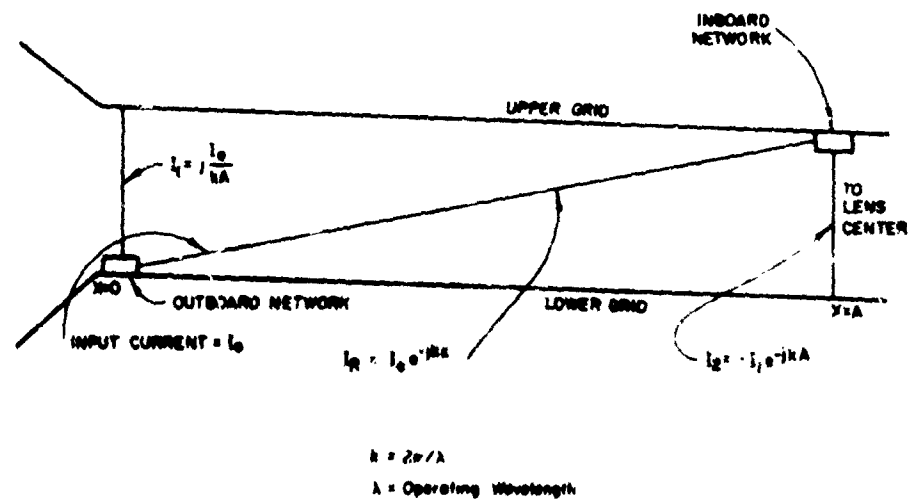


Fig. 5.2 Idealized Currents on Feeds Consisting of a Ramp and End Dipole Elements

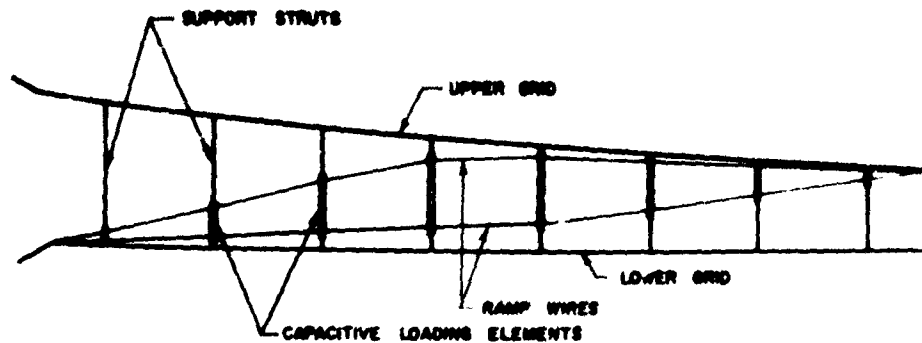


Fig. 5.3 Physical Configuration of Ramp Used in Feeds

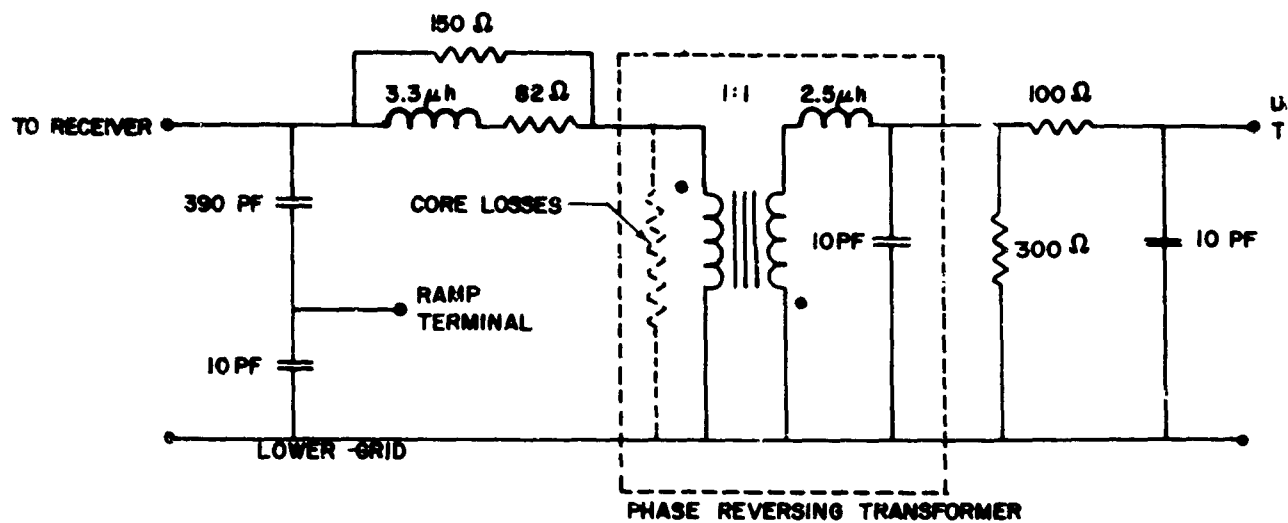
constant at a value equal to that of a wave propagating between the grids. A drawing of the ramp element used in these feeds is shown in Fig. 5.3.

The phasing networks used to establish the currents in the end dipoles are shown in Fig. 5.4.

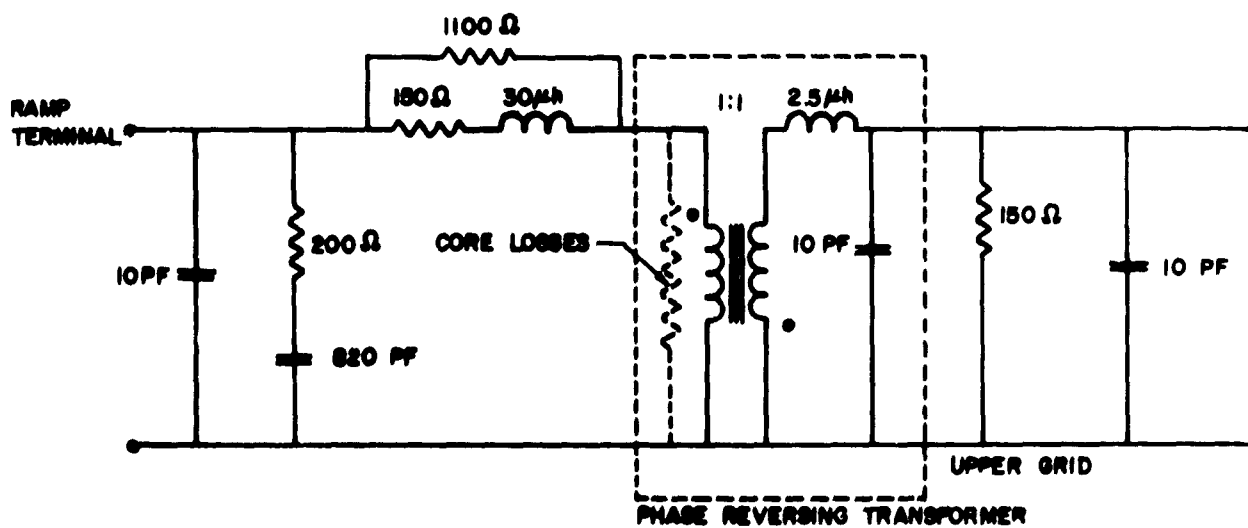
Since the feeds for the Molokai Wire-Grid Lens were designed, the electromagnetic behavior of the lens has been analyzed in considerably more detail on various contracts. 6, 7, 8, 9 As a result of these studies, it is now possible to predict the various properties of the lens, such as patterns, directivity, and efficiency, with considerable accuracy. Using these sophisticated analyses, the patterns and feed efficiency of the lens have been calculated taking into account mutual coupling among all elements of the feeds.

The theoretical azimuthal patterns of the lens are shown in Fig. 5.5 computed for the case that the lens is mounted over a flat earth with a conductivity of 5×10^{-3} mhos per meter and a relative dielectric constant of 15. Each of these patterns is a conical cut taken at the calculated elevation angle θ corresponding to the peak of the main beam. These patterns have a 3-db beamwidth varying from 24 to 7 degrees and acceptably low minor lobes over the complete 3 to 30 Mc band, except at the low end of the band where the minor lobes are somewhat higher than desirable.

The theoretical feed efficiency which is shown in Fig. 5.6 is seen to be quite low. The principal reason for this low efficiency is that the networks, shown in Fig. 5.4, used to establish the proper dipole currents contain resistive elements.



OUTBOARD NETWORK



INBOARD NETWORK

Fig. 5.4 Equivalent Circuits of Inboard and Outboard Phasing Networks on Feeds

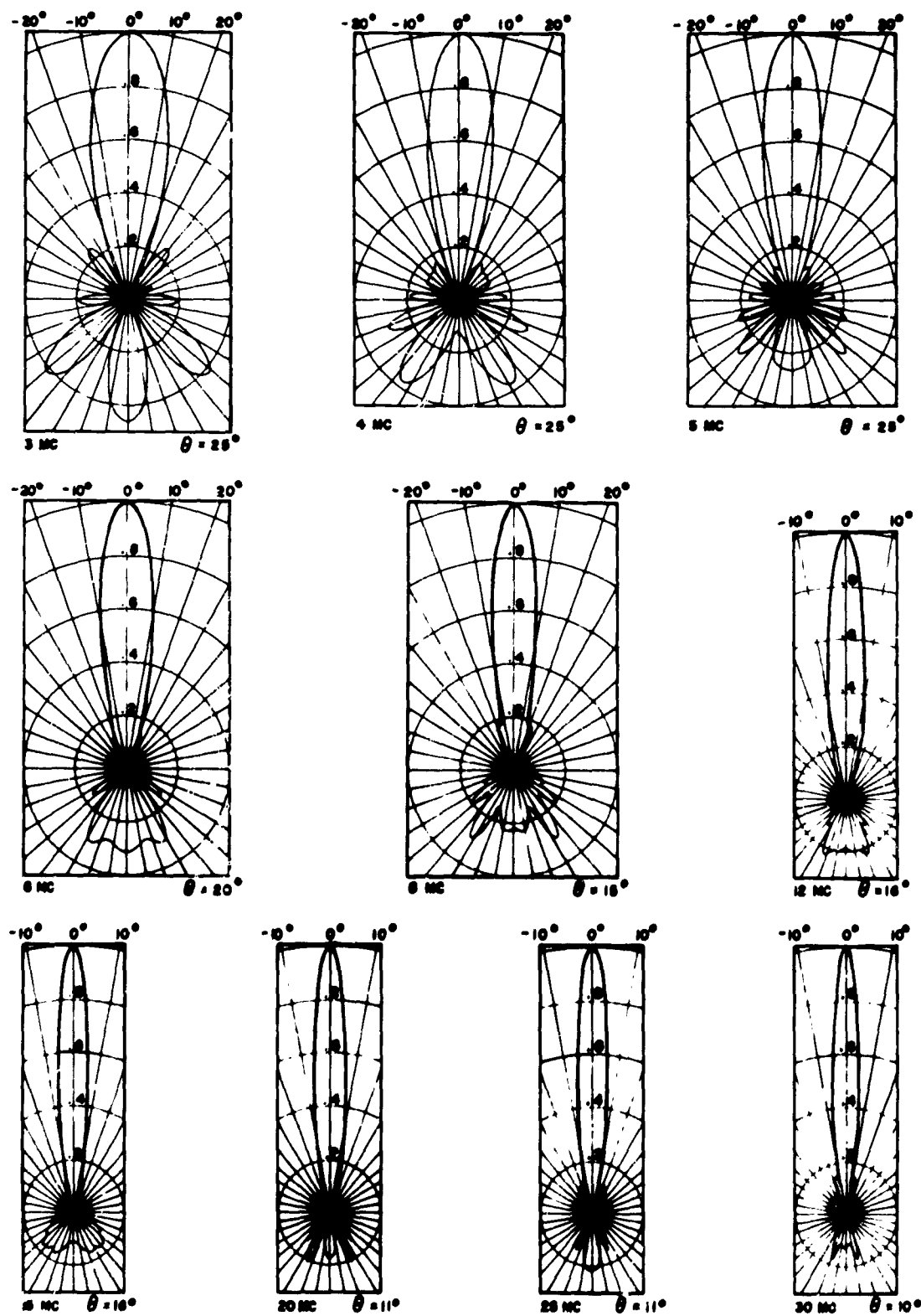


Fig. 5.5 Calculated Azimuth Voltage Patterns of Wire-Grid Lens Antenna at the Elevation Angle, θ , Corresponding to the Peak of the Main Beam

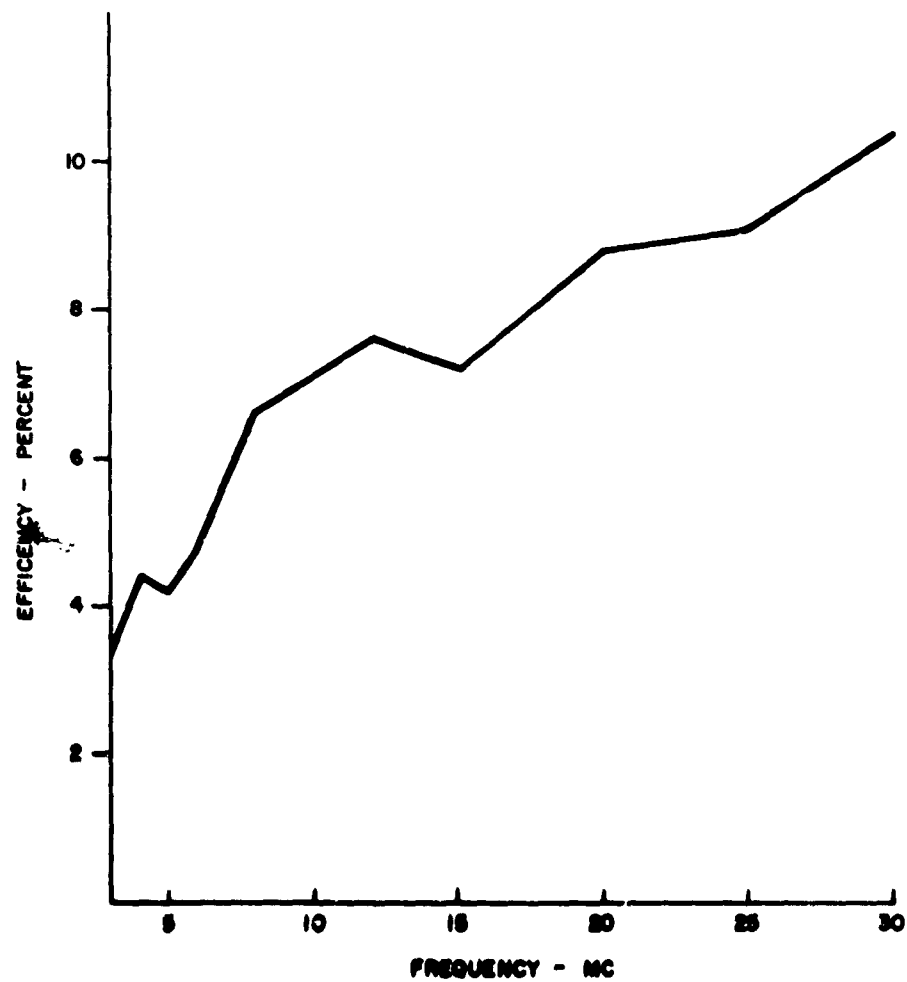


Fig. 5.6 Theoretical Efficiency of the Feeds

6. MEASUREMENT OF RADIATION PATTERNS

6.1 Introduction

This section describes an important phase of the Joint Services Evaluation to measure the radiation patterns of the Wire-Grid Lens Antenna (designed to operate from 3 to 30 Mc) and various reference antennas located at the FAA receiver station Molokai. These measurements were made over the 2 to 35 Mc band to test not only the in-band, but also the out-of-band performance of the Wire-Grid Lens Antenna. The patterns were measured by Stanford Research Institute under subcontract to TRG by towing a special transmitter (the Xeledop*) in circles around the site at various elevation angles. The transmitter position as well as the signals received by the antennas being tested were recorded simultaneously by Stanford Research Institute personnel and Naval Research Laboratory personnel. Later, SRI scaled these data into punched cards and plotted them as stereographic contour maps, each showing the antennas's response to one frequency and polarization. From these contour plots some of the more conventional polar cuts and elevation cuts were generated.

6.2 Flight Tests

6.2.1 Xeledop Transmitter

The heart of the measuring system is the Xeledop transmitter. On a cycle of about 1.5 seconds, it pulses through four to eight selected frequencies between 2 and 35 Mc. The electronics and batteries are contained in the central sphere as shown in Fig. 6.1. The arms extending out from the sphere are fed as a balanced dipole antenna whose total length is always less than $\lambda/2$.

The Xeledop can be towed to radiate either horizontally polarized (E_ϕ) or vertically polarized waves (E_θ). The electrical symmetry of the Xeledop is such that its radiated polarization depends only upon its physical orientation. The fins and drag cone shown in Fig. 6.1, with changes in weighting, assure horizontal or vertical orientation in flight to within a few degrees. Reflections from the aircraft are effectively eliminated by towing the Xeledop 250 feet below and behind the plane with a dielectric rope. It has been confirmed--

* An acronym denoting transmitting elementar / dipole with optimal polarization.

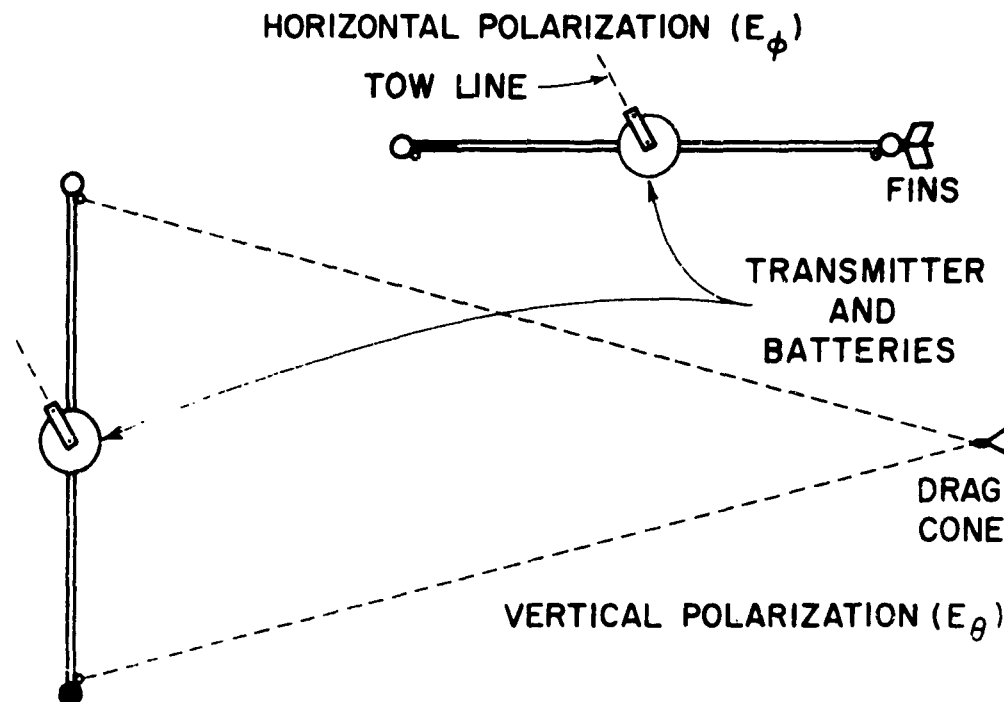


Fig. 6.1 Xeledop Configurations for Vertical and Horizontal Polarizations

by movies of the device in flight and antenna null measurements-- that the cross-polarized component radiated is down at least 25 db for either Xeledop orientation. Because all the hardware was designed to be electrically identical for towing vertically and horizontally, the transmitter power outputs do not change with change of polarization. Hence, in either polarization the device very closely approximates a theoretical elementary dipole source, allowing direct and valid comparisons between the E_ϕ and E_θ antenna patterns and gains.

6.2.2 Aircraft Guidance and Tracking

In addition to the Xeledop transmitter, the aircraft carries a small beacon transmitter and a modified transponder unit. Both are used for position information, the beacon being tracked by ground equipment to provide azimuth and elevation angles for data reduction, and the airborne transponder working with a similar unit on the ground to indicate slant range for the pilot's information.

The ground tracking unit is a Rawin AN/GMD-1B Weather Balloon Tracker, referred to as the GMD operating at a frequency of 1,688 Mc. It uses a steerable dish antenna to follow the aircraft beacon transmitter, and it prints, on adding machine paper, the azimuth, the elevation, and a sequence number (called the GMD Time) every six seconds. Since the angles recorded by the GMD are used later, along with the plane's altitude, to compute the Xeledop's position in space, the accuracy of the GMD is highly important. This accuracy--checked with a built-in optical transit--is more than adequate (less than 0.3-degree error in each angle) in all cases but one, that of elevation angles less than 6 to 8 degrees. At these low angles, ground-reflected rays from the beacon are as strong or stronger than the direct ray, so the tracker does not measure the elevation angle consistently or correctly. The azimuth readings, however, remain accurate. In the case of those low angles, the radius of the pilot's orbit is assumed--for data reduction--to be known (an average of actual ranges calculated from runs at higher elevation angles), rather than computed exactly from the elevation angle and the aircraft altitude. It is interesting to note that the GMD was not affected by the maze of lens and rhombic wires at the Molokai antenna site.

The transponder system aids the pilot in flying accurate orbits, permitting operation without ground reference points (as above water or a cloud deck). This system (termed the Pilot's Deviation Indicator or PDI) measures the slant range between aircraft and ground site and continuously displays to the pilot, on a meter, deviations from a pre-set slant range. The result is a left-or-right indication showing the pilot how well he is maintaining his orbit. Although the measured ranges are not recorded for use in data reduction, the PDI serves two vital functions:

- (1) It allows the assumption of a perfect orbit for the reduction of low-angle data, as noted above,
- (2) By improving the pilot's orbits, it provides more nearly constant elevation angles, so that all the angles desired can be covered without redundancy, and no gaps will appear in the contour plots for lack of data at some angles.

Cross checks between the actual aircraft flight paths and the desired paths, made with and without the PDI, have shown that the PDI is very helpful, reducing range variations at a 5-mile radius from about a mile to less than a tenth of a mile.

To find the aircraft position in space, a third parameter is required, besides azimuth and elevation or slant range. The aircraft's

altitude has been chosen for this, because a pilot can normally hold an assigned altitude with sufficient accuracy (± 50 feet) using his standard barometric altimeter. No continuous recordings are made of altimeter readings; the altitude is assumed to be held constant at the desired value during any given run.

For this measurement program, the various elevation angles to be measured were obtained by increasing the aircraft altitude from one orbit to the next, using the same slant range with a total of nine data orbits to cover the 3 to 55 degree range for vertical polarization flights and four to five orbits in the limited 5 to 30 degree range for horizontal polarization. The slant ranges were chosen to exceed $2D^2/\lambda$ for the lens antenna aperture. For the extreme of the frequency range (35 Mc) the slant range should have been at least 5 miles. Since the aircraft's operating ceiling was 21,000 feet, the range had to be reduced to measure high elevation angles. During the actual measurements, the range varied from 4 to 8.5 miles. The range was never less than D^2/λ , however, so the amplitude errors introduced by the reduced ranges should have been less than a few per cent¹⁰ and thus are negligible.

6.2.3 Receiving and Recording Technique

Patterns on the Anchorage, Nandi-Canton and Sydney lens feeds and double dipole reference antenna were recorded simultaneously by SRI using the receiving recording system shown in Fig. 6.2. Pattern data were also simultaneously recorded by NRL personnel utilizing additional multicouplers and strip recorders on the San Francisco lens feed, the reference monopole, the lens excited at its center to operate as a biconical antenna, and the FAA San Francisco rhombics 4A, 4B and 4C. A system similar to that shown in Fig. 6.2 was used for the NRL recorded data. The dotted line indicates the measurement terminals and the point of calibration for both the SRI and NRL recorded data.

Each test antenna looked into a standard load (within 1.5 to 1 VSWR referred to 50 ohms) at this point; the voltages recorded across these loads were the primary relative-gain information (see, for example Fig. 7.2). These measurement terminals led to multicouplers which, in turn, fed AN-R390A/URR receivers, one for each antenna at each measurement frequency. For most of the antennas, the AGC outputs of the receivers were used to drive the pens of the multichannel strip-chart recorders. The AGC circuitry within the receivers had been modified to extend their logarithmic response characteristics at low signal levels to give a useful dynamic range of about 100 db. Since these recorders could display only 40 db of change without sacrificing

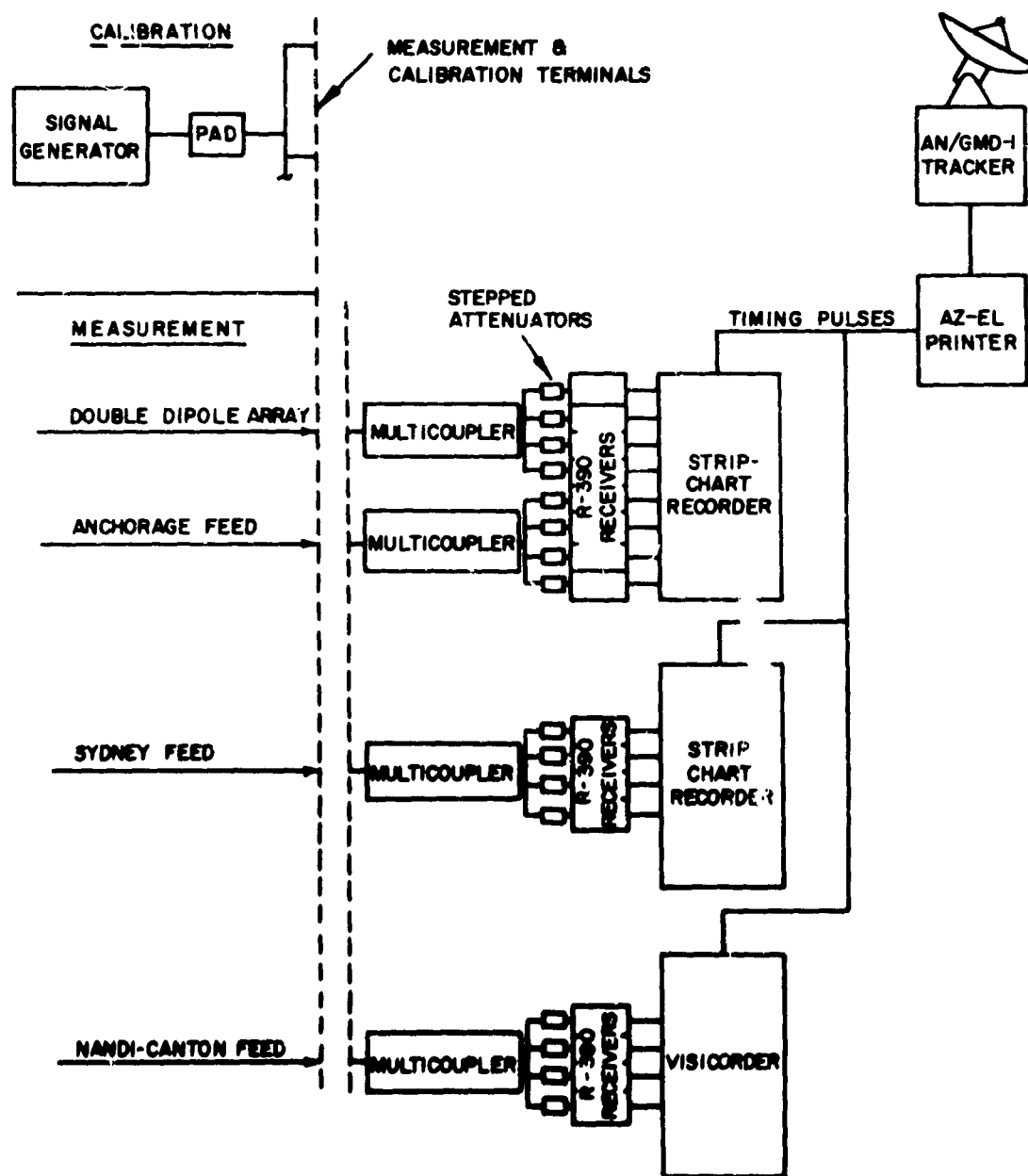


Fig. 6.2 Block Diagram of Measuring System Used by Stanford Research Institute. A similar measuring system was used for the data recorded by the Naval Research Laboratory

amplitude resolution, push-button attenuators were used before each receiver. The operators set these attenuators to keep the input signals within the recorder response range. Since the minimum attenuator step size is 10 db, errors occurring in field marking or later handling of these settings could be readily detected during the data-reduction process.

For the Nandi-Canton feed patterns a Visicorder was used to record the signals. However, the impedance of the AGC was too high to drive the galvanometers. Therefore, it was necessary to generate a 3-kc tone with the receiver's beat-frequency oscillator, rectify and filter the audio output, and use it to drive the galvanometers. The resulting signals were noisier than the AGC outputs; an ambiguity was thus introduced into the scaling of these records. The operator could not monitor the recording because the traces were recorded photographically on special paper taking several seconds to "develop," and the traces had to be overlapped to get sufficient resolution. Hence, no attenuators could be used, and each channel was set for a 70-db dynamic range. Since the response was compress for high signals, the main-beam amplitude resolution was not equal to that of the pen recorders.

Esterline Angus recorders were used to record signals from the lens used as a biconical antenna at frequencies of 2.6 Mc, 15.3 Mc Rhombic 4A at 4.1 Mc and 5.6 Mc; Rhombic 4B at 5.6 Mc; and the NRI monopole at 9.1 Mc, 15.3 Mc and 21.5 Mc. Because the response time of the Esterline Angus is quite slow, the accuracy of these patterns is less than that of the other patterns.

For calibration all the antenna input terminals were connected in parallel at the interface of a Hewlett-Packard Model 606A signal generator padded down to 5-ohm output impedance. A voltage staircase in 10-db steps was recorded on each channel before each orbit. Although a known voltage range was recorded on each channel, gains cannot be compared between frequencies because the Xeledop's actual radiated power is not known.

To correlate the amplitude recordings with the GMD azimuth and elevation data, a marker pulse was put on both strip charts when the GMD time was advanced. The operator positively identified certain pulses by deleting them and labeling the blank spot. When numbered, a pulse directly related a pair of printed azimuth and elevation readings to a position on the strip charts.

6.3 Data Reduction

The capability of the Xeledop pattern-measuring technique for collecting large quantities of data economically depends upon the use of

computers and semiautomatic scaling devices in the data reduction. Each contour plot represents about 1,800 position and amplitude readings or data points, which must be scaled from the strip charts, then corrected, normalized, and contoured. The essential steps in processing the data are summarized here (the computer programs are not needed for an understanding of the results). A block diagram of the processing is shown in Fig. 6.3.

Two sets of data records must be combined to find an antenna's pattern: the amplitude record on the strip charts and the printed azimuth and elevation record from the GMD. The GMD data is simply key-punched into IBM cards. For the strip charts, a semiautomatic Gerber GOAT is used to convert the amplitude data (Xeledop pulse envelope) into an analog signal, which is digitized and punched into IBM cards. The operator reads each point by manually crossing two hairlines over it and pushing a button which triggers the digitizer and keypunch. For patterns in this measurement program, the GOAT was set to read the amplitudes directly in decibels by drawing up a special curved line (one of the crossing hairlines) to match each calibration staircase. The amplitudes were read in parallel from the strip chart, with enough points being taken to define each curve accurately. The GMD time and other identifying information were also recorded on the card. Since each card is unique and complete in itself, the cards do not need to be in any particular order, and incorrect card deck assembly cannot cause undetectable errors in later computer runs.

After the cards have been checked against the original strip charts, the amplitude-data and GMD cards for one antenna and one polarization, with appropriate headers, are fed into a Burroughs B5C00 computer. This machine performs several operations on each amplitude-data card.

- (1) It finds azimuth and elevation angles from the GMD cards for the particular time. If the elevation angles for the run were invalidated by ground reflections, it computes an average value by assuming that the aircraft flew at constant altitude and at the same average slant range as in the previous runs.
- (2) It calculates the aircraft's position from azimuth, elevation, and altitude and then finds the azimuth and elevation of the Xeledop with respect to the antenna (rather than the relationship of the aircraft to the GMD).

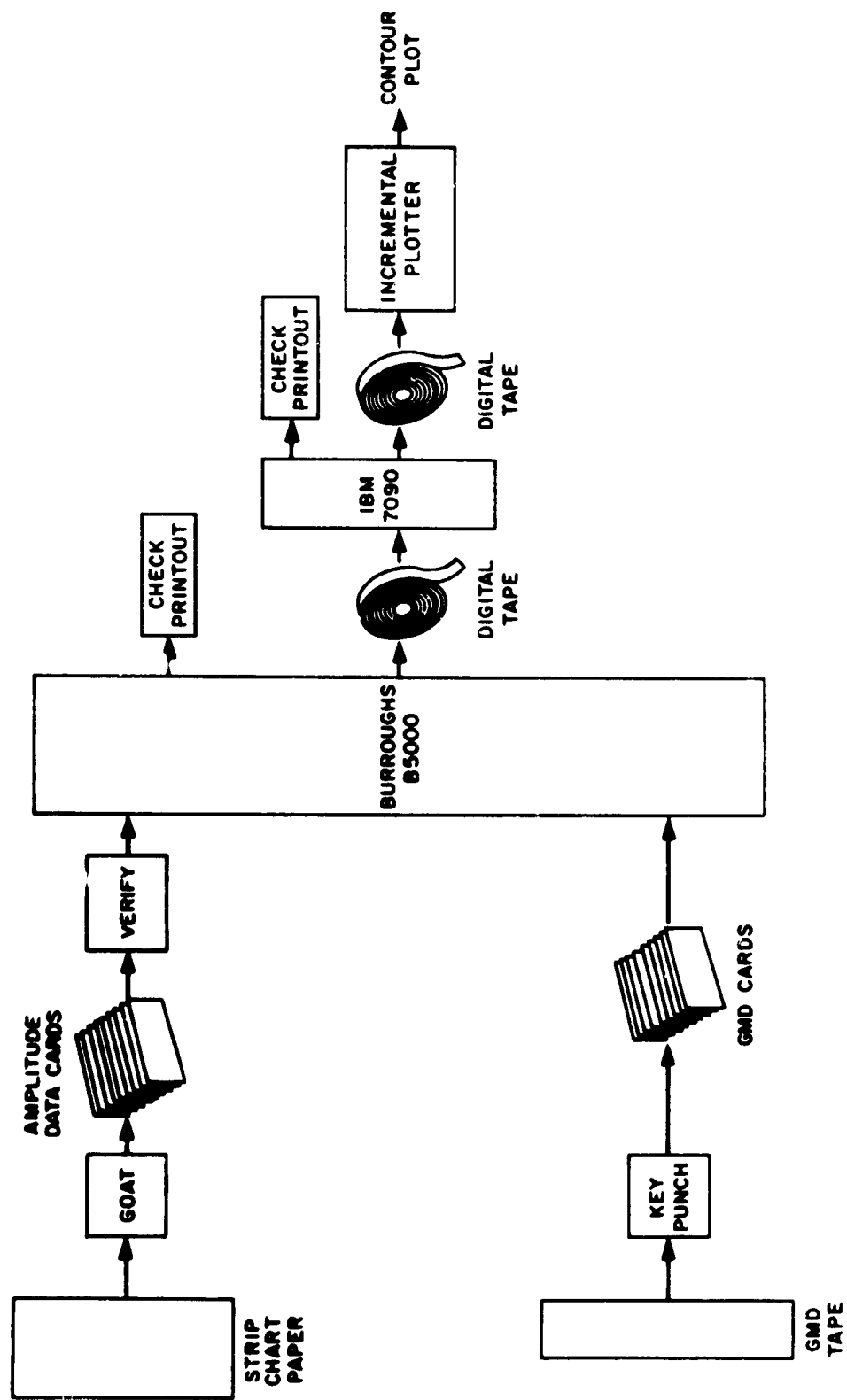


Fig. 6.3 Block Diagram of Data Processing System

- (3) It corrects each amplitude (expressed in decibels) for the attenuator setting.
- (4) It corrects each amplitude for range variations from the nominal 5 miles between the test antenna and Xeledop by adding

$$20 \log_{10} \left(\frac{R_{\text{miles}}}{5} \right) \quad .$$

- (5) If the measurement was taken with vertical polarization, it corrects each amplitude for the Xeledop's transmitting pattern by subtracting

$$20 \log_{10} \left(\cos (\text{elevation angle}) \right) \quad .$$

- (6) It checks for a variety of human and mechanical errors.
- (7) It prints out any error messages.

When it has corrected and checked all the data points, it then:

- (1) Normalizes them, setting the maximum recorded value equal to 0 db.
- (2) Prints out the normalized data points and the maximum values (later used to find relative gains).
- (3) Writes a digital magnetic tape containing all the data and some labeling, in proper format for a contour-plot program.

The printed output of the B5000 is then checked for error messages and improbable data values, and it is rerun if necessary. If the output is all right, the tape is sent to an IBM 7090 computer with a special contour-plotting program.* This program operates in two sections:

* A proprietary item purchased from Computer Laboratories, Inc., Houston, Texas.

- (1) It takes the random input data and finds equivalent values at the mesh points of a 100-by-100 grid. Simple plane-surface interpolation is used to find these gridded values, so no extraneous maxima or minima are introduced, which could occur with higher-order surface-fitting techniques.
- (2) It computes the contour lines based on the gridded data and writes a magnetic tape of instructions for the final contour plotting.

The final contour plot is drawn on a California Computer Products(Cal-Comp) incremental plotter. The plotter also labels the drawing and puts on the registry marks required later for the azimuth and elevation grid overlay. The contour plot is visually checked to ensure that it is reasonable and represents the original data.

6.4 Pattern Data Display

The antenna patterns are presented in two forms. One consists of the conventional polar and elevation cuts. The other consists of stereographic contour maps, which may appear at first glance to be unnecessarily complicated. They have, however, several advantages, which are discussed following an explanation of how to read them.

Each contour map shows all the amplitude data taken on one antenna, for one polarization, at one frequency. The plot can be visualized in several ways. For instance, one can picture placing a large hemisphere over the antenna being measured, then drawing the field-strength contours on its surface. The contour plots are viewed as two-dimensional maps of this hemisphere as it appears from directly above (see Fig. 6.4), where elevation angles are plotted on a linear scale. Hence, the zenith angle is at the center of the plot; azimuth angles appear as radials; and elevation angles are concentric circles. The outer rim of the plot is the horizon, or 0-degree elevation. The azimuth angles numbered around the rim of the plot are in degrees relative to the nominal main-beam direction of the antenna, rounded to the nearest degree. As an example, for the Anchorage lens feed and the double-dipole array, 0-degree azimuth on the plot is actually 5 degrees from true north.

The contour interval is 3 db, with the highest amplitude recorded for each plot taken as 0 db. This measured 0-db point is not shown, because its position is misleading without detailed knowledge regarding the aircraft orbits. However, the location of the actual maximum may be estimated from the other contours.

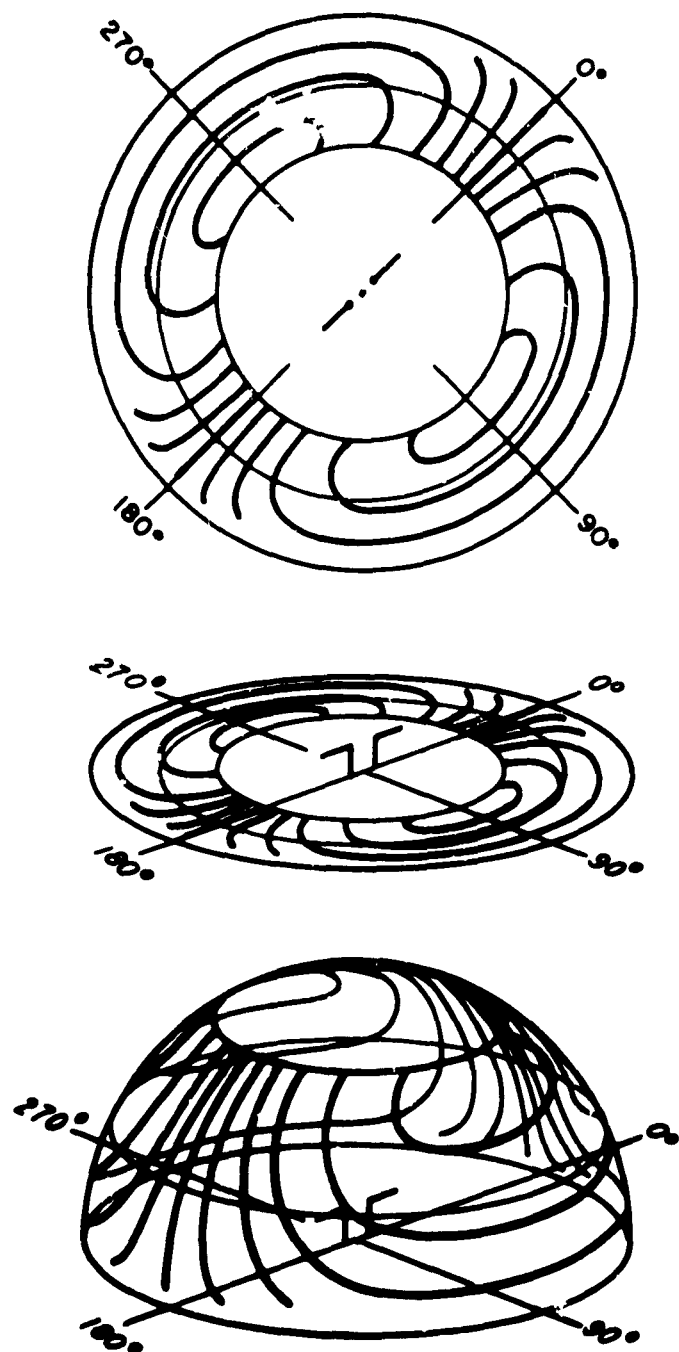


Fig. 6.4 A Contour Plot as a Map of a Hemisphere

The stereographic plot has merits both intrinsically as a data display and extrinsically through its adaptability to the Xeledop measurement technique. As a data display, it has the advantage of showing in one diagram the complete characteristics of the antenna at one frequency much more clearly than any series of polar cuts could. It also emphasizes the energy distribution as a function of solid angle, a better measure of the usefulness of any antenna for communications than azimuthal beam width.

The contour plots are also very well suited to the way in which the data is taken. Since the aircraft does not fly perfect orbits about each antenna, the elevation angles actually sampled vary during any given orbit and from one set of antennas to another. Thus, it would be neither accurate nor adequate simply to plot the measured amplitude as a function of azimuth on a polar chart. Some means of interpolation between data taken at the various elevation angles is required, because the sampling of each antenna pattern is essentially random. The contour plot program does this by finding the surface indicated by the available data.

Once the program has found this surface (drawn the contour plot), polar cuts can easily be taken at any constant elevation angle of interest, and elevation cuts can be taken at any azimuth angle. The polar and elevation cuts presented later in this report have been generated in this manner.

6.5 Accuracy Considerations - General

When the accuracy of the Xeledop technique is evaluated, a distinction must be made between inaccuracy of values and limitations of sampling. This distinction is clear if one remembers how the measurements are made: by flying a transmitter around the site in separate orbits over a period of time. The more accurately correlated values would be the ones from a single orbit. The time lapse between orbits allows some equipment drift; hence correlation between successive orbits becomes a little less accurate. Conversely, sampling of the azimuthal pattern is very good, continuous for all practical purposes, while sampling of the elevation pattern is limited to nine orbits. Low signal levels (occurring at low frequencies), do not affect the accuracy of a given data point, but since some points are lost because of noise, the contour plot of the pattern is distorted by this limited sampling.

The accuracy of pattern values is principally governed by the stability of the ground equipment and the Xeledop (both of which appear to be very good) and the precision of the strip-chart scaling. Evidence

from overlaps, rereading, and the general correlation of the data indicates that systematic and predictable errors have been effectively eliminated, leaving a random scattering in strong-signal data of about 1.0 db during a run and 1.5 db between runs, or 1/3 to 1/2 contour interval. The best criterion for the significance of features in a pattern is: If the deviation is less than one-half the distance between the contour lines, it can be ignored; otherwise, it is significant. This is also true for the Visicorder data (Nandi-Canton feed), except that the scatter is somewhat larger, probably about 2 db, so only features involving more than 2/3 contour interval are significant. Angles are measured more precisely than 1 degree in both azimuth and elevation, but because the nominal main-beam direction is rounded to the nearest degree, the final plotted accuracy is about ± 1 degree in azimuth.

Since the pattern sampling in elevation is limited, structure narrower than a few degrees in elevation is lost. In azimuth, the smallest features that can be shown are limited by the contour-plot mesh size--about 2 degrees at 20-degree elevation. For these reasons, this technique cannot precisely reproduce a sharp null. The angular position of such a null is accurately indicated, however, and the value shown on the contour plot is a valid upper bound for its signal strength. Hence, if -30 db is shown, the null was as low as, or very likely lower than, -30 db. The 2-degree mesh size, as well as the high data scatter, also led to the loss of the 3-db contours on the higher-frequency Nandi-Canton patterns.

In evaluating any azimuthal deflections of the main-beam response from its nominal direction, all these factors must be considered, with the potential error being ± 1 degree $\pm 1/3$ contour interval.

6.5.1 Forward and Reverse Orbits

To check the accuracy of polarisation, tracking and data reduction, one normal counter-clockwise orbit was also flown clockwise around the site. Both runs were sent through the standard B5000 program, and the corrected values were plotted. The results for a check of the three feeds are shown in Figs. 6.5 through 6.16 with the normal orbit plotted as a solid line and the reverse orbit as a dotted line. By chance, this check was a worst case. The normal run was the day's first (on fresh Xeledop batteries), and the reverse orbit was the last run of the day (with batteries nearly exhausted). In addition, the whip antenna on the lens (see Sec. 6.5.2) was accidentally disconnected during the normal orbit and reconnected for the reverse. The elevation angles did not repeat exactly either but varied from 20 to 23 degrees as shown in Fig. 6.17. Incidentally, the general trend of these curves (high at 120 degrees and low at 300

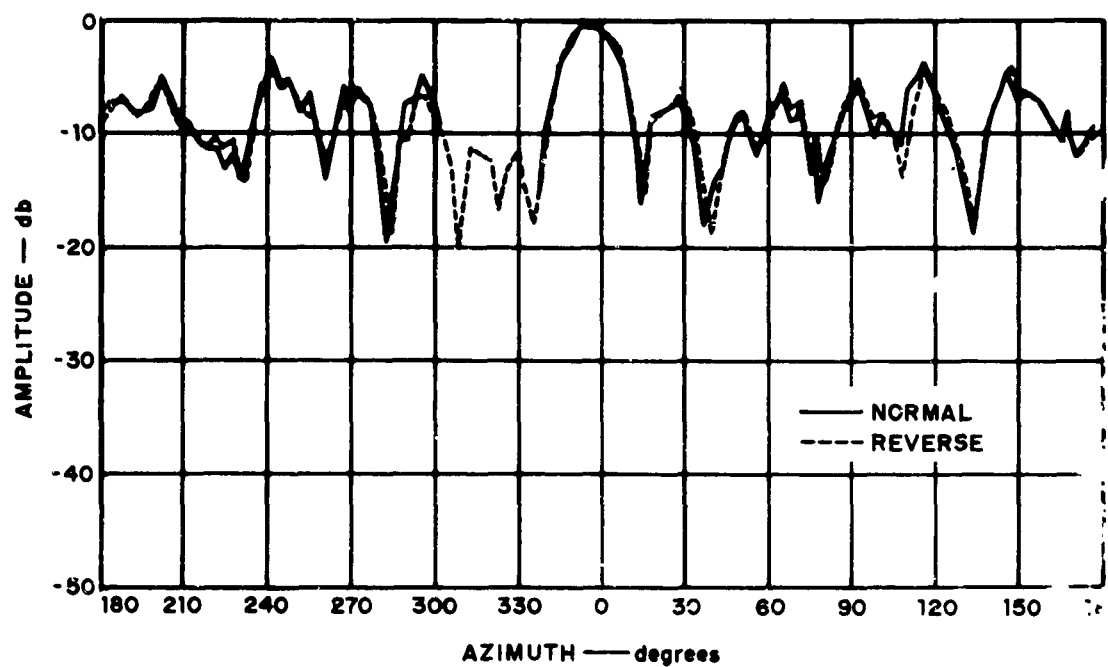


Fig. 6.5 Anchorage Feed at 4.1 Mc

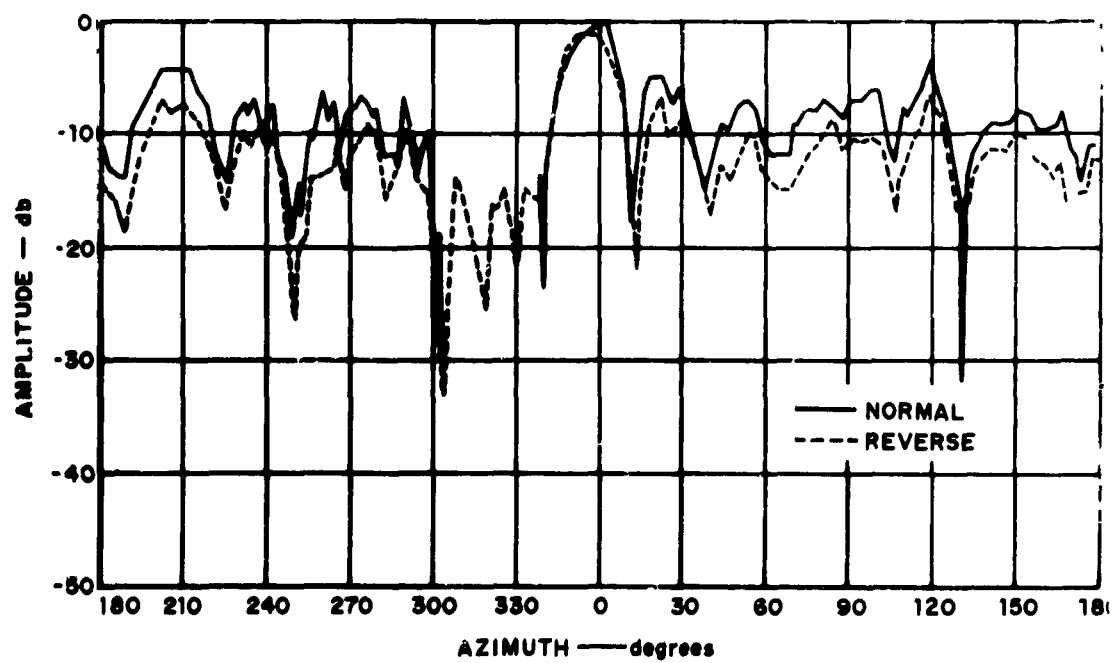


Fig. 6.6 Anchorage Feed at 5.6 Mc

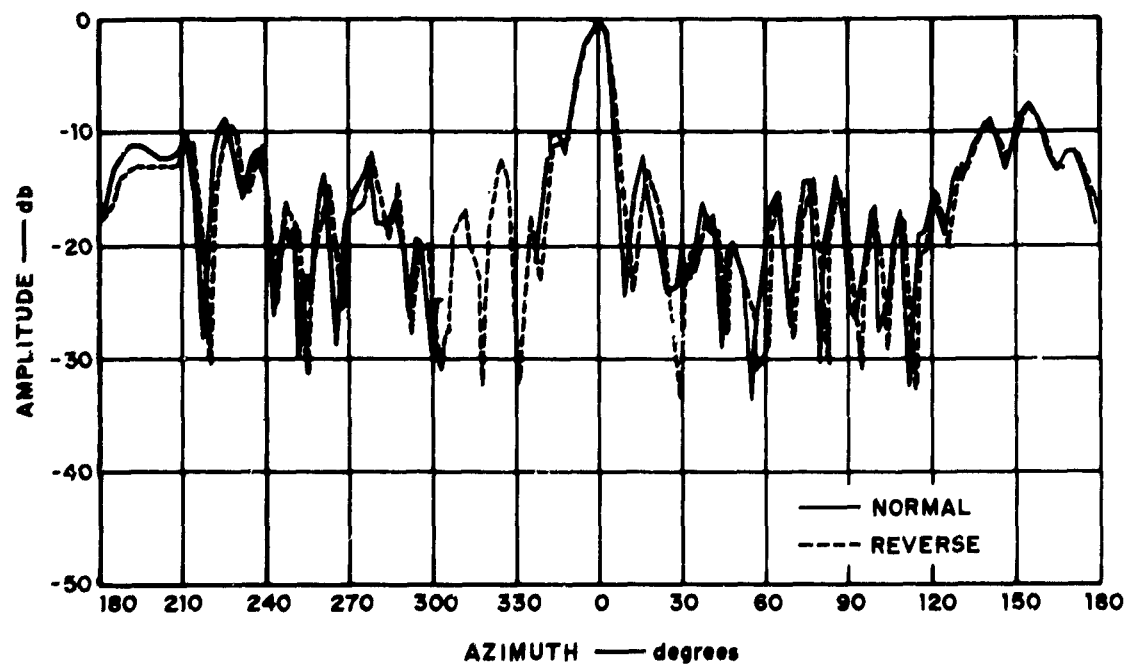


Fig. 6.7 Anchorage Feed at 9.1 Mc

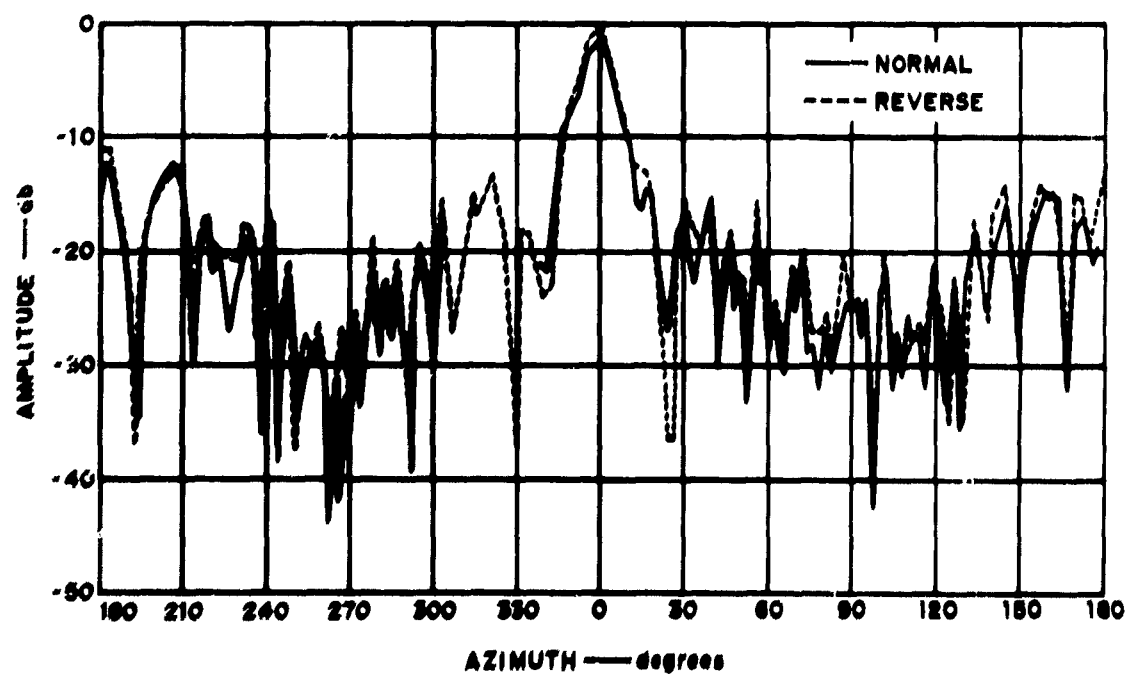


Fig. 6.8 Anchorage Feed at 15.3 Mc

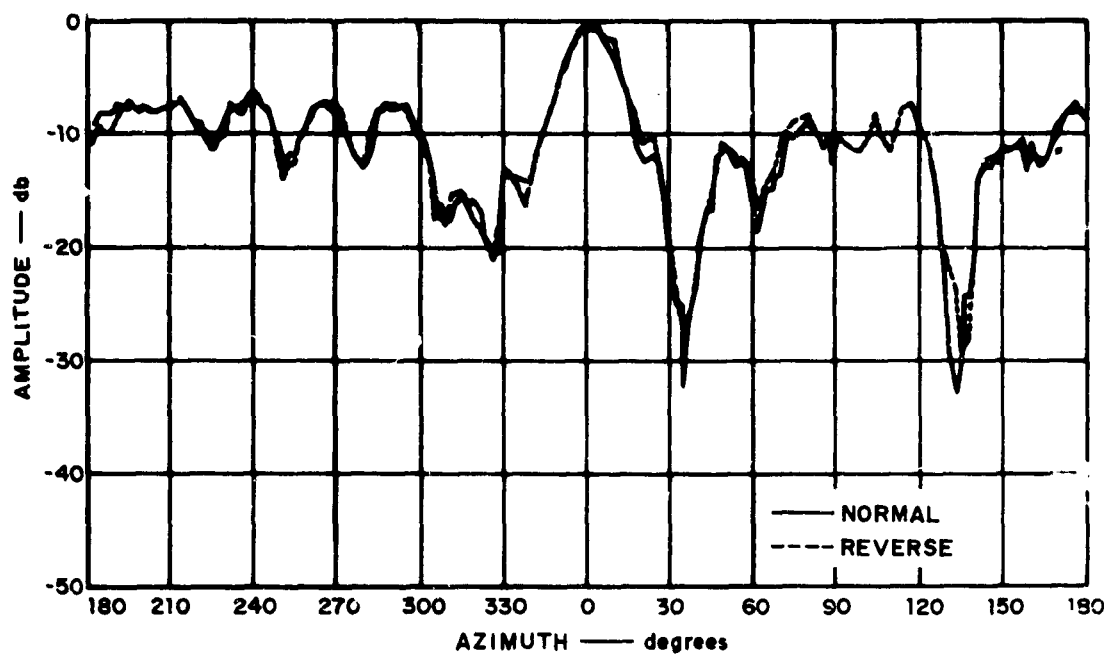


Fig. 6.9 Sydney Feed at 4.1 Mc

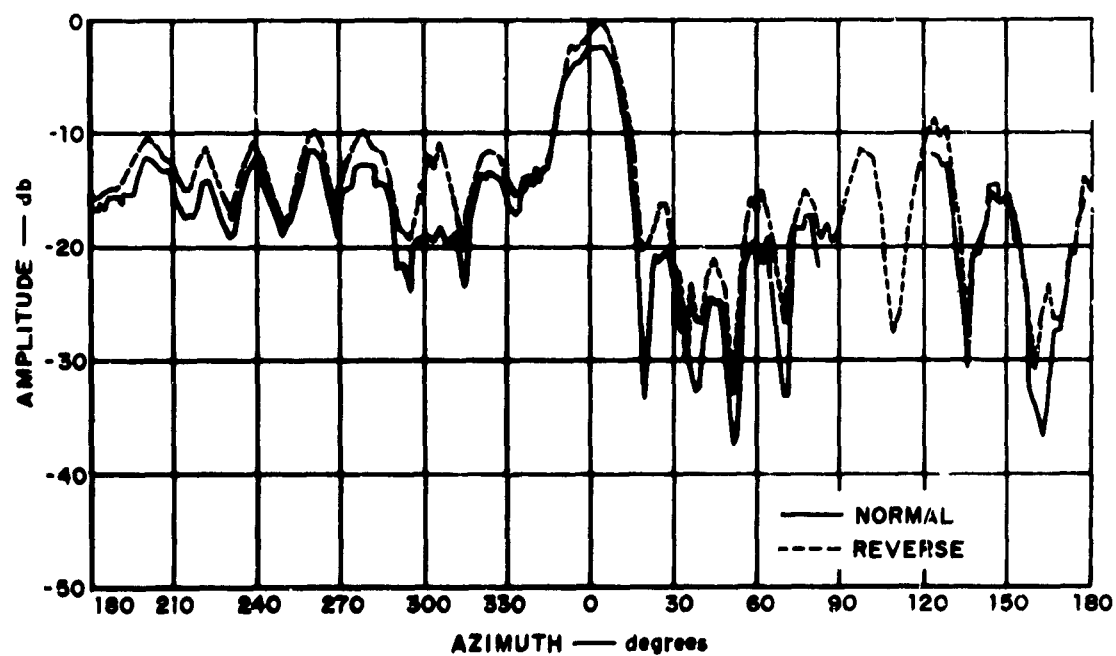


Fig. 6.10 Sydney Feed at 5.6 Mc

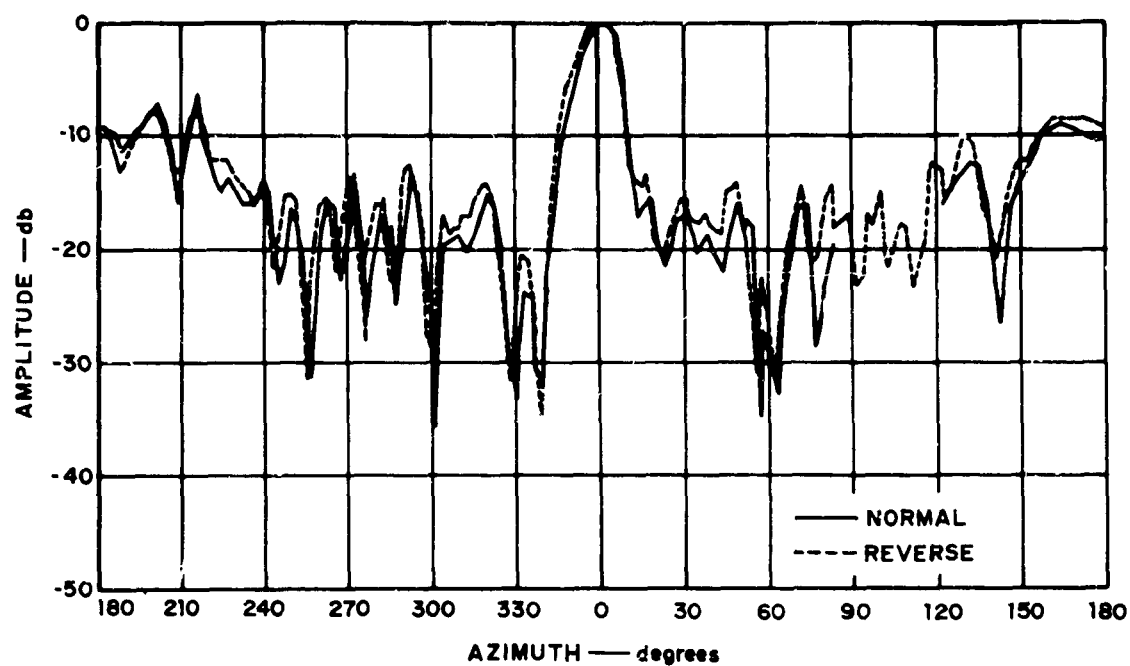


Fig. 6.11 Sydney Feed at 9.1 Mc

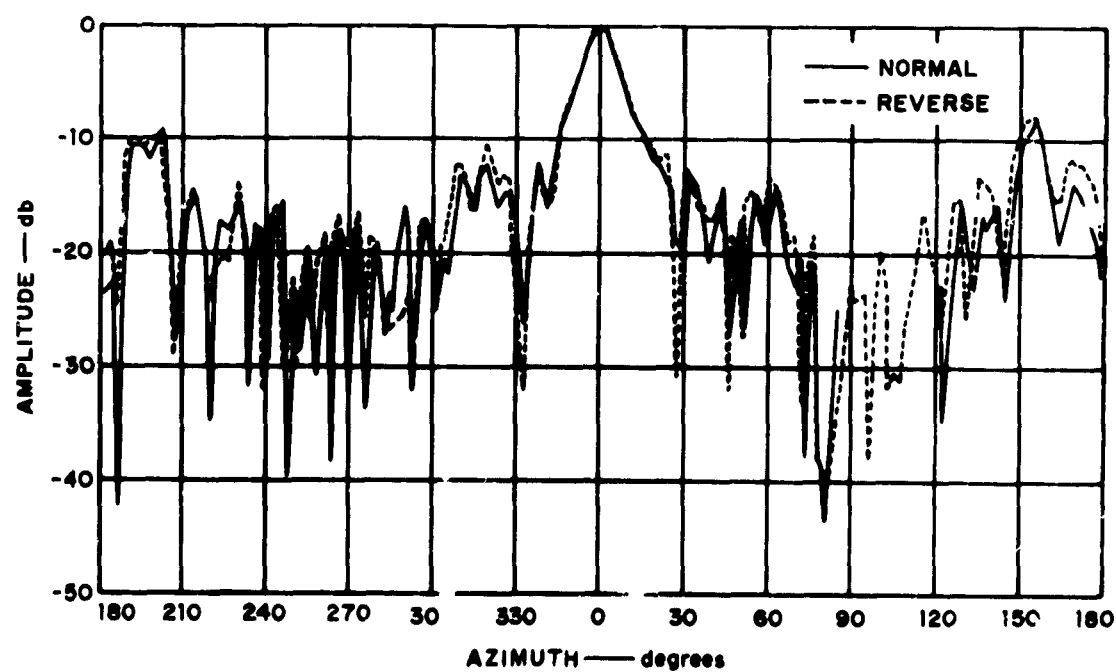


Fig. 6.12 Sydney Feed at 15.3 Mc

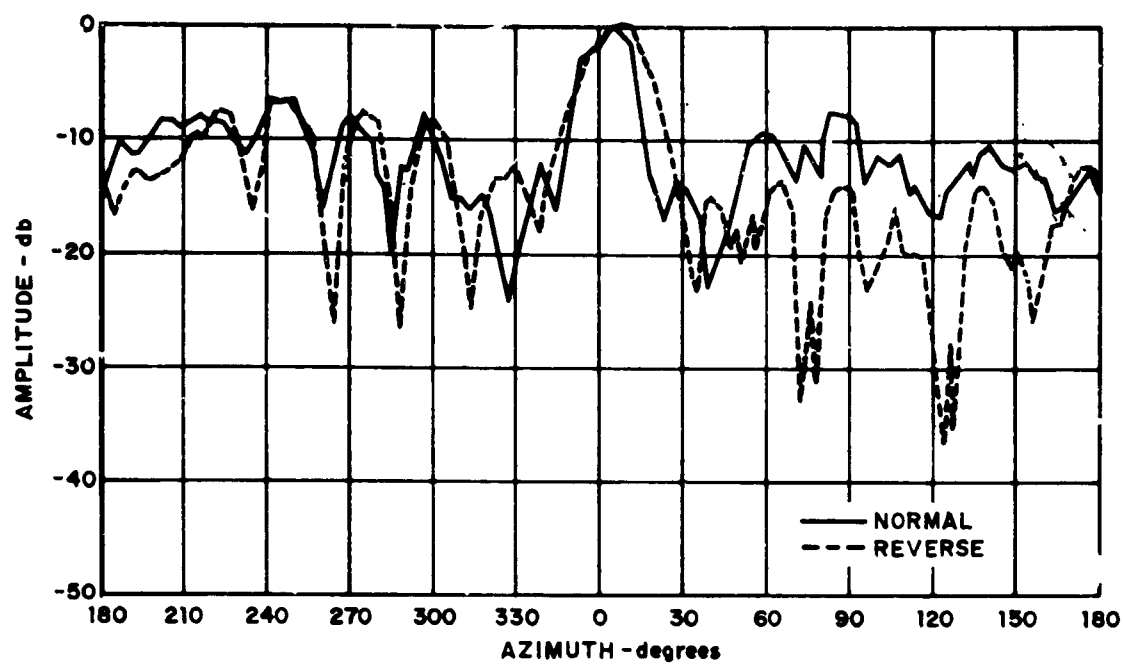


Fig. 6.13 Nandi-Canton Feed at 4.1 Mc

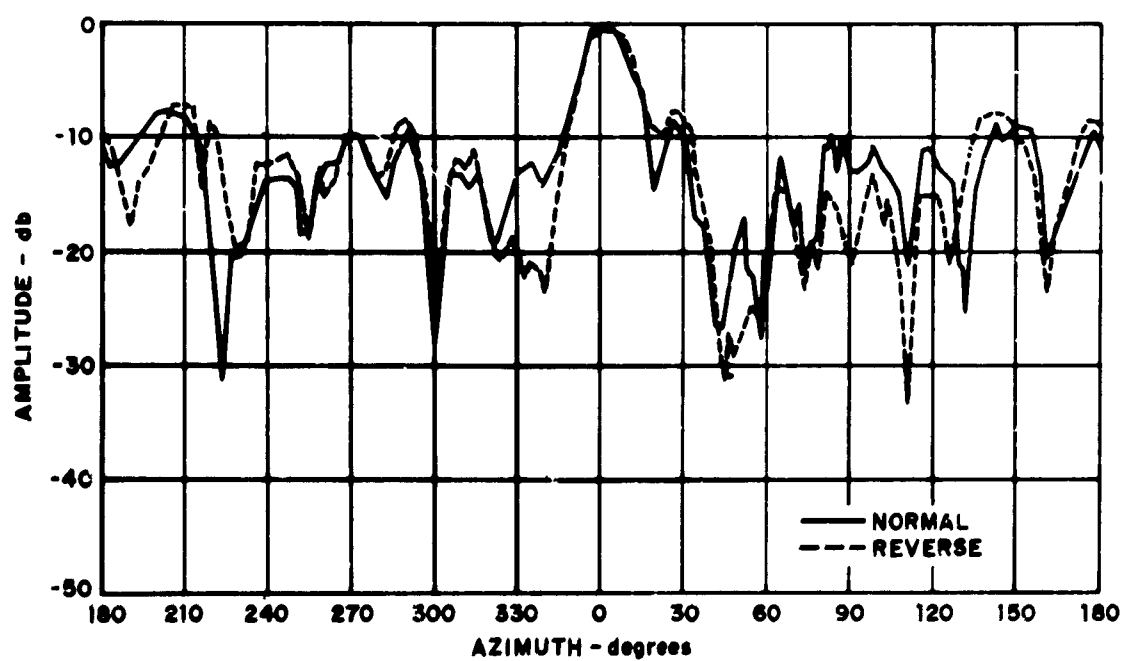


Fig. 6.14 Nandi-Canton Feed at 5.6 Mc

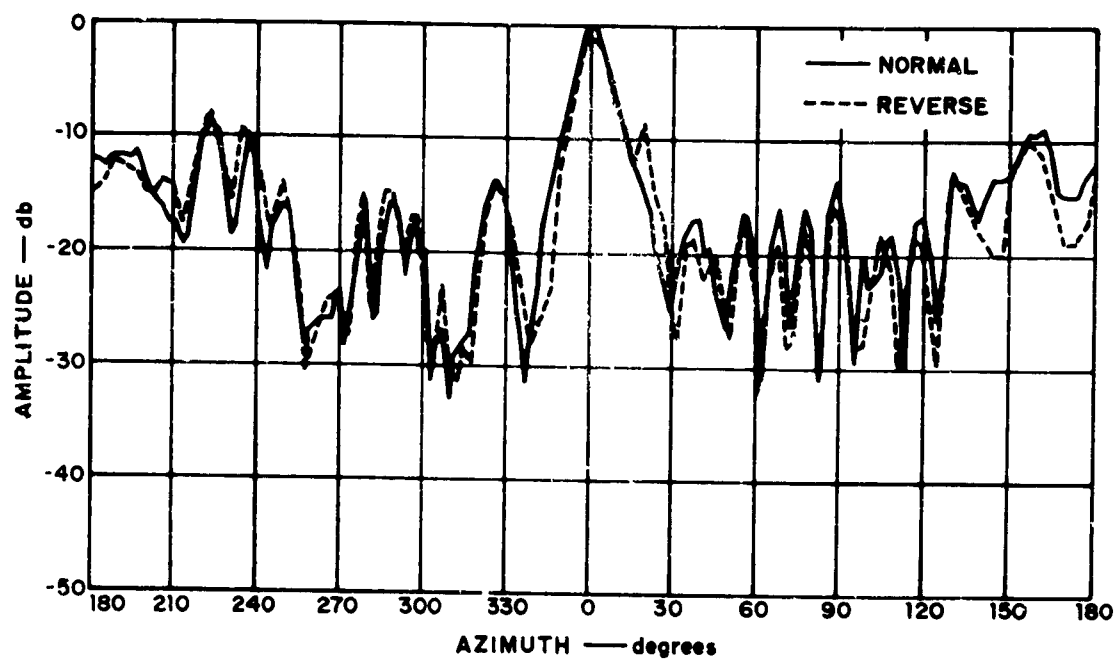


Fig. 6.15 Nandi-Canton Feed at 9.1 Mc

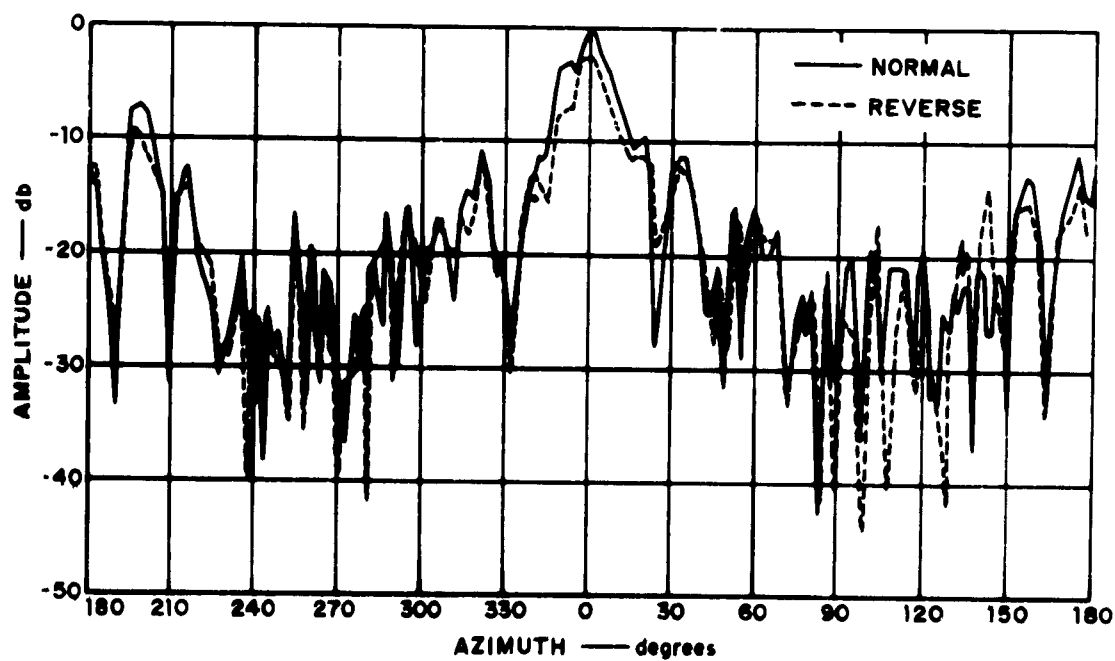


Fig. 6.16 Nandi-Canton Feed at 15.3 Mc

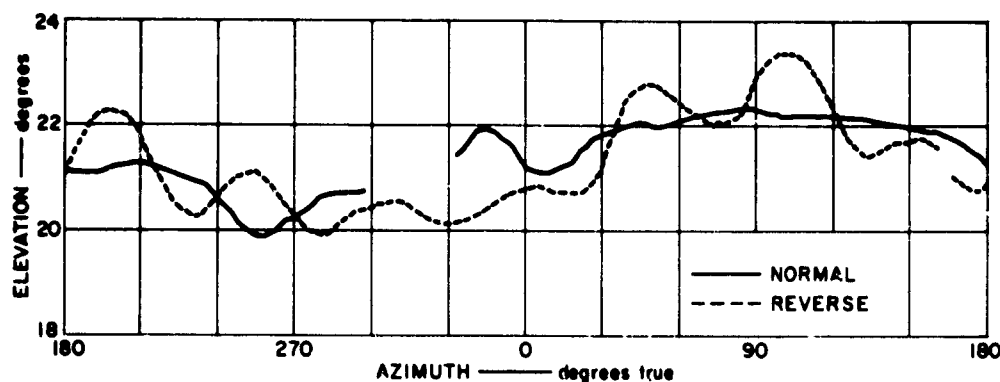


Fig. 6.17 Variation in Elevation Angle During Reverse-Orbit Test

degrees) is due to the offset between the lens and the center of the pilot's orbit, which the computer has corrected for. All things considered, the correspondence is excellent, with differences well within the stated bounds. Since any significant polarization impurity would have caused the nulls to shift considerably, it is evident that significant tipping of the Xeledop or reradiation from the aircraft did not occur.

6.5.2 Whip Antenna Above Lens

A small whip antenna was mounted on top of the lens during most of the flight tests, with the upper wire grid used as its ground plane. Originally, it was intended that this whip would be used as an omnidirectional reference antenna. However, its measured radiation patterns were too irregular for this purpose. The whip antenna was fed from a coaxial line dropped through the center of the lens. Theoretical considerations indicated that the presence of the whip and the coaxial feed line should not affect the lens patterns. To check the effect of this whip on the patterns of the lens, an orbit was flown with the whip in place (see Figs. 6.18 and 6.19) and immediately repeated with the whip and feed cable removed. These orbits were at about 3-degree elevation (exact GMD elevation data is not available), which is well below the elevation peak of the main beam. The signal strengths in the main beam differed slightly, but these changes were not consistent and could easily have been due to a slight change in elevation at these low angles. Thus the effect of the whip was negli-

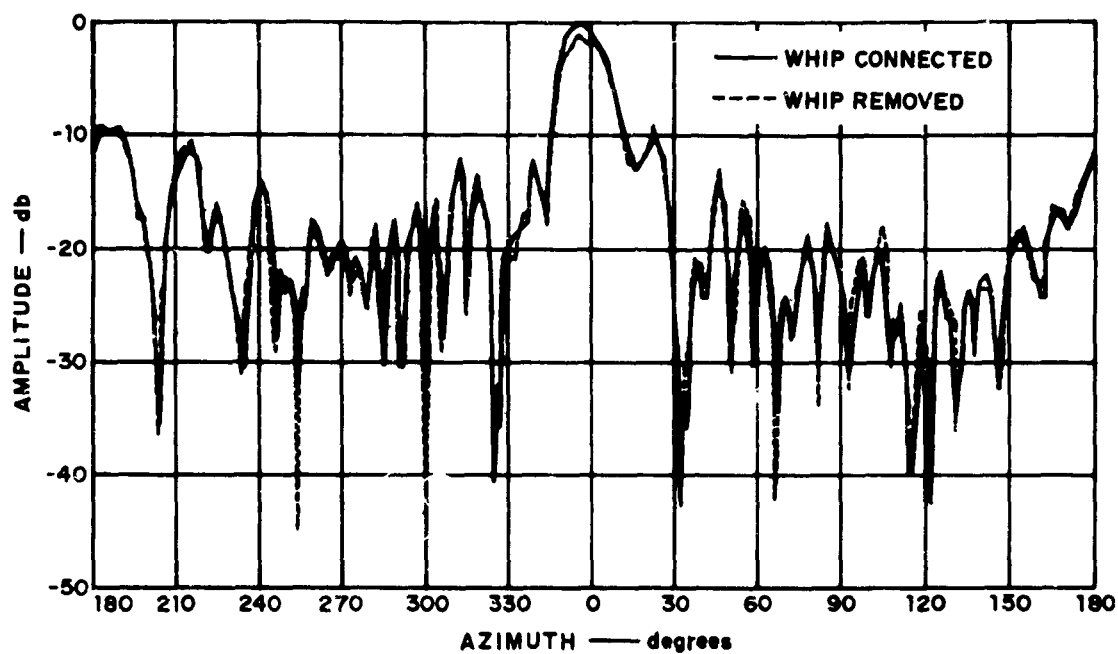


Fig. 6.18 Effect of Whip Antenna on Anchorage Feed Pattern at 11.8 Mc

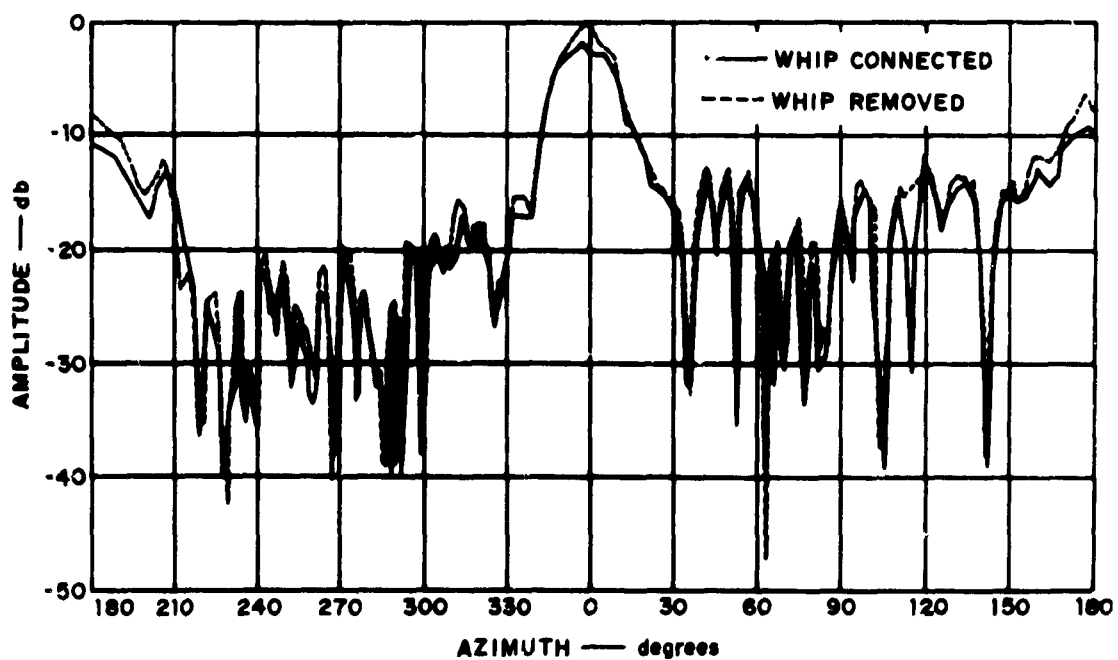


Fig. 6.19 Effect of Whip Antenna on Sydney Feed Pattern at 11.8 Mc

6.6 Measured Radiation Patterns

This section presents a summary comparison of the measured and calculated patterns of the Wire-Grid Lens Antenna together with a summary of the measured patterns of the San Francisco Rhombics 4A, 4B and 4C. The actual patterns measured and reduced by the techniques and procedures outlined in the foregoing sections constitute a mass of material too large to be incorporated in the body of the report without seriously compromising the continuity of the text. They are, therefore, included as Appendix B, following the main body of the textual material of the report, but self-contained and easily accessible.

Figure 6.20 shows a comparison of the calculated and measured azimuth 3-db beamwidths of the Wire-Grid Lens Antenna. The calculated azimuth beamwidths are measured at the elevation angle corresponding to the elevation peak of the main beam and were obtained from the patterns shown in Fig. 5.5. The measured azimuth 3-db beamwidths for the Anchorage, Nandi-Canton, Sydney, and San Francisco feeds were obtained from the contour plots in Fig. B.1 through B.36. The agreement between the measured and calculated beamwidths is seen to be quite close on the average although substantial deviations are observed for the patterns of the different feeds at a number of frequencies due primarily to site perturbations.

Figure 6.21 shows a comparison between the calculated and measured minor lobe level of the Wire-Grid Lens Antenna. As before, the calculated minor lobe levels were obtained from the patterns in Fig. 5.5 corresponding to the elevation peak of the main beam, while the measured maximum minor lobe levels for the various feeds were obtained from Figs. B.1 through B.36. The measured minor lobe levels plotted in Fig. 6.21, which represent the maximum minor lobe levels recorded using the Xeledop instrumentation, are generally higher than the calculated levels; level variations from feed to feed are attributed to site perturbations. Another reason the measured minor lobes are higher is that the calculated minor lobes were obtained only for the elevation angle corresponding to the peak of the main beam, while the maximum measured minor lobe levels were determined from the contour plots for the measured range of elevation angles extending from approximately 5 to 55 degrees.

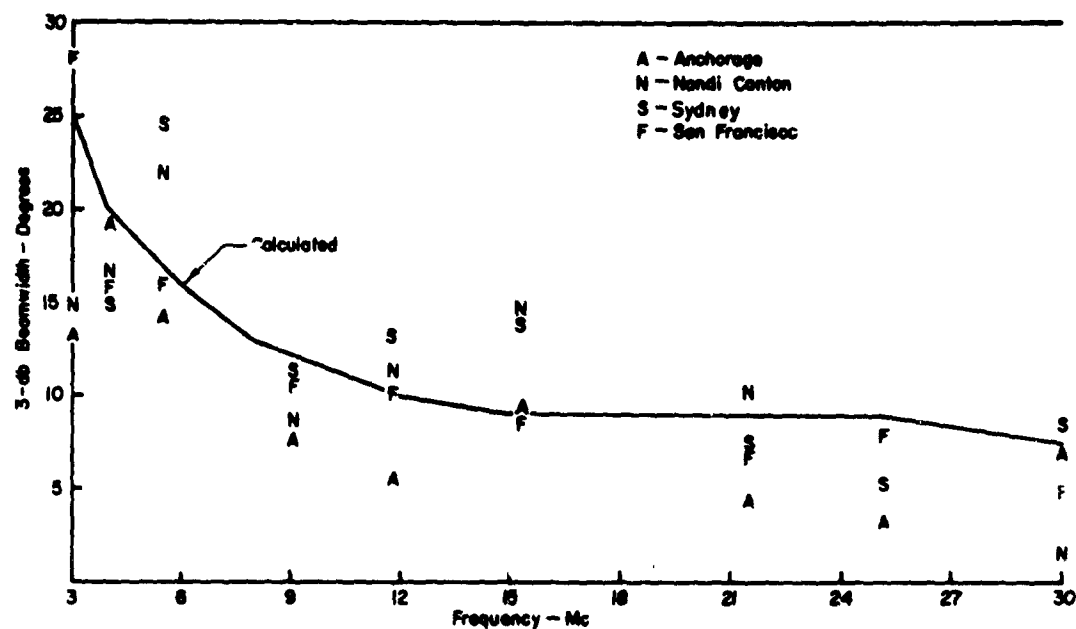


Fig. 6.20 Comparison of Calculated and Measured 3-db Azimuth Beamwidth of Wire-Grid Lens Antenna

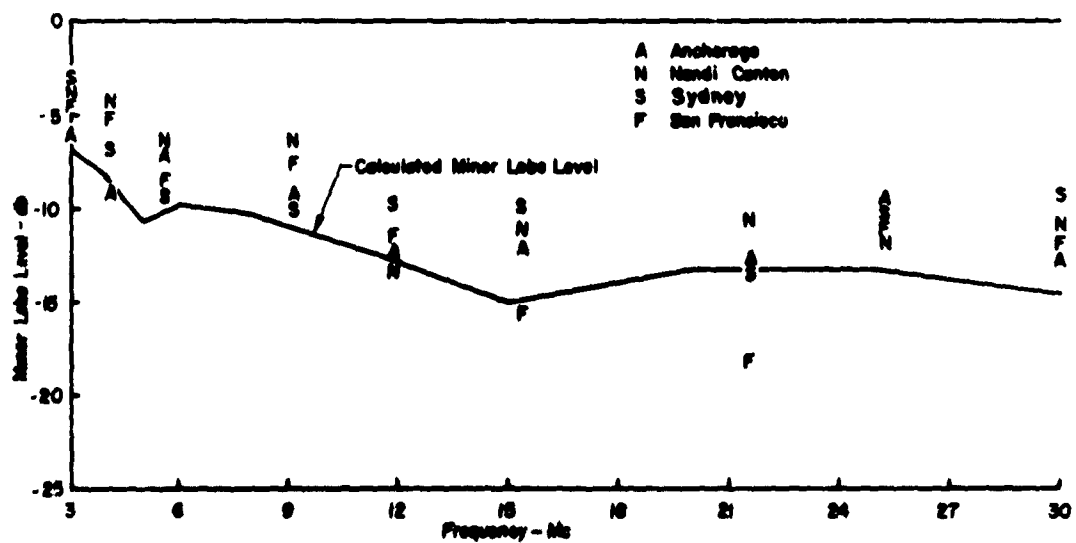


Fig. 6.21 Comparison of Calculated Maximum Minor Lobe Level at Peak of Main Beam and Maximum Measured Minor Lobe Level for Wire-Grid Lens Antenna

Figure 6. 22 shows a comparison of the calculated and measured elevation upper and lower 3-db contours. Correlation between calculation and measurement is reasonably good but is not as good as the correlation between calculated and measured azimuth beamwidths. However, this is not expected since the elevation patterns of HF antennas are influenced to first order not only by the ground conductivity but also by terrain irregularities; while azimuth patterns, measured through the peak of the main beam, are only influenced to first order by terrain irregularities.

Figure 6. 23 shows a comparison of the calculated elevation coverage of the lens compared with the measured elevation coverage desired for point-to-point data communication¹¹ for which the Molokai lens was designed. Also shown on the same figure is the measured coverage desired for ship-to-shore and air-to-ground data communications.^{12, 13} This figure displays the upper and lower 3-db elevation angles of the beam as well as the elevation of the beam maximum. The elevation angles of arrival of 90 per cent of such signals lie below the curves labeled 90 per cent while only 10 per cent of the signals have elevation angles of arrival below the curves labeled 10 per cent. Thus 80 per cent of the arriving signals have elevation angles between these curves, which for the intended point-to-point service always lie between the upper and lower 3-db elevation contours for the Wire-Grid Lens Antenna.

Figures 6. 24 through 6. 26 show the measured performance of the nested Rhombics 4A, 4B, and 4C used on the San Francisco circuit within their design frequency bands. These data were obtained from the contour plots in Figs. B. 52 through B. 61. The measured 3-db azimuth beamwidths of the three antennas displayed in Fig. 6. 24 are reasonably constant in their design bands. The upper and lower elevation 3-db points of the rhombics displayed in Fig. 6. 25 show a substantially greater variation with frequency. The measured elevation coverage of the rhombics for point-to-point service agrees reasonably well with the signal arrival angle contours of Fig. 6. 23 at the upper end of the band. The measured maximum minor lobe levels of the rhombics are displayed in Fig. 6. 26. They are all acceptably low except for that of Rhombic 4A at 6 Mc which has a very high back lobe presumably due to site effects.

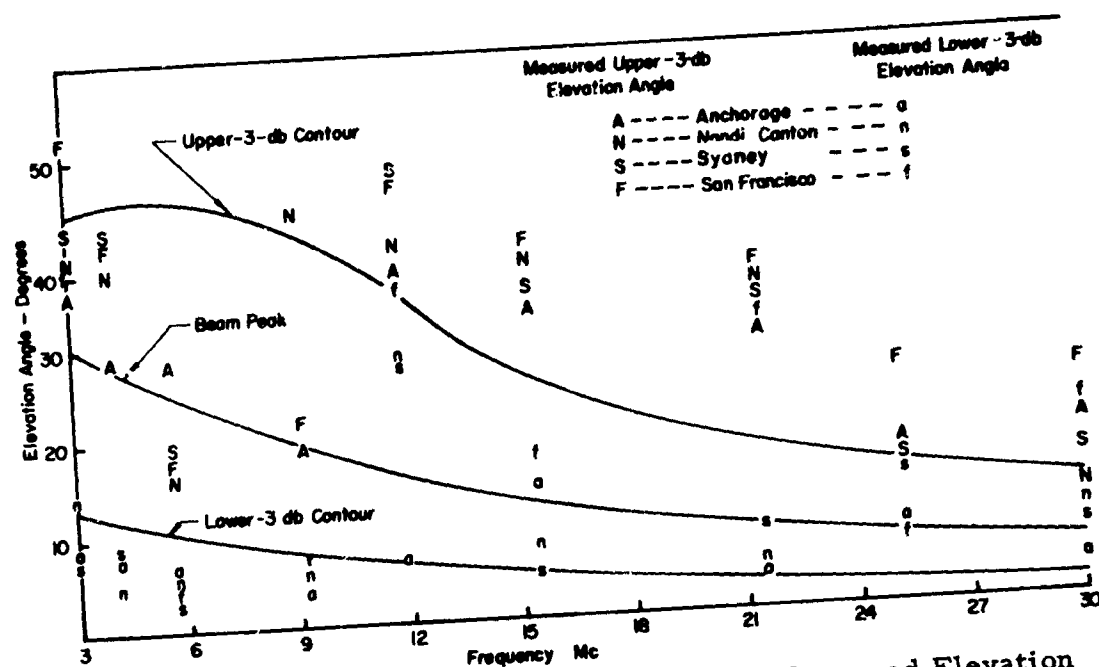


Fig. 6.22 Comparison of Calculated and Measured Elevation -3 db Beam Contours for the Wire-Grid Lens Antenna

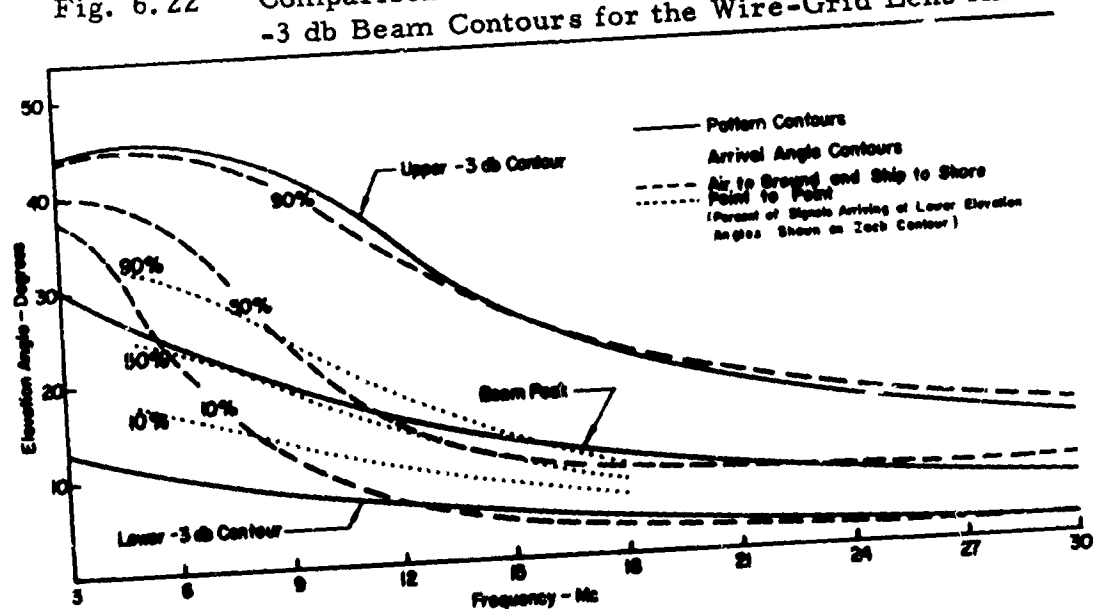


Fig. 6.23 Measured Elevation Pattern Coverage of Wire-Grid Lens Antenna and Expected Distribution of Arrival Angles for HF Point-to-Point Communications

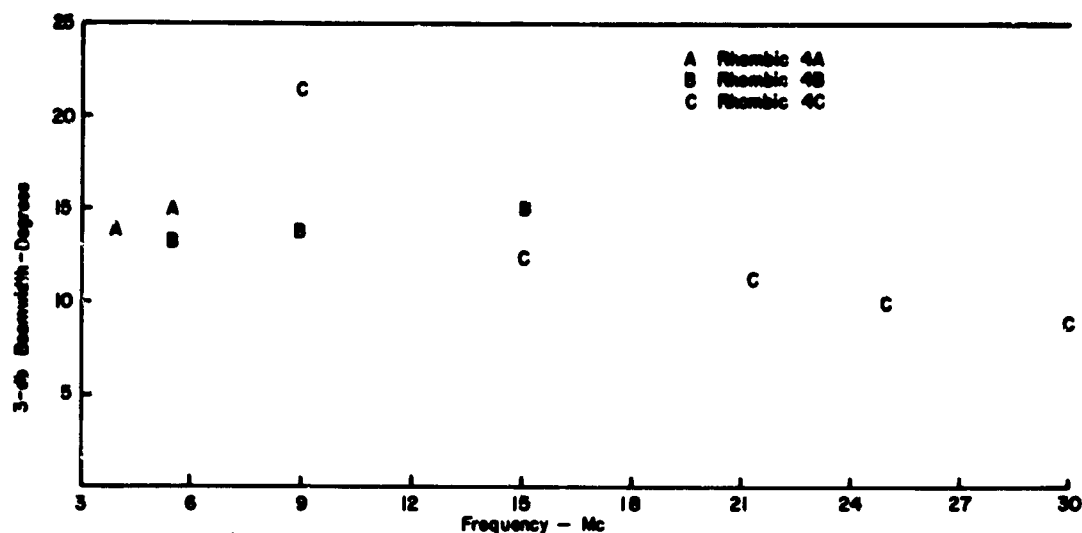


Fig. 6.24 Measured 3-db Azimuth Beamwidths of San Francisco Rhombics 4A, 4B and 4C

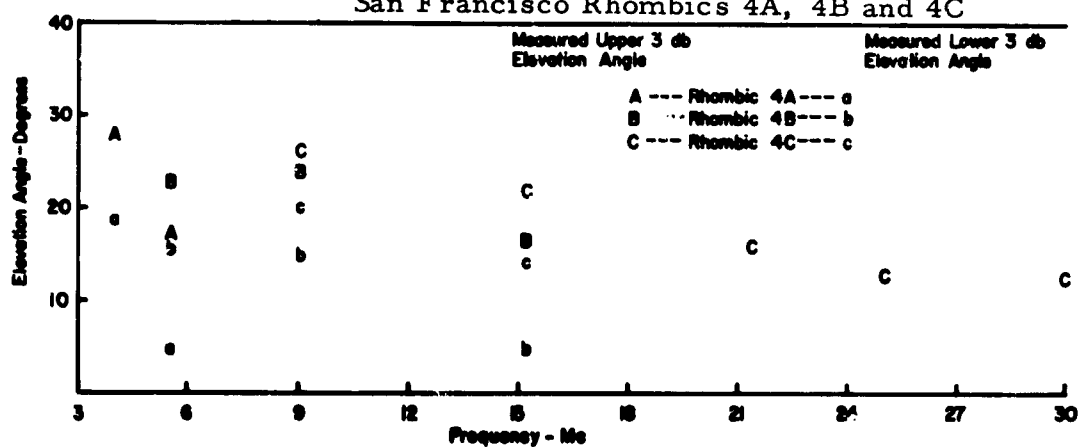


Fig. 6.25 Measured Elevation 3-db Beam Points of San Francisco Rhombics 4A, 4B and 4C

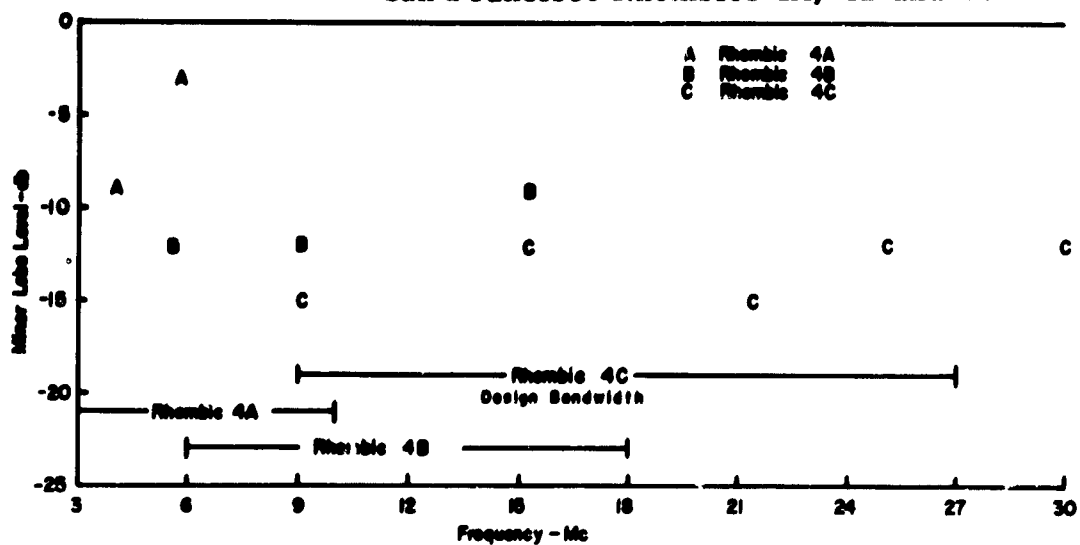


Fig. 6.26 Measured Minor Lobe Level of San Francisco Rhombics 4A, 4B and 4C

7. LENS GAIN

During the Joint Services Evaluation, the relative gain of the Wire-Grid Lens Antenna was measured in two different ways, and its absolute gain was measured in one way. These gain measurements are discussed in this section and the measured values of lens gain are compared with values calculated using techniques developed on various study contracts, 6,7,8,9. It is found that while the directivity of the lens is quite high, its gain is relatively low -- primarily because the lens feeds used during the evaluation were relatively inefficient.

7.1 Measured Relative Lens Gain Using the Xeledop Transmitter

One technique used to measure the relative gain of the lens was to compare the maximum signals received at the multicoupler terminals of the various test antennas from the Xeledop transmitter used in the pattern measurements (described in Sec. 6) as it circled the site. The Xeledop constitutes a convenient, constant-strength signal source because its power output at any test frequency is essentially independent of polarization and does not change appreciably with time. The results of these measurements, which exclude the transmission line losses between the antenna terminals and multicoupler terminals, are presented in Fig. 7.1. Gain data obtained from the Esterline Angus recordings (see Sec. 6.2) have been excluded from Fig. 7.2 because it is of questionable accuracy. In this presentation all maximum signals received at the various antenna terminals are normalized with respect to those received at the Anchorage feed terminals. As would be expected, this maximum received signal occurred for each antenna with the Xeledop located at different azimuth and elevation angles.

The signals received on the Anchorage feed, Nandi-Canton feed, Sydney feed, and the double dipole reference antenna were recorded by SRI personnel, while the signals received on the San Francisco feed, the lens operating as an omniazimuthal biconical antenna, and the NRL monopole were recorded by NRL personnel. The calibration procedure used by each group was internally consistent. However, the reference calibration level for the signals recorded by the NRL group was about 3 db lower. Therefore, in order to effect a comparison between the SRI data and the NRL data, the level of the NRL data should be increased by about 3 db. Inspection of the signals received on the Nandi-Canton and Sydney feeds shows that they are sometimes higher and sometimes lower than those received on the Anchorage feed. However, the differences between the signals received on these three feeds are never more than

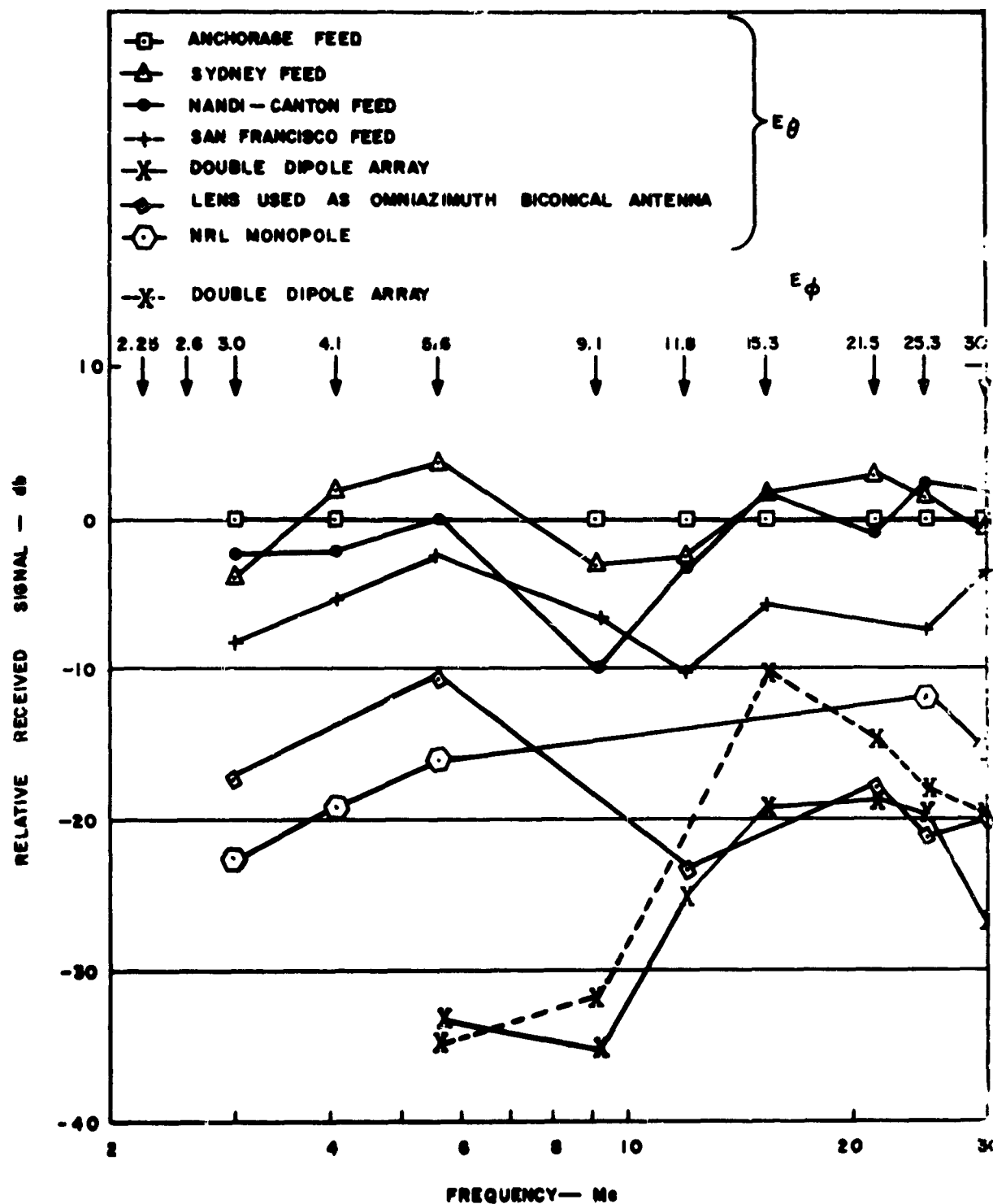


Fig. 7.1

Maximum Relative Principally Polarized Signals Received from Xeledop at Antenna Terminals of Various Test Antennas (Calculated From Data Measured at Multicoupler Terminals)

3 db (if one excludes the 9.1 Mc point on the Nandi-Canton feed as being a bad datum point). It is believed that these oscillatory differences are due primarily to the site effects discussed in Sec. 4 and Appendix B. On the other hand, the signals received by the San Francisco feed recorded by NRL are seen to be consistently lower, by about 3 db, than those received by the other feeds.

The signals received from the NRL monopole and the lens operating as an omniazimuth biconical horn are seen to be much lower than those received on the lens, as is to be expected since these antennas have much lower directivity. The signals received on the double-dipole reference antenna are also seen to be lower than those received on the lens due in large part to the relatively inefficient balun used with it.

Relative gain plots are not shown for the rhombic antennas since transmission line losses for rhombics were found to be erratic. After pattern measurements had been completed using the Xeledop transmitter, it was discovered that the support insulators used with the two-wire transmission lines for the rhombics were found to have excessive leakage. These faulty support insulators caused imbalance to exist on the two-wire lines and increased their attenuation above theoretical. Efforts by on-site NRL personnel to accurately measure the attenuation of the two-wire lines were not successful because of the non-linear, oscillatory nature of attenuation versus frequency. Unstable line attenuation measurements (as much as 15 db) were noted on the two-wire lines. Therefore, coaxial cables* were installed on Rhombics 4B and 4C prior to error-count and signal-to-noise measurements. A measure of the relative gain between the lens and rhombics is discussed in Sec. 7.2.

7.2 Measured Relative Lens Gain Using Arriving Skywave Signals

The other technique used to measure the relative gain was to compare the median signals received on the lens with those received on the station rhombics while copying operational traffic. Because these arriving signals are reflected at least once from the ionosphere during their route they arrive with essentially random polarization at the receiving site. Therefore, they can be received on the average with equal facility by either the vertically polarized lens or the horizontally polarized rhombics, and a direct comparison of the signals received at the terminals of each antenna gives a measure of their relative gain.

* The coaxial line used with Rhombic 4C consisted of 2,600 feet of RG17/U and 990 feet of 7/8 inch, 70-ohm Foamflex. The coaxial line used with Rhombic 4B consisted of 1,000 feet of RG17/U and 2,000 feet of 7/8 inch, 70-ohm Foamflex.

Figures 7.2a and 7.2b show the measured, median, decibel difference between the signals received on the lens and Rhombics 4B and 4C. These rhombics were equipped by NRL with coaxial line instead of the open-wire line. Figure 7.2a shows the calculated decibel difference between the signal levels at the antenna terminals as determined by NRL. Figure 7.2b shows the measured decibel difference between the signal levels at the multicoupler terminals. The decreased disparity between the signal levels at this point occurs because there is more attenuation in the transmission lines between the rhombics and the multicouplers than between the lens and the multicouplers, due to the fact that the rhombics are located at a greater distance from the receiver house.

7.3 Absolute Gain

The technique used to measure absolute gain was to compare the vertically polarized signals received from the Xeledop at the lens terminals with those received at the terminals of the double-dipole gain standard antenna. The double-dipole gain standard is similar to an Adcock antenna. It was designed for this purpose by Dr. H. Brueckmann of USAERDL and fabricated by NRL. Figure 7.3 is a sketch of the antenna showing its principal dimensions and the manner in which its balanced output is converted to an unbalanced output.

It is to be noted that the two elements of this array are fed out-of-phase so that its array factor resembles a figure of eight with a null plane perpendicular to the array axis. The patterns in the plane of the array are somewhat more narrow than that in the plane perpendicular to the array because of the element factor of the individual elements.

The array was constructed so that the dipole elements could be oriented in the vertical position for use when the lens was receiving vertically polarized signals, and in the horizontal position when the lens was receiving horizontally polarized signals (cross-polarized).

The gain of the lens relative to that of the double-dipole array can be calculated by means of the expression,

$$\frac{G_L}{G_D} = \frac{\eta_L D_L}{\eta_D D_D} = \frac{P_L}{P_D} \cdot \frac{4 R_o R_D}{|R_o + R_D + jX_D|^2} \cdot \frac{|R_{oL} + R_L + jX_L|^2}{4 R_{oL} R_L} \quad (7.)$$

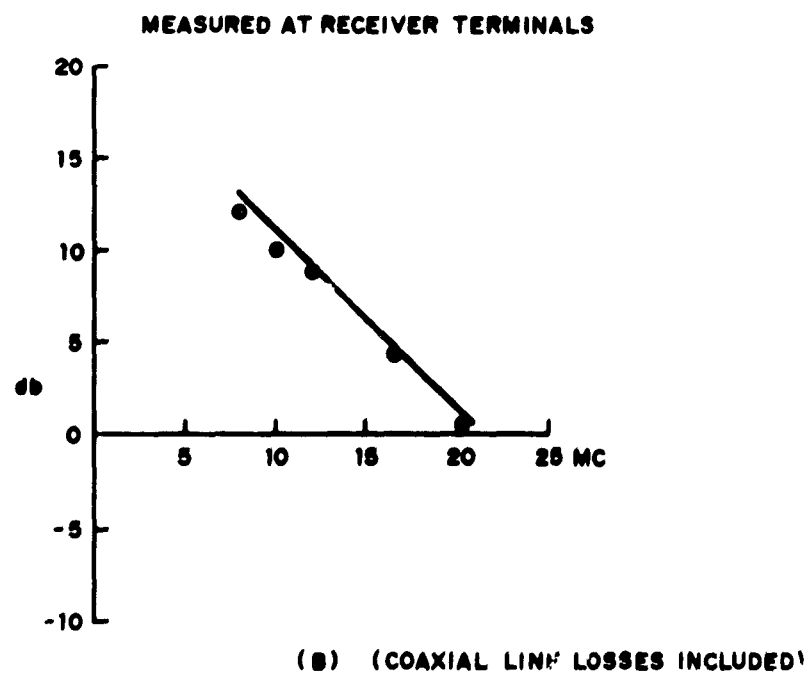
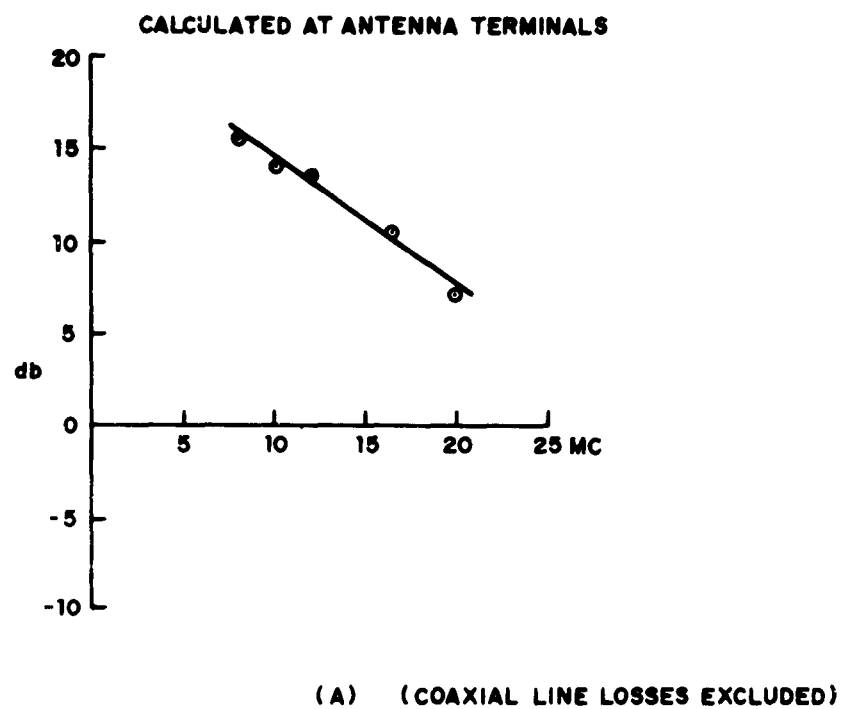


**Fig. 7.2 Ratio of Median Signal Levels on Rhombics
to That on Lens**

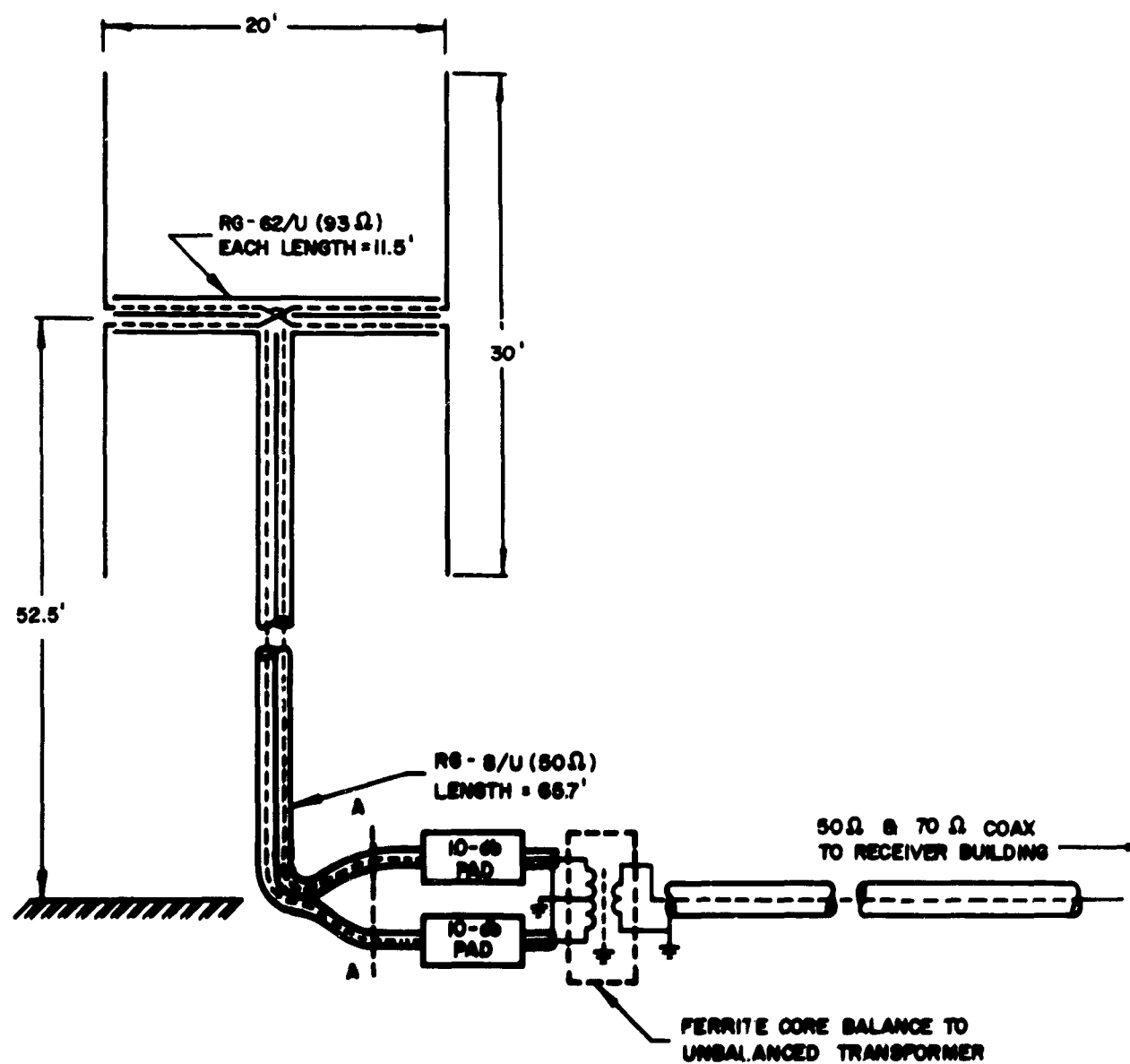


Fig. 7.3 Double-Dipole Gain Standard Antenna

where

R_{oL} = characteristic impedance of transmission line
connected to the lens -70 ohms

R_o = characteristic impedance of transmission line
connected to the double dipole -100 ohms

$Z_L = R_L + jX_L$ = input impedance at lens terminals (the T-junction)

$Z_D = R_D + jX_D$ = input impedance at double dipole terminals AA

P_L = power received in a matched detector at the lens terminals

P_D = power received in a matched detector at the double-
dipole terminals

$G_L = \eta_L D_L$ = lens gain

η_L = lens efficiency

D_L = lens directivity

$G_D = \eta_D D_D$ = double-dipole gain

η_D = double-dipole efficiency

D_D = double-dipole directivity .

The VSWR of the lens feeds was always less than 2:1 so it is possible without significant error to set $R_L + jX_L = R_{oL}$. Then Eq. (7.1) becomes

$$\frac{G_L}{G_D} = \frac{P_L}{P_D} \cdot \frac{4 R_o R_D}{|R_o + R_D + jX_D|^2} = \frac{D_L \eta_L}{D_D \eta_D} \quad (7.2)$$

The input impedance of the double-dipole antenna oriented to receive both vertically and horizontally polarized signals was measured by NRL personnel and found to be the same, within experimental accuracy, for both orientations of the dipoles. The measured input impedance for the double dipole oriented to receive vertically polarized signals is shown plotted on a Smith Chart in Fig. 7.4. In this plot, the impedance data have been referred to the dipole terminals. To effect this transformation, it was assumed that the connecting transmission lines have a uniform characteristic impedance of 100 ohms and that their equivalent electrical length (measured in meters of air line) is 34.2 meters. It was further assumed that the connecting lines were lossless although, as discussed later, the small loss of the cables has a profound effect on the antenna input resistance and efficiency, particularly at the low-frequency end of the band.

The gain and radiation resistance for the vertically oriented double-dipole antenna have been calculated by Dr. M. Andreasen of TRG, Incorporated, using a digital computer to solve the appropriate integral equation for the current distribution on the radiating elements. In this analysis the radiation resistance has been calculated on the assumption that the antenna is radiating into free space, since the mutual coupling between the antenna and its image in the ground is small. Its directivity has been calculated as though the antenna were mounted over a perfectly conducting ground. His results are shown in Table 7.1. It is seen that the radiation resistance, which is quite low at the low-frequency end of the band, has a substantial value at the high-frequency end of the band where the individual dipole elements are almost one wavelength long. On the other hand, the directivity of the antenna decreases very slowly with increasing frequency.

Table 7.1

Double Dipole Calculated Directivity and Radiation Resistance

f-Mc	R _A -ohms	Directivity-db
5.6	0.343	8.51
9.1	2.66	8.47
11.8	8.68	8.40
15.3	33.1	8.28
21.5	269.	8.02
25.3	354.	7.91
30.0	165.	7.44

The fact that the antenna radiation resistance at low frequencies is so much lower than the 100-ohm characteristic impedance level of the connecting transmission lines magnifies the effect of the small loss in these lines. A straightforward analysis shows that if a load impedance $Z_A = R_A + jX_A$ is connected to a transmission line of characteristic impedance Z_{0a} that has a total electrical length of β radians and a total attenuation of α nepers, the ratio η of the power delivered to R_A to that entering the line is

$$\eta = \frac{R_A}{R_{IN}} \frac{1}{\left[\frac{Z_A}{Z_0} \sinh(\alpha + j\beta) + \cosh(\alpha + j\beta) \right]^2} \quad (7.3)$$

where R_{IN} is the input resistance of the terminated line. When

$$\beta = \frac{\pi}{2}, \pi, \frac{3\pi}{2}, \dots$$

Eq. (7.3) simplifies to

$$\eta = \frac{1}{1 + \alpha \left[\frac{R_A}{Z_0} + \frac{R_0}{R_A} + \frac{X_A^2}{R_A Z_0} \right] + \alpha^2} \quad (7.4)$$

Values of η close to those predicted by Eq. (7.4) obtain for intermediate values of β .

Table 7.2 presents the measured values of lens gain obtained using the vertically polarized double-dipole antenna as the gain standard. The first column headed

$$10 \log_{10} \frac{P_L}{P_D}$$

shows the measured ratio of the power received on a matched 70-ohm detector at the Anchorage feed terminals to that received at a matched 100-ohm detector at the double-dipole terminals AA (see Fig. 7.3). The second column headed

$$10 \log_{10} \frac{4 R_0 R_D}{|R_0 + R_D + jX_D|^2}$$

Table 7.2

Measured Values of Lens Gain

f-Mc	$10 \log_{10} \frac{P_L}{P_D}$	$10 \log_{10} \frac{4 R_o R_D}{ R_o + R_D + jX_D ^2}$	$10 \log_{10} \eta_D$	$10 \log_{10} D_D$	$10 \log_{10} G_L$
5.6	21.2	-7.6	-19.7	8.51	2.4
9.1	21.3	-7.4	-10.2	8.47	12.2
11.8	9.2	-5.6	-4.1	8.40	7.9
15.3	2.5	-1	-0.9	8.28	8.9
21.5	-2.4	-2	-1	8.02	2.6
25.3	-3.2	-2.5	-1.6	7.91	0.6
30.0	+4.7	-2	-1.6	7.44	8.5

P_L/P_D = ratio of power received in matched detectors at the Anchorage feed terminals to that received at double-dipole antenna terminals AA (see Fig. 7.3)

R_o = 100 ohms

$R_D + jX_D$ = double-dipole input impedance at terminals AA

η_D = double-dipole antenna efficiency (due to losses in lines between double-dipole terminals and terminals AA)

D_D = double-dipole antenna directivity

G_L = lens gain

shows the ratio of the power received at the double-dipole terminals AA in a 100-ohm detector to the available power which would be received in a conjugate matched detector (i.e., one having an input impedance of $R_D - jX_D$). The third column headed $10 \log_{10} \eta_D$ shows the values of double-dipole efficiency due to losses in the connecting cables calculated from Eq. (7.4). In this calculation, the theoretical values of the radiation resistance R_A from Table 7.1 were used together with the values of X_{IN} measured at terminals AA from Fig. 7.4, which are very close to the values of X_A . The fourth column headed $10 \log_{10} D_D$ is the theoretical directivity of the double-dipole antenna obtained from Table 7.1. The fifth column headed $10 \log_{10} GL$, which is the sum of the other four columns, is the measured lens gain.

These measured values of gain have been plotted in Fig. 7.5 together with the calculated values of gain and directivity for the Wire-Grid Lens Antenna. There is considerable scatter in the measured values of gain. It is believed that this scatter is caused principally by perturbations of the waves incident on the lens and the double dipole due to the irregular terrain at the site and the presence of other near-antennas.

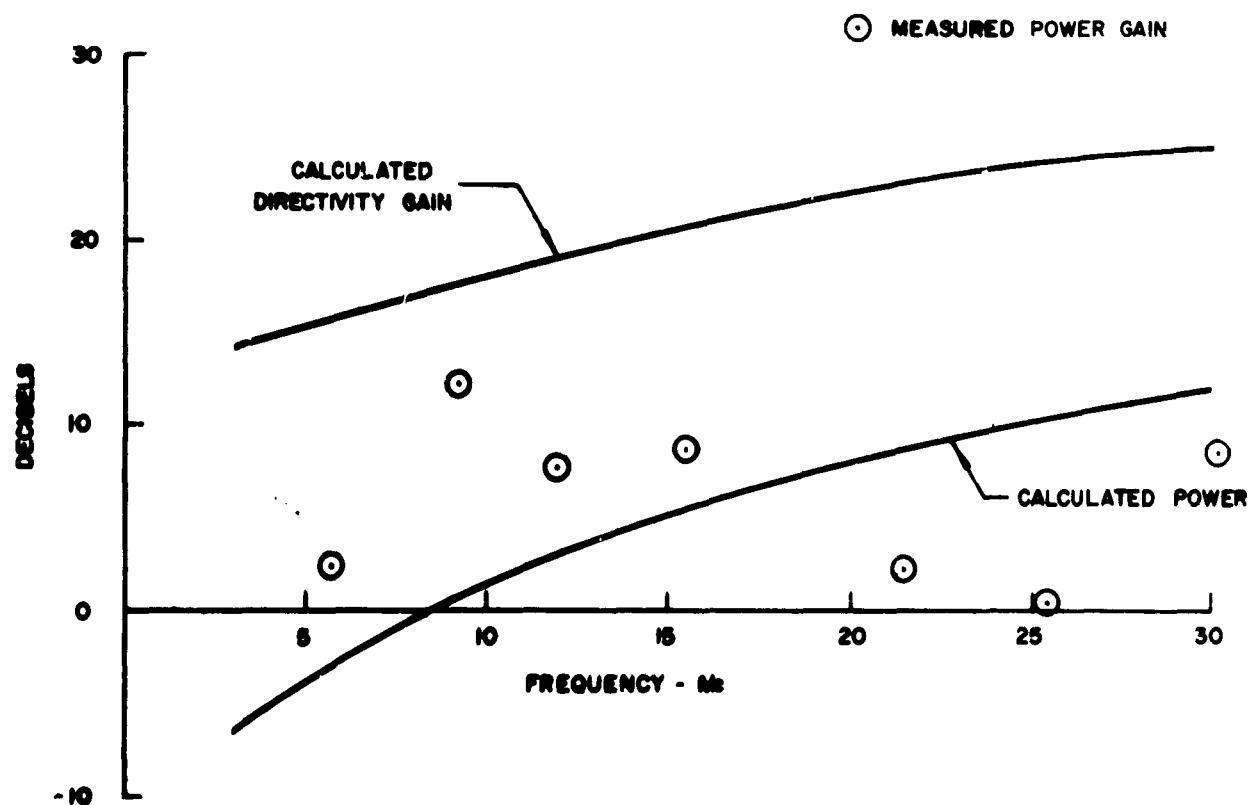


Fig. 7.5 Directivity and Gain of Wire-Grid Lens Antenna

8. COMMUNICATION TRAFFIC ERROR RATES

8.1 Operational Traffic Error Count Evaluation Using FAA Developed Equipment

8.1.1 Introduction

Another phase of the Joint Services Evaluation was a comparison of the binary error rate of 100 word per minute operational message traffic carried principally in the 5 to 24 Mc band and received on both the lens and the station rhombics. These tests, which were conducted for a five-month period in the Spring and Summer of 1964, demonstrated that over the 5 to 24 Mc test band the error rates for operational messages received on the lens and the rhombics were very similar. The technique used for measuring these errors was developed by Mr. K. H. Quin of the FAA using readily available equipment. A feature of this system is the fact that it does not require a cooperative transmitter (which sends a known message) as do most such systems. A majority of the data accumulated using the FAA equipment were recorded by NRL personnel.

8.1.2 FAA Error Measuring Equipment

A block diagram of the automatic equipment used to measure the binary error rates is shown in Fig. 8.1. As can be seen from the figure, messages received simultaneously on the diversity channel and on the simplex channel are compared in a binary error detector. Non-comparisons between the binary bits received on the two channels are then totaled by an electronic counter and printed out on tape.

The diversity comparator is a decision making device that selects whichever one of the diversity elements is receiving the stronger signal. If one assumes the diversity comparator is perfect and that the probability of receiving an error on the diversity channel is zero then each non-comparison registered by the binary error detector represents an error for the simplex antenna. Under this assumption, a summation of the errors recorded, when a rhombic and the lens are used alternately as the antenna in the simplex channel, gives a measure of the binary error rate for each simplex antenna.

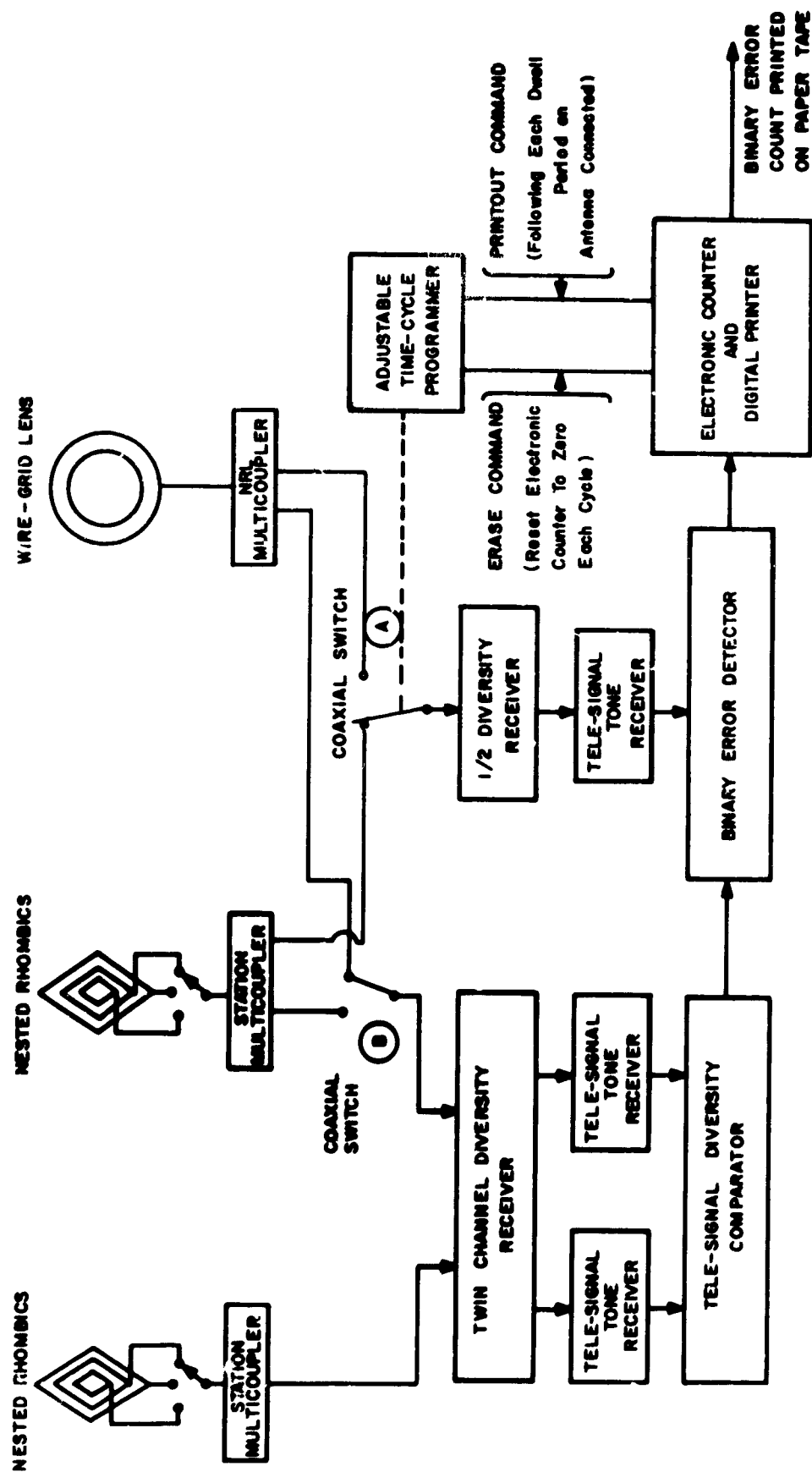


Fig. 8.1 FAA Binary Error Recording System

A number of factors modify this picture of the operation of the equipment. One is the fact that the probability of an error occurring on the diversity channel, while quite low, is not zero. Another is the fact that one of the antennas used in the diversity channel is also used as one of the simplex antennas. Therefore, part of the time this simplex antenna is being compared to itself so that no errors can be recorded, even though errors actually occur. Thus, a bias is introduced in favor of the antenna being compared with itself. Since the diversity standard consisted of two rhombics part of the time and the lens and the rhombic part of the time, a bias was introduced in favor of the rhombic part of the time and in favor of the lens the remainder of the time. Still other factors which modify the operation are: line attenuation between the antennas and measuring equipment, receiver unbalance in the two channels and the duty factor of the received transmissions. The effect of each of these factors on the accuracy of the results is considered in subsequent sections.

8.1.3 Analysis of FAA Error Measuring Equipment

In order to obtain a quantitative measure of the effect of these imperfections, a probability analysis was made of the system shown in Fig. 8.1 which is presented in Appendix A. This analysis shows that by using two rhombics for the diversity pair part of the time, and the lens and a rhombic as the diversity pair the remainder of the time, a quantitative measure of the error rate for the lens and the rhombic is obtained, which is very close to the true error rate.

Figure 8.1 shows the measuring set-up arranged so that one of the three rhombics in the left hand nest, and the lens, are used as the diversity pair. By throwing switch B to the left, two rhombics would be connected as the diversity pair.* The coaxial switch, A, which is actuated by the adjustable time cycle programmer, connects either the lens, or one of the rhombics in the right hand nest, to operate as the simplex antenna. During the error-counting measurements of the 100 word per minute teletype messages, the switch was cycled at five-minute intervals. Thus, a total of 5 minutes x 100 words per minute x 6 characters per word x 7 binary bits per character = 21,000 binary bits nominal were received during each five-minute period.

* In the original system devised by the FAA, a pair of rhombics was used as the diversity pair. Switch B was added after the first three months of operation so that the lens and a rhombic could also be used as a diversity pair. Substantially all the data recorded during the last three months of the test were recorded using the lens and a rhombic as the diversity pair.

The analysis presented in Appendix A shows that when the two identical rhombics are used as the diversity pair, the number of errors, $E(L)$, recorded for the lens and the number of errors, $E(R)$, recorded for the rhombic, each operating in simplex will be

$$E(L) = N_1 p(L) \left[1 + \frac{p(R)}{p(L)} \cdot \frac{2}{1+n} \right] \quad (8.1)$$

$$E(R) = N_1 p(R) \quad (8.2)$$

where

- $p(L)$ = true probability of an error being received on the lens
- $p(R)$ = true probability of an error being received on the rhombic
- N_1 = number of binary bits received on the lens assumed equal to the number of bits received on the rhombic
- n = a measure of the effectiveness of the diversity system (ratio of probability of an error being received on one of the diversity antennas when it does not control the system to the probability of an error being received when it does).

During the measurements, the diversity comparator was adjusted so that each receiver in the diversity pair controlled the system half the time, in conformity with the assumption made in deriving Eqs. (8.1) and (8.2). These equations show that the number of errors recorded for the simplex rhombic antenna will be the true number of errors, $N_1 p(R)$, while the number of errors recorded for the lens will be greater than the true number of errors, $N_1 p(L)$.

When the lens and a rhombic are used as the diversity pair, the number of errors recorded for the lens and the rhombic operating in simplex will be

$$E(L) = N_2 p(L) \left[\frac{1 + mn}{1 + n} \right] \quad (8.3)$$

$$E(R) = N_2 p(R) \left[1 + \frac{1 + m}{1 + n} \right] \quad (8.4)$$

where

- N_2 = number of binary bits received on the lens
assumed equal to the number of bits received
on the rhombic
- m = ratio of probability of an error being received
on the diversity system when the lens controls,
to the probability of an error being received
when the rhombic controls.

Again, it has been assumed that each receiver in the diversity pair controls the system half the time. In this case, it is seen that the true number of errors are not counted for either the lens or the rhombic. The number of errors counted for the lens, however, is more nearly correct than the number counted for the rhombic. If one assumes that $m = 1$, it is seen that the true number of errors are counted for the lens and a larger number are counted for the rhombic, a situation exactly opposite that obtained when two rhombics are used as the diversity pair.

The following situation exists when two different diversity pairs are used during a run. If the diversity pair consists of a pair of rhombics while N_1 bits are received on the simplex lens as well as on the simplex rhombic, and if the diversity pair consists of the lens and a rhombic while N_2 bits are received on the simplex lens as well as the simplex rhombic, then the total errors, $E(L)$, recorded for the lens and the total errors, $E(R)$, recorded for the rhombic will be

$$E(L) = p(L) \left[N_1 \left(1 + \frac{2}{(1+n)m} \right) + N_2 \frac{(1+mn)}{1+n} \right] \quad (8.5)$$

$$E(R) = p(R) \left[N_1 + N_2 \left(1 + \frac{1+m}{1+n} \right) \right] \quad (8.6)$$

where it has been assumed that $p(L)/p(R) = m$. That is, the true ratio of probability of errors for the lens and a rhombic is the same as the ratio of the probability of an error being received on the diversity system, when the lens is controlling, to the probability of an error being received when the rhombic is controlling. Remembering that the definition of true number of errors, $E^1(L)$, received on the lens is

$$E^1(L) = p(L) (N_1 + N_2) \quad (8.7)$$

and the true number of errors $E^1(R)$ received on the rhombic is

$$E^1(R) = p(R) (N_1 + N_2) \quad (8.8)$$

it is seen that,

$$\frac{E(L)}{E^1(L)} = \left[\frac{\frac{1}{N_2} (1 + \frac{2}{(1+n)m})}{1 + \frac{1}{N_1}} + \frac{\frac{1}{N_1} \cdot \frac{(1+mn)}{1+n}}{1 + \frac{1}{N_2}} \right] \quad (8.9)$$

and,

$$\frac{E(R)}{E^1(R)} = \left[\frac{\frac{1}{N_2}}{1 + \frac{1}{N_1}} + \frac{\frac{1}{N_1} (1 + \frac{1+m}{1+n})}{1 + \frac{1}{N_2}} \right] \quad (8.10)$$

When $m = 1$ and $N_1 = N_2$ it is seen that the ratio $E(L)/E(R)$ of the number of errors recorded for the lens and the rhombic will be equal to the true ratio of probabilities $p(L)/p(R)$ of errors for the lens and the rhombic, and in this case one also finds $E(L)/E^1(L) = E(R)/E^1(R) = 1 + 1/1 + n$. The actual number of binary bits received during the evaluation when the lens and a rhombic were used as a diversity pair were greater than the number of binary bits received when the two rhombics were used as the diversity pair, so that $N_1 < N_2$.

8.1.4 Measured Error Rates Using the FAA Technique

The results of the error-counting measurements obtained are shown plotted on cumulative probability paper in Figs. 8.2 through 8.5 for the frequencies of 5 Mc, 6 Mc, 8 to 13 Mc and 16 to 24 Mc, and in Fig. 8.6, which is a composite of the results in Figs. 8.2 through 8.5, for all the frequencies from 5 to 24 Mc. This composite figure was obtained by plotting all the measured error-count data in the 5 to 24 Mc band in the same fashion that it is plotted for each of the bands in Figs. 8.2 through 8.5. In each figure the data have been plotted on semi-log paper for both the lens and the rhombic to show the percent of samples having an error rate less than the value of the abscissa. It is shown in Appendix A how the ratio of the probability of errors being received on the lens to the probability of errors being received on the rhombic $p(L)/p(R)$, can be obtained from the ratio of Eqs. (8.5) and (8.6) for various values of n . This process has been carried out using as the value of $E(L)/E(R)$ the ratio of the binary error rates in Figs. 8.2 through 8.6 for the lens and the rhombic corresponding to the case where 50 per cent of the five-minute samples have an error rate less than that of the abscissa (i. e., the median error rate). The results are presented in Table 8.1 for assumed values of $n = 10$ and $n = 15$ which correspond to the range of improvement to be expected from the diversity system. It is seen that $p(L)/p(R)$ is very close to the measured ratio $E(L)/E(R)$. Thus, a direct comparison of the performance of the lens and the rhombics as presented in Figs. 8.2 through 8.6 gives measure of their relative performance. Also shown in the table, but subject to the uncertainties listed in Sec. 8.1.2, are the ratios $E(L)/E'(L)$ and $E(R)/E'(R)$. An inspection of these ratios shows that the measured number of errors for the lens and the rhombic are only slightly higher than the true number of errors received. Thus, it can be concluded that the curves of Figs. 8.2 through 8.6 also give a measure of the absolute error rates for the lens and the rhombics when receiving operational traffic.

Several antenna combinations were used as the test system diversity standard while accumulating the FAA data as shown in the tabulation of Table 8.2. The 'Circuit 350' rhombics listed consisted of a pair of rhombics, while unidentified, are assumed to be the proper combination for the frequency as selected by the FAA station personnel. The tabulation shows some out-of-band rhombics were used in diversity which resulted, at times, in the selection of that rhombic for comparison to the standard. Such data have been eliminated and do not appear in Table 8.2; but in some cases where an in-band rhombic was used to compare to the standard, which may have consisted of one out-of-band rhombic, the data were retained. Thus, in all cases the lens was compared with rhombics 4A, 4B, or 4C operating within their design bands.

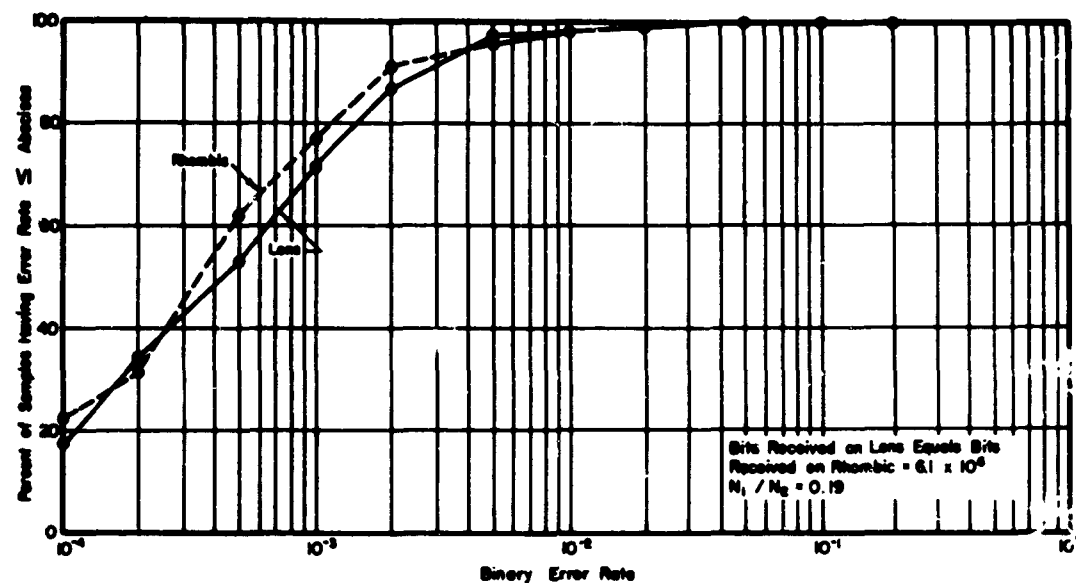


Fig. 8.2 Binary Error Rates for Rhombics and Wire-Grid Lens at Molokai when Receiving San Francisco Signals at 5 Mc

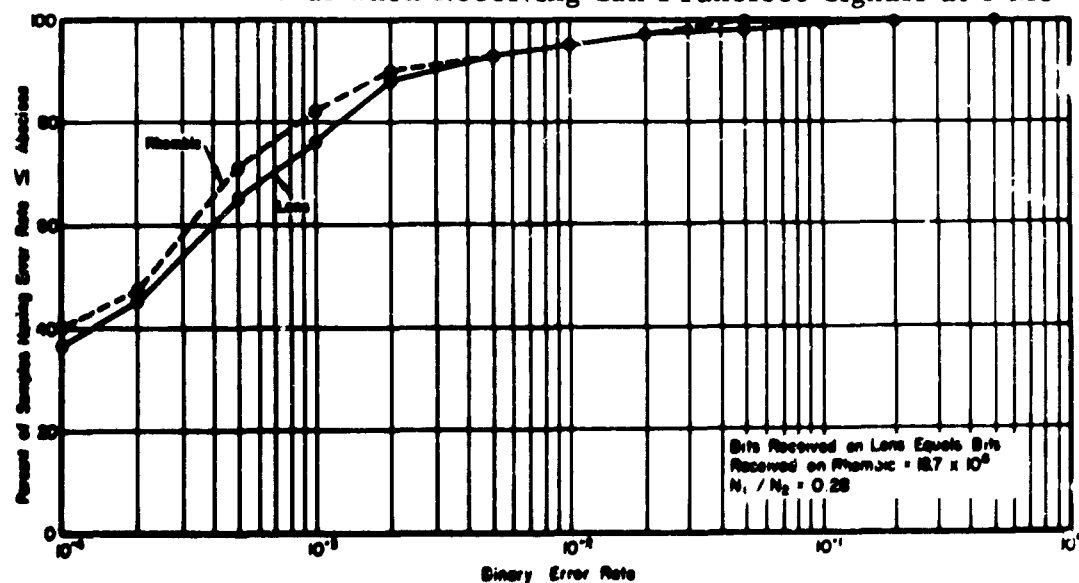


Fig. 8.3 Binary Error Rates for Rhombics and Wire-Grid Lens at Molokai when Receiving San Francisco Signals at 6 Mc

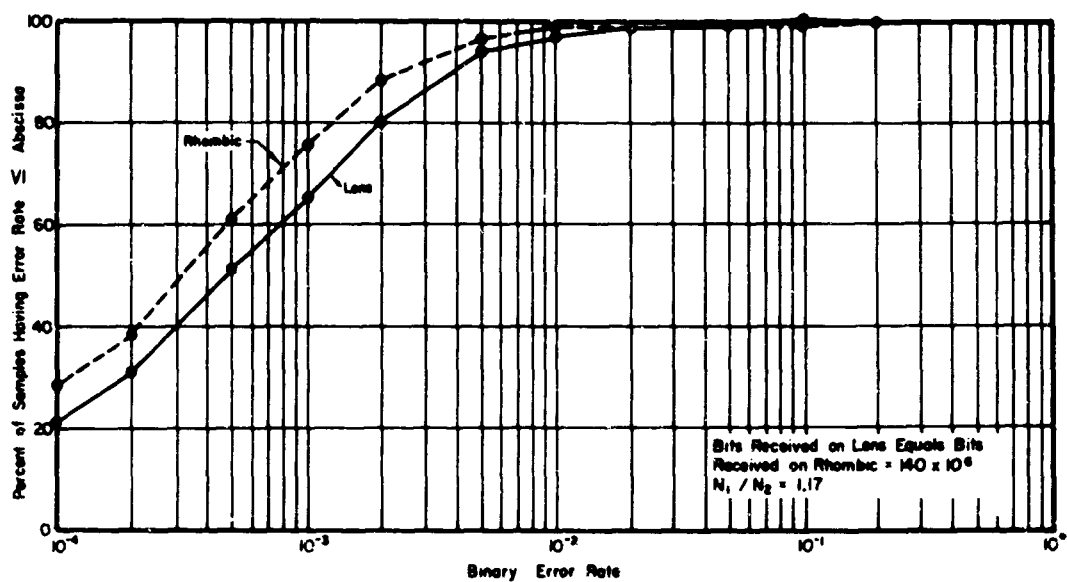


Fig. 8.4 Binary Error Rates for Rhombics and Wire-Grid Lens at Molokai when Receiving San Francisco Signals at 8 - 13 Mc

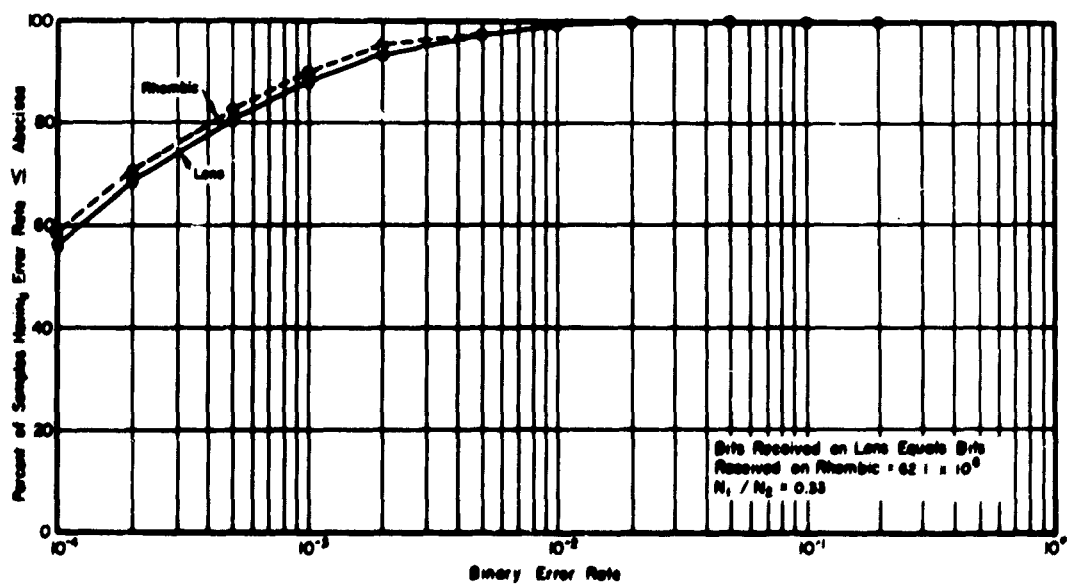


Fig. 8.5 Binary Error Rates for Rhombics and Wire-Grid Lens at Molokai when Receiving San Francisco Signals at 16 - 24 Mc

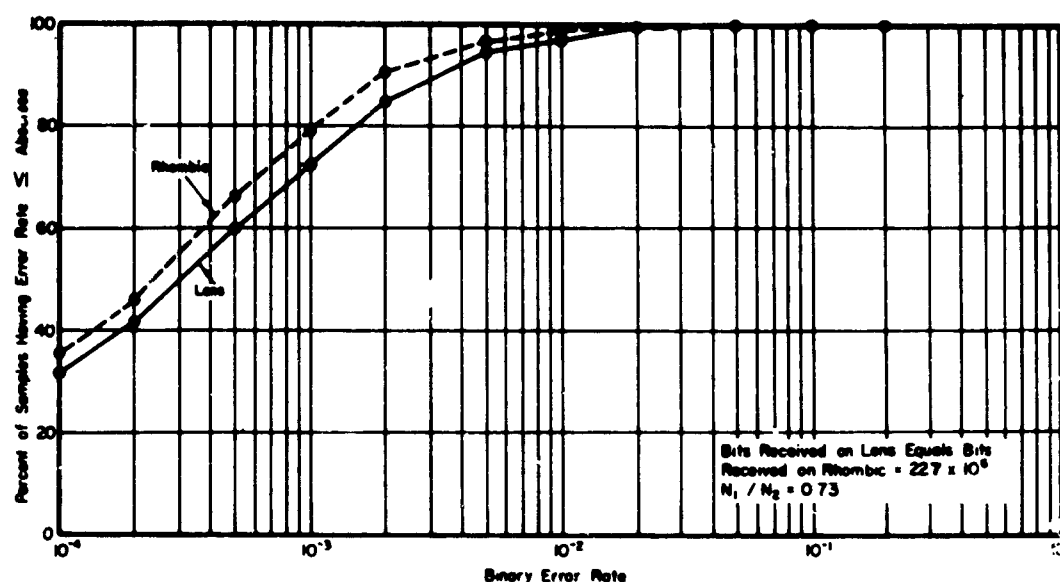


Fig. 8.6 Binary Error Rates for Rhombics and Wire-Grid Lens at Molokai When Receiving San Francisco Signals at 5 - 24 Mc

A summary of the data in Table 8.2 is presented in Table 8.3 to show the percentage of time in each frequency band that each diversity standard was used to measure the performance of an in-band rhombic. For the total period of time data were recorded in the 5 to 6 Mc band, an out-of-band rhombic was used as part of the diversity standard 10.6 percent of that time; in-band rhombics were used in diversity 16.5 percent of the total time of recording data in the frequency band; and for 72.9 percent of the time an in-band rhombic and lens were in the diversity standard. In the total recording time for the 8 to 13 Mc band, 6.5 percent of the time an out-of-band rhombic was used in diversity; 55.5 percent of the time in-band rhombics were used; and 37.9 percent of the time the lens/in-band rhombic combination was used. For the total time in the 16 to 24 Mc band, only 2.1 percent of the time was an out-of-band rhombic used in diversity; 24.9 percent of the time in-band rhombics were used; and 73 percent of the time the combination lens/in-band rhombic was used. The exact effect of these various diversity standards upon the error-count recorded for the simplex antenna under test cannot be stated since the diversity error rate for the several diversity antenna combinations is unknown.

Table 8.1

Measured Error Rates for the Wire-Grid Lens Antenna Receiving
Operational Traffic Determined Using the FAA Measuring Techniques

f-Mc	N_1/N_2	$E(L)/E(R)$	n	$p(L)/p(R)$	$E(L)/E'(L)$	$E(R)/E'(R)$
5	.19	1.2	10	1.2	1.18	1.19
5	.19	1.2	15	1.17	1.11	1.14
6	.28	1.1	10	1.08	1.13	1.20
6	.28	1.1	15	1.05	1.11	1.15
8-13	1.17	1.49	10	1.34	1.21	1.1
8-13	1.17	1.49	15	1.33	1.16	1.07
16-24	.33	1.1	10	1.12	1.11	1.14
16-24	.33	1.1	15	1.10	1.05	1.10
5-24	.74	1.26	10	1.2	1.17	1.11
5-24	.74	1.26	15	1.19	1.12	1.08

N_1/N_2 = ratio of bits received using two rhombics as diversity standard to hits received using lens and rhombic as diversity standard

n = ratio of probability of an error being received on one of the diversity antennas when it does not control the system to the probability of an error being received when it does

$p(L)/p(R)$ = probability of error being received on lens to the probability of an error being received on rhombic

$E(L)/E'(L)$ = ratio of measured lens errors to received lens errors

$E(R)/E'(R)$ = ratio of measured rhombic errors to received rhombic errors

$E(L)/E(R)$ = ratio of measured errors on lens and rhombic

Table 8.2

Antennas Used During the FAA Error-Count Evaluation

Frequency Mc	Diversity Standard		Number of Five-Minute 21,000-Bit Sam			
			Lens	Rhombic 4A	Rhombic 4B	Rhomb
5	Lens	Rhombic 4A	63		63	
5	Lens	Rhombic 4C	14		13	
5	Lens	Rhombic 3B	50		49	
5	Rhombic 3B	Rhombic 4B	22		23	
5	Circuit 350 rhombics		21		23	
5	Lens	Rhombic 4A	96	96		
5	Lens	Rhombic 3A	23	23		
6	Lens	Rhombic 3A	57	56		
6	Lens	Rhombic 4A	41	44		
6	Lens	Rhombic 4A	207		210	
6	Lens	Rhombic 3A	192		208	
6	Lens	Rhombic 3B	135		131	
6	Lens	Rhombic 3C	64		65	
6	Rhombic 4A	Rhombic 3B	46		48	
6	Rhombic 3C	Rhombic 4C	46		47	
6	Circuit 350 rhombics		102		102	
8 - 13	Lens	Rhombic 4A	157		135	
8 - 13	Lens	Rhombic 4B	207		205	
8 - 13	Lens	Rhombic 3A	19		16	
8 - 13	Lens	Rhombic 3B	1245		1222	
8 - 13	Lens	Rhombic 3C	80		77	
8 - 13	Rhombic 4A	Rhombic 3A	5		4	
8 - 13	Rhombic 3B	Rhombic 4B	139		134	
8 - 13	Rhombic 3C	Rhombic 4C	123		125	
8 - 13	Circuit 350 rhombics		2707		2698	
8 - 13	Lens	Rhombic 4A	204			19
9 - 13	Lens	Rhombic 4B	163			15
8 - 13	Lens	Rhombic 4C	114			11
8 - 13	Lens	Rhombic 3A	45			4
8 - 13	Lens	Rhombic 3B	293			30
8 - 13	Lens	Rhombic 3C	83			8
8 - 13	Rhombic 3A	Rhombic 4A	8			
8 - 13	Rhombic 3B	Rhombic 4B	85			8
8 - 13	Circuit 350 rhombics		462			46

(table continued on following page)

Table 8.2 (continued)

Antennas Used During the FAA Error-Count Evaluation

Frequency Mc	Diversity Standard		Number of Five-Minute 21,000-Bit Samples			
			Lens	Rhombic 4A	Rhombic 4B	Rhombic 4C
16 - 24	Lens	Rhombic 4A	62			67
16 - 24	Lens	Rhombic 4B	94			95
16 - 24	Lens	Rhombic 4C	80			79
16 - 24	Lens	Rhombic 3B	457			446
16 - 24	Lens	Rhombic 3C	81			83
16 - 24	Lens	Rhombic 3A	7			8
16 - 24	Rhombic 3B	Rhombic 4B	58			56
16 - 24	Circuit 350 rhombics		292			296
16 - 24	Lens	Rhombic 4A	46		47	
16 - 24	Lens	Rhombic 4B	86		84	
16 - 24	Lens	Rhombic 4C	292		294	
16 - 24	Lens	Rhombic 3B	441		434	
16 - 24	Lens	Rhombic 3C	580		568	
16 - 24	Rhombic 4A	Rhombic 4B	8		7	
16 - 24	Rhombic 3C	Rhombic 4C	77		76	
16 - 24	Circuit 350 rhombics		316		320	

Table 8.3

Summary of Antennas Arranged According to Frequency Bands Used in the FAA Error-Count Tests

Percent Samples Available for Analysis in Three Test Frequency Groups for Various Space Diversity Antennas						
Test Frequency Band	5 - 6 Mc		8 - 13 Mc			16 - 24 Mc
Test Rhombic Showing Design Frequency Band	Rhombic 4A 3 - 10 Mc	Rhombic 4B 6 - 18 Mc	Rhombic 4A 3 - 10 Mc	Rhombic 4B 6 - 18 Mc	Rhombic 4C 9 - 27 Mc	Rhombic 4C 9 - 27 Mc
In-Band Rhombic Antennas in Diversity	-	16.5%	0.5%	46%	9%	11.7%
Out-of-Band Rhombic Antennas in Diversity	-	3.9%	-	2%	-	-
Less and In-Band Rhombic in Diversity	18.7%	54.2%	6.9%	20%	11%	26%
Less and Out-of-Band Rhombic in Diversity	-	6.7%	-	1.3%	3.2%	0.3%

8.2 Error-Count Evaluation Using NRL Developed Techniques

Another evaluation of the traffic error rate of the Wire-Grid Lens was conducted by NRL with the aid of a cooperative transmitter located at Woodbridge, Virginia, transmitting 600 character-per-minute RYRY test messages. These messages were received on the San Francisco lens feed and the San Francisco station Rhombics 4B and 4C which are oriented within approximately 1.5 degrees of Woodbridge. The transmission frequencies used during this evaluation were determined by existing frequency allocations. Therefore, it was necessary to operate at second and third choice frequencies, as determined from long term predictions. Data were recorded during periods of strong signals and also in the transition period to provide complete distribution of error rates. This method of operation, combined with the facts that the Woodbridge to Molokai circuit was about twice as long as that from San Francisco to Molokai and characters were counted rather than binary bits, caused the measured character error rate for both the lens and the station rhombics to be about fifteen times higher than the binary error rate obtained during the FAA error rate evaluation using operational signals.

8.2.1 NRL Error-Count Measuring Technique

The test messages sent from Woodbridge were non-frequency diversity, narrow-band FSK signals transmitted for twenty-minute periods followed by ten-minute periods when the transmitter output was shut off. However, for one minute during the middle of each off period an identification signal was transmitted.

Figure 8.7 is a block diagram of the basic radio test receiving system used by NRL. It is seen that the radio teletype signals were received simultaneously on the San Francisco feed of the lens and on either Rhombic 4B or 4C. Signals picked up by the antennas were conducted by transmission lines to the receiver building housing the test equipment. Here the signals were distributed to the test equipment by multicouplers so as not to interfere with the normal station operation. The multicoupler used with the Wire-Grid Lens Antenna was supplied by NRL while the multicouplers used with the rhombics were FAA station multicouplers. The two receiving channels were frequently checked to assure that they were operating properly and as an added precaution the two systems were alternated between the lens and rhombic multicoupler outputs at the end of each teletype test message.

Analysis of the teletype data obtained at Molokai consisted first of a careful visual inspection of the reperfected tapes at which time the tapes were cut into frames corresponding to the interval between the times the receiving equipments were alternated between test antennas.

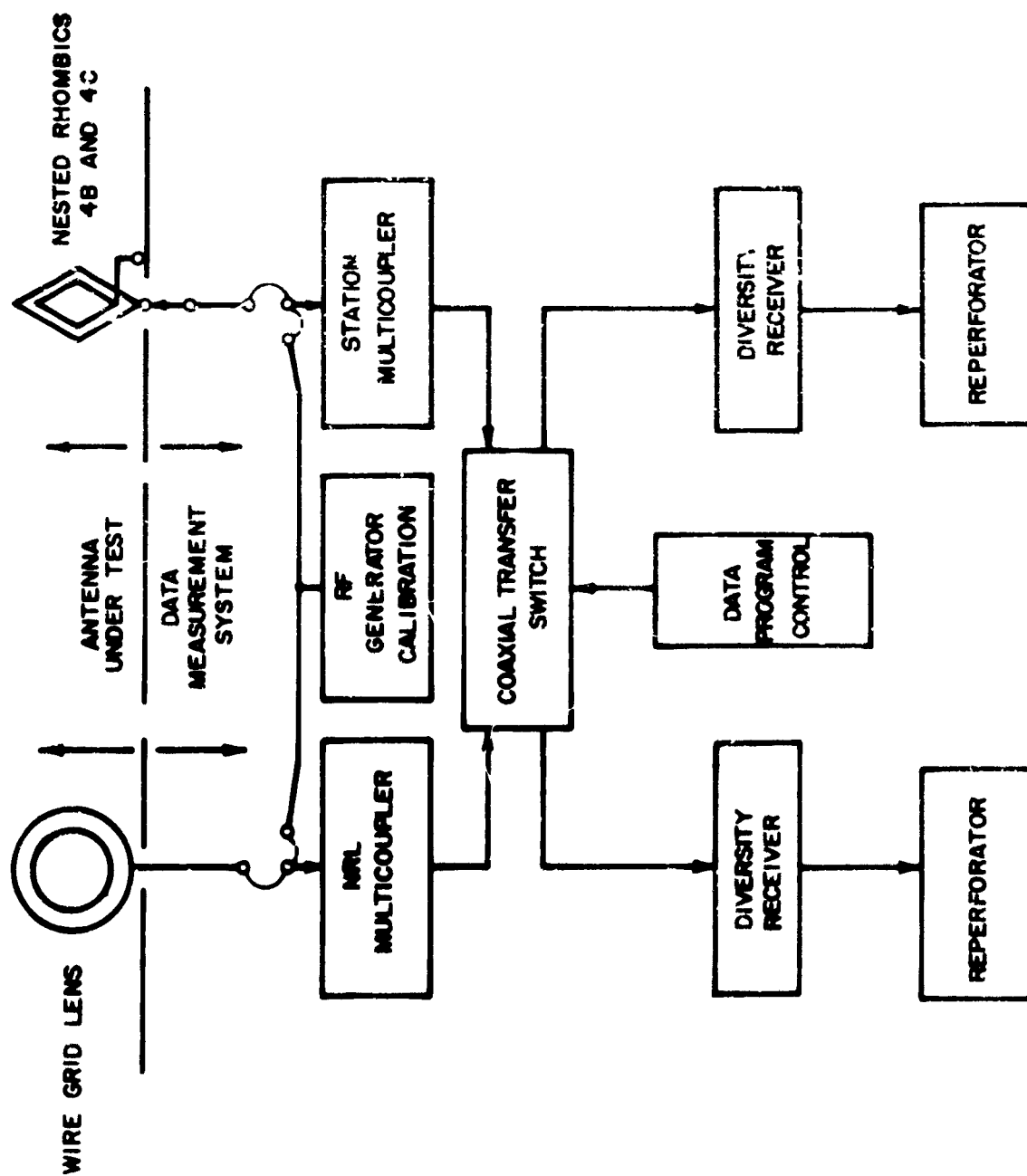


Figure 1-1-1. NRL Testbed for Antenna Measurement System

Each frame in which receiver or transmitter test equipment failures were determined to have occurred was discarded. If a frame was discarded for one test antenna, the simultaneous frame on the other test antenna was also discarded regardless of the message quality of that frame. Second, the total number of characters and the total number of character errors in each frame were then separately and automatically counted by feeding the tape through a tape reader and logic network whose outputs were connected to totalizing counters. If the total number of characters counted was less than the total number of characters known to have been sent, then the difference in these totals was added to the number of errors read on the totalizing counter and this sum is considered to be the number of errors received. The error rate for each frame was calculated by dividing the total number of errors received by the total number of characters known to have been sent. Each of the frames was classified as having an error rate equal to or less than a given value.

Figures 8.8 through 8.12 show the results of the NRL error-count measurements plotted on cumulative probability paper for the test frequencies of 8, 10.7, 12 to 13.6, 17.5 and 20 Mc. A summary of these results for the 8 to 20 Mc band is shown in Fig. 8.13, which is a composite of all the results in Figs. 8.8 through 8.12. This composite figure was obtained by plotting all the measured error count data in the 8 to 20 Mc band in the same fashion that it is plotted for each of the six test frequencies. The ratio of the measured character error rate for the lens and rhombic from Fig. 8.13 is 1.5 over the 8 to 20 Mc band.

8.2.2 NRL Signal and Noise Amplitude Data Measurement Technique

Signal amplitude measurements conducted by NRL for the Wire-Grid Lens Antenna evaluation utilized the signal which was transmitted at constant amplitude for the NRL radio teletype tests. Noise amplitude measurements were conducted during the ten-minute intervals at the hour and half hour times when the transmitter output was shut off. The factor measured for both signal and noise amplitude data was an AGC voltage proportional to the received rf energy. Figure 8.14 is a block diagram of the signal and noise amplitude test receiving system. As may be noted in Fig. 8.14, a signal or noise was recorded simultaneously with the Wire-Grid Lens Antenna and the rhombic antenna. The signal and noise data were recorded for each antenna on both a magnetic tape recorder operating in the FM mode and a multi-channel strip chart recorder. The magnetic tape recordings were used for automatic data reduction at NRL. The strip chart recordings were used for qualitative information during the tests and reduction of the data, and for obtaining calibration curves of the characteristics of the active electronic recording equipment. Receiver bandwidths utilized with each antenna were determined to be comparable during the tests. In order

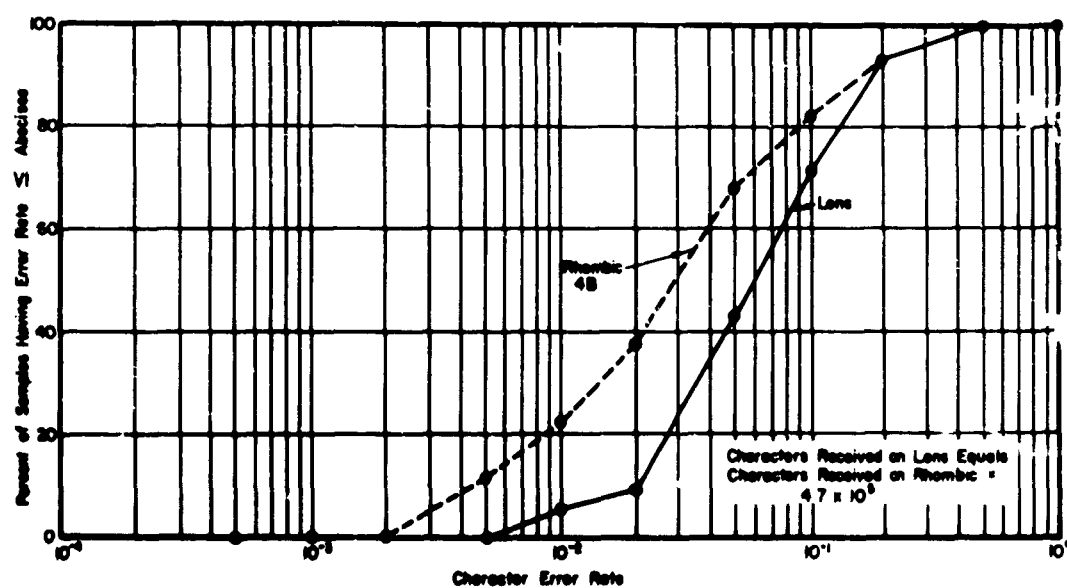


Fig. 8.8 Character Error Rates for Rhombic and Wire-Grid Lens at Molokai when Receiving 600 character-per-minute RY Test Signals from Washington at 8 Mc

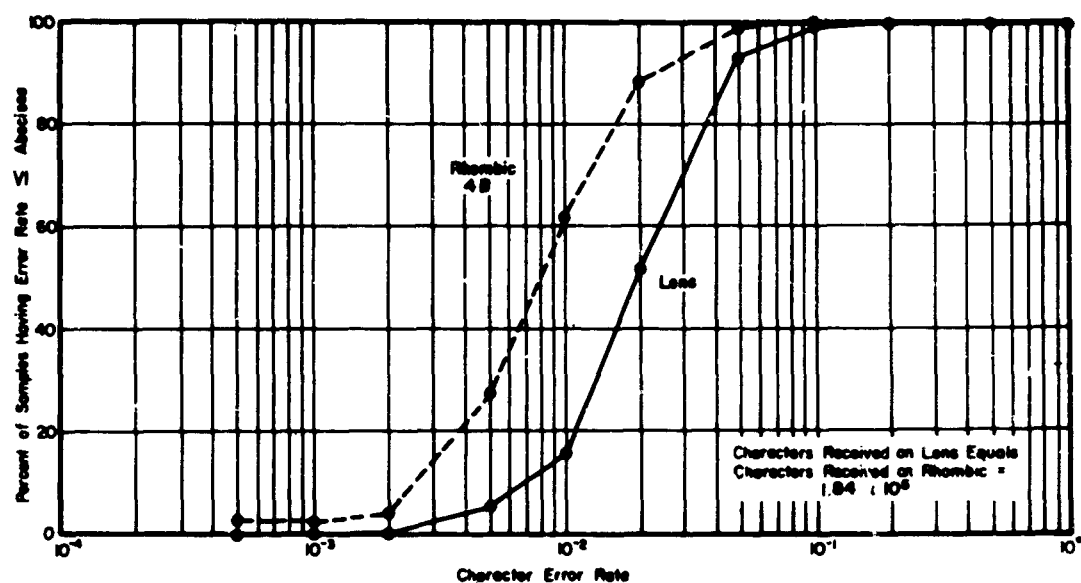


Fig. 8.9 Character Error Rates for Rhombic and Wire-Grid Lens at Molokai when Receiving 600 character-per-minute RY Test Signals from Washington at 10.7 Mc

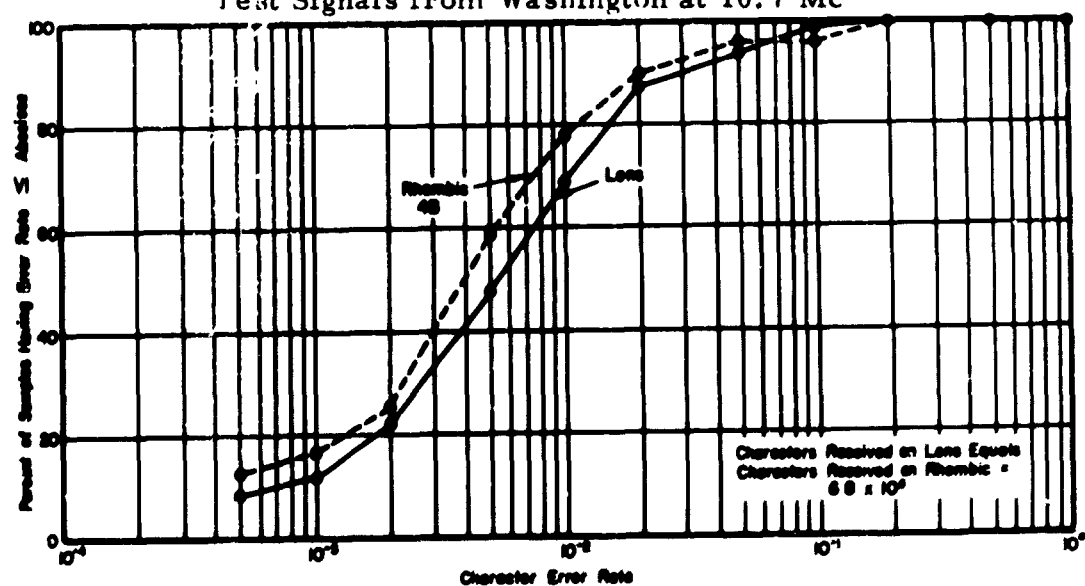


Fig. 8.10 Character Error Rates for Rhombic and Wire-Grid Lens at Molokai when Receiving 600 character-per-minute RY Test Signals from Washington in the 12-13.6 Mc Band

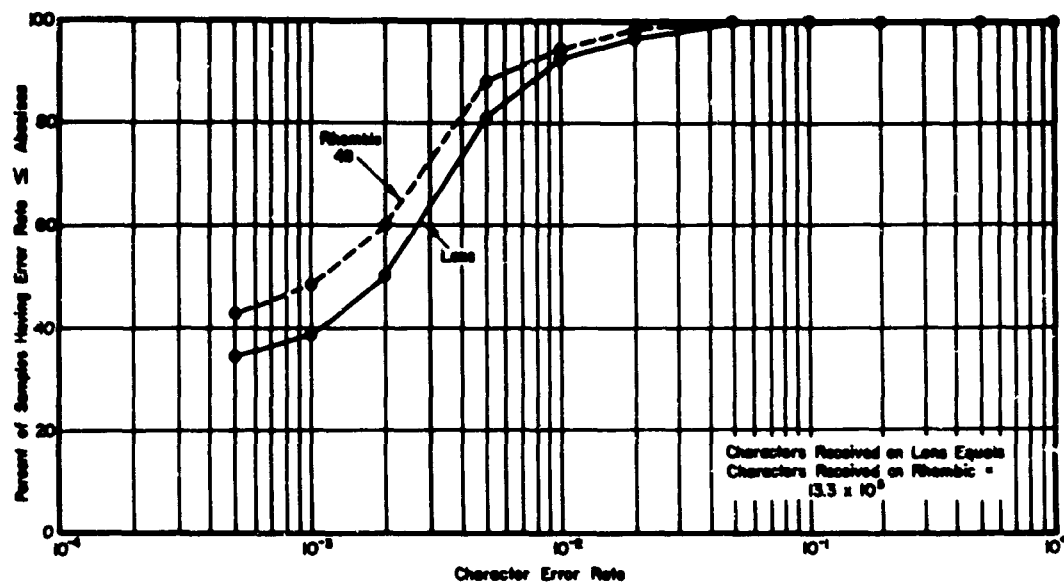


Fig. 8.11 Character Error Rates for Rhombic and Wire-Grid Lens at Molokai when Receiving 600 character-per-minute RY Test Signals from Washington at 17.5 Mc

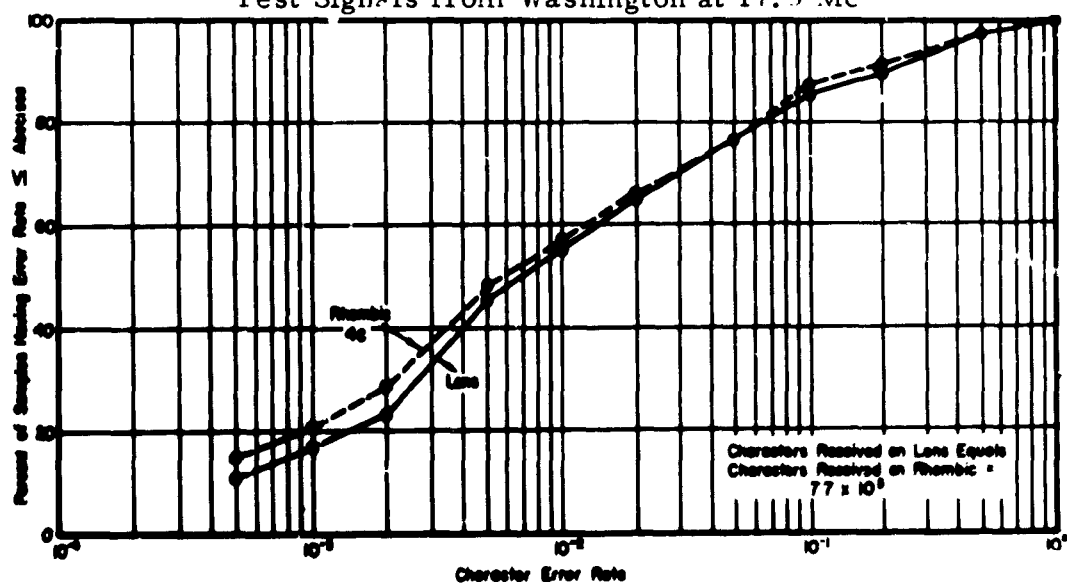


Fig. 8.12 Character Error Rates for Rhombic and Wire-Grid Lens at Molokai when Receiving 600 character-per-minute RY Test Signals from Washington at 20 Mc

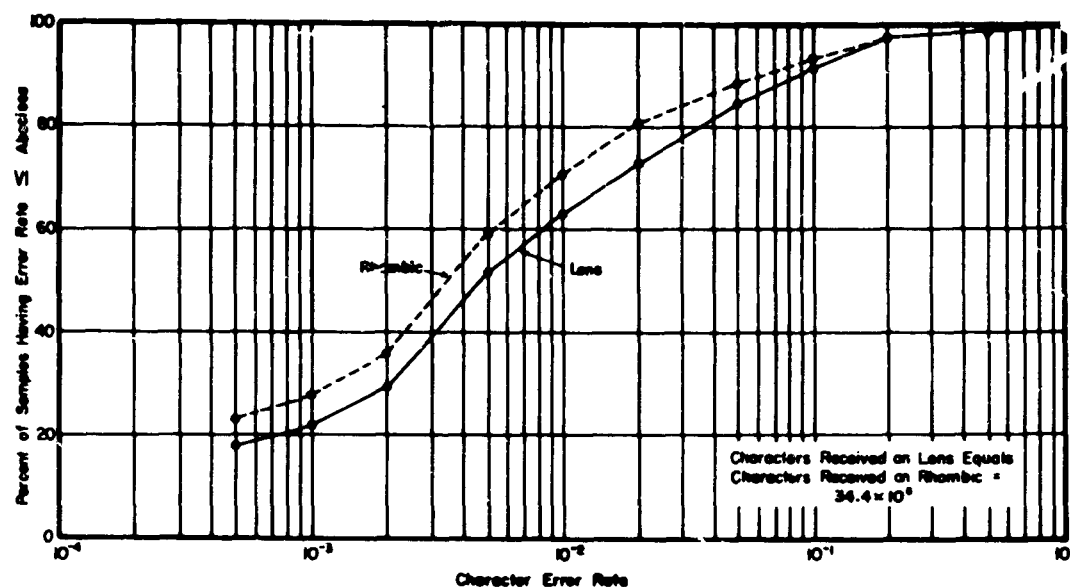
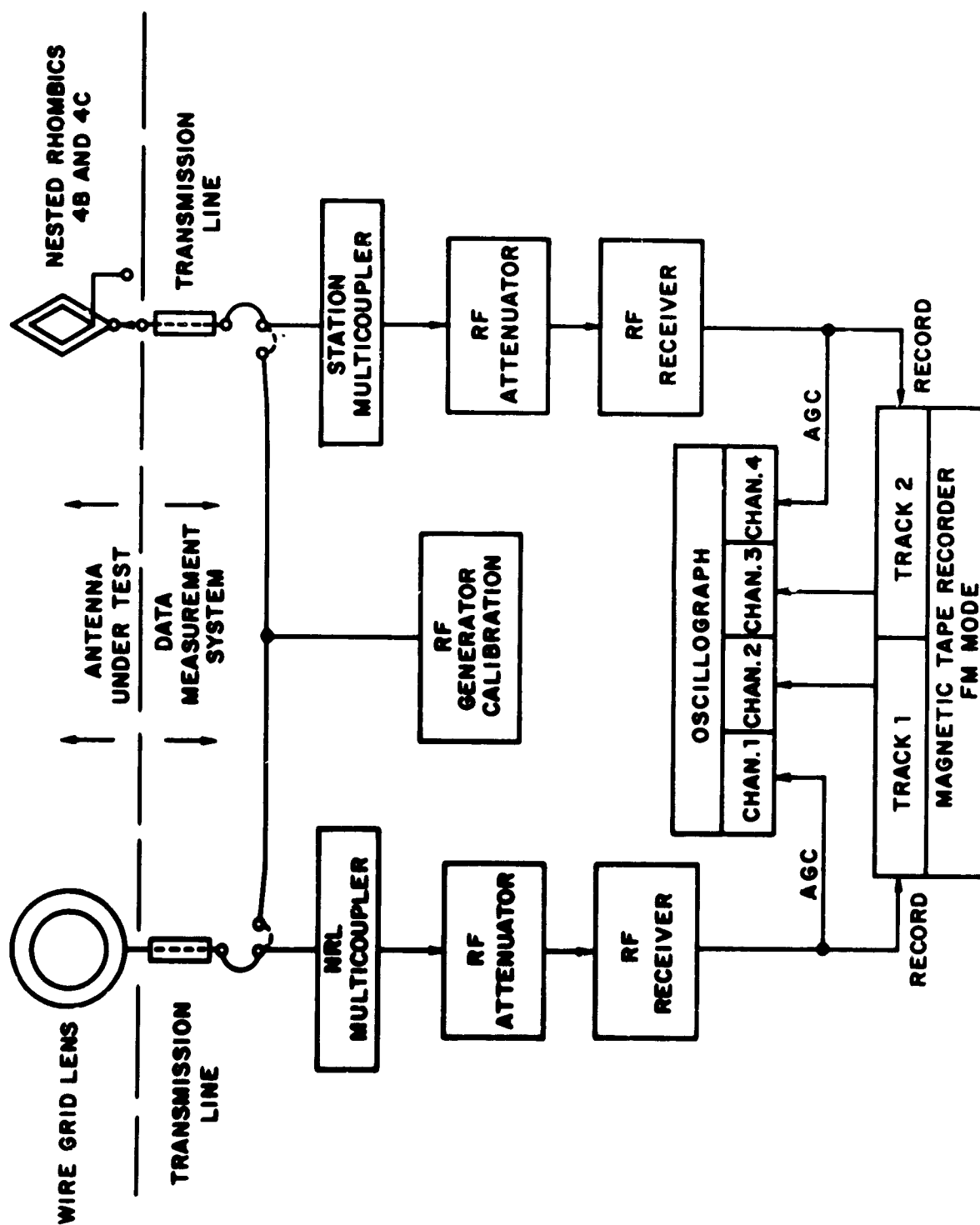


Fig. 8.13 Character Error Rates for Rhombic and Wire-Grid Lens at Molokai When Receiving 600 character-per-minute R Y Test Signals from Washington in the 8-20 Mc Band

to determine signal and noise amplitude and to account for possible changes in recording equipment characteristics, frequent calibrations of the equipment were made with a standard signal generator common to both recording systems at the antenna multicoupler inputs. Finally, transmission line attenuation characteristics were determined by standard measurement techniques. The signal and noise data from the magnetic tapes were sampled 1,000 times per second and reduced to cumulative amplitude probability distributions by a computer developed by NRL for this purpose.

Figure 8.15 presents a summary of the NRL signal-to-noise ratio data at the antenna terminals obtained at five different test frequencies ranging from 8 to 20 Mc. These data were calculated from the measured signal-to-noise ratio data at the receiver terminals using the values of coaxial line attenuation listed in Table 8.4. These graphs are probability distribution showing the percent of time the signal-to-noise ratio (S/N) exceeded a given value. The 8 and 17 Mc curves were developed from data recorded during periods free of man-made interference (QRM) and indicate that in the presence of atmospherics only, the rhombics provided a S/N ratio that averaged about 3 db higher than the lens antenna at these test frequencies. Data used to plot the 10 and 12 Mc curves were influenced by QRM. At 20 Mc, the noise data contained in the curves are thermal noise limited about 95 per cent of the time.



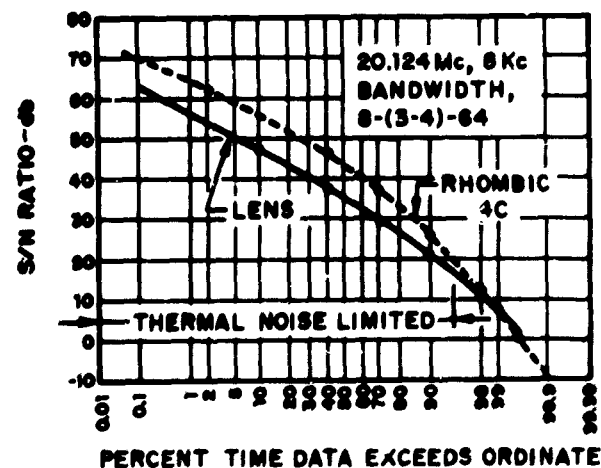
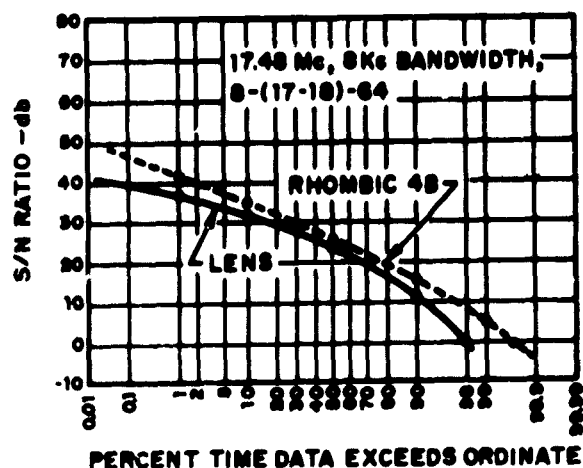
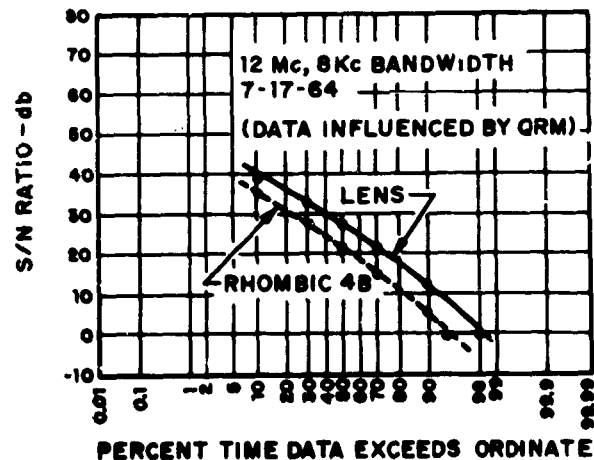
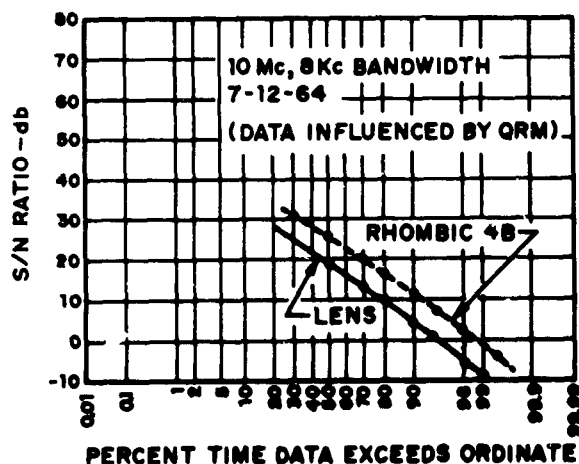
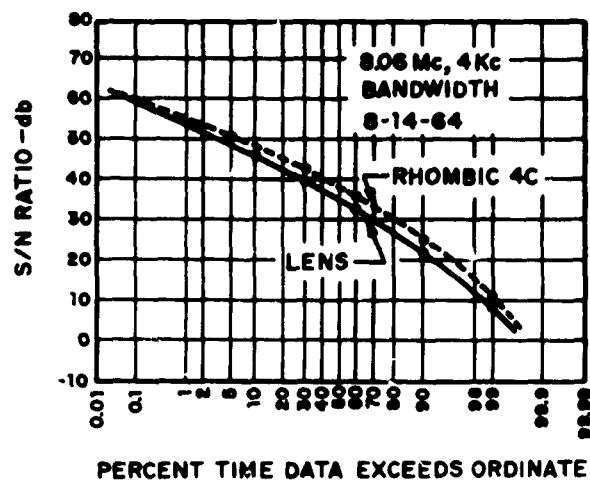


Fig. 8.15 Summary of the NRL Signal-to-Noise Ratio Data at the Antenna Terminals Obtained at Five Different Test Frequencies Ranging from 8 to 20 Mc

8.2.3 NRL Radio Teletype Test Results

A tabular summary of the results of the measurements made by NRL on the Molokai Wire-Grid Lens Antenna and rhombic antennas is given in Table 8.4. This table indicates approximate frequencies used during the test program; noise factors determined from active electronic equipment, passive hardware, and the antennas; percent of time that atmospheric noise was above system noise; typical values of external noise levels for June-August as determined by NBS; as well as the ratio of median error rates of the lens and the rhombics.

The noise factor measured at the input to the antenna multicoupler, supplied by NRL for the Wire-Grid Lens Antenna San Francisco feed, was measured by standard techniques at NRL before and after its use in the Molokai tests. This antenna multicoupler exhibited a noise factor given in Table 8.4 of approximately 5.5 db over the 5 to 25 Mc frequency range for which it was tested. Although the noise factor of the station multicouplers was not measured directly, their noise factor were based on the statistical noise measurements made at Molokai to be about 5.5 db and therefore they are listed in Table 8.4 as having a noise factor of not less than 5.5 db.

Transmission line attenuation is given in Table 8.4 for the specific transmission lines in use. For the lens antenna, the only transmission line loss considered is that associated with the San Francisco feed. The lens line loss varied from 2.5 db at 8 Mc to 4.3 db at 20 Mc. For the rhombic antennas, the transmission line losses are those associated with San Francisco Rhombics 4B (6 to 18 Mc) and 4C (9 to 27 Mc). Open-wire transmission lines are used by the FA with the rhombic antennas. The calculated attenuation for a normal open wire line of a length to feed Rhombics 4B and 4C as shown in Table 8.2 would range from 1.5 db at 8 Mc to 2.5 db at 20 Mc. However, the open wire lines in existence for these antennas at the time tests were conducted in Molokai were found to have higher than normal attenuation. Therefore as mentioned previously, the open-wire lines feeding Rhombics 4B and 4C were replaced with coaxial transmission lines. The attenuation in the coaxial lines feeding Rhombics 4B and 4C was measured to be 5.4 db at 8 Mc to 12.4 db at 20 Mc.

The data measurement system noise factor may be determined by adding transmission line losses in db to the antenna multicoupler input noise factor in db. As shown in Table 8.4, the data measurement system noise factor for the lens antenna varies from 8.0 db at 8 Mc to 9.8 db at

Table 8.4

Summary of NRL Wire-Grid Lens Antenna Evaluation Measurements

Frequency in Mc	Active Equip- ment Noise Factor in db (at antenna multi- coupler input)		Transmission Line Losses in db								Data Mea- sure- ment System Noise Factor in db		Percent Time External Noise was Above Receiv- ing System Noise		Median Signal in Rhombic Relative to Level in Lens in db		Receiving System Noise Factor in db		External Noise in db Above KTB (NBS Quarterly Noise)		Median Error Rate Ratio (Non- diversity)
			Rhombic				Lens														
			Open-wire (calculated) Coaxial				Rhombic														
			4B	4C	4B	4C	Lens														
8	5.5	<5.5	2.5	1.5	-	5.4	7.6	8.0	10.9	45	>45	15.5	26.5	13.9	-	-	2.1				
10	5.5	<5.5	2.8	-	-	6.0	8.3	8.3	11.5	50	>50	14.3	25.6	14.5	31	$\frac{42}{17}$	2.4				
12	5.5	<5.5	3.1	2.0	-	6.6	9.1	8.6	12.1	50	>50	13.7	25.3	15.1	-	-	1.3				
16.5*	5.5	<5.5	3.7	-	2.1	7.8	11.0	9.2	13.3	45	>45	-	22.9	16.3	-	-	1.8				
20	5.5	<5.5	4.3	-	2.5	9.0	12.4	9.8	17.9	5	> 5	-	21.1	20.9	22	$\frac{27}{17}$	1.0				

* All measurement made on 4B (6 - 18 Mc) instead of 4C (19 - 27 Mc)

20 Mc. For the rhombic antennas, the measurement system noise factor varies from 10.9 db to 17.9 db from 8 to 20 Mc, respectively. The data measurement system noise factor is greater for the rhombic when compared to the lens system by 2.9 db at 8 Mc to 8.1 db at 20 Mc.

In addition to the losses in the transmission lines connected to the antennas there are losses in the antennas themselves which further degrade the receiving system noise factors. In the case of the rhombic antenna the ohmic losses in the antenna system and in the termination impedance contribute to the loss factor. For the Wire-Grid Lens Antenna, the ohmic losses in the antenna system and lens feed terminating impedances, and coupling losses between the Wire-Grid Lens and the lens feed contribute to the loss factor. As an approximation toward determining the receiving system noise factor, an rf loss factor of 3 db has been assumed for the rhombic test antennas at each of the test frequencies. This loss is essentially related to the rhombic termination impedance and in the practical case does not vary significantly with frequency. With this assumption the rhombic antenna receiving system noise factor can be said to vary from 13.9 db at 8 Mc to 20.9 db at 20 Mc as shown in Table 8.4. From the cumulative amplitude probability distribution results, the median signal level recorded from the rhombic antenna relative to the median signal level recorded from the Wire-Grid Lens Antenna as given in Table 8.4 (and Fig. 7.2) varies from 15.5 db at 8 Mc to 8.3 db at 20 Mc. The difference between the rhombic median signal level and the lens median signal level is the difference in rf losses between the two test antennas, since the pattern measurements in Appendix B show their directivities to be approximately equal.

Therefore, the approximate lens antenna receiving system noise factor can be determined by summing the assumed rhombic loss, the difference in median signal level between the rhombic and lens antennas, and the data measurement system noise factor. As shown in Table 8.4, the lens receiving system noise factor varies from 26.5 db at 8 Mc to 21.0 db at 20 Mc.

The last column in Table 8.4 shows the ratio of the median error rate for the lens and the station rhombics when receiving transmissions from the Woodbridge transmitter. It is observed that there is a correlation between the median error rates and the system noise factors for the lens and the rhombic receiving systems. At the low-frequency end of the band where the noise factor for the lens receiving system is much higher than that for the rhombic receiving system,

the median error rate for the lens is higher, while at the high-frequency end of the band where the noise factors are comparable the median error rates are essentially equal.

8.3 Noise Levels at Molokai

The atmospheric noise levels at Molokai are quite low as indicated by the NBS reports.¹⁴ The median noise levels in db above KTB (i. e., in db above thermal noise) in regions having the noise grade 2.5 characteristic of Molokai as determined from Reference 11 (a 1955 NBS publication) are 45 db at 5 Mc, 29 db at 10 Mc, 23 db at 20 Mc and 21 db at 30 Mc. A comparison with the NBS noise data in the NBS Quarterly Noise Data from Kekaha, Hawaii, for June, July and August 1963 (1964 is not currently available) shows a median noise level in db above KTB of 31 db at 10 Mc and 22 db at 20 Mc--almost exactly the same as the 1955 predictions. These 1963 median noise levels together with the upper and lower deciles are also shown in Table 8.4.

Reference to Table 8.4 shows that the noise factor of the rhombic receiving system is typically less than the expected median external noise level except at 20 Mc where it is equal to the median external noise level. On the other hand, the higher noise factor of the lens receiving system (due primarily to the relatively low coupling efficiency of the feeds) is only slightly less than the expected median external noise level at all test frequencies. These conclusions are borne out by the NRL noise measurement data listed in Table 8.4 which show that the percentage of time that external noise was above system noise at any frequency was correlated with the receiving system noise factor. Thus, at 20 Mc where the noise factors of the receiving systems were equal, external noise was above system noise on each receiving system for equal lengths of time. At lower frequencies, where the noise factor of the lens receiving system is greater, external noise was above system noise on the lens for a smaller percentage of the time.

8.4 Discussion of FAA and NRL Error-Count Tests

The error rate of FSK messages received at HF carrier frequencies is affected by the signal-to-noise ratio of the received signal, the propagation characteristics of the path between the transmitter and receiver and the directivity of the receiving antenna. When the signal-to-noise ratio at the receiver lies in the range of approximately 0 - 20 db it is found that the error rate is inversely proportional to signal-to-noise ratio. The equivalent noise at the input of HF receivers consists both of internal or thermal noise, which has a time independent average value, and external or atmospheric noise which has a time dependent average value and contains a number of large, high-amplitude spikes

because it is generated by atmospheric. Usually the atmospheric noise predominates at HF frequencies; however, in both the FAA and NRL tests a substantial fraction of the receiving system noise was thermal noise as explained in Sec. 8.2.3. As might be expected, the error rate for a given signal-to-noise ratio depends primarily on the average power of the noise and is essentially independent of its statistical variation with time. However, Bello¹⁵ has shown theoretically that for simplex operation a receiving system limited by thermal noise of a given average power will have a higher error rate than one limited by atmospheric noise of the same average power.

At signal-to-noise ratios greater than 30 to 35 db, the error rate approaches an asymptotically constant value that is essentially independent of signal-to-noise ratio and instead depends primarily on the propagation characteristics of the medium between the transmitter and receiver and the directivity of the receiving antenna. The principal characteristic of the propagation medium which affects the error rate is the fact that signals can simultaneously propagate through it between the transmitter and receiver in multiple modes each having varying attenuation, varying time delay and varying doppler frequency shift. Consequently, the resultant signal arriving at the receiving antenna, which is a summation of the signals arriving by the various propagation paths, exhibits variations in amplitude, time delay and doppler frequency shift, substantially greater than those experienced for the individual modes.

As mentioned previously, the FAA error-count measurements were made for the lens and rhombics using operational traffic which on the average had a high signal-to-noise ratio. Consequently the FAA error-count data in Figs. 8.2 through 8.6 give a measure of the relative directivities of the lens and the station rhombics. Figure 8.6, which is a summary of all the FAA data covering the 5 to 24 Mc band, shows that the measured median binary error rate for the rhombics is 2.5×10^{-4} while that of the lens is 3×10^{-4} .

The NRL error-count data shown in Figs. 8.8 through 8.13 were also recorded under high signal-to-noise ratios but, in addition, data were recorded for a small percentage of the time in the transition region where the signal-to-noise ratio is quite low. As a consequence, the NRL data are a function not only of the propagation path characteristics and the lens and rhombic directivities but also of the signal-to-noise ratios of the two receiving systems as explained in Sec. 8.2.3. At the low-frequency end of the band where the receiving system noise figure for the lens was substantially higher than that of the rhombics, it is seen that the error rate for the rhombic is lower. On the other hand, at the upper end of the band where the receiving system noise figures are about equal, the measured error rates are also essentially equal. Figure 8.13, which is a composite of all the NRL error-count data for the 8 to 20 Mc frequency band, shows that the median character error rate for the rhombics is 3.5×10^{-3} while that of the lens is 4.5×10^{-3} .

9. CONCLUSIONS

The results of the Joint Services Evaluation presented in this report demonstrate that the HF Wire-Grid Lens Antenna, which is circular in shape, functioned as a directive, wide-band seven-beam receiving antenna.

Extensive airborne pattern measurements confirmed the predicted beam-forming properties of the lens over its design band of 3 to 30 Mc with degradation at the band extremities. Comparison of the lens patterns with those of the FAA station rhombics shows that they were comparable between 5 and 25 Mc. The measured patterns are affected by the peculiarities of the terrain at the Molokai site and introduce a measure of uncertainty in the evaluation.

The error-count measurements of the lens receiving system and station rhombic receiving systems are comparable within a factor of 1.3 to 1 favoring the rhombics. The FAA error-count measuring technique when used with operational messages received from San Francisco, California, in the 5 to 24 Mc band resulted in a binary error rate ratio of 1.2 to 1 for the rhombics to lens. The NRL error-count technique when receiving test messages from Woodbridge, Virginia, in the 8 to 20 Mc band resulted in a median character error ratio of 1.3 to 1 for the rhombics to lens. These measurements are also subject to peculiarities of terrain and system installation and must be viewed accordingly.

For the conditions prevailing at the Molokai site and test instrumentation, the signal measurements showed the station rhombic antennas to have a nominal 10-db advantage in power gain over the lens antenna. The signal-to-noise ratio calculations showed the rhombics to have a 2 to 3 db advantage over the lens.

The HF Wire-Grid Lens Antenna as tested can provide satisfactory point-to-point data communications in the 5 to 24 Mc band as determined by error-count comparison with FAA station nested rhombics.

10. **RECOMMENDATIONS**

It is recommended that the HF Wire-Grid Lens Antenna which was retrofitted, as described in Appendix C, with two optimized feeds in the Fall of 1965, be retrofitted with five additional optimized feeds and an appropriate evaluation be performed.

REFERENCES

1. R. L. Tanner, E. M. T. Jones, M. G. Andreasen, E. D. Sharp, "Development and Testing of HF Wire-Grid Lens Antenna," Final Report, Vol. I, Contract ARDS-598, TRG Project W102, TRG-West, Menlo Park, California (March 1964).
2. G. D. Hadorn, "Development of HF Wire-Grid Lens Antenna," Interim Report, Project No. 113-23D, Report No. RD-64-38, Federal Aviation Agency, Systems Research and Development Service, Communications Development Division, Washington, D. C. (May 1964).
3. R. L. Tanner, M. G. Andreasen, E. D. Sharp, J. C. Greene, "An Investigation of the HF Wire-Grid Lens Antenna for Direction Finding," Final Report, Contract AF30(602)-2742, TRG Project W101, TRG-West, Menlo Park, California (April 1963).
4. E. M. T. Jones, J. C. Greene, "The Design, Fabrication and Installation of a Wire-Grid Lens for HF Radio Direction Finding," Report No. 7, Contract AF 30(602)-3110, TRG Project W106, TRG, Incorporated (April 1965).
5. F. B. Harris, Jr., R. L. Tanner, E. M. T. Jones, "Optimized Feeds for the Wire-Grid Lens HF Antenna at the FAA Receiver Station, Molokai, Hawaii," Final Report, Contract ARDS-598, Modification No. 14, Report No. RD-65-128, TRG-West Project W102, prepared by TRG, Incorporated, a subsidiary of Control Data Corporation, Menlo Park, California (Dec 1965).
6. F. B. Harris, Jr., E. D. Sharp, R. L. Tanner, "The Design of Improved Feeds for the HF Wire-Grid Lens Antenna at Rome Air Development Center," Final Report, Contract AF 30(602)-3517, TRG Project W113, TRG, Incorporated, Menlo Park, California (June 1965).
7. M. G. Andreasen, E. D. Sharp, "Electromagnetic Theory of Wire-Grid Lens Antenna," Report No. 4, Contract DA 36-039 AMC-02248(E), TRG Project W107, TRG-West, Menlo Park, California (August 1964).
8. M. G. Andreasen, F. B. Harris, Jr., E. D. Sharp, "Mathematical Model for Luneburg Lens," Report No. 3, DOD Contract, TRG Project W114, TRG, Incorporated, Menlo Park, California (June 1965).

REFERENCES (continued)

9. E. D. Sharp, "Mathematical Analysis of Luneburg Lens," Report No. 1, DOD Contract, TRG Project W117, TRG, Incorporated, Menlo Park, California (September 1965).
10. S. Silver, Microwave Antenna Theory and Design, M. I. T. Rad. Lab. Series, Vol. 12, p. 199 (McGraw Hill Book Company, Inc., New York 1949).
11. H. T. Friis, C. B. Feldman, "Multiple Unit Steerable Antenna," Proc. IRE, pp. 841-917, (July 25, 1937)
12. J. F. Cline, "A New Approach to the Evaluation of HF Aircraft Antennas," Stanford Research Institute, Tech. Report 72, Project 2494, Contract AF 19(604)3458 (March 1961).
13. J. F. Cline, R. L. Tanner, "A New Approach to the Evaluation of HF Aircraft Antennas," IRE Trans. AP Vol AP-10 No. 3 pp. 254-264, (May 1962).
14. W. Q. Crichlow, D. F. Smith, R. N. Morton, W. R. Corliss, "Worldwide Radio Noise Levels Expected in the Frequency Band 10 Kilocycles to 100 Megacycles," National Bureau of Standards Circular 557, Washington. D. C. (August 1955).
15. P. A. Bello, "Error Probabilities Due to Atmospheric Noise and Flat Fading in HF Digital Communications Systems," Conference Record, First IEEE Communications Convention, Boulder, Colorado (June 7-9, 1965).

APPENDIX A

An Analysis of the Error Counting System Developed by the FAA for Testing the Moikoi Wire-Grid Lens Antenna

The error counting system devised by K. H. Quin of the FAA Pacific Region and described in Section 3 is intended to compare the errors received on the test channel of the Wire-Grid Lens operating in simplex with the error count received on a rhombic antenna operating in simplex on the same circuit. One standard of comparison used for both test antennas is a dual diversity rhombic antenna system. Because the test rhombic is one element of the diversity pair, this test method gives rise to a certain bias in favor of the rhombic. The reason for this bias is that the test rhombic, being also a part of the diversity comparison "standard," is at times being compared with itself and will register no errors even though errors actually occur. The other standard of comparison used for both test antennas is a dual diversity system composed of one rhombic and the lens. This system gives rise to a bias in favor of the lens, since the lens being part of the diversity standard is at times being compared with itself.

The purpose of this Appendix is to analyze these systems quantitatively by means of probability theory to ascertain the amount of bias thus introduced in each case.

Figure A-1a shows a simplified block diagram of the system arrangement using a dual diversity rhombic antenna system when the "errors" transmitted by the lens, designated as Antenna C, are being counted. Figure A-1b shows the arrangement when "errors" are being counted for the test rhombic, which is designated as Antenna B. An "error," as registered by the system, is a failure of coincidence on a binary bit basis, of the demodulated signals obtained from the diversity system and from the particular simplex system being tested. The signal from the diversity system is always assumed to be correct, even though the diversity output may, in fact, be wrong and the simplex output actually correct. Such a situation will occur a finite--though small--percentage of the time.

Figure A-2 shows the system when the lens and a rhombic are used for the diversity standard. As in the previous case, Antennas A and B are the diversity standard, while Antenna C is the isolated test antenna. Figure A-2a shows the system arrangement when the "errors" transmitted by the test rhombic (Antenna C) are being counted while Fig. A-2b shows the system arrangement when the "errors" transmitted by the lens (Antenna B) are being counted.

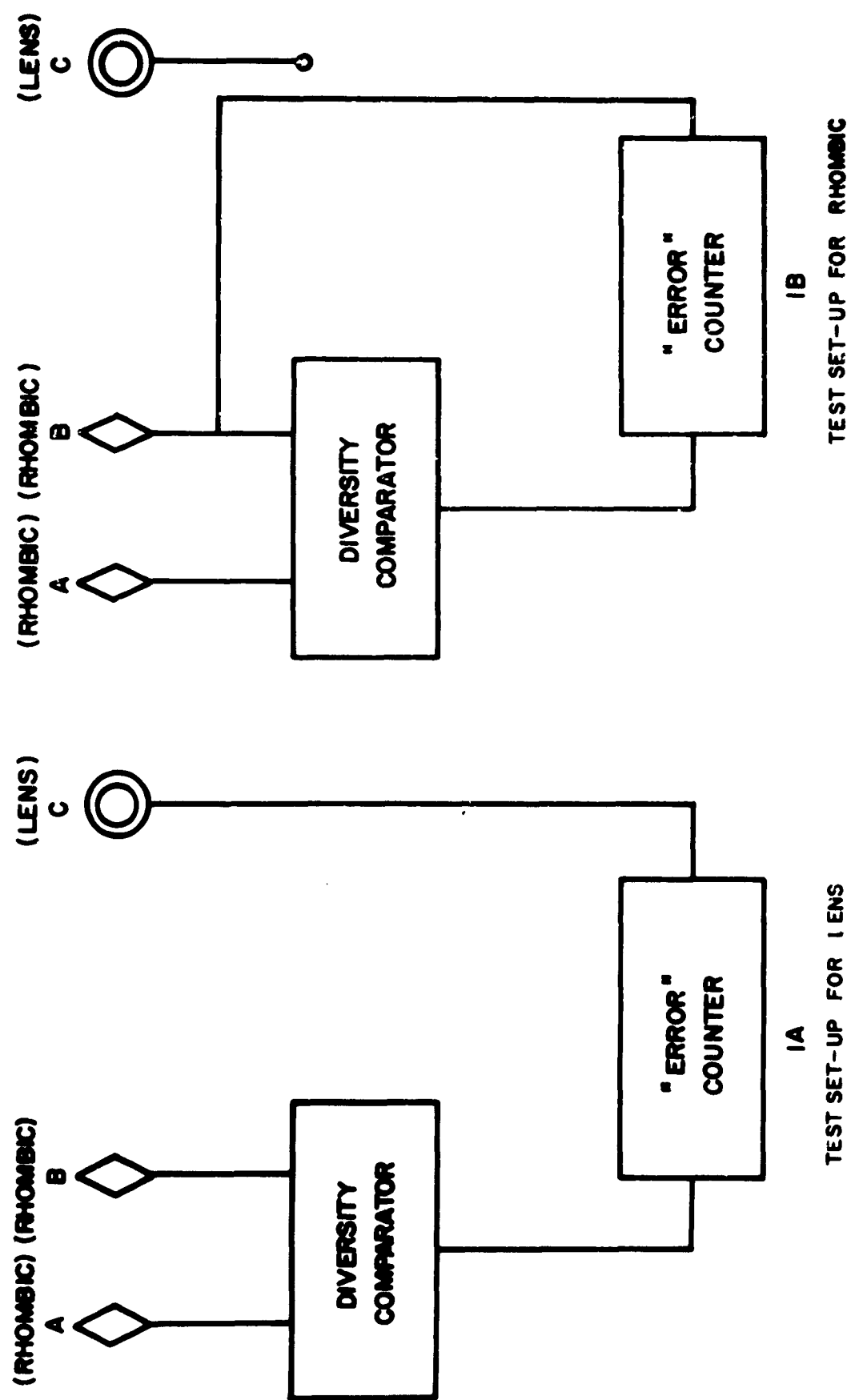


Fig. A.1 Test Set-up to Measure "Binary Errors" on the Lens and a Rhombic II and a Pair of Rhombics at the Diversity Standard

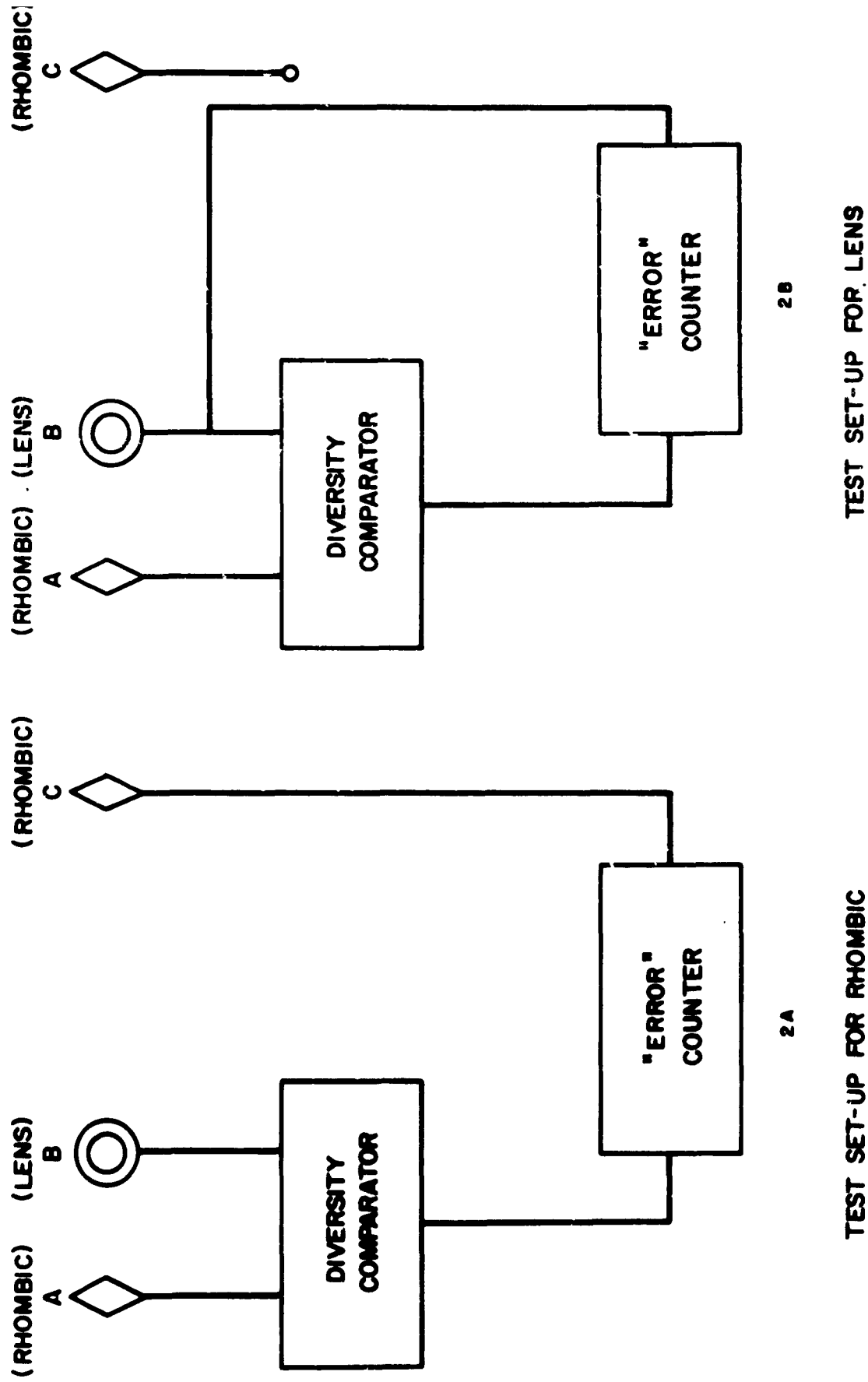


Fig. A.2 Test Set-up to Measure "Binary Errors" on the Lens and a Rhombic Using the Lens and a Rhombic as the Diversity Standard

The diversity comparator (Tele-Signal Corporation Model 1 is a decision making device which selects whichever one of the diver elements is receiving the stronger signal. To analyze the operation this system it is therefore possible to define the following quantities:

Define:

- a_1 = probability that error occurs in A while A controls
- a_2 = probability that error occurs in A while B controls
- b_1 = probability that error occurs in B while B controls
- b_2 = probability that error occurs in B while A controls
- c = probability that error occurs in C
- α = probability that A controls system
- β = probability that B controls system
- e_b = probability of "error" being registered for Antenna
- e_c = probability of "error" being registered for Antenna

In the foregoing, error (without quotation marks) means a error; "error" (with quotation marks) means an indicated error. As pointed out previously, "errors" will be indicated in a small percent of instances due to an error in the comparison "standard" (the diver system) rather than the antenna under test. e_c , as defined, will con therefore, of a sum of two terms. The first term (call e_{c1}) will be to an error in Antenna C when the diversity system is correct. The second term (call e_{c2}) arises as the result of errors in the diversity system while the Antenna C is actually correct.

In terms of the quantities previously defined, e_{c1} can be st mathematically as

$$e_{c1} = [(1-a_1) \alpha + (1-b_1) \beta] \cdot c . \quad (A-$$

As will be evident upon consideration, the term in square brackets i the probability that no error is transmitted by the diversity system.

Similarly, e_{c2} can be stated mathematically as

$$e_{c2} = (1-c) [a_1 \alpha + b_1 \beta] . \quad (A-$$

The term in parentheses is the probability that no error occurs in Antenna C while the term in brackets is the probability that an error does occur in the diversity system. Thus, the total probability that an "error" will be registered for Antenna C is

$$e_c = e_{c1} + e_{c2} = [(1-a_1) \alpha + (1-b_1) \beta] \cdot c + (1-c) [a_1 \alpha + b_1 \beta] . \quad (A-3)$$

Part of the second term can be absorbed in the first, simplifying the expression slightly,

$$e_c = [(1-2a_1) \alpha + (1-2b_1) \beta] \cdot c + [a_1 \alpha + b_1 \beta] . \quad (A-4)$$

For "errors" registered by Antenna B, similar arguments can be applied. Thus,

$$e_b = e_{b1} + e_{b2} , \quad \text{where} \quad (A-5)$$

as with Antenna C e_{b1} is a term giving the probability of "errors" being registered for Antenna B due to actual errors in Antenna B and correct signal in the comparison "standard" while e_{b2} is the probability of "errors" being registered when Antenna B is correct while the "standard" is in error. In terms of the probabilities previously defined,

$$e_{b1} = (1-a_1) \alpha \cdot b_2 \quad (A-6)$$

$$e_{b2} = a_1 \alpha \cdot (1-b_2) .$$

It will be observed that the preceding expressions contain no terms with the factor β . It will be recalled that this factor is a measure of the proportion of time that Antenna B controls the system and that, by definition, no error will be registered during that time since Antenna B is being compared with itself. Thus,

$$\begin{aligned} e_b &= (1-a_1) \alpha b_2 + a_1 \alpha (1-b_2) \\ &= \alpha [(a_1 + b_2) - 2a_1 b_2] . \end{aligned} \quad (A-7)$$

The expressions for e_c and e_b are too complicated to learn much from in their present form; however, they can be simplified by making certain assumptions about the diversity system. In the tests the diversity combiner was always adjusted so that Antennas A and B each controlled the system half the time. Therefore,

$$\alpha = \beta = 1/2. \quad (A-8)$$

To permit analysis of situations where Antennas A and B are different as in the setup in Fig. A-2, the ratio of b_1 to a_1 can be formed yielding

$$\frac{b_1}{a_1} = m. \quad (A-9)$$

Then,

$$e_c = \left[1 - b_1 \left(1 + \frac{1}{m} \right) \right] \cdot c + \frac{b_1}{2} \left(1 + \frac{1}{m} \right) \quad (A-10)$$

$$e_b = 1/2 \left[\frac{b_1}{m} + b_2 - 2 \frac{b_1 b_2}{m} \right]$$

Now recognize that b (the total error probability for Antenna B) is given by

$$b = \beta b_1 + \alpha b_2 = 1/2 (b_1 + b_2). \quad (A-11)$$

The ratio of error probability when Antenna B does not control the diversity system to the error probability when it does is

$$\frac{b_2}{b_1}$$

which is defined to be

$$n = \frac{b_2}{b_1}. \quad (A-12)$$

Then, by manipulation,

$$b_1 = \frac{2b}{1+n} \quad (A-13)$$

$$b_2 = \frac{2nb}{1+n}$$

Substituting Eq. (A-13) in Eq. (A-10),

$$e_c = \left[1 - \frac{2b}{1+n} \left(1 + \frac{1}{m} \right) \right] \cdot c + \frac{b}{1+n} \left(1 + \frac{1}{m} \right) \quad (A-14)$$

$$e_b = \frac{b}{m(1+n)} + \frac{nb}{1+n} - \frac{4nb^2}{(1+n)^2} .$$

The probabilities b and c are on the order of 10^{-3} or less so that no significant error is made in neglecting terms b^2 and bc . When these terms are neglected it is found that

$$\begin{aligned} e_c &= c + \frac{b}{(1+n)} \left(1 + \frac{1}{m}\right) \\ e_b &= b \left[\frac{1+mn}{1+n} \right] \end{aligned} \quad (A-15)$$

First, it is instructive to consider the case when two rhombics are used as a diversity standard as in Fig. A-1. Then it is reasonable to let $a_1 = b_1$ so that $m = 1$. In this case, Eq. (A-15) becomes

$$\begin{aligned} e_c(L) &= c(L) + \frac{2b(R)}{1+n} && \text{(Lens)} \\ e_b(R) &= b(R) && \text{(Rhombic),} \end{aligned} \quad (A-16)$$

where parentheses enclosing either L or R have been used to indicate which probabilities refer to the lens, (L) , and rhombic, (R) . Thus, in this instance, the measured probability of error $e_b(R)$ for the rhombic (Antenna B) is the same as its true probability of error $b(R)$, for the rhombic. On the other hand, the measured probability of error $e_c(L)$ for the lens (Antenna C) is greater than the true probability of error $c(L)$, for the lens by the term $2b(R)/(1+n)$.

Next, the setup in Fig. A-2 will be considered when the lens and a rhombic are used as the diversity pair. Here it is reasonable to assume that the ratio, m , (the probability $b_1(L)$ that an error occurs in Antenna B (lens), when B controls the system, to the probability $a_1(R)$ that an error occurs in Antenna A (rhombic), when A controls the system), is equal to

$$\frac{b(L)}{c(R)} ,$$

(the ratio of the probability $b(L)$ of an error being received on the lens to the probability $c(R)$ of an error being received on the rhombic). Thus, we have approximately,

$$\frac{b(L)}{c(R)} \approx \frac{b_1(L)}{a_1(R)} = m . \quad (A-17)$$

Substituting Eq. (A-17) into Eq. (A-15) yields,

$$\begin{aligned} e_c(R) &= c(R) + \frac{b(L)}{(1+n)} \left(1 + \frac{1}{m} \right) = c(R) \left[1 + \frac{1+m}{1+n} \right] \quad (\text{Rhombic}) \\ e_b(L) &= b(L) \left[\frac{1+mn}{1+n} \right] \quad (\text{Lens}), \end{aligned} \quad (\text{A-18})$$

where the tacit assumption is made that

$$n = \frac{b_2}{b_1}$$

is the same in the setups shown in Figs. A-1 and A-2. Inspection of Eq. (A-18) shows that the measured probability of error on both the lens, $e_b(L)$, and the rhombic, $e_c(R)$, is greater than the true error probabilities $b(L)$ and $c(R)$ for the lens and rhombic respectively. Furthermore, in contradistinction to the results obtained using the measuring setup in Fig. A-1, the measuring setup in Fig. A-2 introduces a bias in favor of the lens since

$$\frac{e_c(R)}{c(R)} > \frac{e_b(L)}{b(L)}$$

To compensate for the opposite biases obtained in the two measuring setups, binary error data were recorded for both of them. To see how this works quantitatively, let the total number of binary bits received on the setup in Fig. A-1 be $2N_1$, and the total number of binary bits received on the setup in Fig. A-2 be $2N_2$. Then using Eqs. (A-16) and (A-18), the total number of errors $E(L)$ recorded for the lens is

$$E(L) = N_1 \left[c(L) + \frac{2b(R)}{1+n} \right] + N_2 \cdot b(L) \cdot \left(\frac{1+mn}{1+n} \right), \quad (\text{A-19})$$

while the total number of errors $E(R)$ recorded for the rhombic is

$$E(R) = N_1 b(R) + N_2 \cdot c(R) \left[1 + \frac{1+m}{1+n} \right]. \quad (\text{A-20})$$

Now define $p(L)$ as the true probability of an error being received on the lens and $p(R)$ as the true probability of an error being received on the rhombic. Then,

$$\begin{aligned} p(L) &= c(L) = b(L) \\ \text{and} \quad p(R) &= c(R) = b(R). \end{aligned} \quad (\text{A-21})$$

Using Eq. (A-21), and remembering from Eq. (A-17) that $p(L)/p(R) = m$, Eqs. (A-19) and (A-20) become respectively,

$$E(L) = p(L) \left[N_1 \left(1 + \frac{2}{(1+n)m} \right) + N_2 \cdot \frac{(1+mn)}{(1+n)} \right] \quad (A-22)$$

$$E(R) = p(R) \left[N_1 + N_2 \left(1 + \frac{1+m}{1+n} \right) \right]$$

It is instructive to make some reasonable assumptions about the values of the quantities in Eq. (A-22) to get a feeling for the measured errors, $E(L)$ and $E(R)$. First, it will be assumed that the lens and the rhombic have the same error rate so that $p(L)/p(R) = m = 1$. Then,

$$\begin{aligned} E(L) &= p(R) \left[N_1 \left(1 + \frac{2}{1+n} \right) + N_2 \right] \\ E(R) &= p(R) \left[N_1 + N_2 \left(1 + \frac{2}{1+n} \right) \right] \end{aligned} \quad (A-23)$$

which shows that the measured errors for the two antennas will be the same if the number of samples taken on the two setups are the same (i. e. $N_1 = N_2 = \frac{N}{2}$). Furthermore, if the diversity system were perfect and received no errors so that $n \rightarrow \infty$, the measured errors would be identical with the actual received errors, $(p(R) N)$. If n is a reasonably large number (i. e. 5-10), it is seen that the measured errors are only slightly greater (17 percent to 9 percent) than the actual received errors. In the more general case, where $N_1 \neq N_2$, the value of m can be determined from Eq. (A-22) in terms of the measured ratio "R" defined as,

$$"R" = \frac{E(L)}{E(R)} \quad (A-24)$$

for various values of n .

Forming the ratio of the Eq. (A-22) and rearranging, it is found that

$$m^2 + m \left[\frac{\frac{N_1}{N_2} + 1 - "R"}{n} + \frac{N_1}{N_2} \right] + \frac{\frac{N_1}{N_2} (2 - "R") - 2 "R"}{n} - "R" \left(1 + \frac{N_1}{N_2} \right) = 0. \quad (A-25)$$

The value of m which satisfies Eq. (A-25) is

$$m = -\frac{1}{2} \left[\frac{\frac{N_1}{N_2} + 1 - "R"}{n} + \frac{N_1}{N_2} \right]$$

$$+ \sqrt{\frac{1}{4} \left[\frac{\frac{N_1}{N_2} + 1 - "R"}{n} + \frac{N_1}{N_2} \right]^2 + "R" \left(1 + \frac{N_1}{N_2} \right) \left(\frac{\frac{N_1}{N_2} (2 - "R") - 2 "R"}{n} \right)}$$

APPENDIX B

Measured Radiation Patterns

B. 1 General

This Appendix presents all of the pattern data recorded during the Joint Services Evaluation. A majority of the pattern information is presented in the form of the previously described contour plots, because they contain a great deal of information in a compact form. This form of presentation is not widely understood and therefore a considerable number of patterns are plotted in the more familiar polar form. The patterns have been divided by frequency into two main groups. Thus, all the in-band patterns obtained for each of the test antennas in the 3 to 30 Mc design band of the Wire-Grid Lens Antenna appear in one group, while all the out-of-band patterns obtained for each of the test antennas outside the 3 to 30 Mc design band appear in another group. The patterns comprising the in-band group are divided into four subgroups. The first subgroup contains all the principal polarization contour plots of each of the antennas. The second subgroup contains all cross-polarized contour plots of each of the antennas. The third subgroup contains all of the principal polarization polar patterns, while the fourth contains all of the cross-polarized polar patterns.

The same division into subgroups is maintained for the out-of-band patterns except that there are only two subgroups since fewer out-of-band patterns were recorded. The first subgroup contains all the principal polarization contour plots of each antenna, while the second subgroup contains all the principal polarization polar plots of each antenna.

In the case of the directive antennas, the azimuth coordinates have been oriented so that zero degrees corresponds to the nominal pointing direction of the antenna. Thus, deviations of the symmetry axis of the antenna patterns from zero degrees are a measure of the asymmetries of the antenna or of site perturbations. The double-dipole antenna was always oriented to point toward Anchorage. In the case of the omniazimuthal antennas, zero degrees corresponds to true North.

All the descriptive material about the various patterns appears in the following sections before the patterns are presented. This format has been adopted so that the descriptive material will not become "lost" amongst the patterns.

B. 2 In-Band Patterns (All patterns recorded in the 3 to 30 Mc frequency band)

B. 2.1 Principal Polarization Contour Plots of In-Band Patterns

The majority of the recorded contour patterns are principal polarization patterns covering the 3 to 30 Mc design band of the Wire-Grid Lens Antenna. In each of these contour plots, the highest amplitude recorded is 0 db. Its position is not shown explicitly, however, it can be inferred from the other contours. Falling within this category are the vertically polarized (E_{θ}) contour patterns of: the Anchorage feed, the Sydney feed, the Nandi-Canton feed, the San Francisco feed, the Wire-Grid Lens Antenna excited at its center as an omniazimuthal biconical antenna, the NRL monopole and the double-dipole reference antenna oriented to receive vertically polarized signals. Also falling within this category are the horizontally polarized (E_{ϕ}) contour patterns of: the San Francisco rhombics 4A, 4B, and 4C, as well as the double-dipole reference antenna oriented to receive horizontally polarized signals.

Inspection of the principally polarized lens contour patterns reveals that each of the lens feeds produced quite similar far field patterns. At the high frequency end of the band, where the dimensions of the lens are large in terms of wavelength, the patterns are narrowest and the minor lobe level is quite low. As frequency decreases the width of the main beam increases somewhat and the minor lobe level rises, although it is still acceptably low for use as a communications receiving antenna. The measured beamwidths and minor lobe patterns are presented in Sec. 6. A summary comparison of the calculated and measured lens performance is also shown in Figs. 6.20 through 6.22.

An indication of the severity of the site effects described in Sec. 4 which affect the lens patterns can be obtained from an inspection of the patterns of the reference antennas: the NRL monopole, the Gain Standard Double Dipole and the lens excited as an omniazimuthal biconical antenna. The NRL monopole was mounted in a relatively isolated location near the crest of a hill as can be seen by reference to Fig. 4.1. Its patterns shown in Figs. B.45 to B.51 should theoretically be independent of azimuth. At frequencies of 9.1, 15.3, 25.3 and 30.0 Mc, the patterns generally conform to this ideal, while at frequencies of 4.1, 5.6 and 21.5 Mc, they deviate from it.

The patterns of the double-dipole antenna should vary approximately as the cosine squared of the azimuth angle when it is oriented to receive vertically polarized E_θ signals and as the cosine of the azimuth angle when it is oriented to receive horizontally polarized E_ϕ signals. The measured E_θ patterns are shown in Figs. B.62 to B.68, while the measured E_ϕ patterns are shown in Figs. B.69 to B.74. A comparison between the E_θ and E_ϕ patterns reveals that E_ϕ patterns conform quite closely to the ideal at all frequencies, while the E_θ patterns conform most closely at frequencies of 21.5, 25.3 and 30.0 Mc. The E_θ pattern distortions observed at the lower frequencies (which in several cases were unfortunately measured over a limited range of elevation angles) were probably caused by the presence of the nearby vertically polarized Wire-Grid Lens Antenna.

The patterns of the lens excited as a Biconical Antenna, which are shown in Figs. B.37 to B.44, should ideally be independent of azimuth angle. Inspection of the patterns shows that, in general, they are not independent of azimuth although the pattern at 15.3 Mc appears to conform reasonably closely with theoretical expectations. Most of these pattern perturbations observed are due to the previously mentioned site effects.

The horizontally polarized patterns of the rhombic antennas are comparable to the vertically polarized patterns of the lens over the 5 to 25 Mc band. However, it is to be observed that three rhombics, 4A, 4B, and 4C, are required to cover the 3 to 30 Mc frequency band covered by the lens. One particularly significant difference between the lens and rhombic patterns is the fact that the main beam of the lens is in general considerably broader in elevation making it receptive to a much greater range of arrival angles for incident sky-waves (see Figs. 6.22 and 6.23). This characteristic, however, is generally not a design requirement for antennas used primarily for HF point-to-point communications. The high back lobe of Rhombic 4A at 5.6 Mc could result from several causes, i. e., site effects, unbalanced two-wire transmission lines, etc.

These rhombic patterns were recorded using the operational FAA two-wire transmission lines to connect the rhombics to the receiver. Subsequent measurements indicated that these two-wire lines had higher attenuation than is customarily experienced because of faulty support insulators. Therefore, the two-wire transmission lines of Rhombics 4B and 4C were replaced with 3/4 inch coaxial line and suitable baluns for the error-count measurements described in Sec. 8.

B.2.2 Cross Polarization Contour Plots of In-Band Patterns

A number of cross polarized contour plots were recorded for the Anchorage and San Francisco feeds of the lens in order to evaluate the significance of the cross polarization. In each of these plots the highest signal recorded is 0 db, although its position is not recorded and must be inferred from the contours. Usually the cross polarized pattern has two peaks, one on either side of the main beam at angular positions separated approximately by the 3-db width of the principally polarized main beam. However, in a number of instances site effects perturb the patterns so this pattern shape is not observed. The highest level of cross polarization measured with respect to the highest level of principal polarization is also shown in each plot. These levels were obtained as the ratio of the maximum signals received on the lens when the Xeledop transmitter was radiating vertically polarized and horizontally polarized signals which are believed to be nearly equal. The fact that cross polarized levels are different, particularly at the high frequency end of the band, is another manifestation of the sensitivity of the cross polarized patterns, to site effects. Since data on cross-polarization measurements were not reduced for the station rhombics, comparative data of the lens versus rhombics for cross-polarization has not been presented.

B.2.3 Principal Polarization In-Band Polar Plots

A number of principal polarization polar plots of the various antenna patterns have been prepared from the computer generated contour plots. These patterns were also generated and plotted by the computer. The computer plot program used draws straight lines between the measured points obtained from the contour plots, thus causing the patterns to have an angular shape rather than the true rounded shape.

In order to facilitate viewing, all the principal polarization patterns at any one frequency (obtained from a single contour plot) are shown on a single page. In general, six patterns appear on each page. The pattern in the upper left is the conical azimuth cut through the peak of the main beam, while the pattern at the upper right is the elevation pattern taken through the peak of the main beam. The middle row of two patterns consists of conical azimuth cuts taken at elevation angles corresponding to the upper and lower elevation 3-db points of the main beam. The bottom row of two patterns consists of conical cuts taken at elevation angles of 5 and 40 degrees. In several cases, there are some deviations from this format. These deviations usually occur either (1) because the patterns at elevation angles of 5 and 40 degrees are coincident with those through the peak of the main beam or the upper and lower 3-db point patterns, or (2) because data were not measured over a sufficient range of elevation angles to generate all six patterns.

The vertically polarized patterns of the Anchorage feed, the Sydney feed and the San Francisco feed are quite similar. The small deviations between them are caused by the previously mentioned site effects. The horizontally polarized patterns of Rhombics 4A, 4B and 4C which together cover the 3 to 30 Mc band for the regular FAA San Francisco circuit are also similar to one another and to the vertically polarized patterns of the lens.

B. 2. 4 Horizontal Polarization In-Band Polar Patterns for the Lens

Horizontal polarization in-band polar plots were prepared for both the Anchorage and San Francisco lens feeds. The maximum of the horizontally polarized radiation typically occurs in two peaks symmetrically located with respect to the main beam as can be observed in several instances. Detailed correlation between the horizontally polarized radiation patterns of the two feeds is not as good as in the case of the vertically polarized patterns because of the previously mentioned increased sensitivity of these patterns to site effects.

B. 3 Out-of-Band Patterns (All patterns recorded at frequencies outside the 3 to 30 Mc design band)

A number of patterns were recorded for the lens at out-of-band frequencies in order to obtain a measure of its maximum bandwidth. It is well known from theoretical considerations that the low-frequency limit of operation of the lens occurs (1) when its diameter measured in terms of wavelength becomes so small that significant lens focusing action cannot occur, and (2) when the horn height, also measured in terms of wavelength, becomes so small that it is no longer well matched to space. The high-frequency limit occurs when the size (in this case five feet) of the square mesh comprising the lens becomes greater than about $1/6$ wavelength. Thus, theoretically, the lowest frequency of operation of the Wire-Grid Lens Antenna can be extended by increasing its size, while its high-frequency limit can be extended by decreasing the mesh size in the lens. This latter effect has been demonstrated on the one-half scale lens built for RADC which has a two and one-half foot square mesh and operates up to a frequency of at least 50 Mc.

B. 3. 1 Principal Polarization Out-of-Band Contour Plots

Principal polarization out-of-band contour plots were measured for the Wire-Grid Lens Antenna on the Anchorage feed, the Nandi-Canton feed, the Sydney feed and the San Francisco feed at frequencies of 2.25 and 2.6 Mc. Inspection of these patterns shows that at 2.25 Mc and 2.6 Mc, no beam-forming action occurs. Hence, it may be concluded that

significant beam-forming action cannot be obtained for a Wire-Grid Lens Antenna having the dimensions of the one at Molokai at frequencies below 3 Mc.

Contour plots were also recorded at 2.6 Mc for the lens excited as an omniazimuthal biconical antenna as well as for the NRL monopole. Both these antennas are seen to have omniazimuthal patterns distorted quite significantly by the site perturbations, as were the in-band patterns described in Sec. B.2.1.

One principal polarization contour plot was recorded at 35 Mc for the San Francisco feed of the Wire-Grid Lens Antenna. Inspection of this plot indicates that a good pattern was obtained having a well formed main beam and low minor lobes. Since the mesh size of the lens at 35 Mc is 0.18 wavelength, it may be concluded that satisfactory operation of the Wire-Grid Lens Antenna can be obtained at frequencies where the mesh size is at least this large in terms of wavelength.

B.3.2 Principal Polarization Out-of-Band Polar Plots

In addition to the previously described low-frequency contour plot measurements at 2.25 and 2.6 Mc, polar plot measurements were also made at 2.0 Mc on the Anchorage feed, Nandi-Canton feed and Sydney feed. Inspection of these patterns reveals, as expected, that no beam-forming action occurs at 2 Mc.



Fig. B.1 Anchorage Feed at 3.0 Mc, E_0

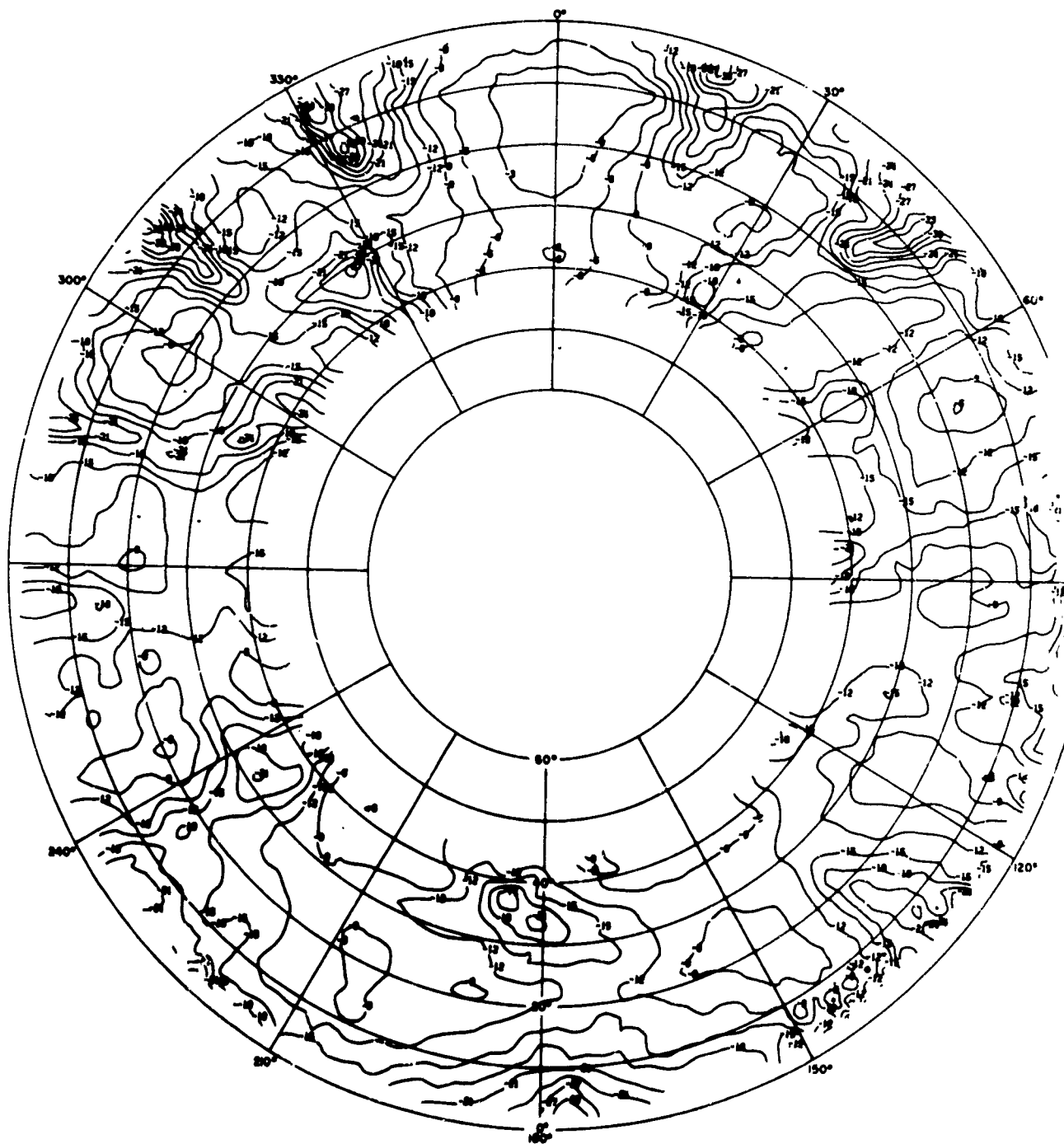


Fig. B.2 Anchorage Feed at 4.1 Mc, E_0

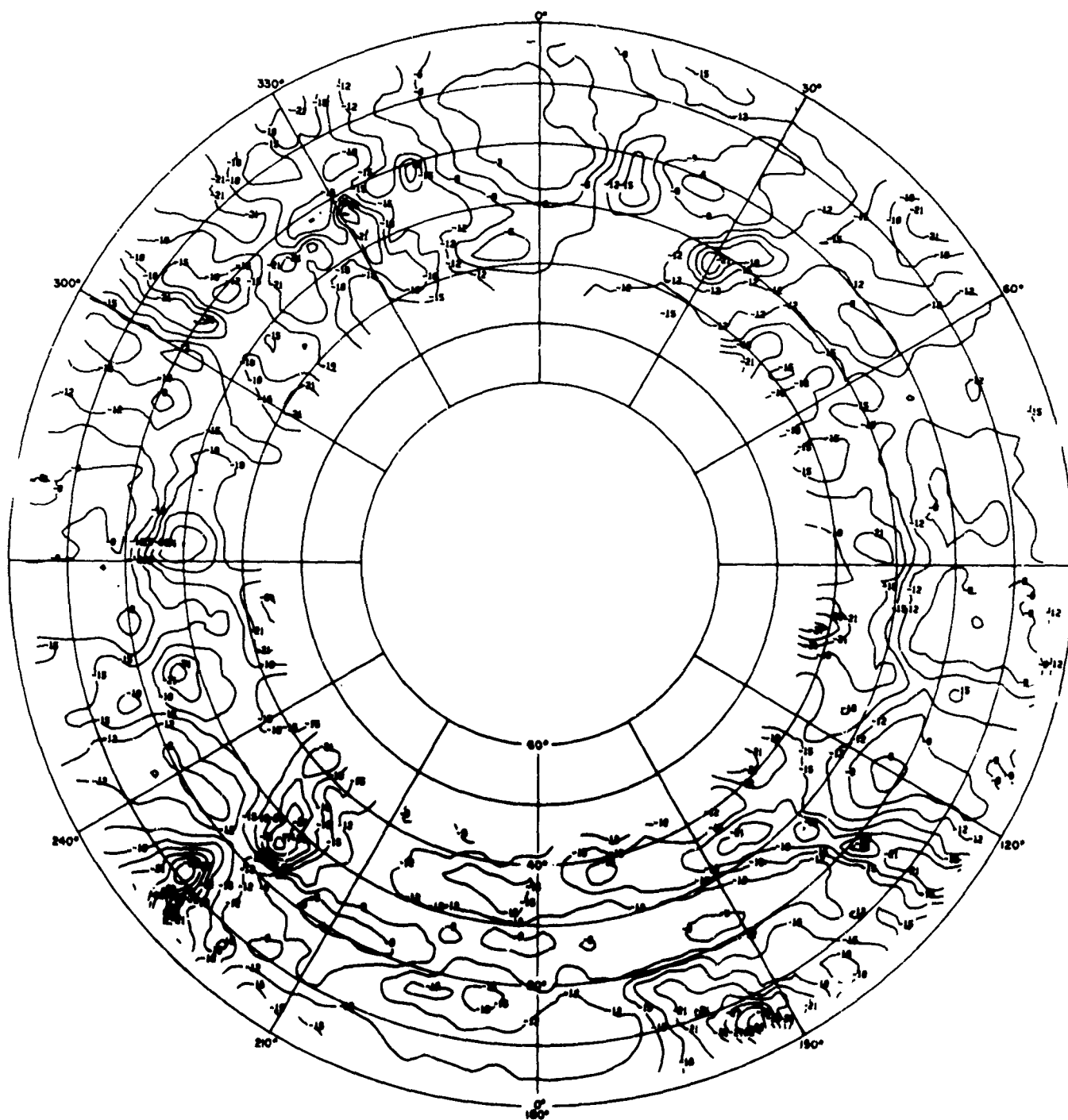


Fig. B.3 Anchorage Feed at 5.6 Mc, E_0

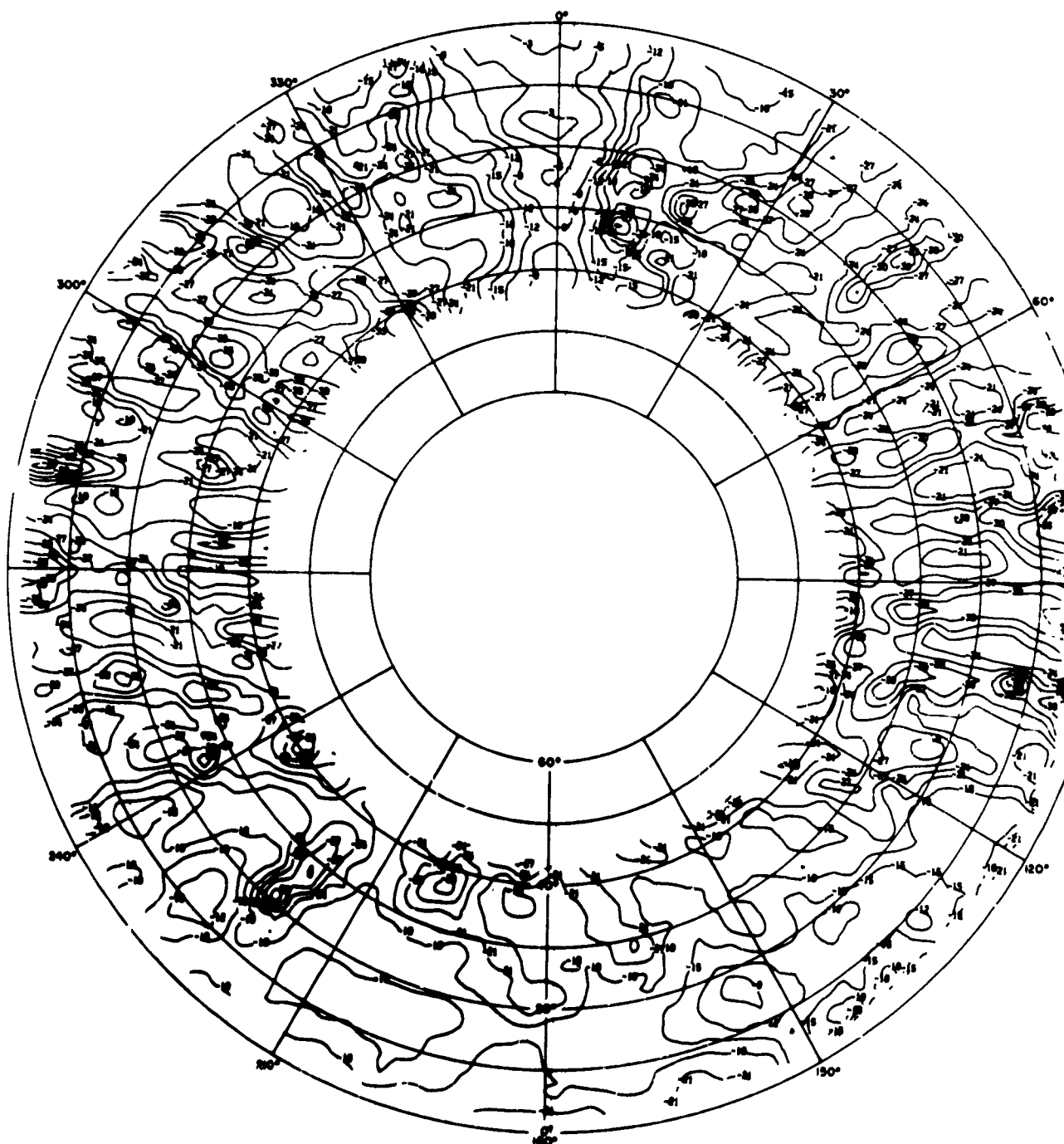


Fig. B.4 Anchorage Feed at 9.1 Mc, E_0

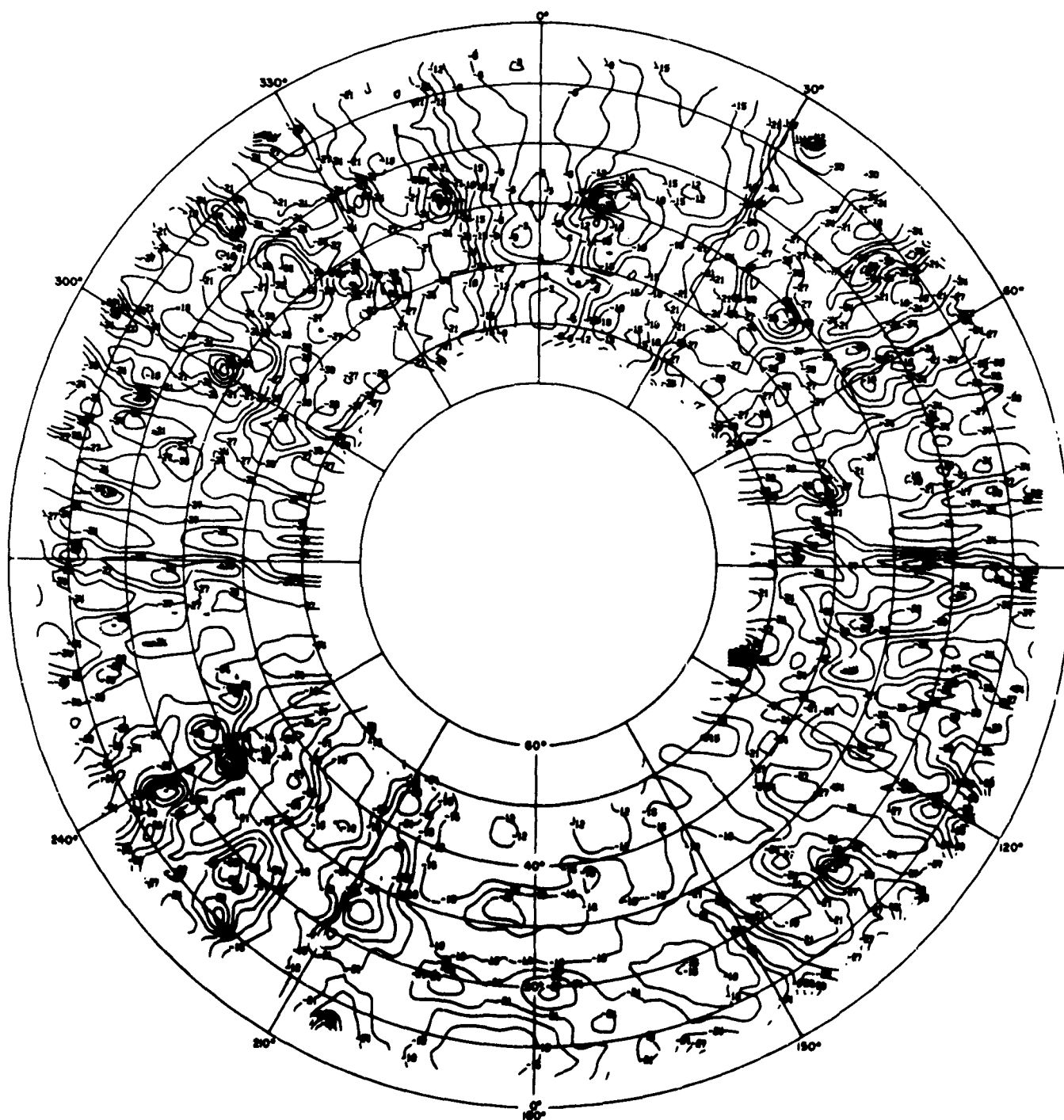


Fig. B.5 Anchorage Feed at 11.8 Mc, E_θ

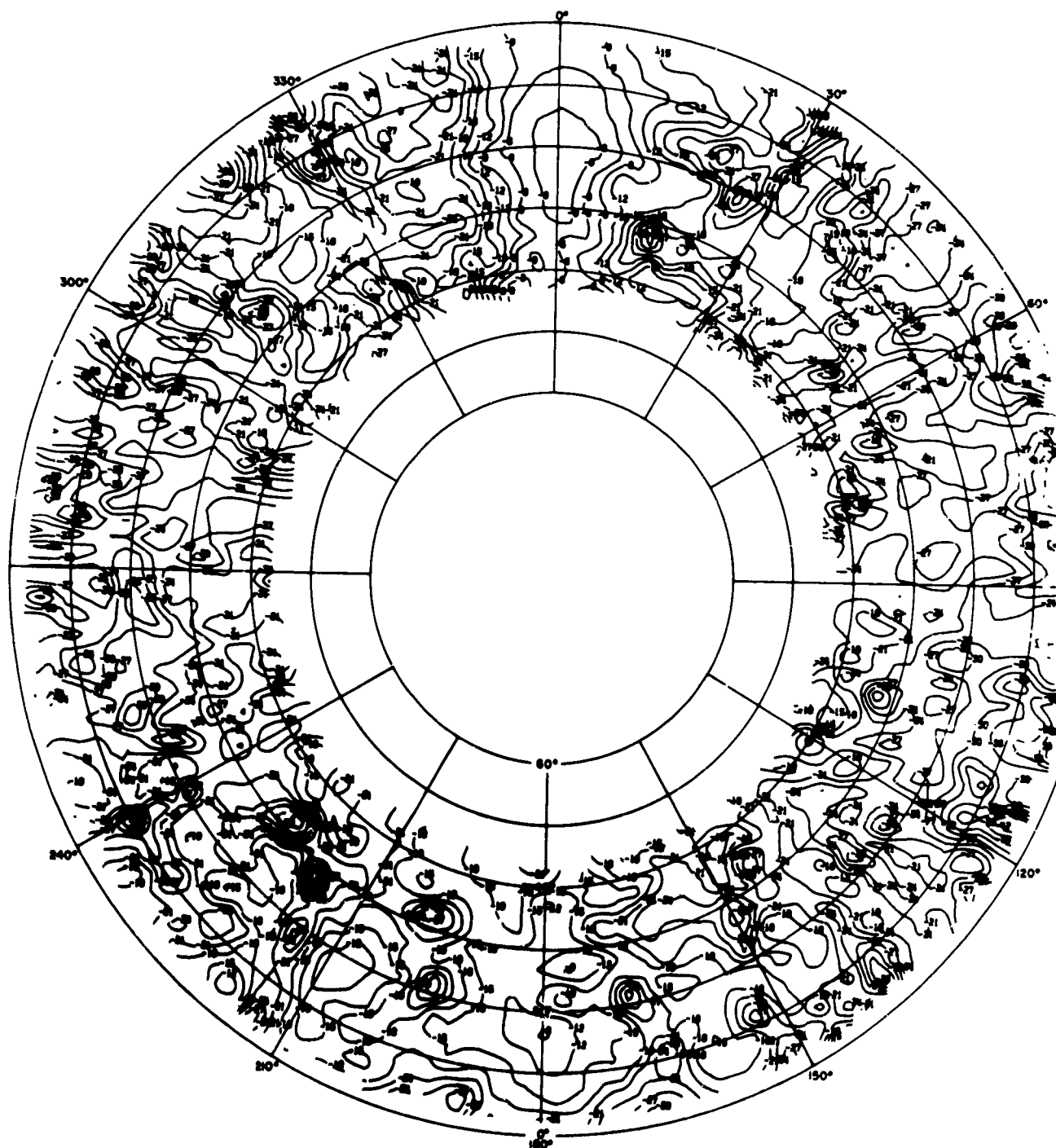


Fig. B.6 Anchorage Feed at 15.3 Mc, E_0

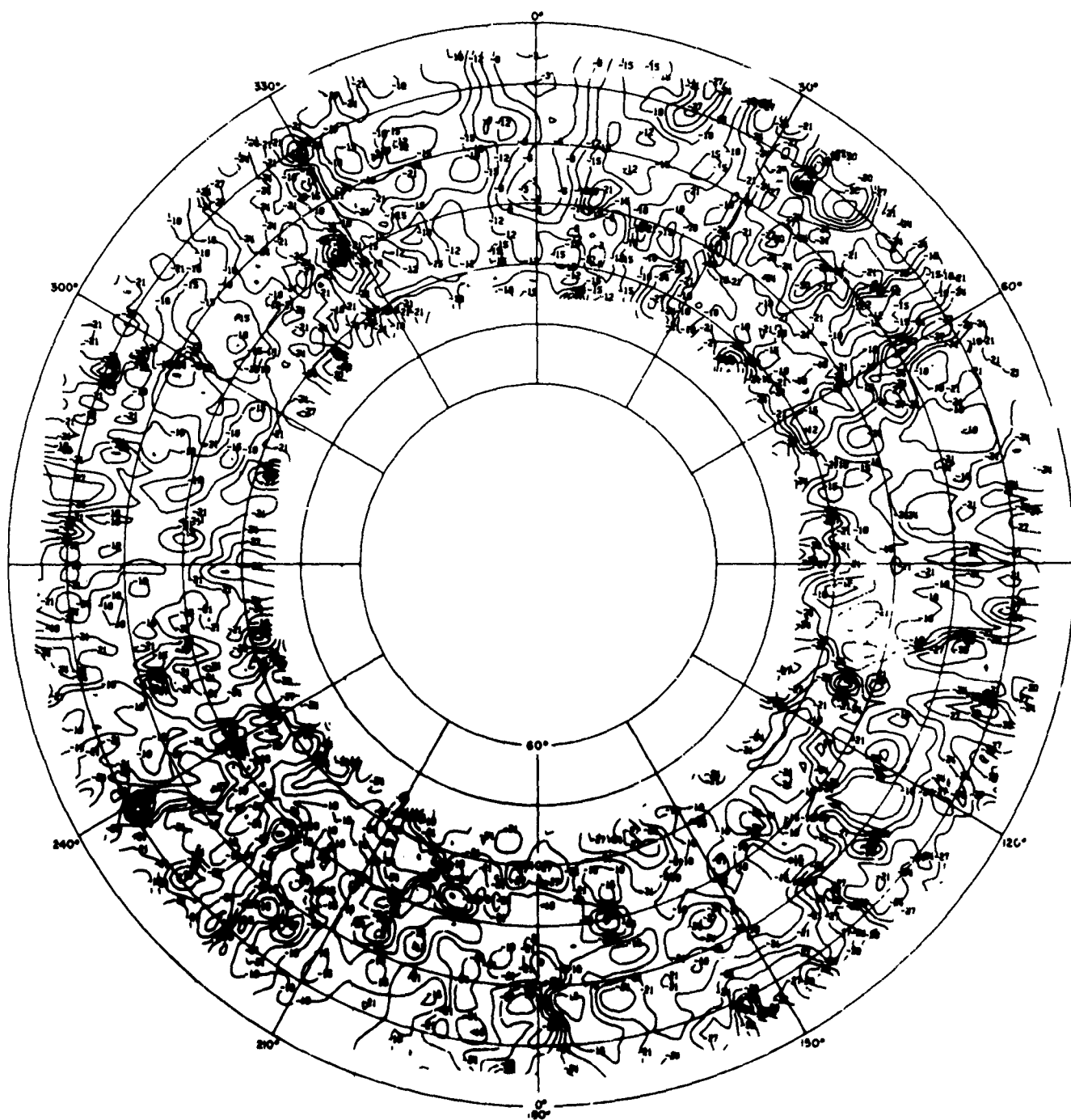


Fig. B.7 Anchorage Feed at 21.5 Mc, E_{θ}

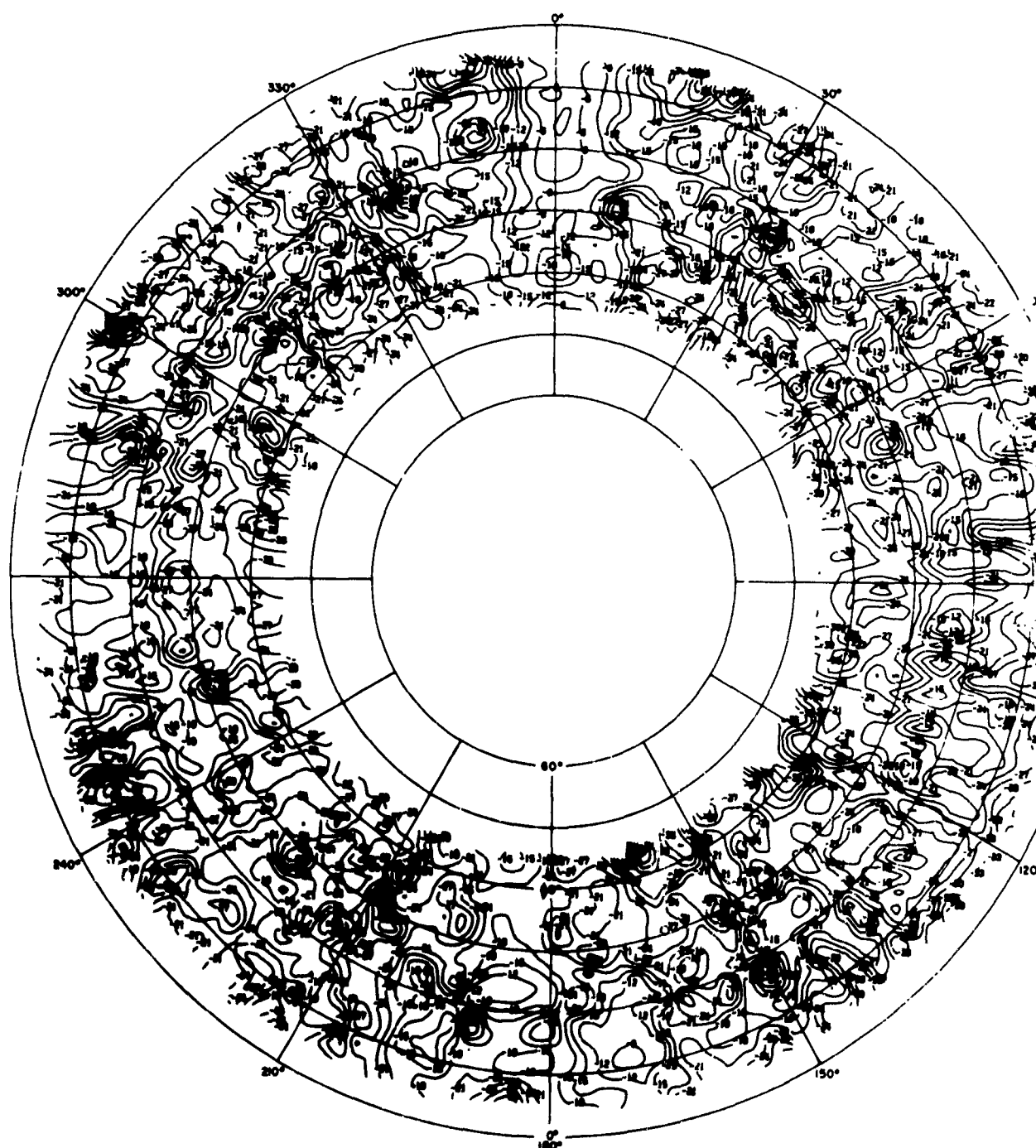


Fig. B.8 Anchorage Feed at 25.3 Mc, E_θ

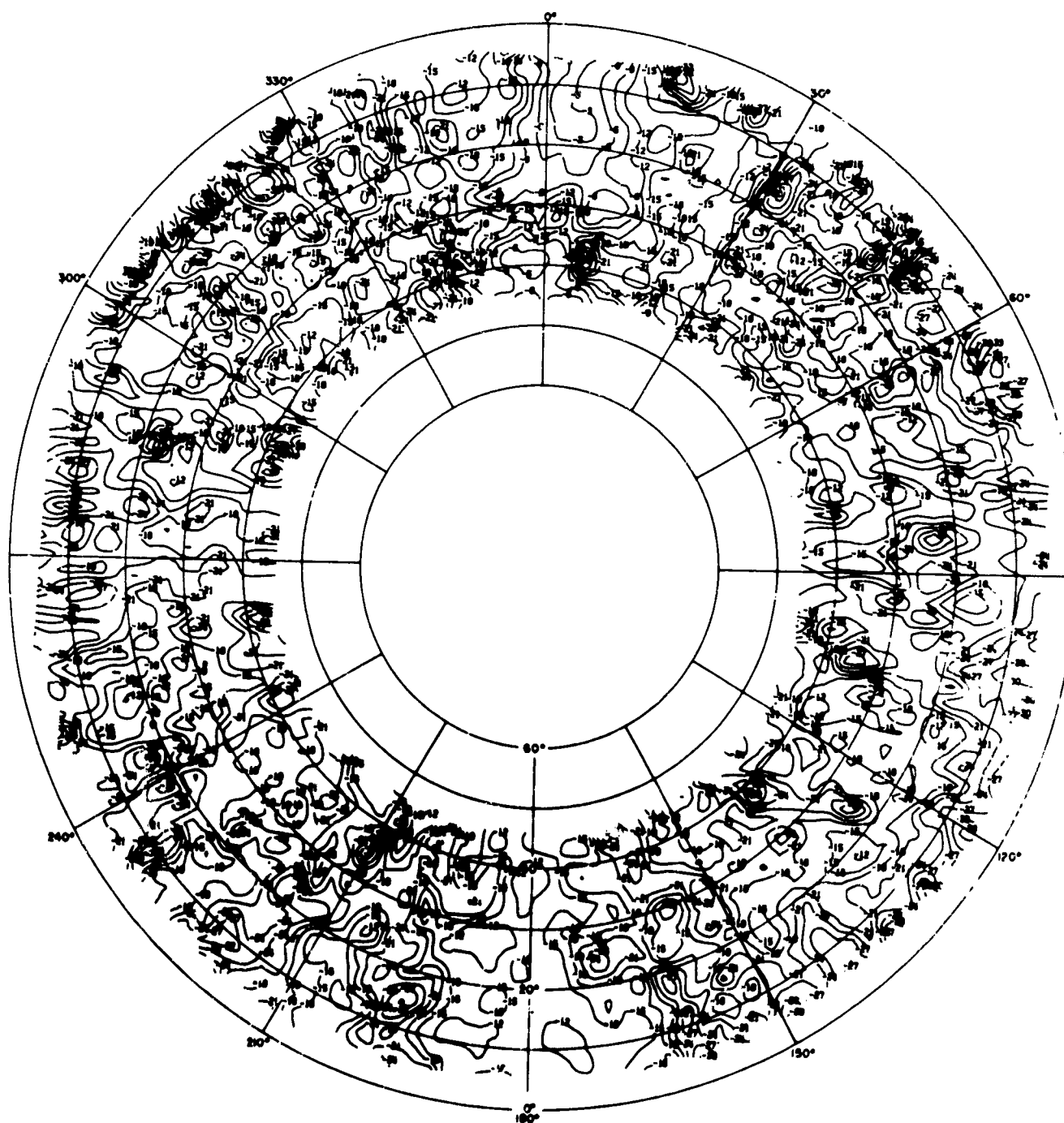


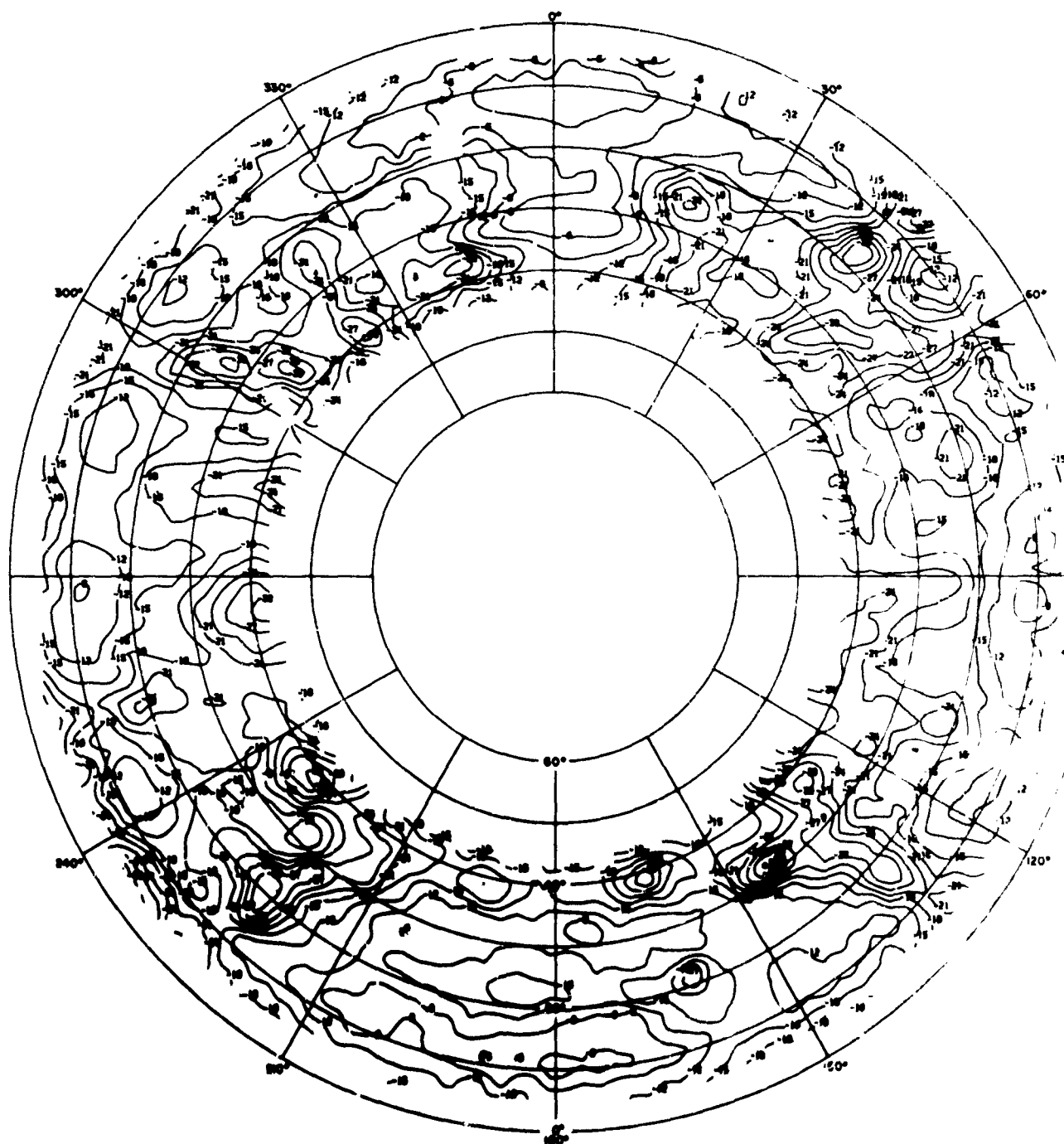
Fig. B.9 Anchorage Feed at 30.0 Mc, E_0



Fig. B.10 Nandi-Canton Feed at 3.0 Mc, E_θ



Fig. B.11 Nandi-Canton Feed at 4.1 Mc, E_θ



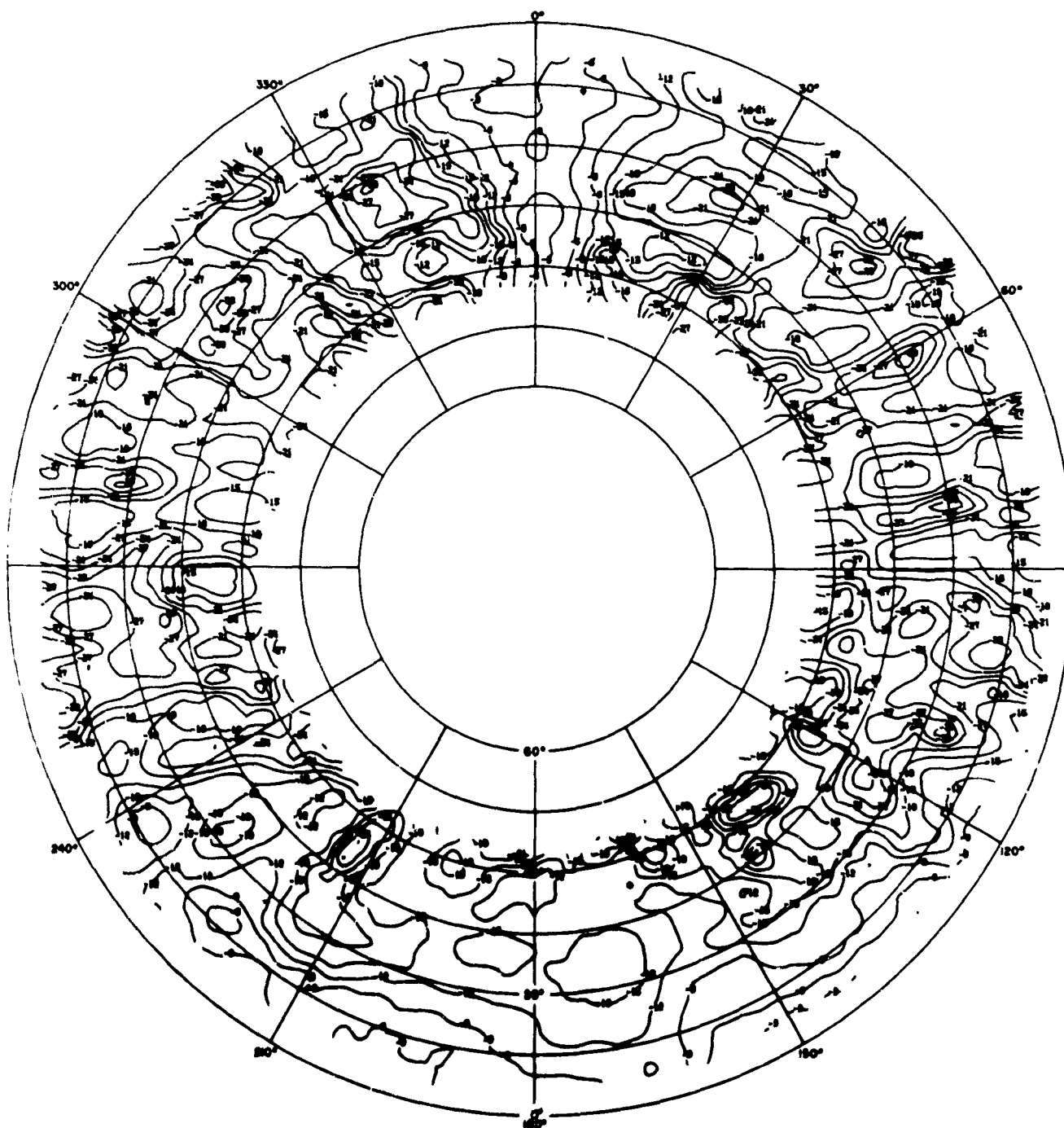


Fig. B.13 Nandi-Canton Feed at 9.1 Mc, E_0

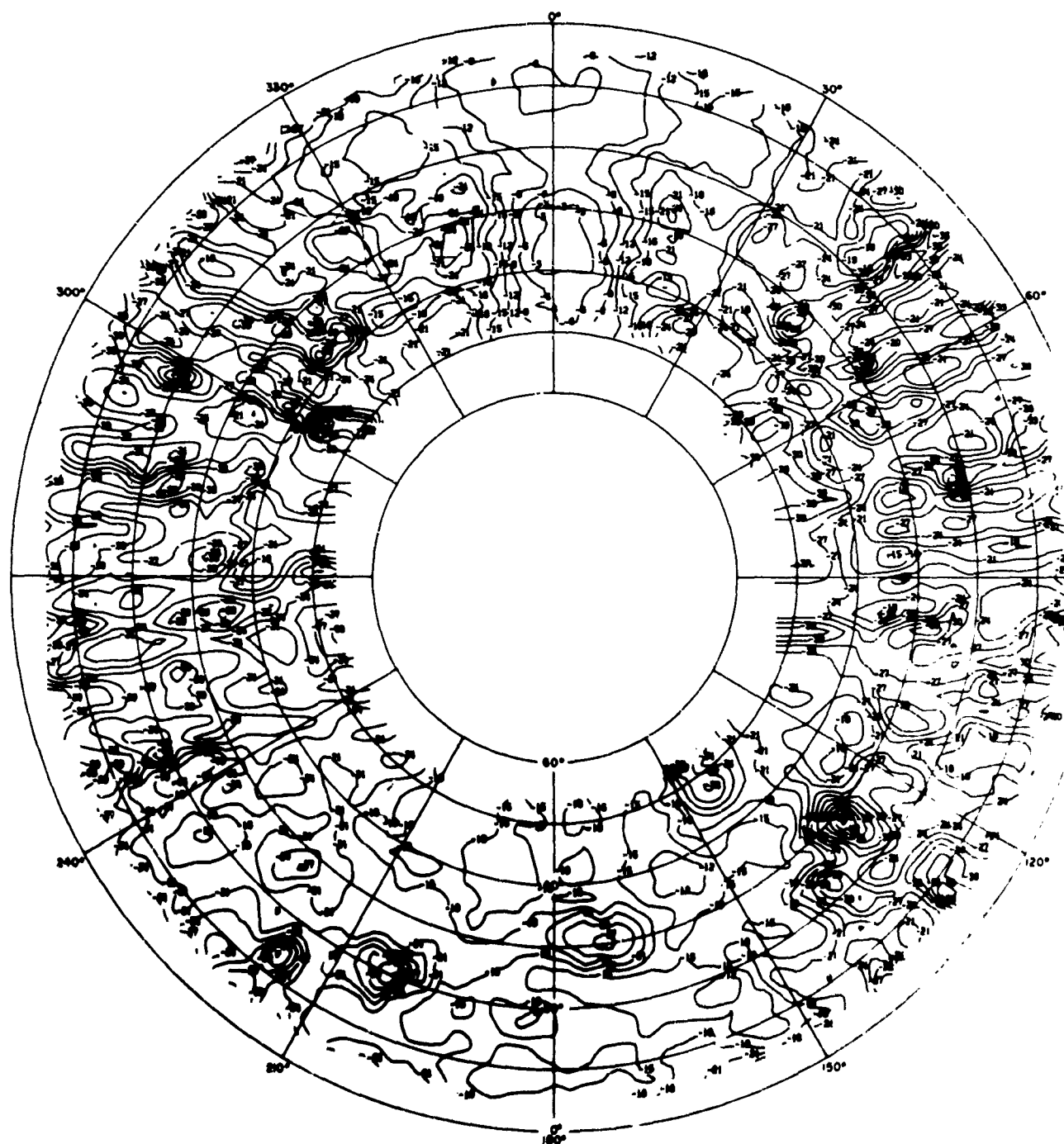


Fig. B.14 Nandi-Canton Feed at 11.8 Mc, E_0

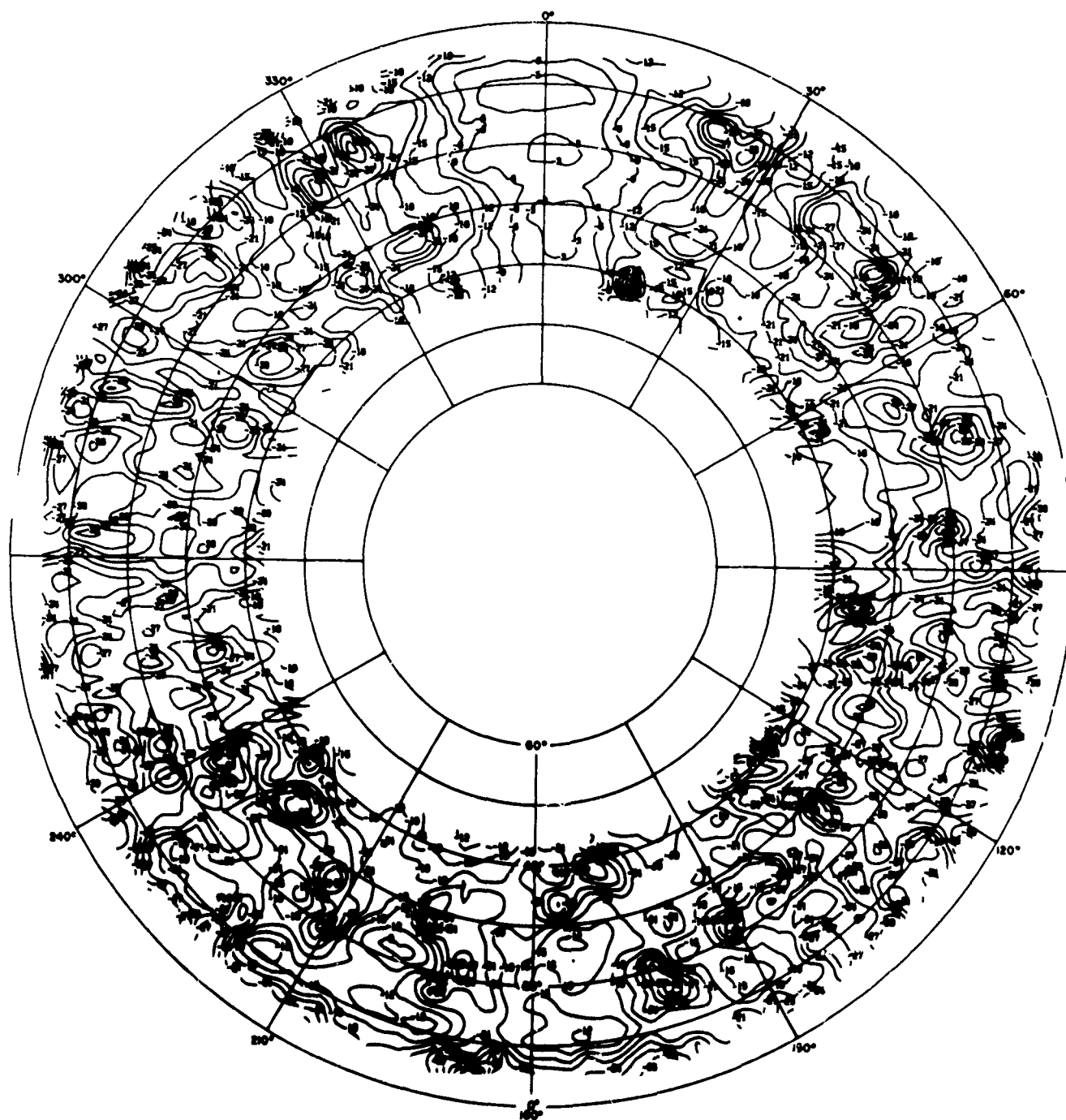


Fig. B.15 Nandi-Canton Feed at 15.3 Mc, E_0

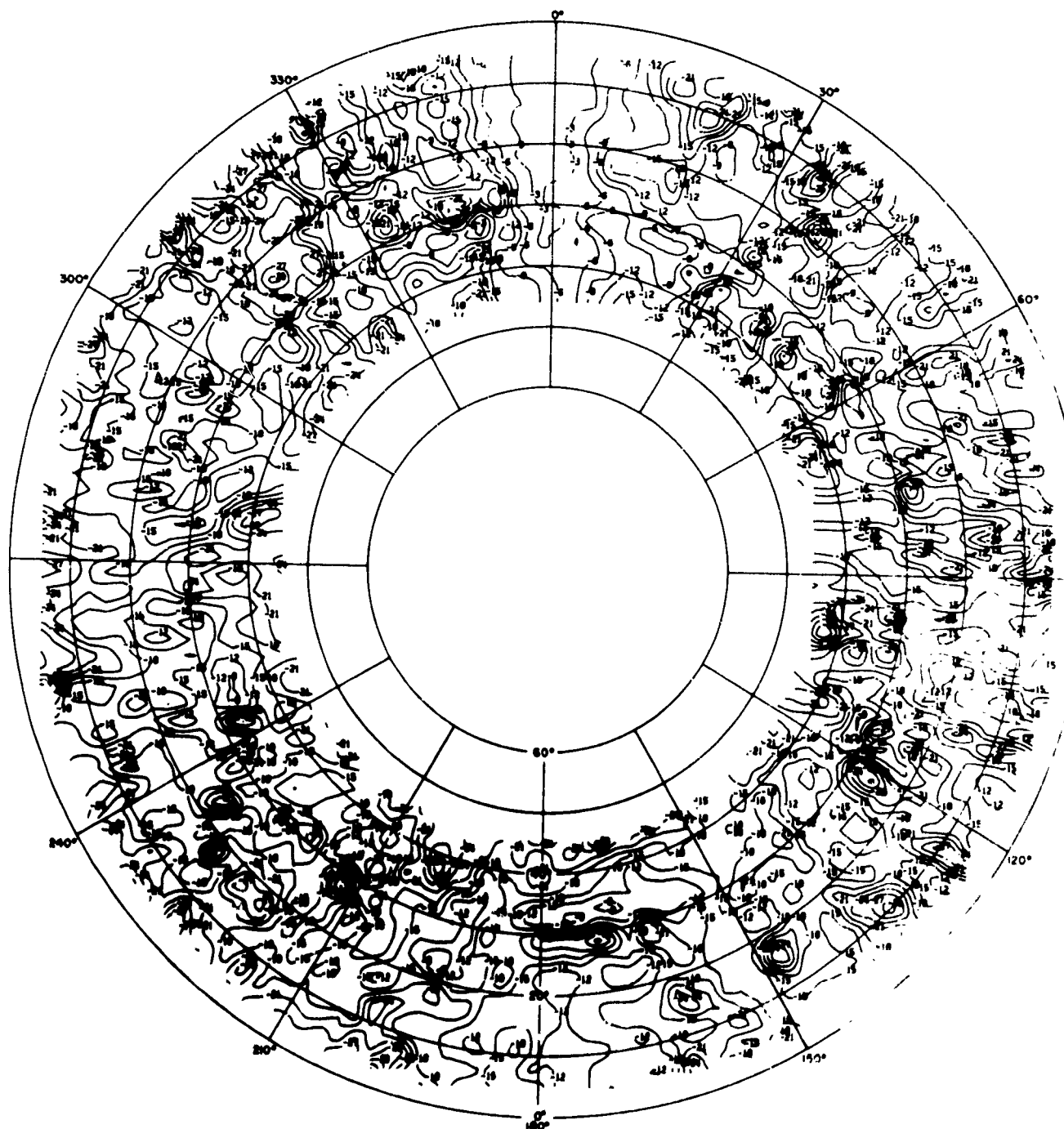


Fig. B.16 Nandi-Canton Feed at 21.5 Mc, E_0

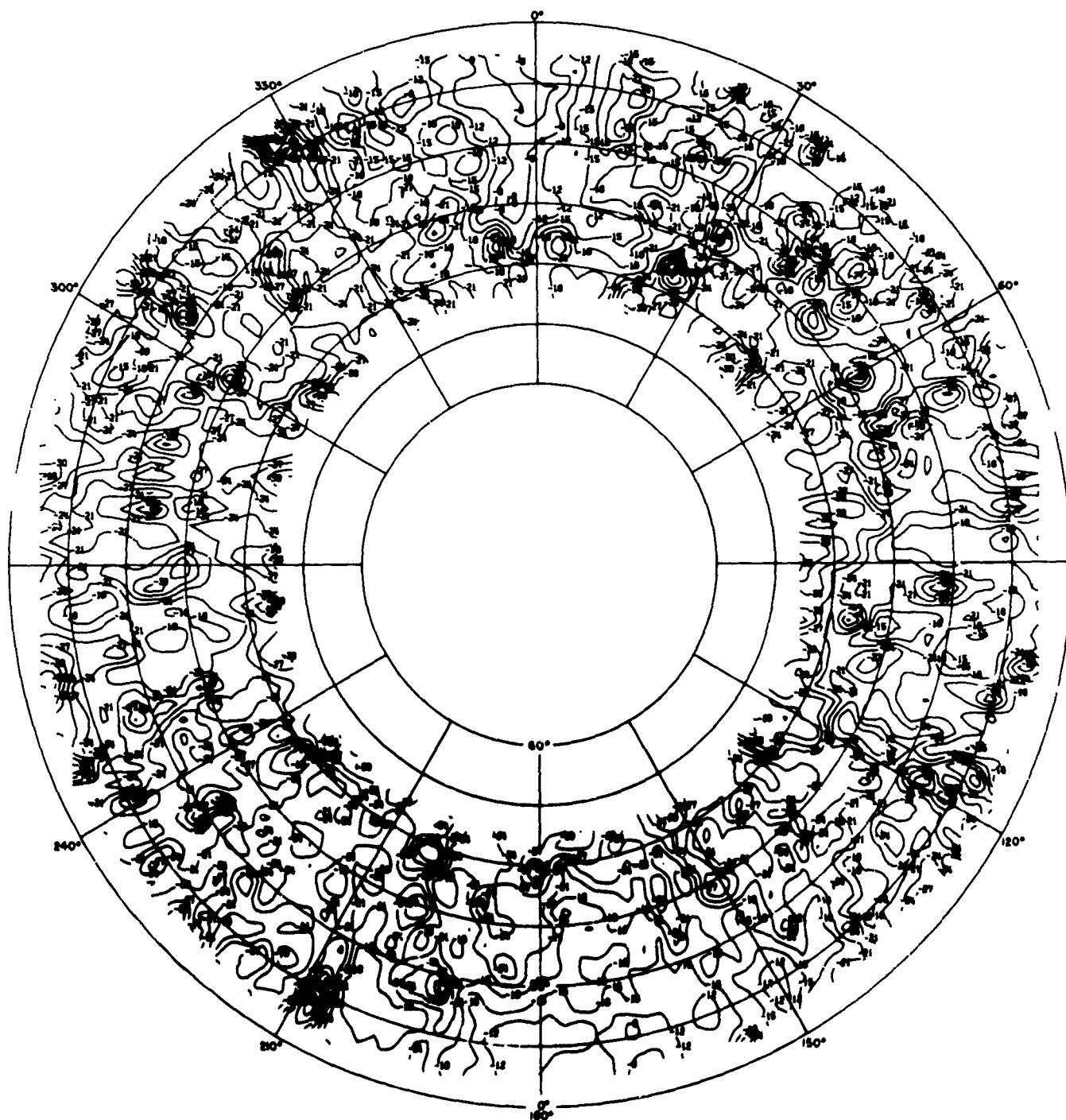


Fig. B.17 Nandi-Canton Feed at 25.3 Mc, E_0

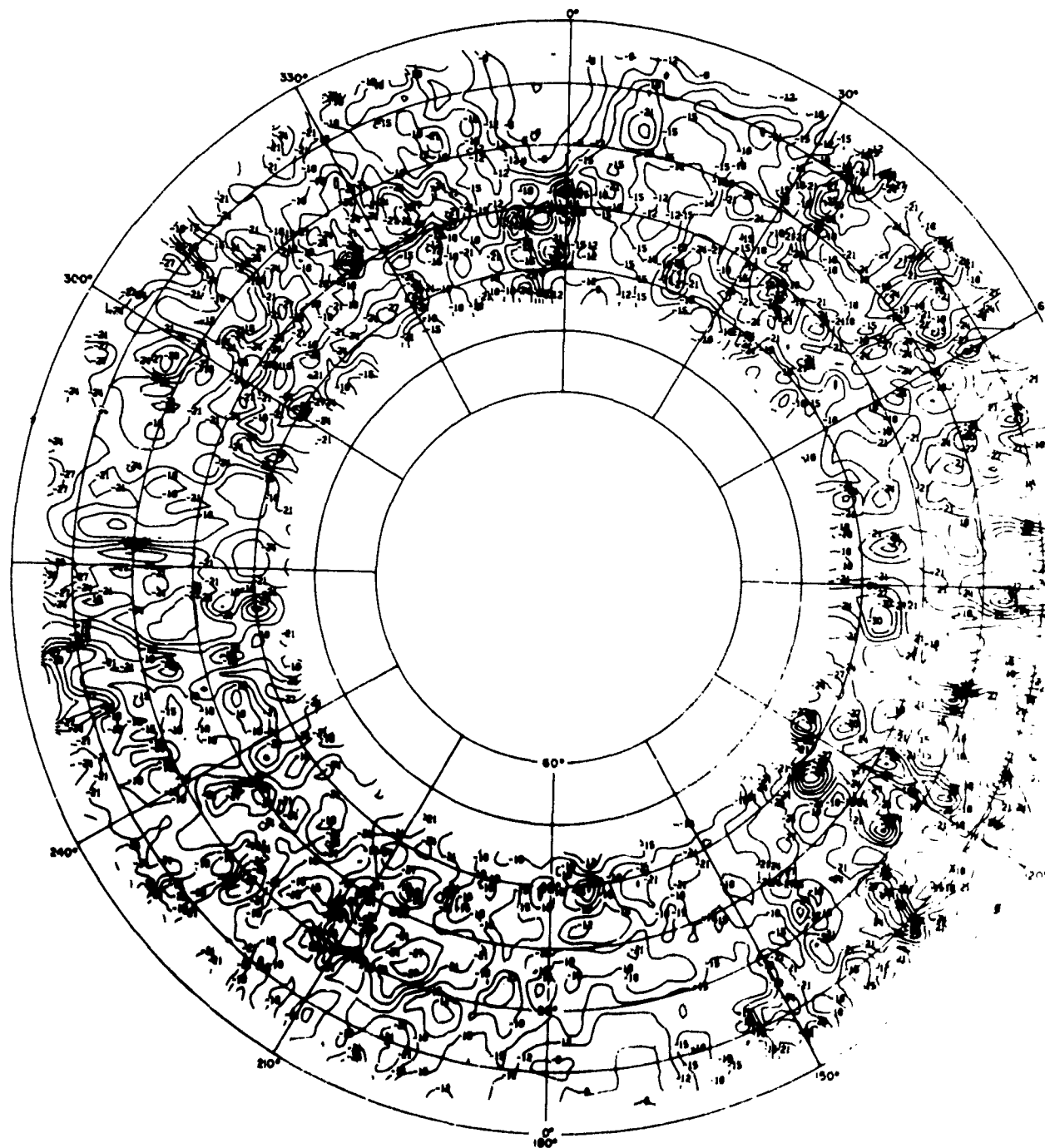


Fig. B.18 Nandi-Canton Feed at 30.0 Mc, E_θ

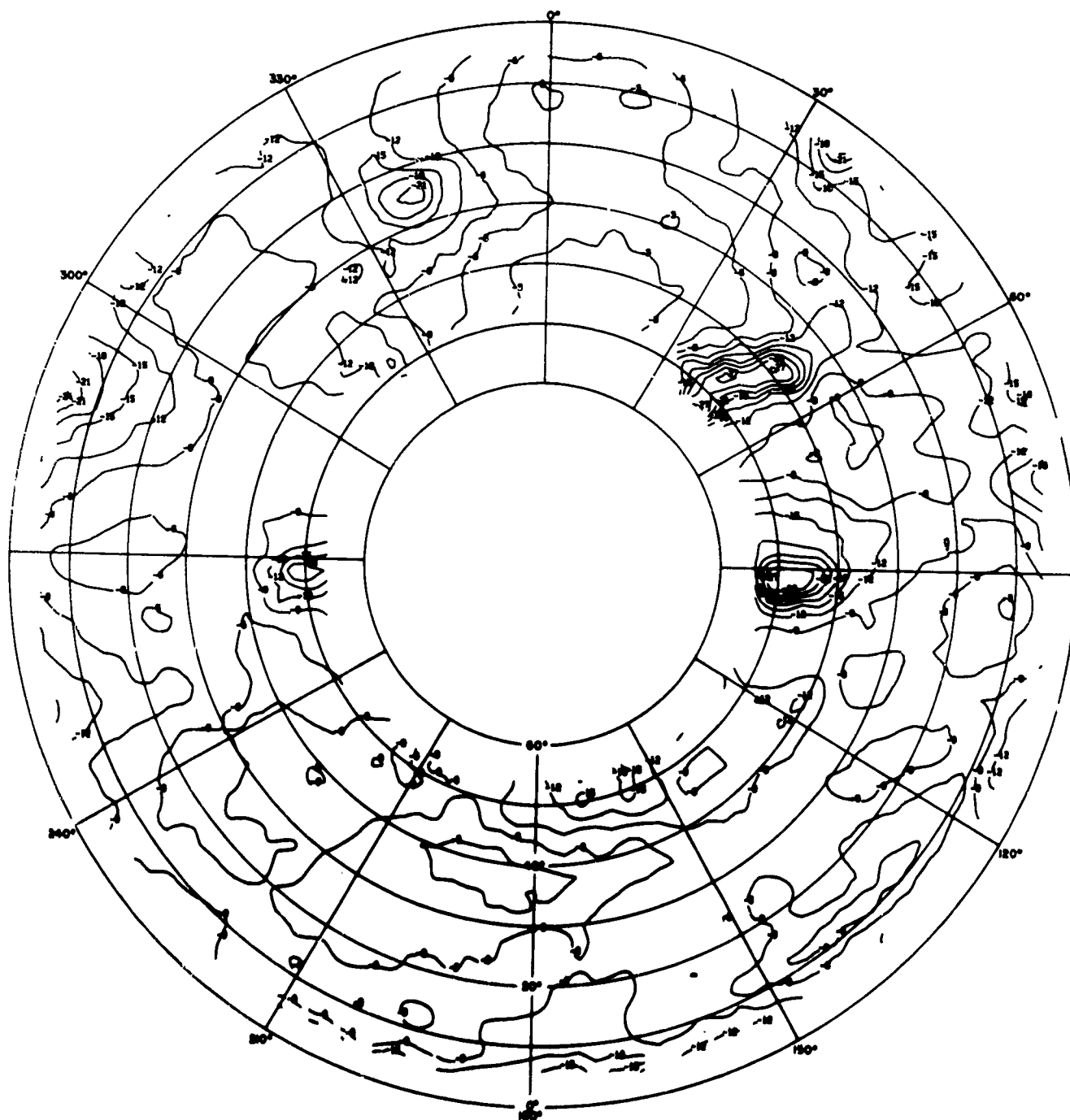




Fig. B.20 Sydney Feed at 4.1 Mc, E_θ



Fig. B. 21 Sydney Feed at 5.6 Mc, E_θ

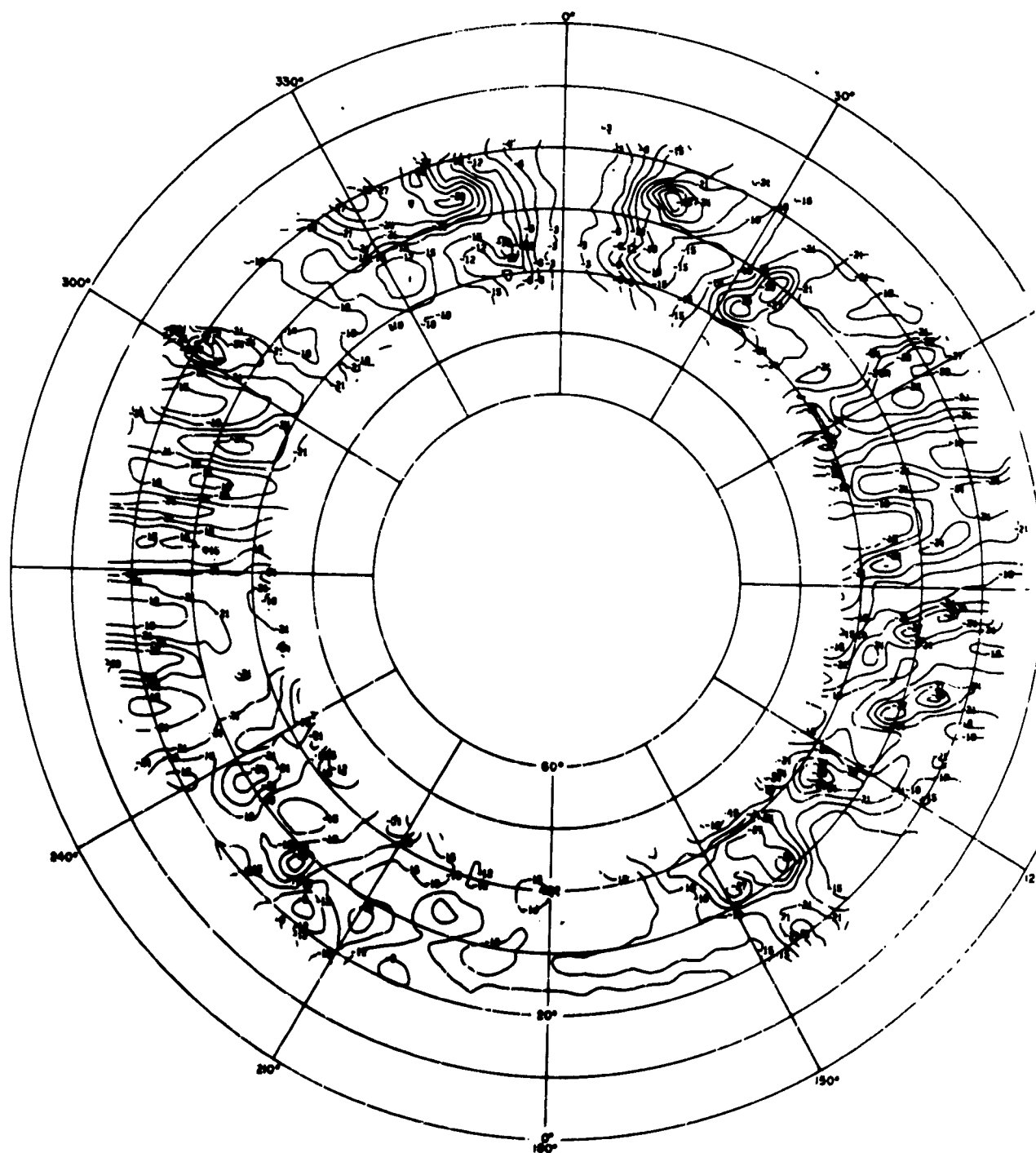


Fig. B.22 Sydney Feed at 9.1 Mc, E_0

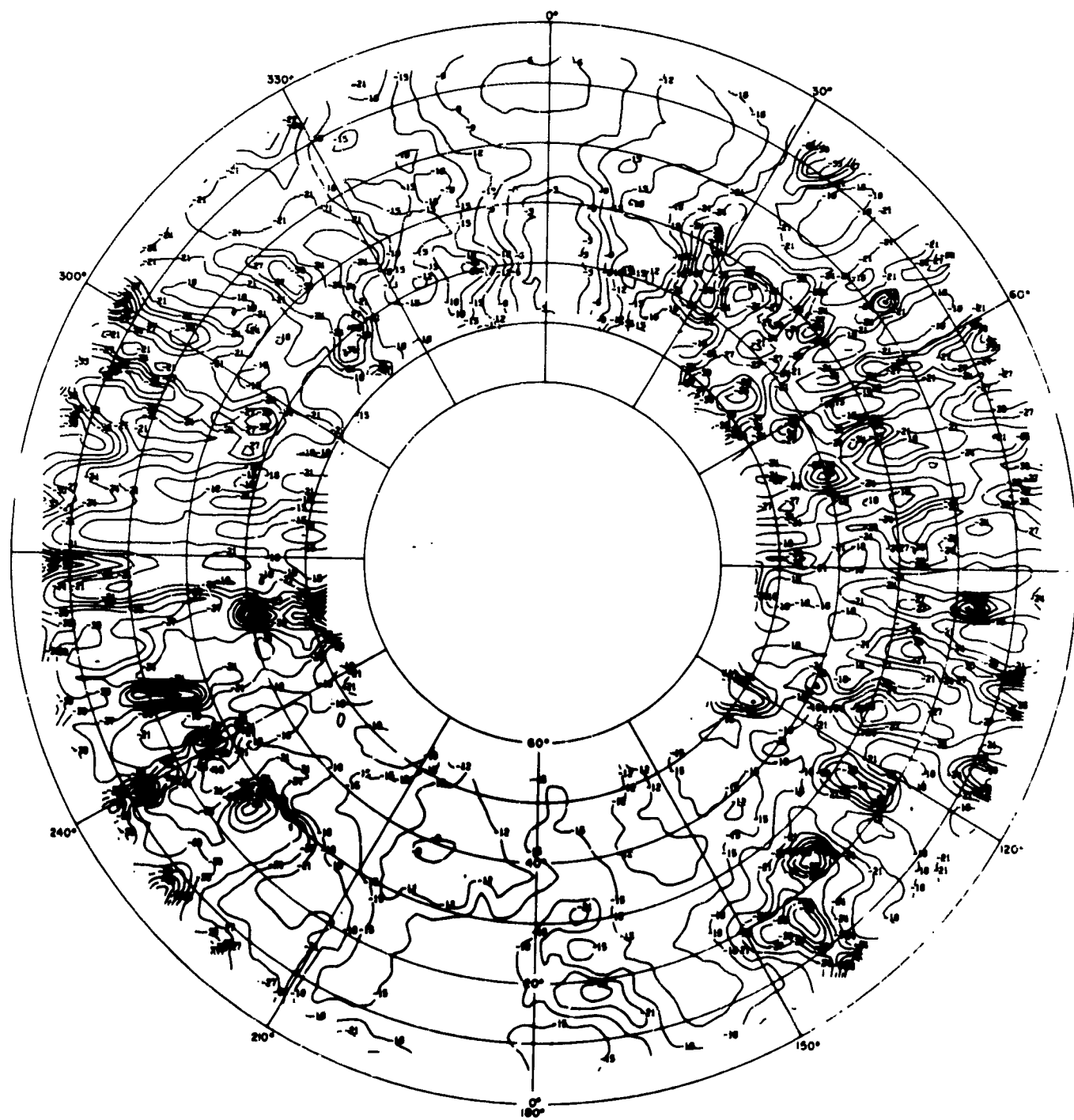


Fig. B.23 Sydney Feed at 11.8 Mc, E_θ

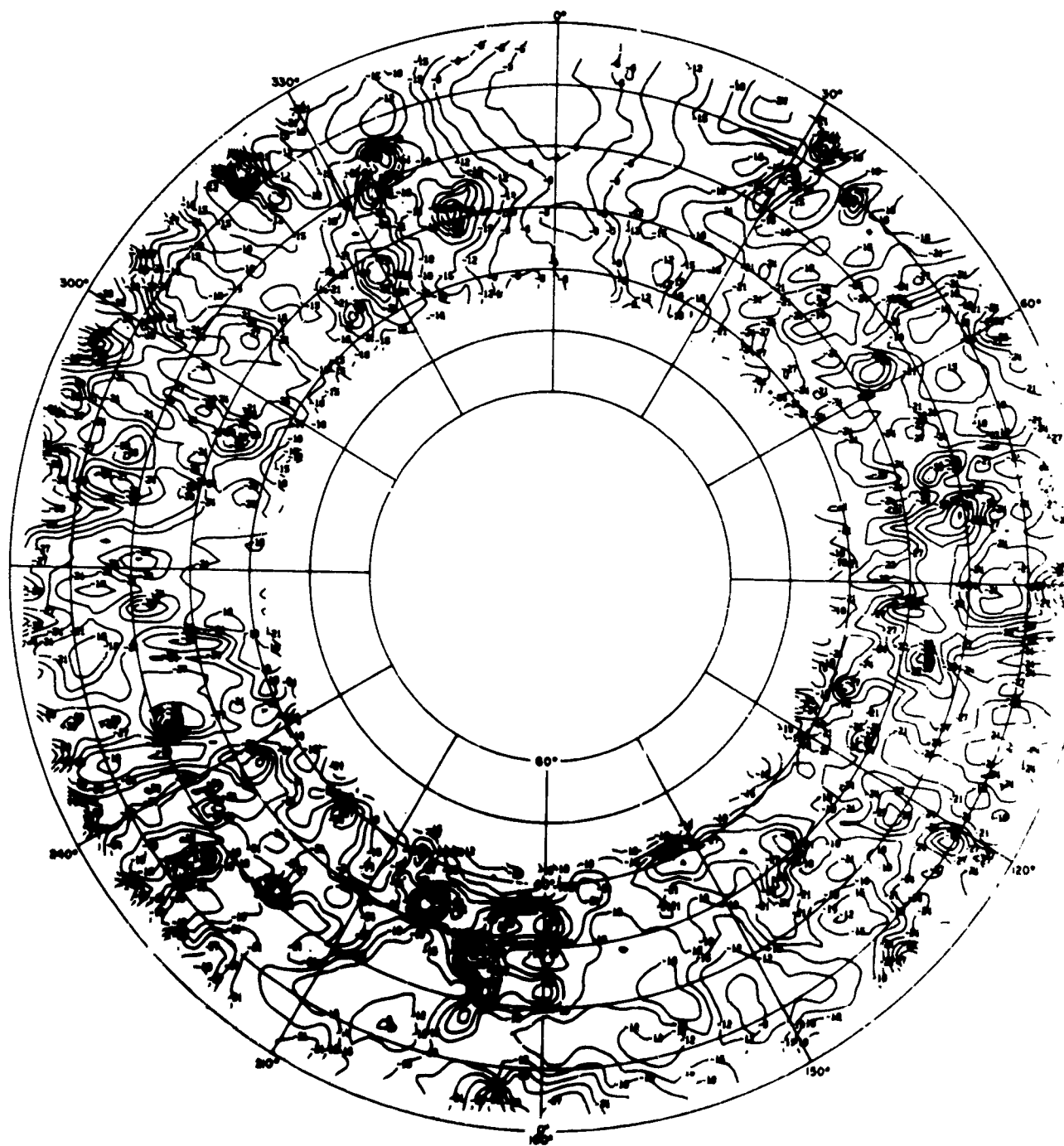


Fig. B.24 Sydney Feed at 15.3 Mc, E_0

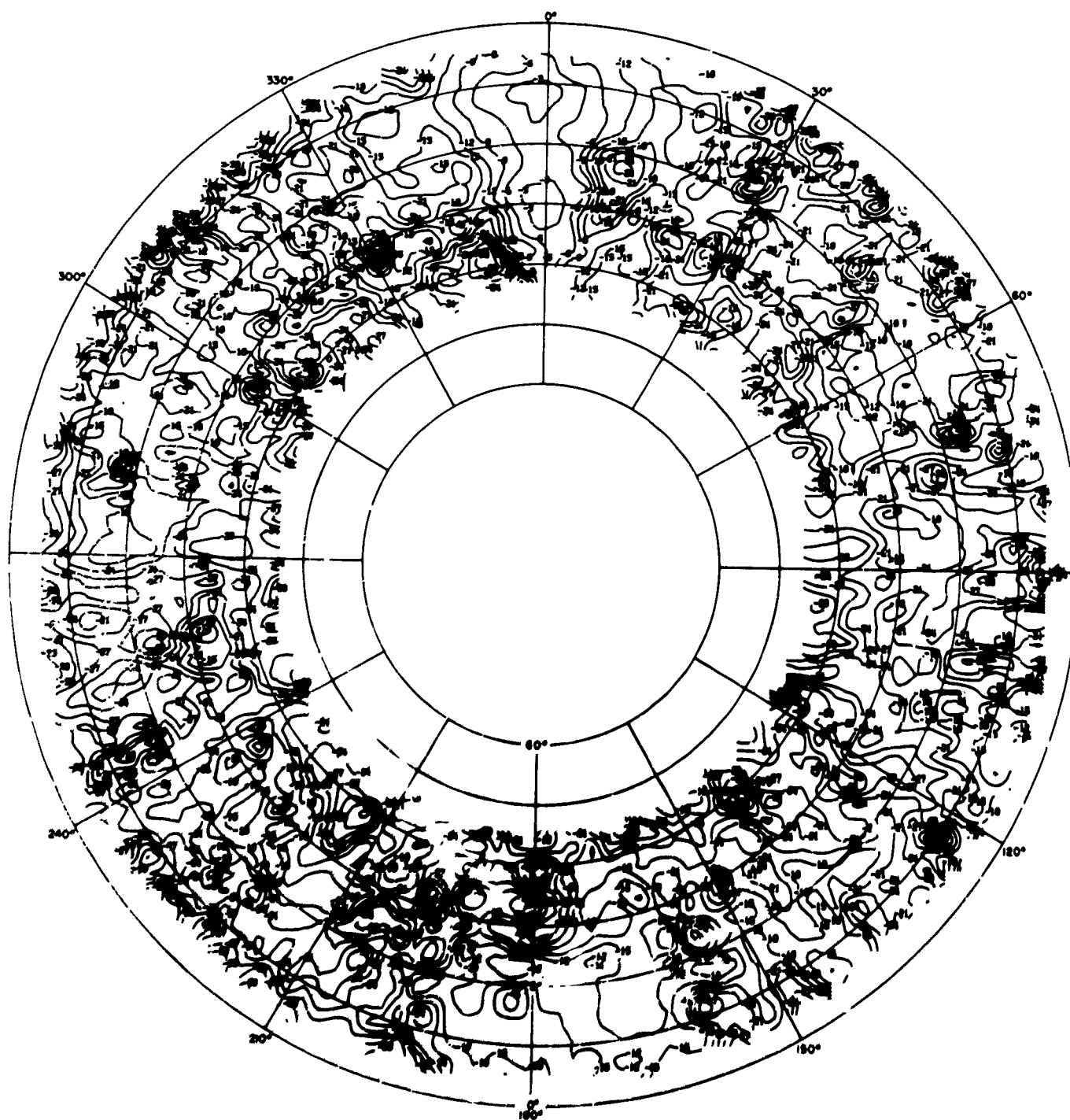


Fig. B.25 Sydney Feed at 21.5 Mc, E_θ

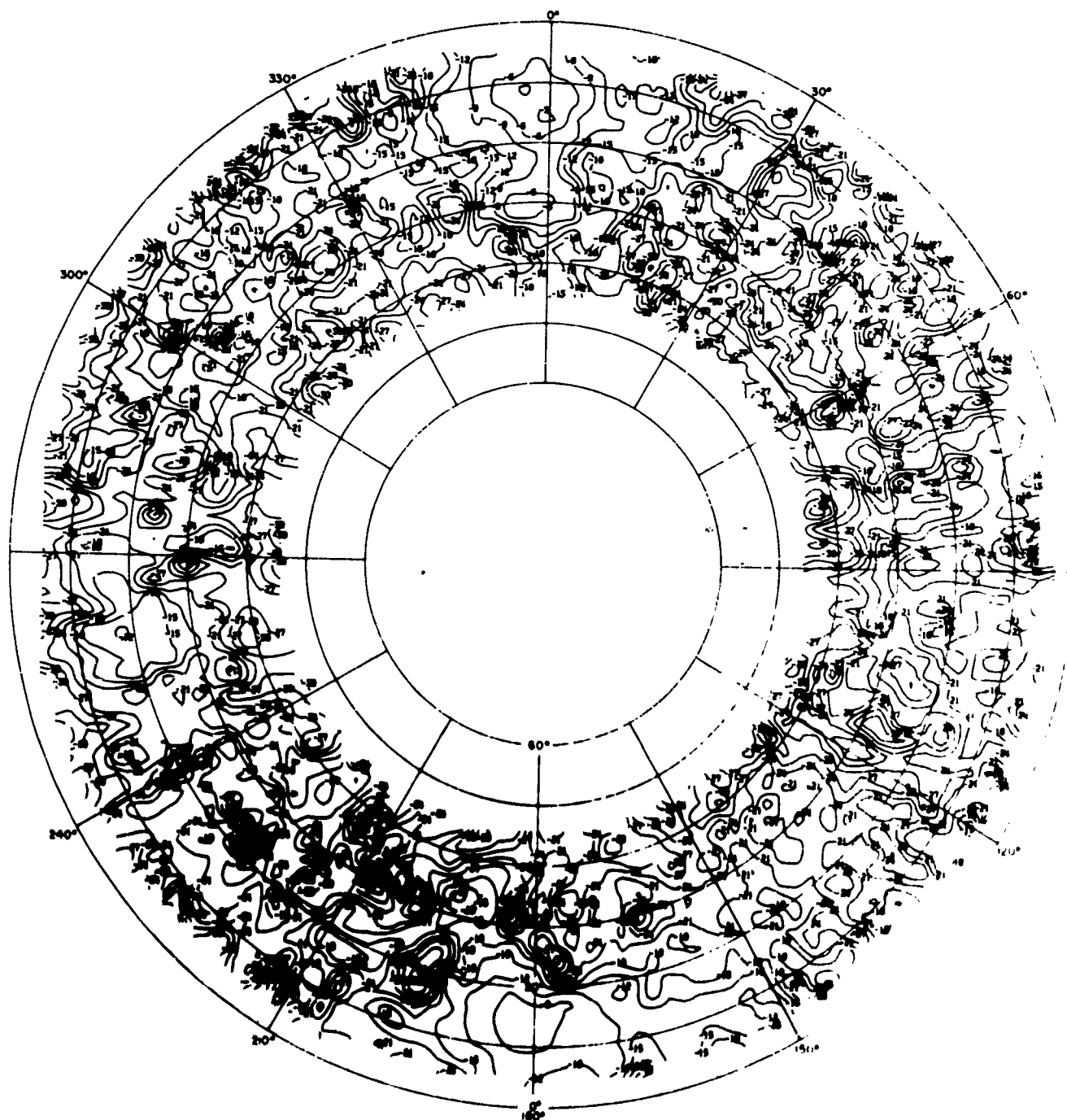


Fig. B.26 Sydney Feed at 25.3 Mc, E_θ

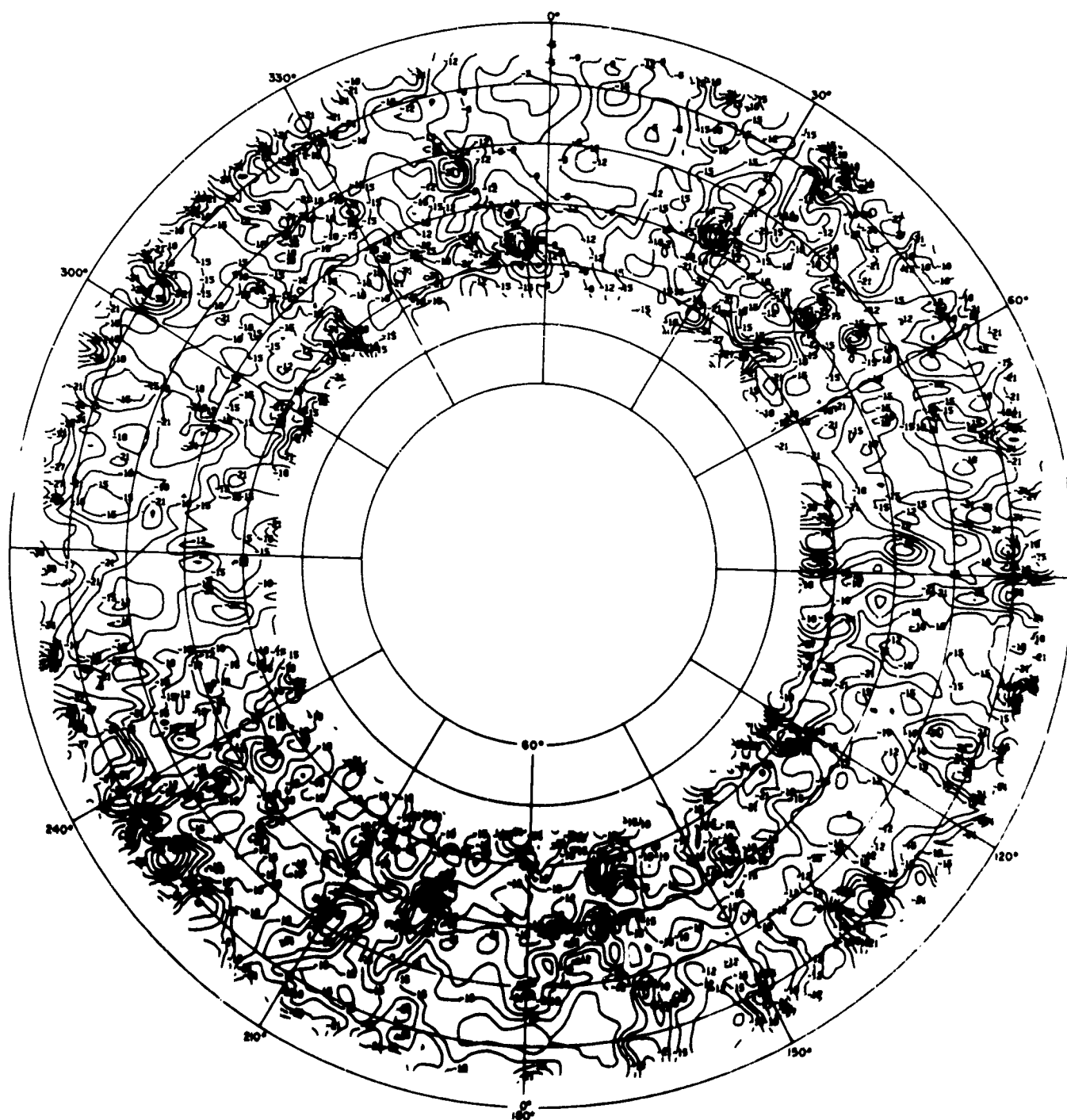


Fig. B.27 Sydney Feed at 30.0 Mc, E_θ

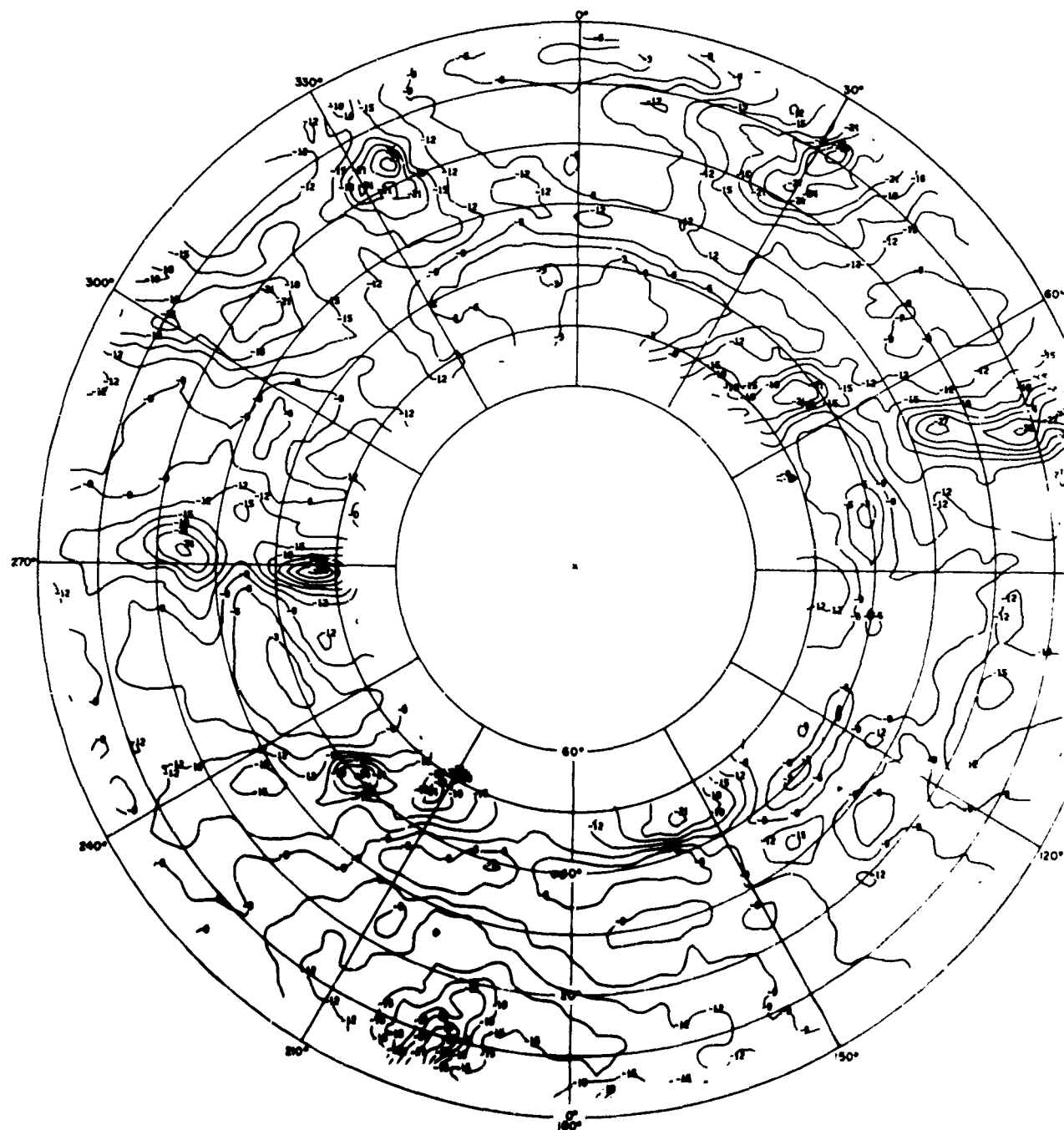


Fig. B. 28 San Francisco Feed at 3.0 Mc. E_{θ}

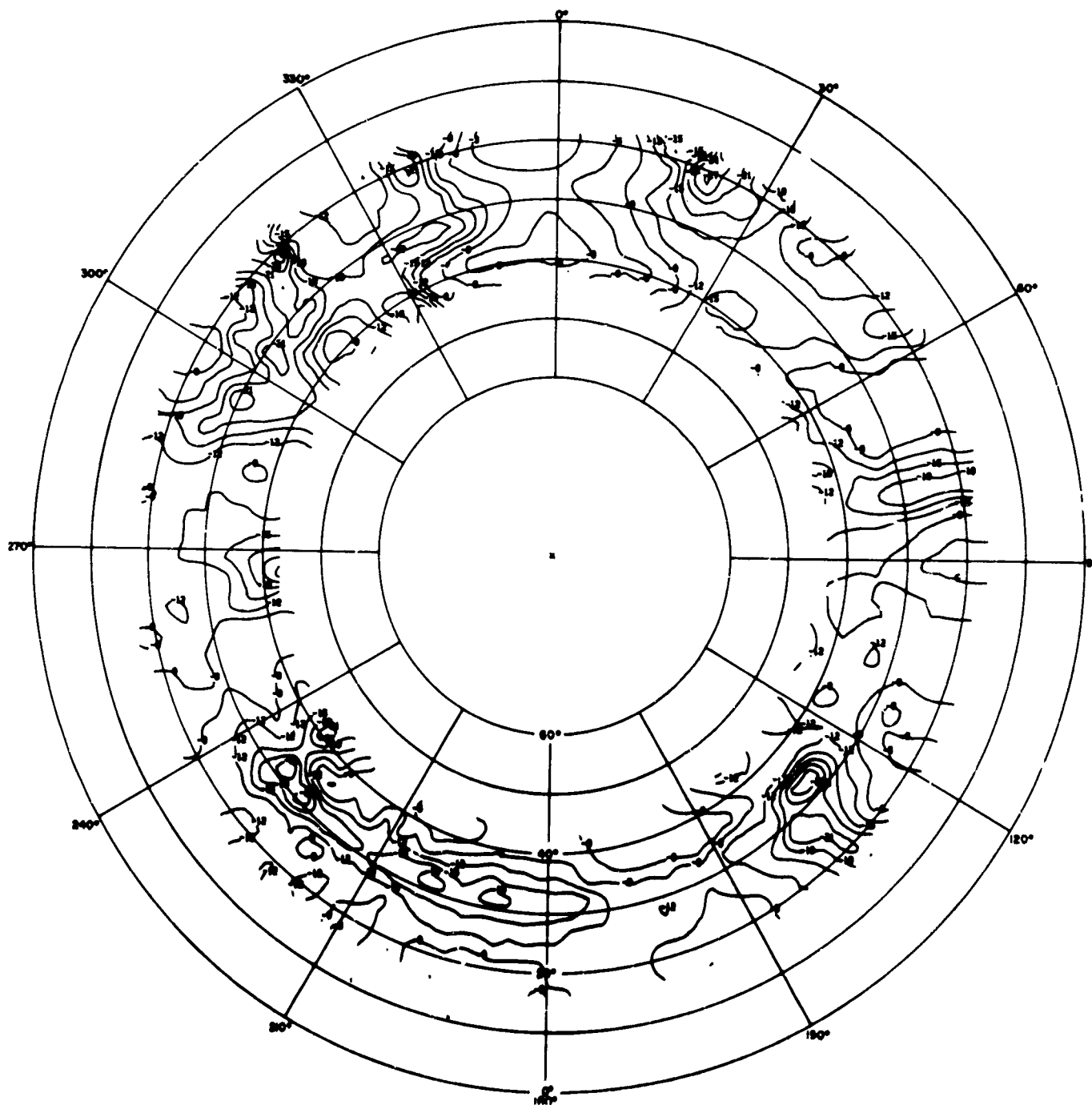


Fig. B. 29 San Francisco Feed at 4.1 Mc, E_{θ}



Fig. B. 30 San Francisco Feed at 5.6 Mc, E_{θ}

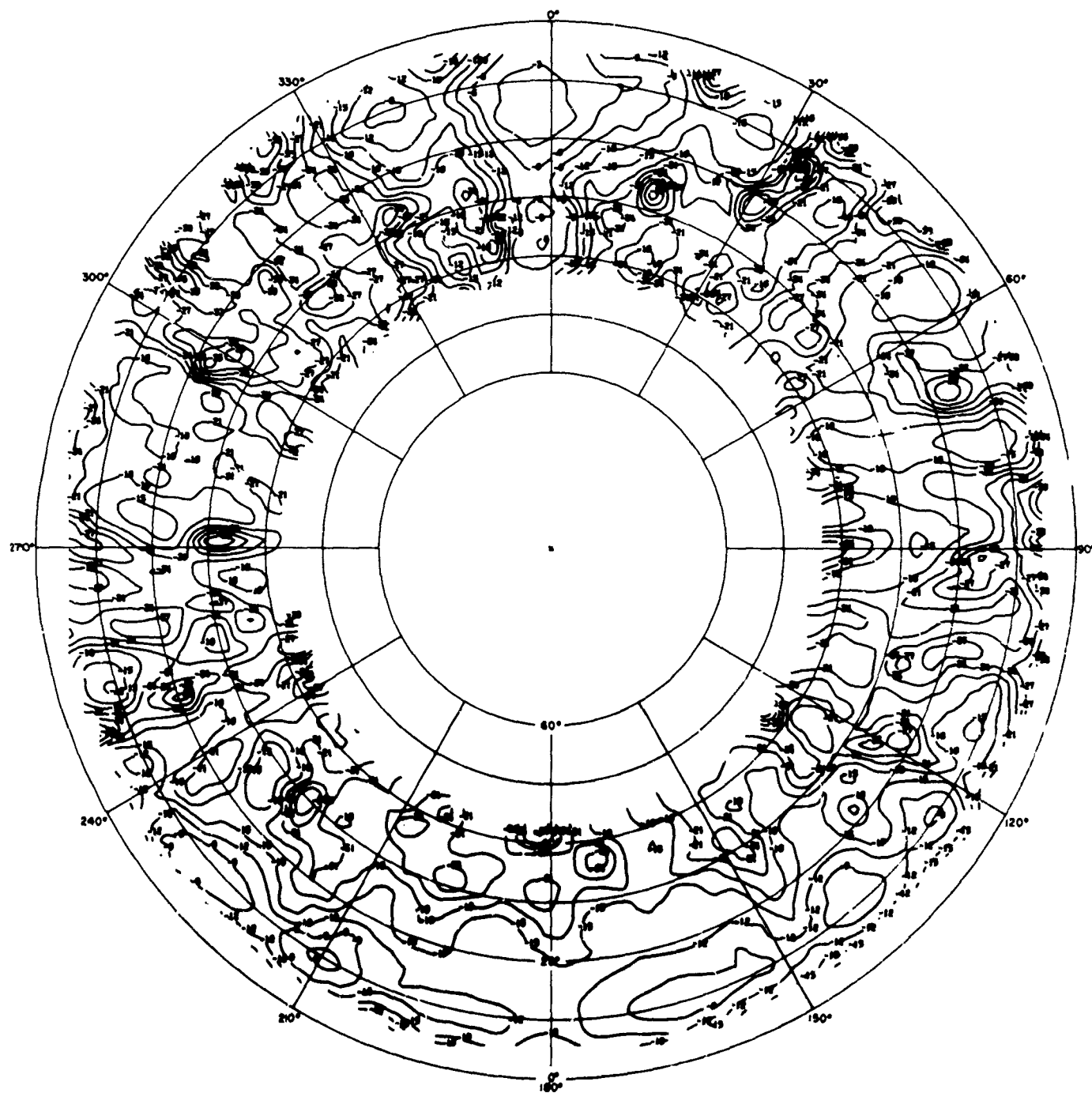


Fig. B. 31 San Francisco Feed at 9.1 Mc, E_0

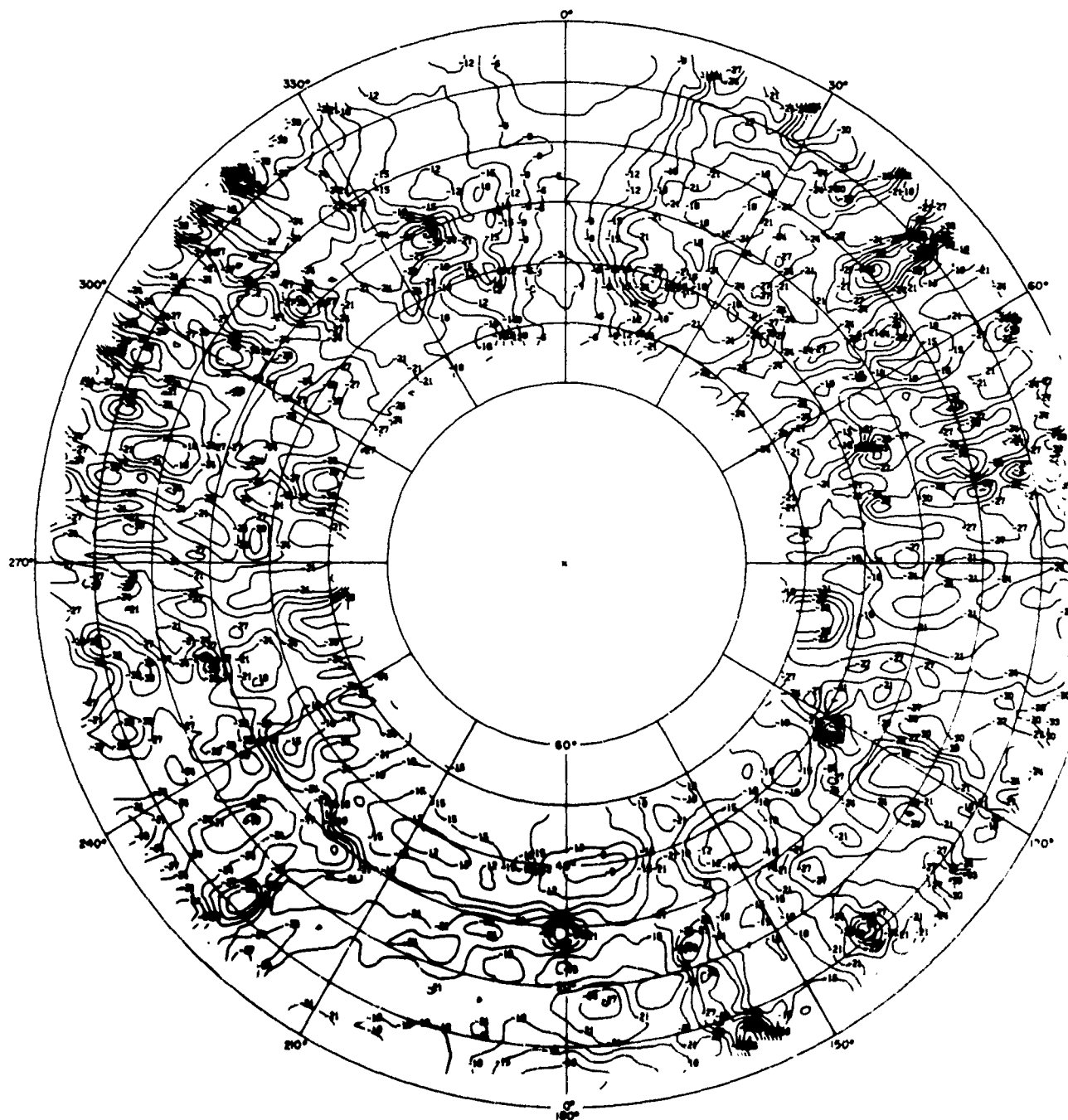


Fig. B. 32 San Francisco Feed at 11.8 Mc, E_{θ}

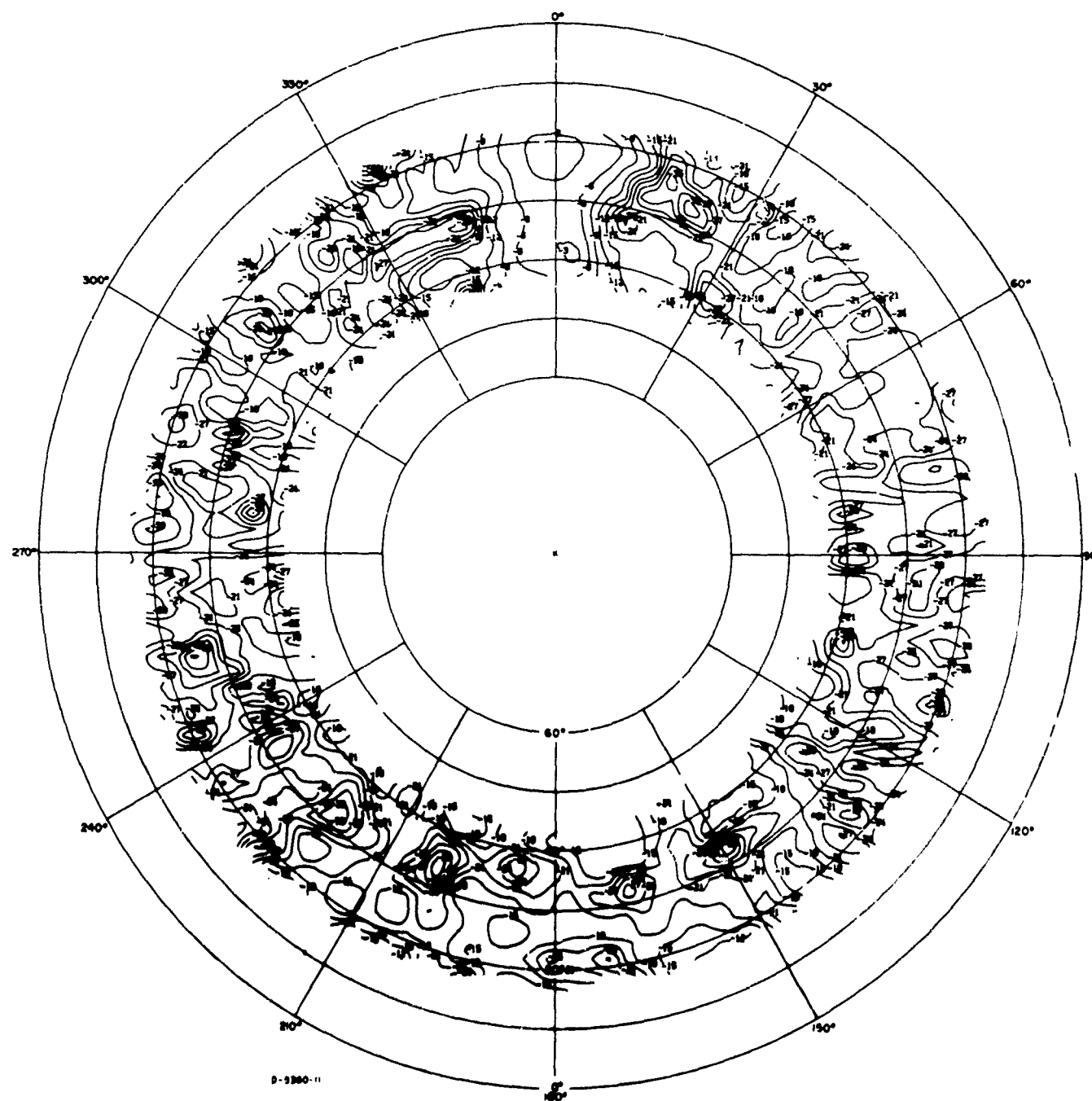


Fig. B. 33 San Francisco Feed at 15.3 Mc, E_0

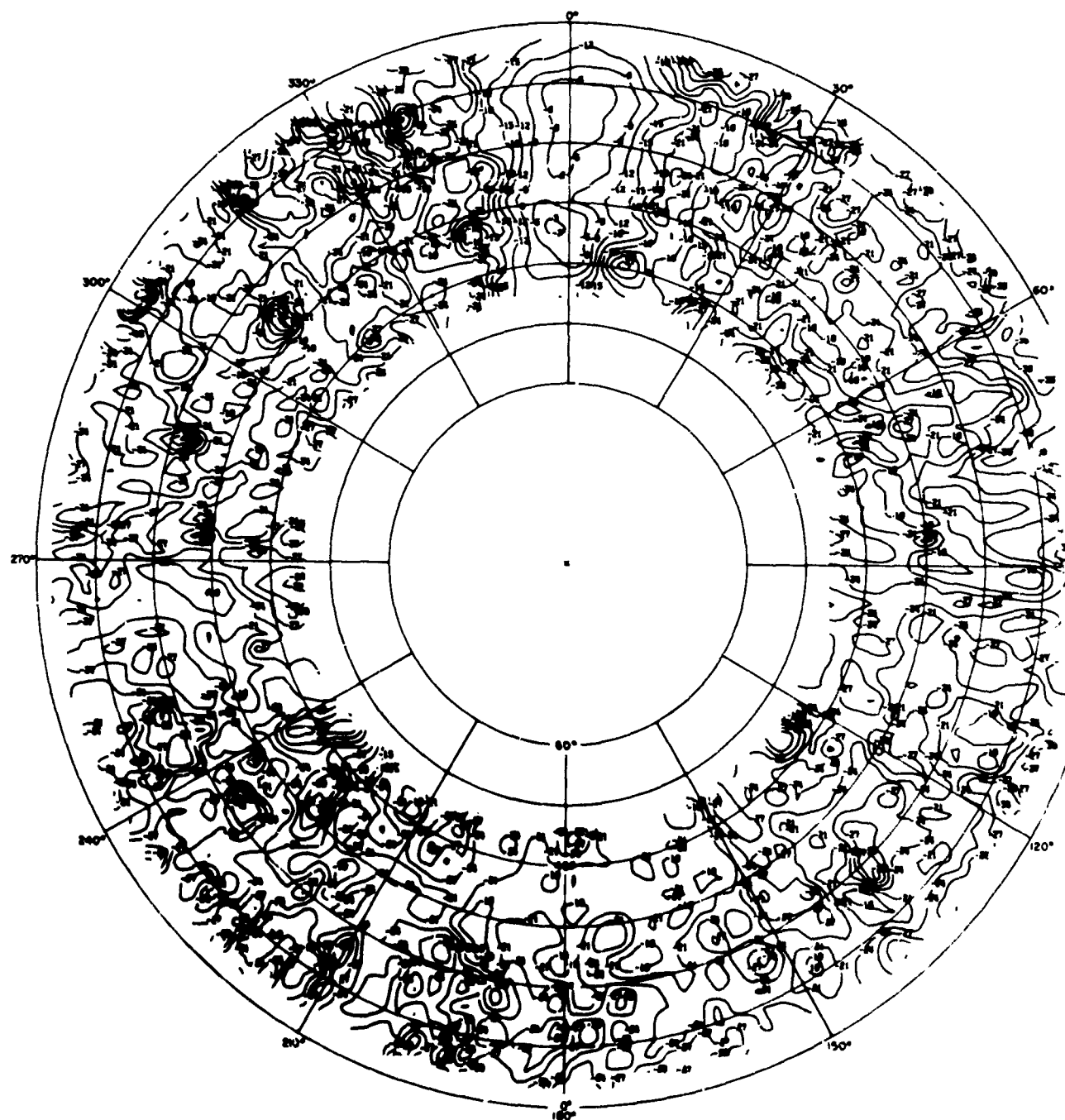


Fig. B. 34 San Francisco Feed at 21.5 Mc, E_θ

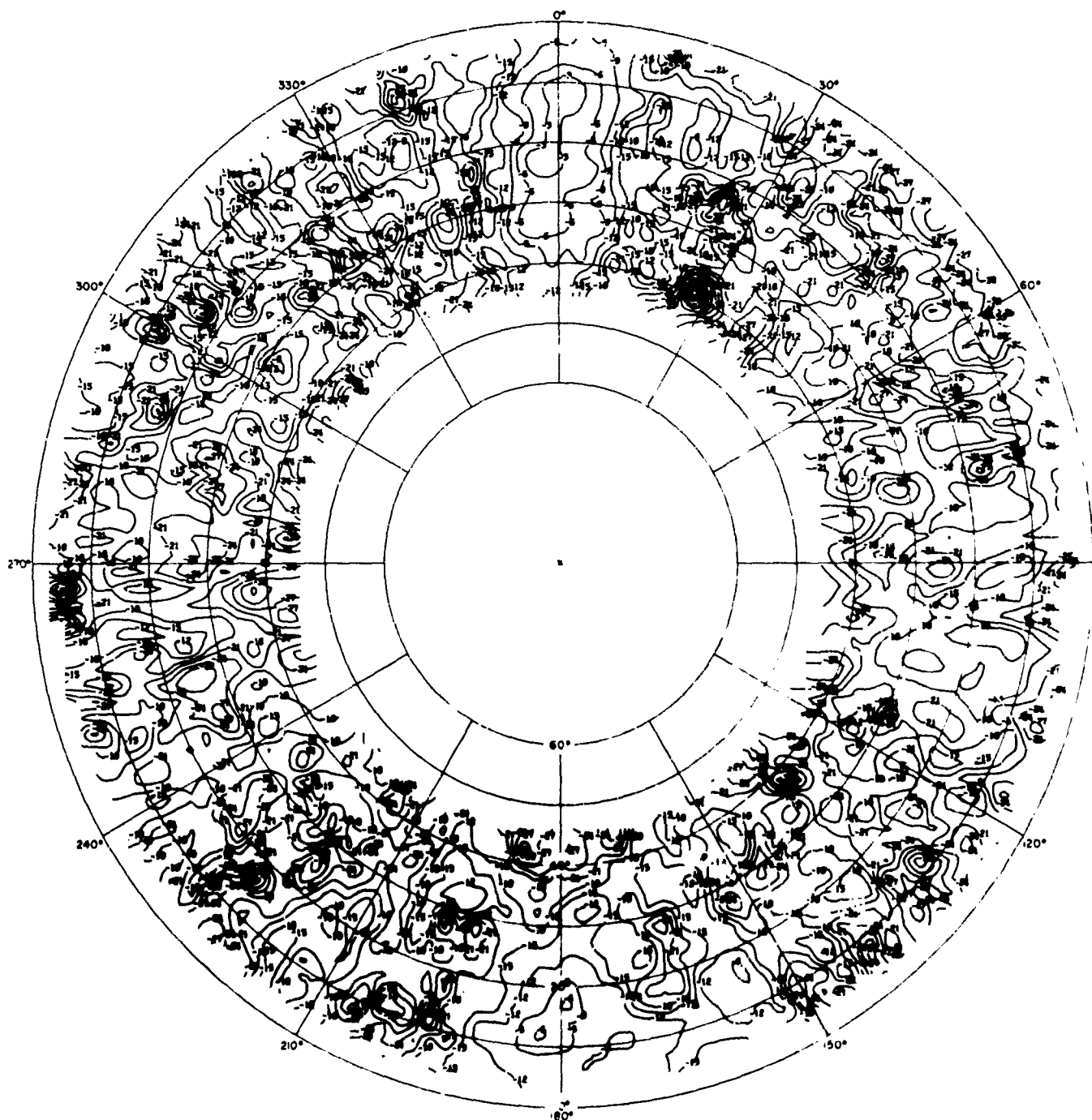


Fig. B. 35 San Francisco Feed at 25.3 Mc, E_0

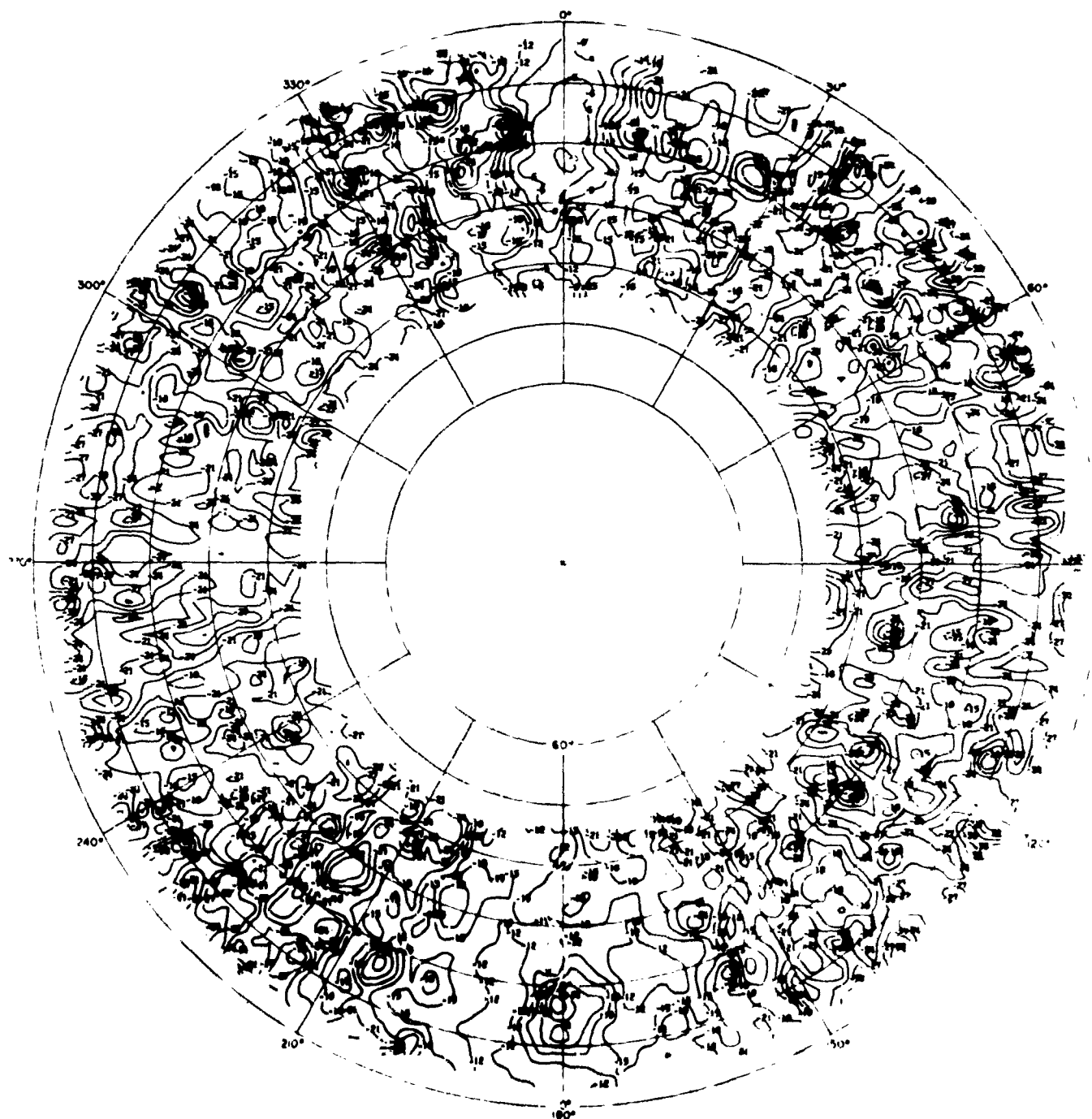


Fig. B. 36 San Francisco Feed at 30.0 Mc. F_{ij}

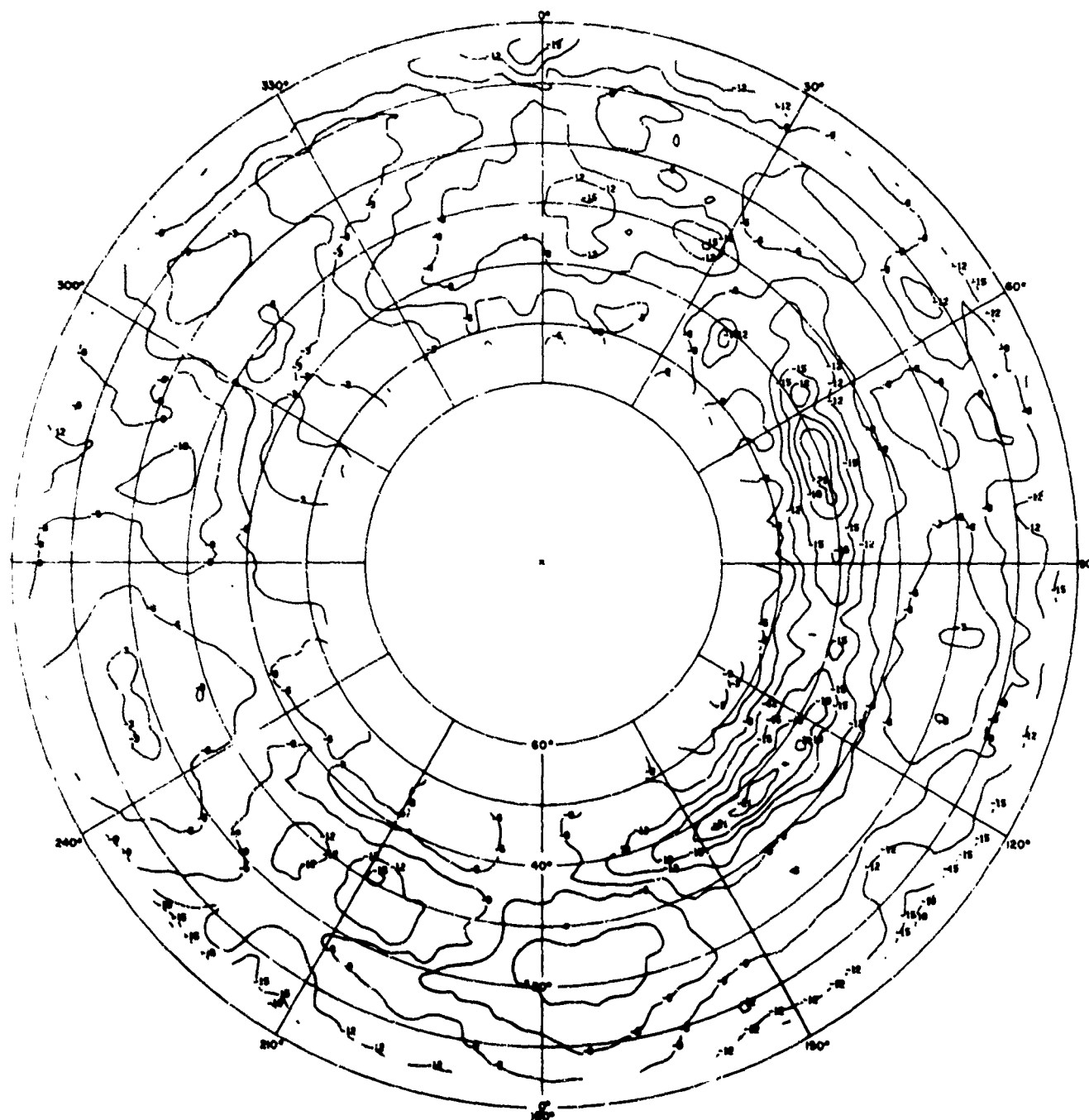


Fig. B. 37 Lens Excited as Biconical Antenna at 3.0 Mc, E_0

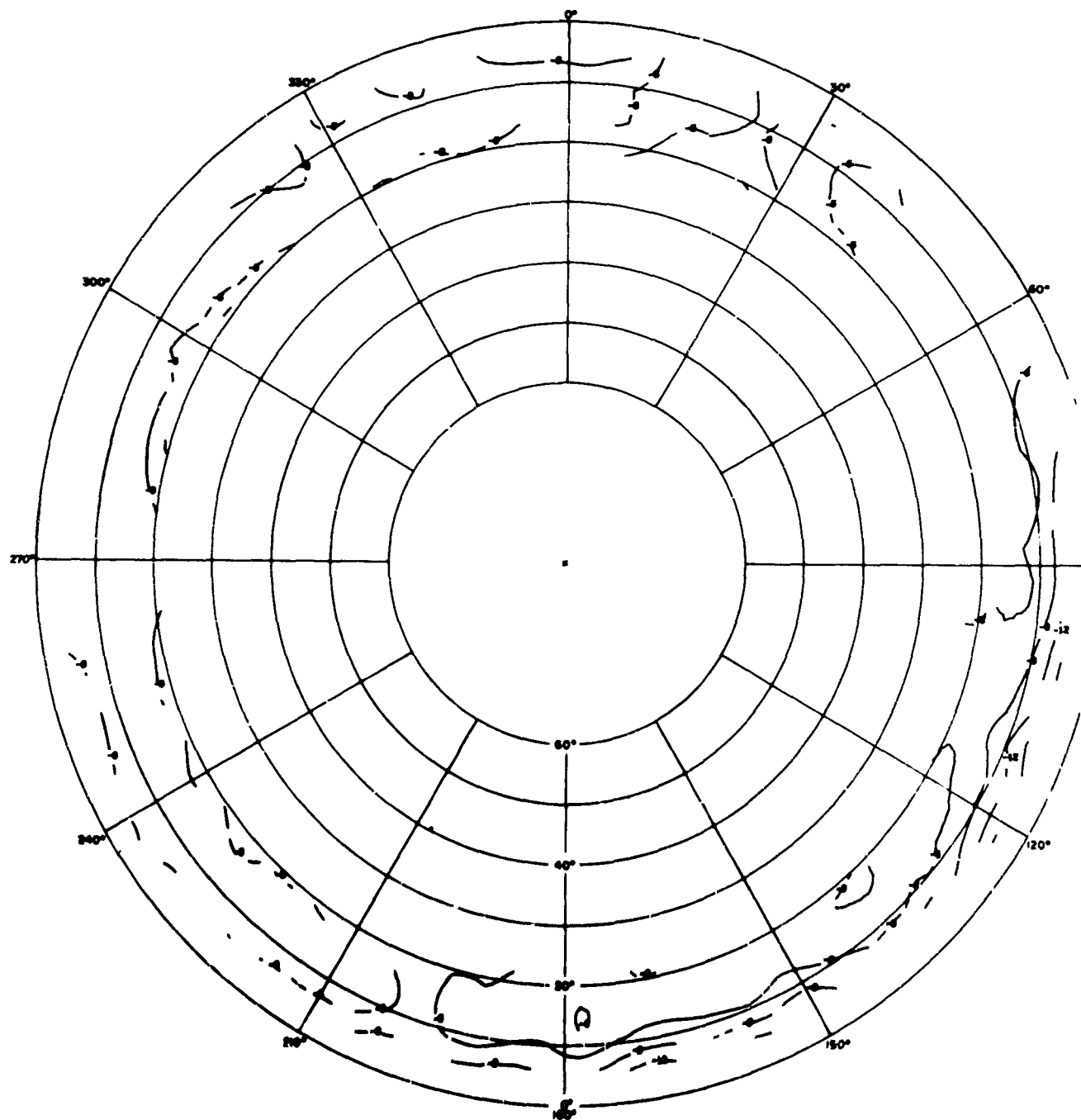
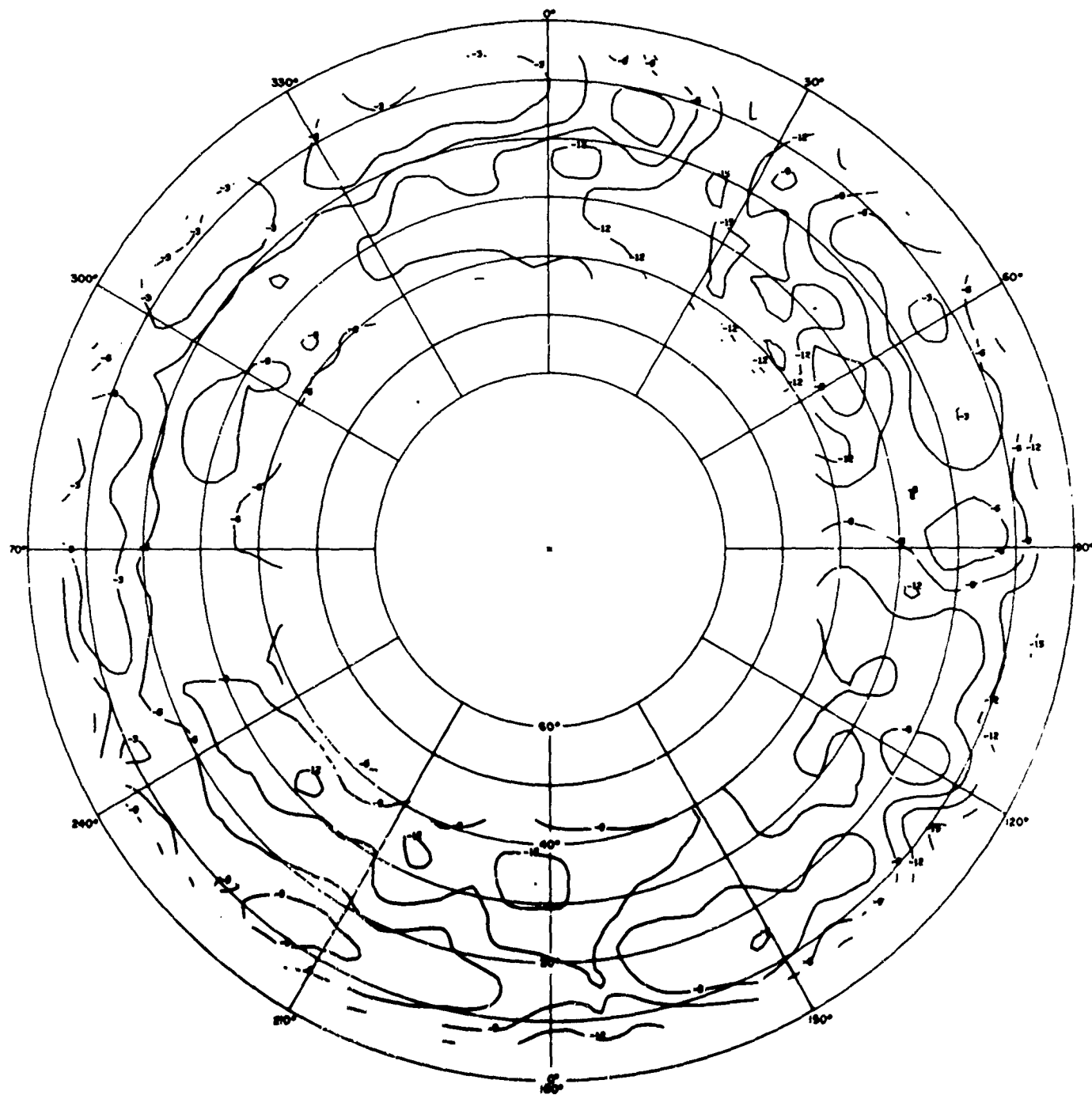


Fig. B. 38 Lens Excited as Biconical Antenna at 5.6 Mc, E_0



Fib. B. 39 Lens Excited as Biconical Antenna at 9.1 Mc, E_θ

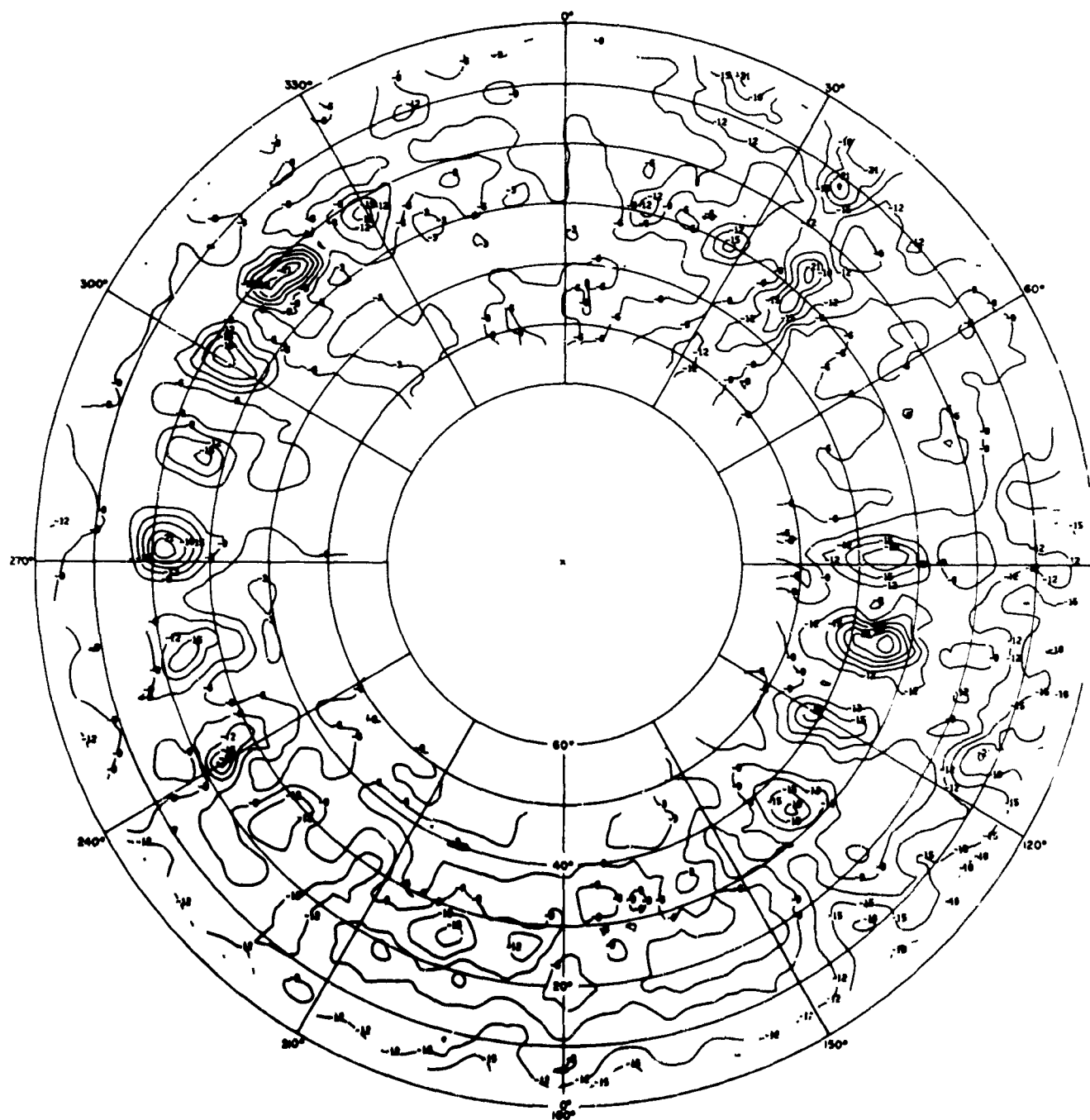
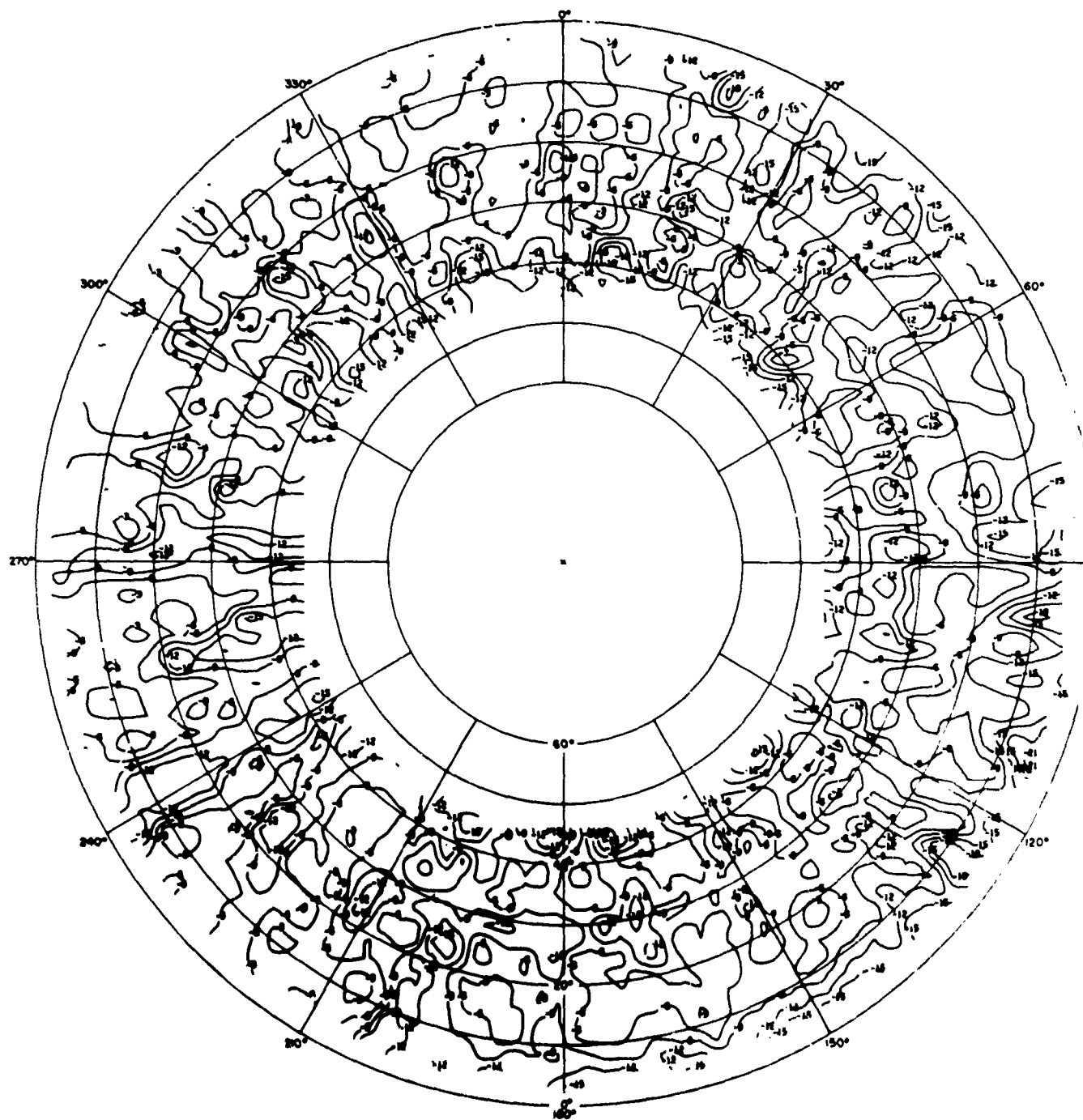


Fig. B. 40 Lens Exc'ed as Biconical Antenna at 11.8 Mc, E_{θ}



Fig. B. 41 Lens Excited as Biconical Antenna at 15.3 Mc, E_{θ}



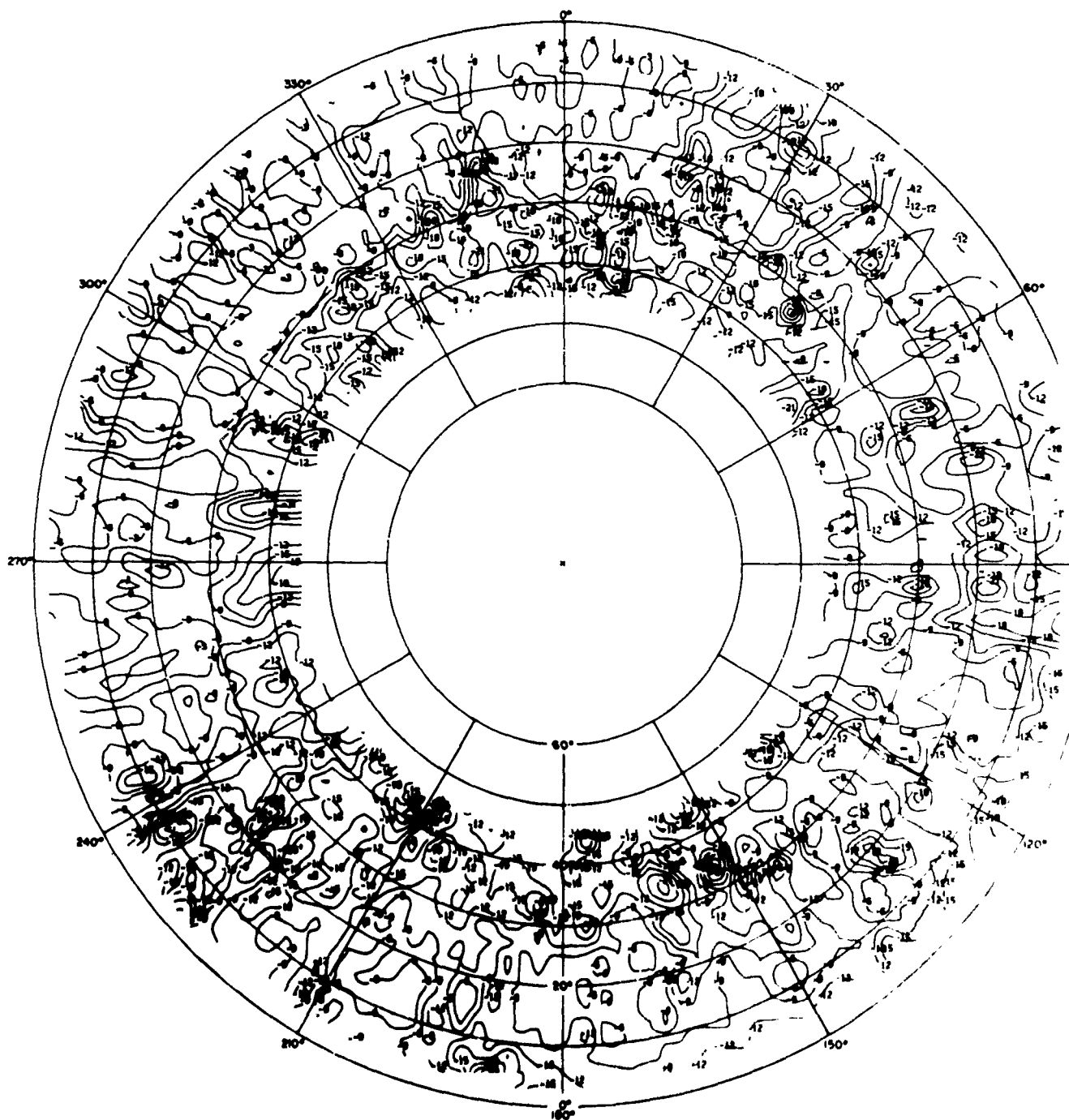


Fig. B. 44 Lens Excited as Biconical Antenna at 30 Mc, E_θ

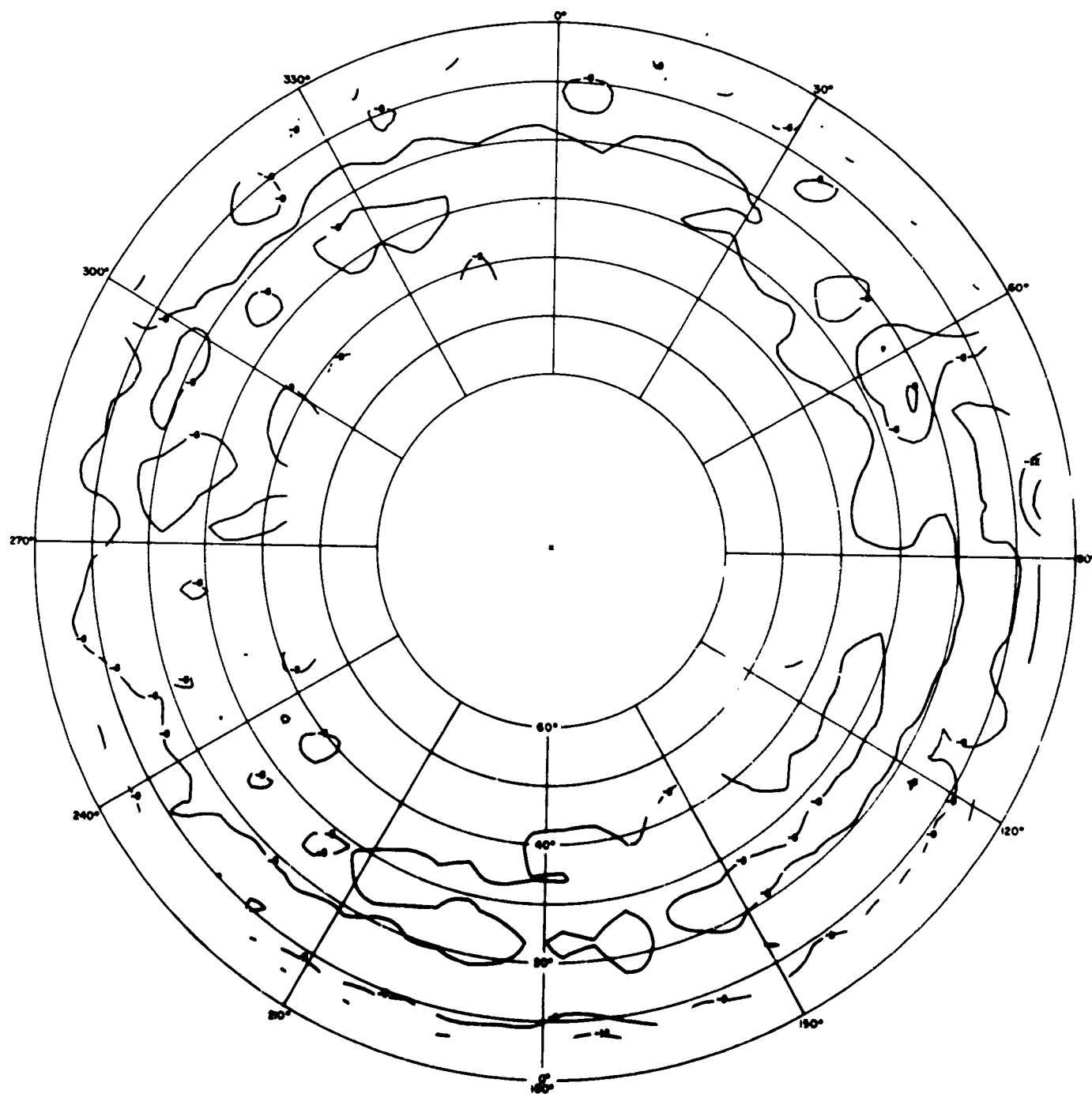


Fig. B. 45 NRL Monopole at 4.1 Mc, E_θ

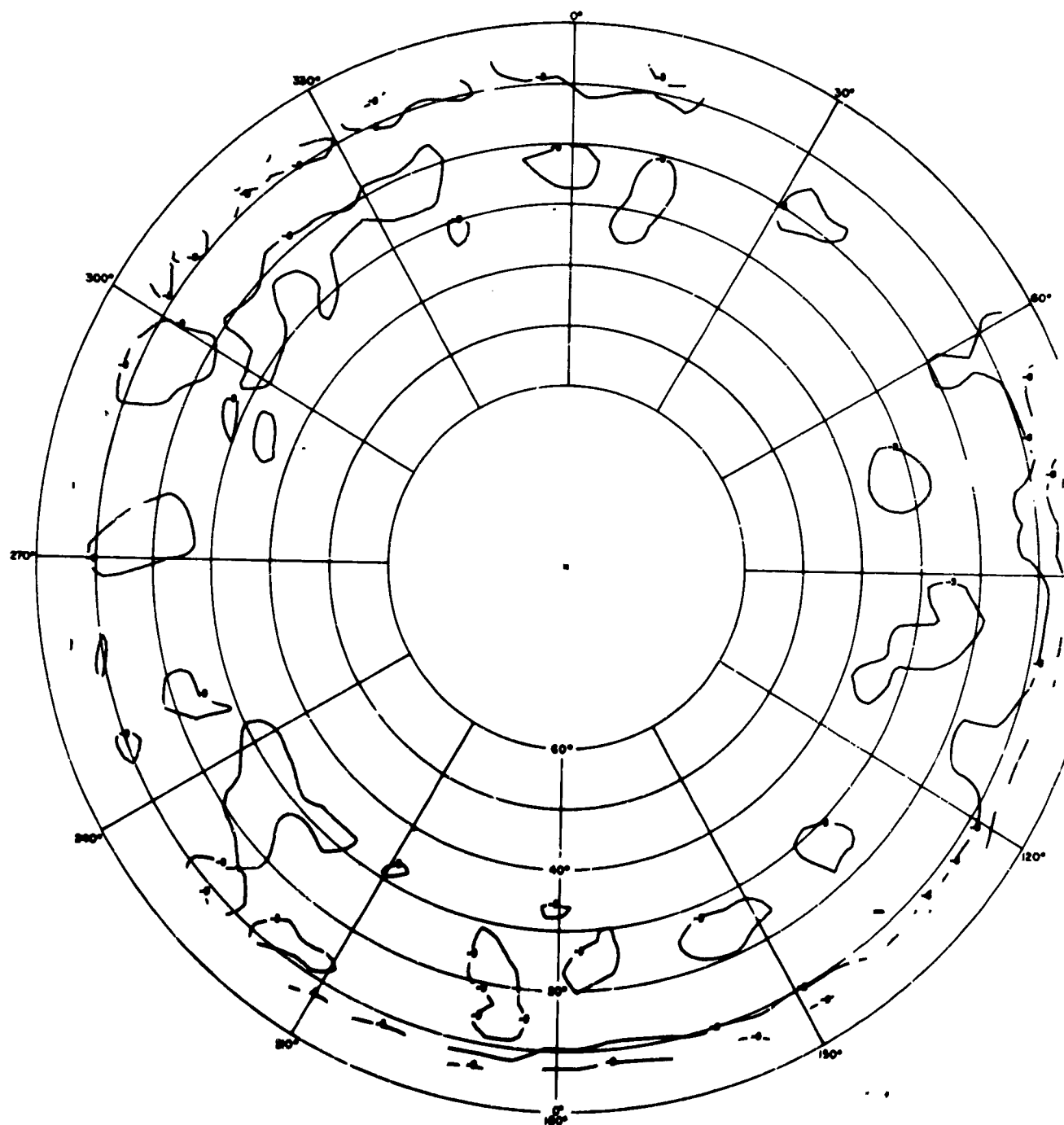


Fig B. 46 NRL Monopole at 5.6 Mc, E_θ

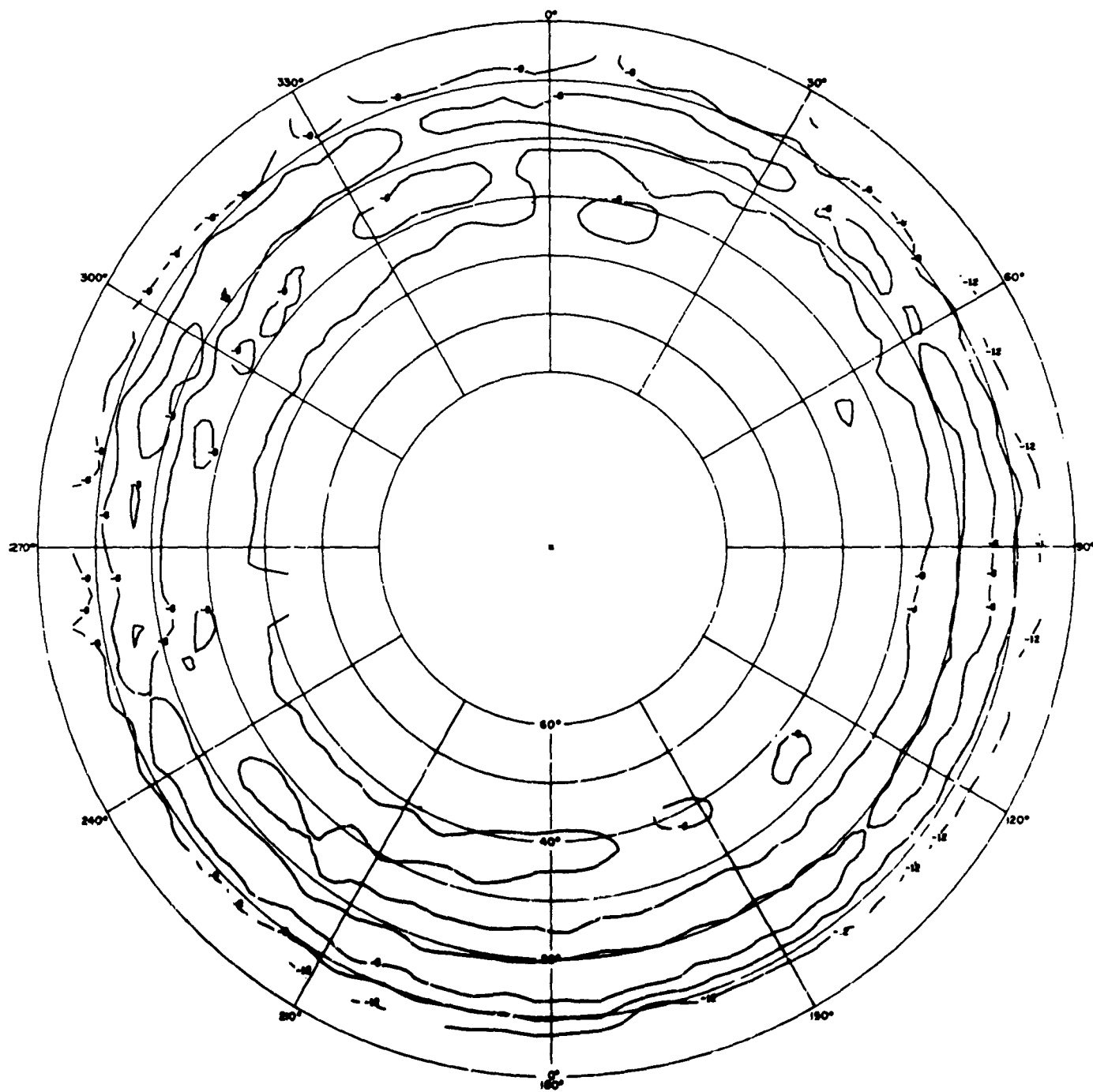


Fig. B. 47 NRL Monopole at 9.1 Mc, E_0

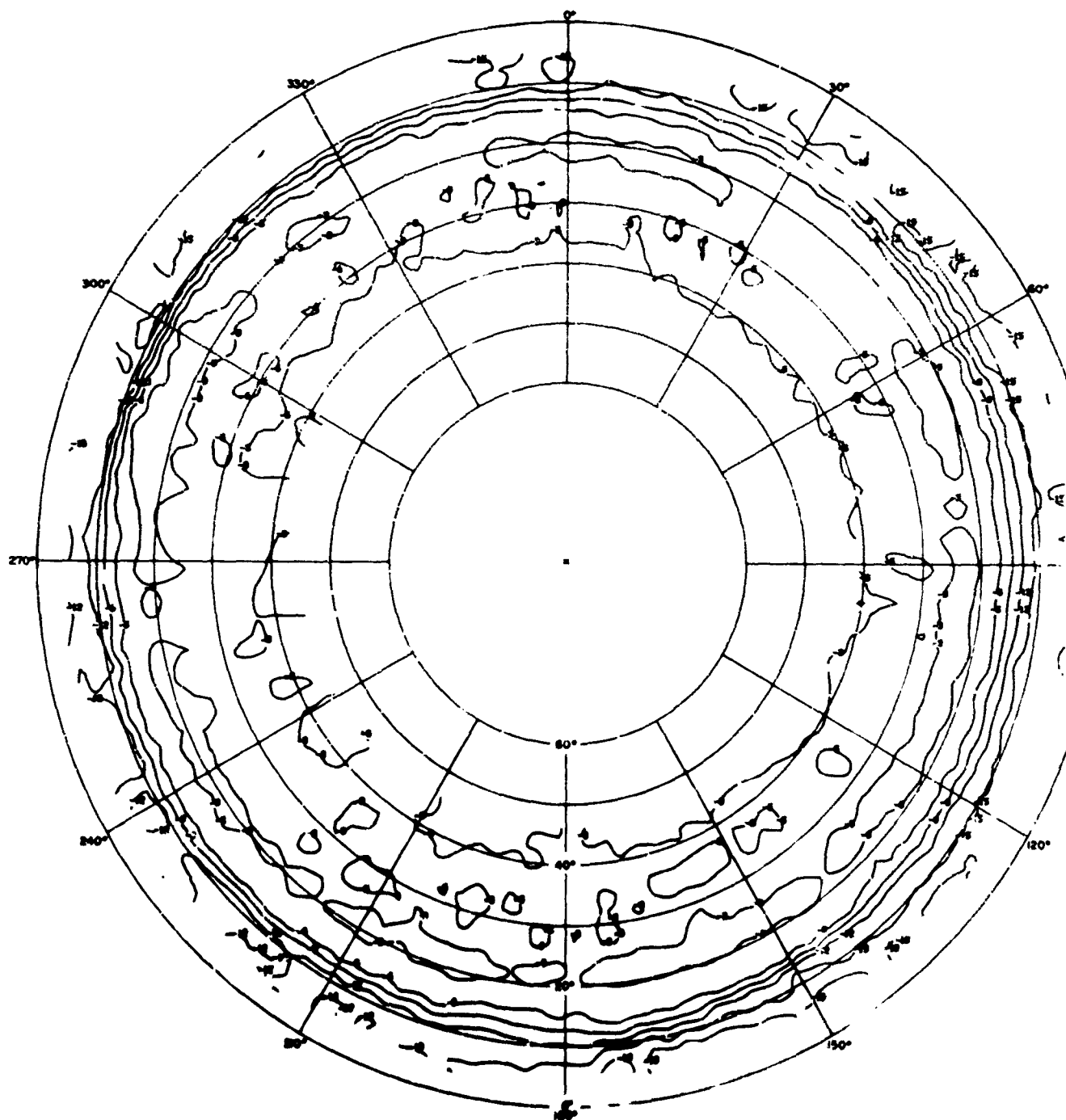


Fig. B. 48 NRL Monopole at 15.3 Mc, E_θ

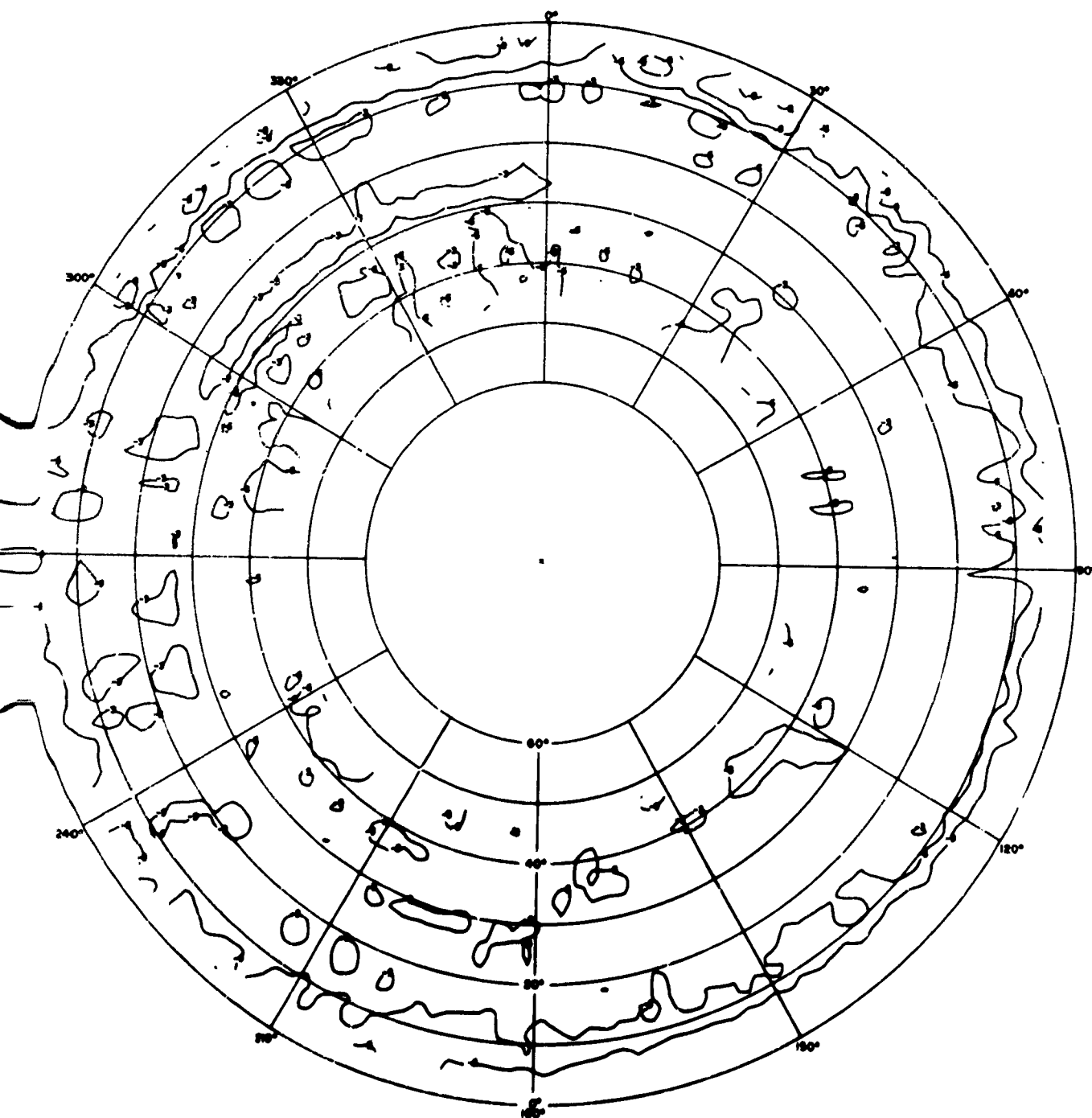


Fig. B. 49 NRL Monopole at 21.5 Mc, E_0

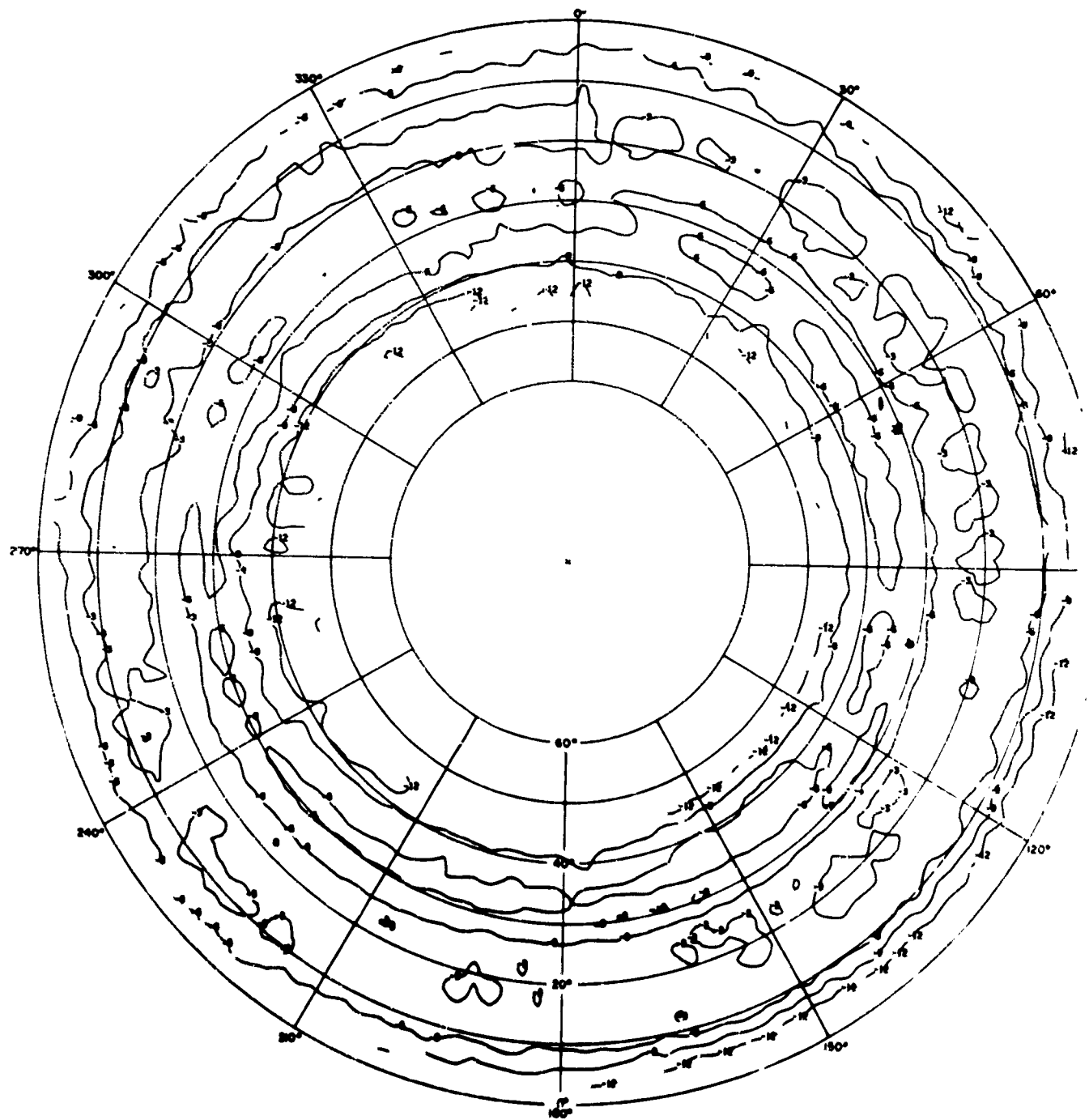


Fig. B. 50 NRL Monopole at 25.3 Mc, E_0

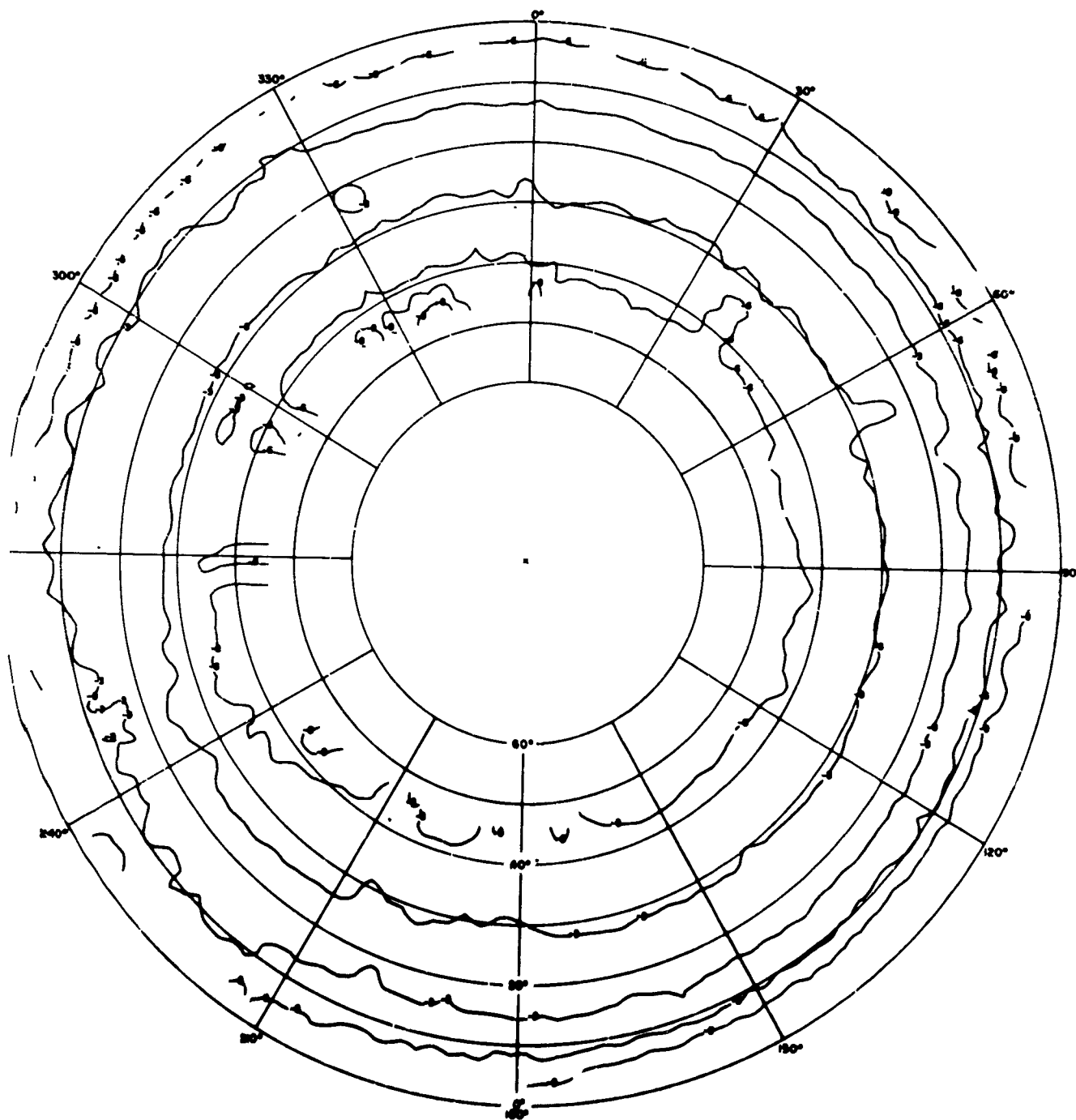


Fig. B. 51 NRL Monopole at 30.0 Mc, E_{θ}

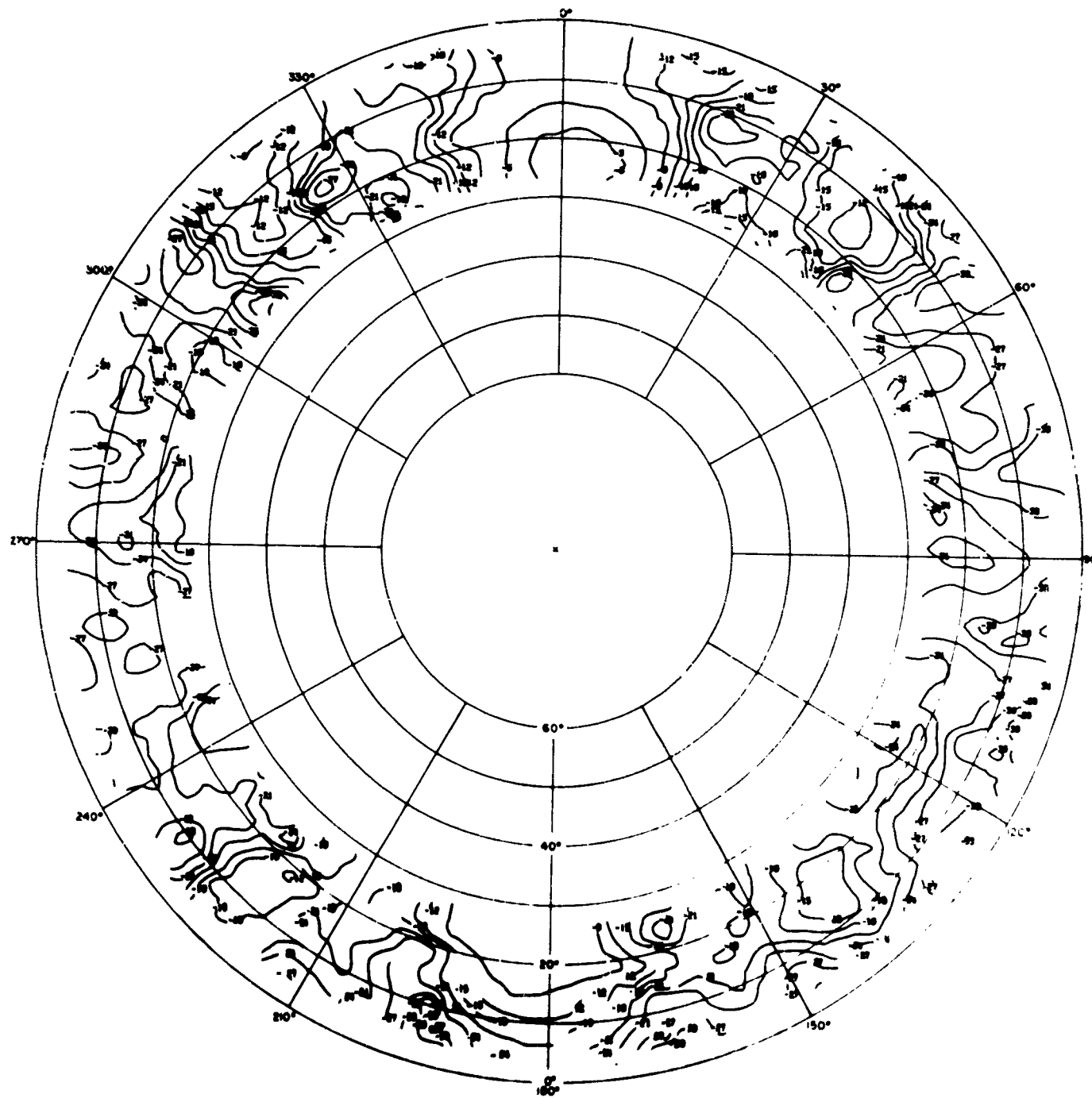


Fig. B.52 Rhombic 4A at 4.1 Mc, E_{ϕ}

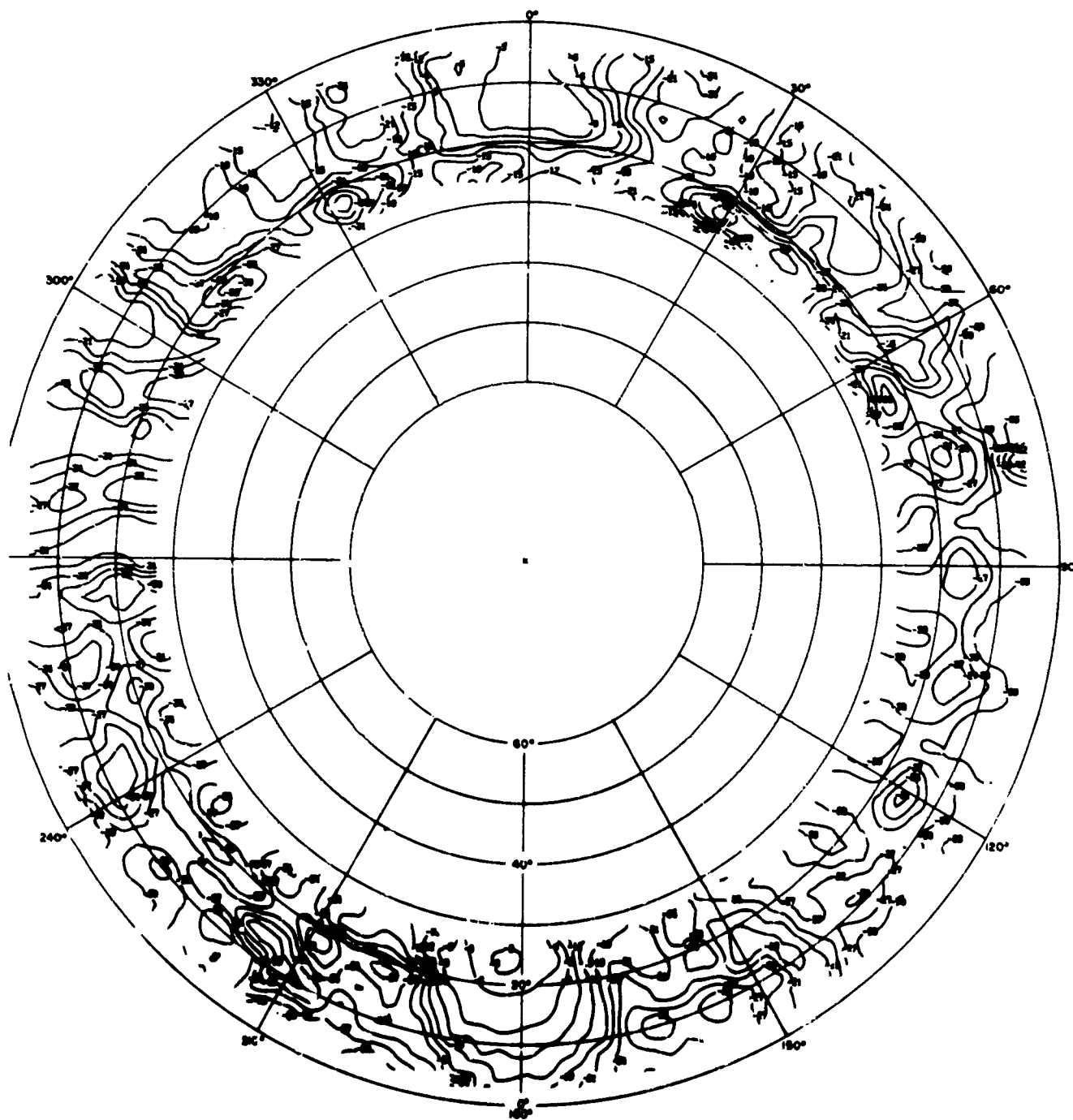


Fig. B.53 Rhombic 4A at 5.6 Mc, E_ϕ

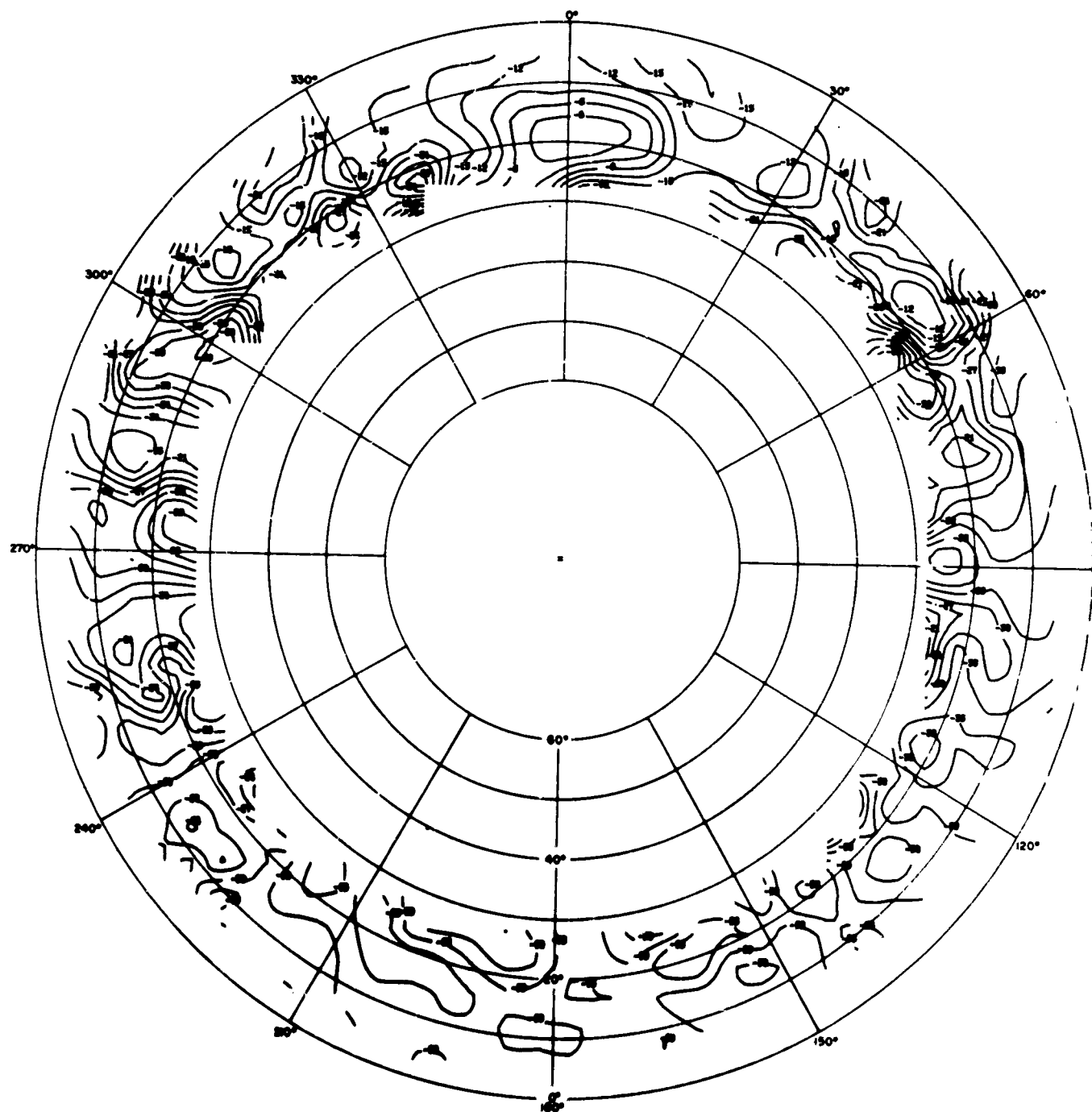


Fig. B. 54 Rhombic 4B at 5.6 Mc, E_{ϕ}

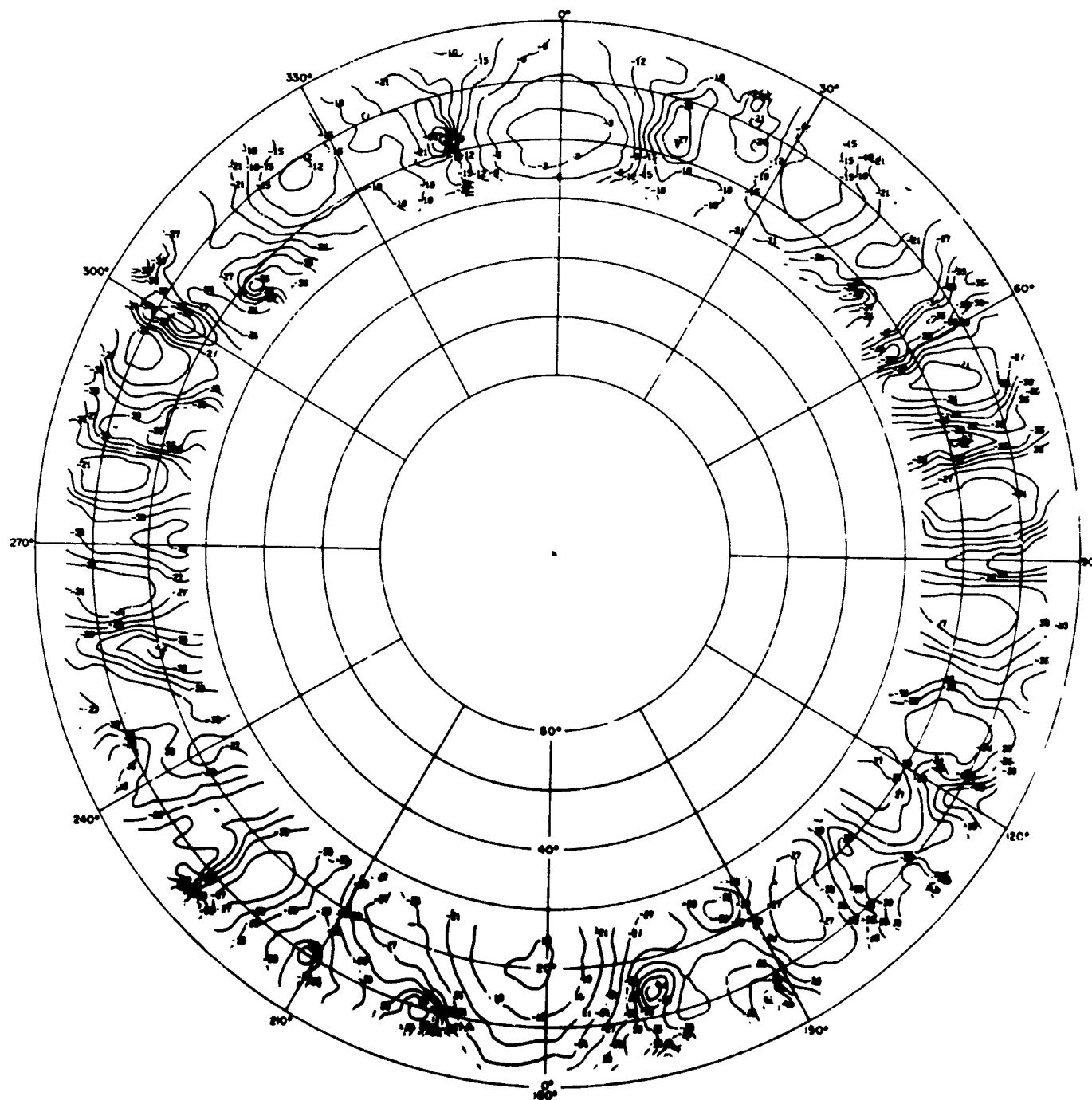


Fig. B.55 Rhombic 4B at 9.1 Mc, E_ϕ

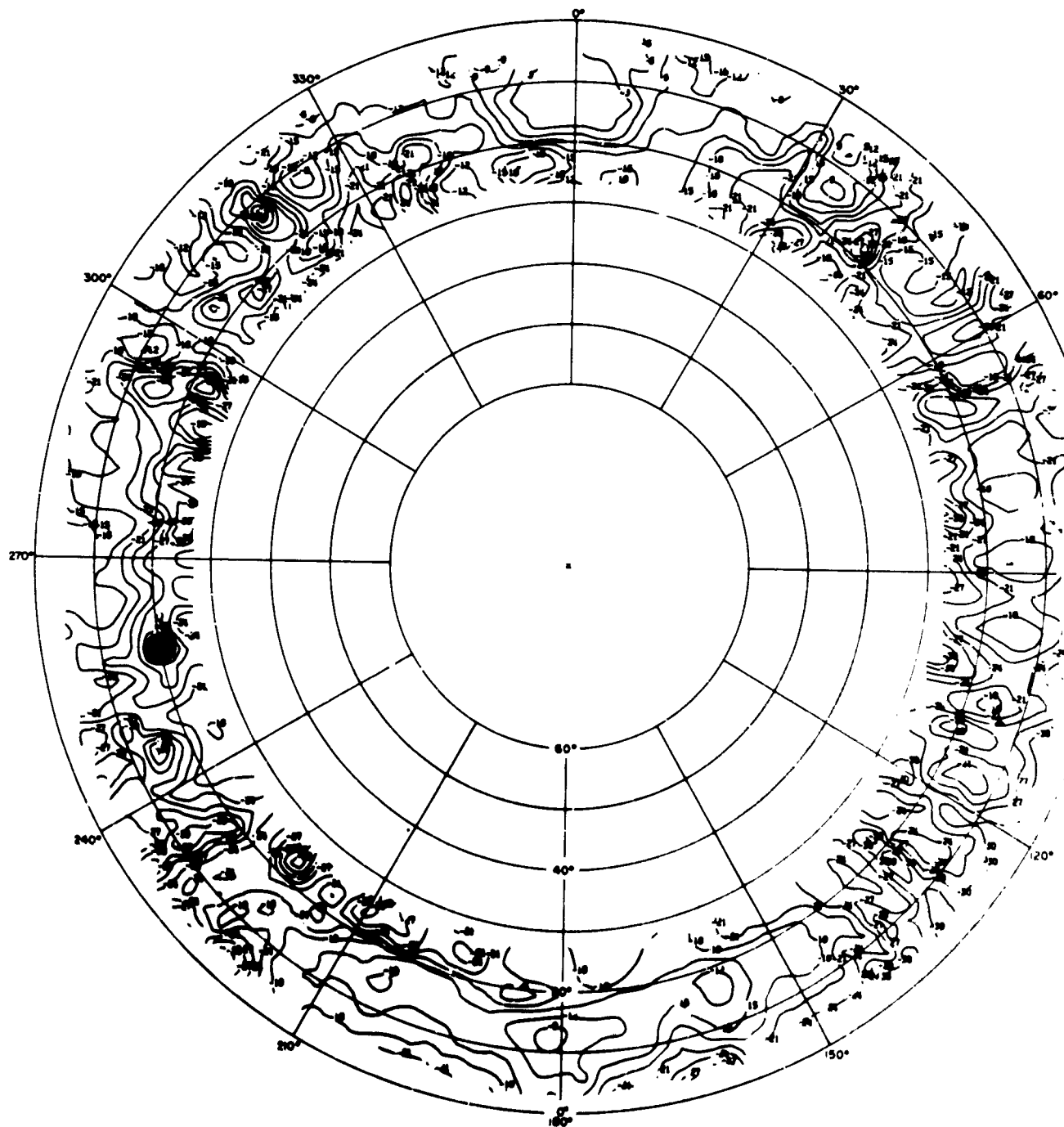


Fig. B. 56 Rhombic 4B at 15.3 Mc, E_{ϕ}

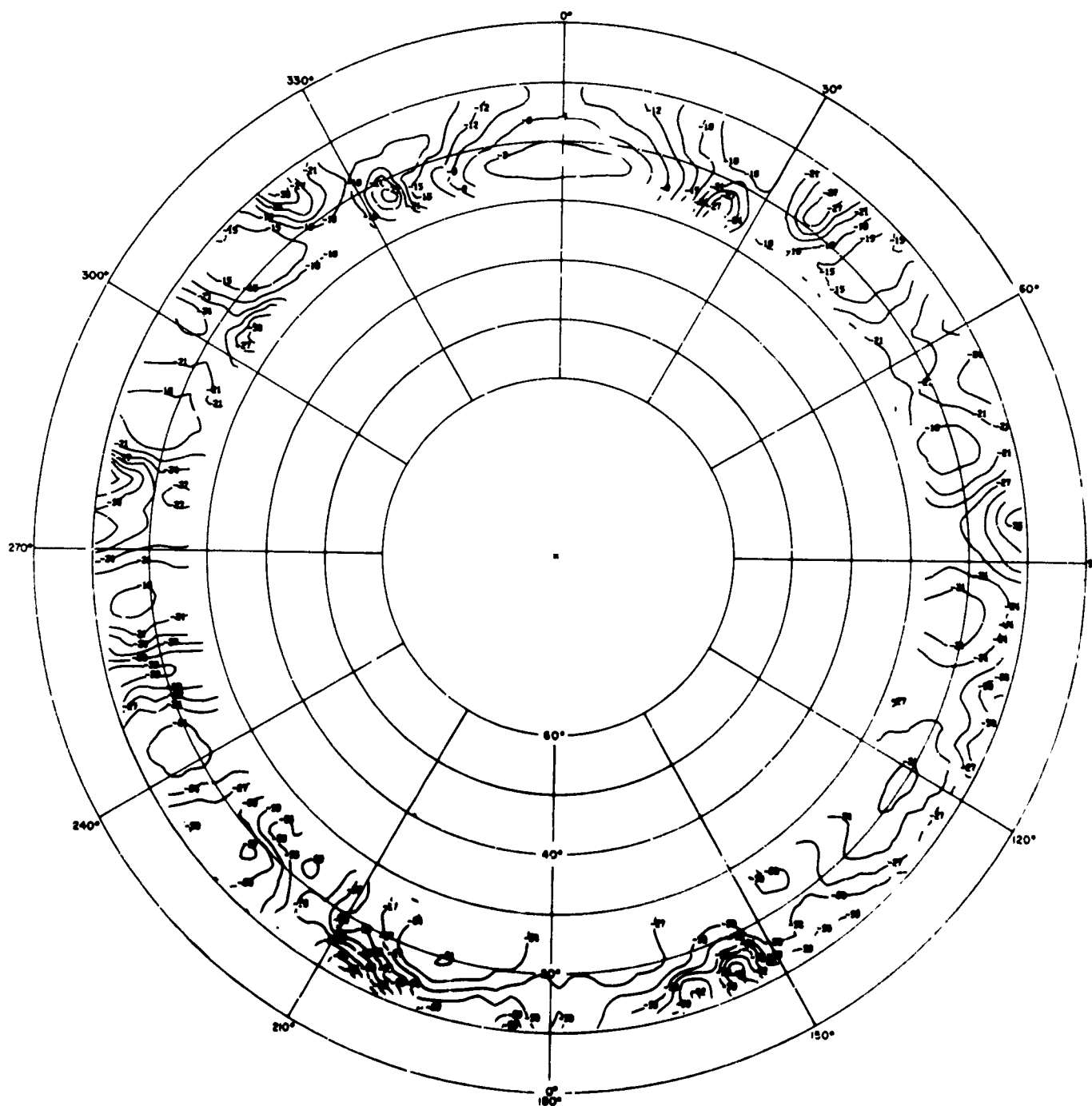


Fig. B.57 Rhombic 4C at 9.1 Mc, E_{ϕ}

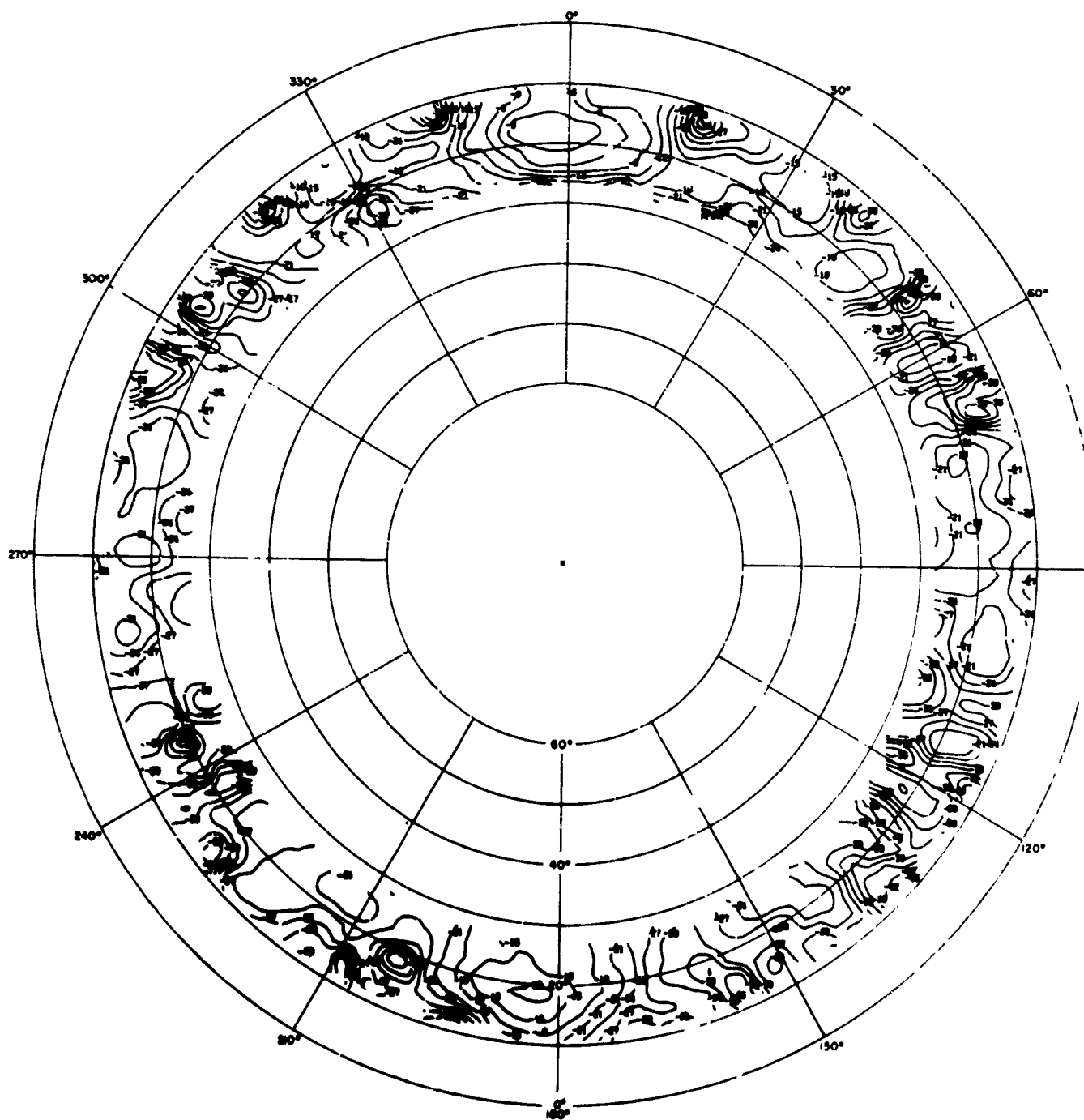


Fig. B. 58 Rhombic 4C at 15.3 Mc, E_{ϕ}

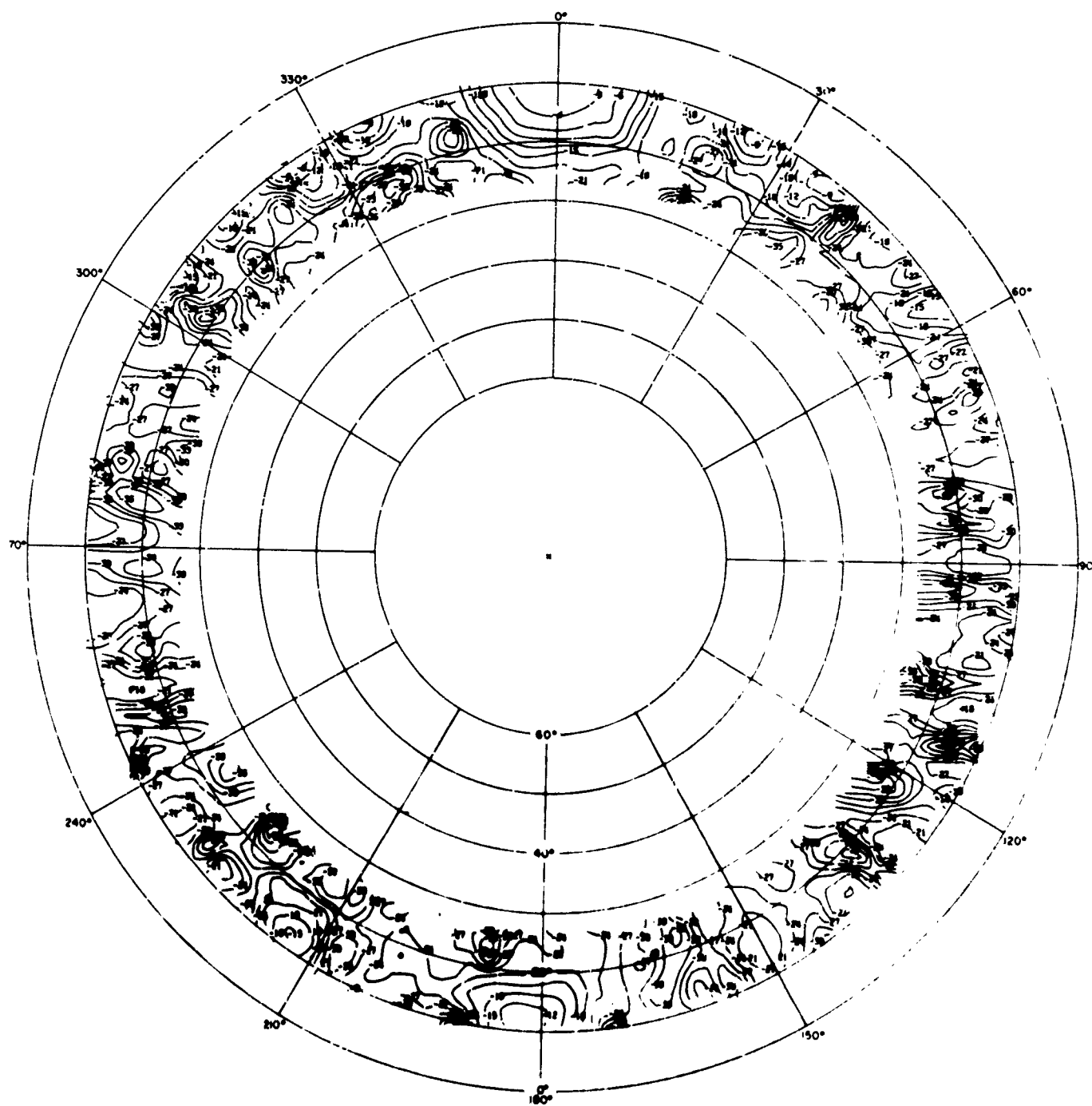


Fig. B. 59 Rhombic 4C at 21.5 Mc, E_{ϕ}

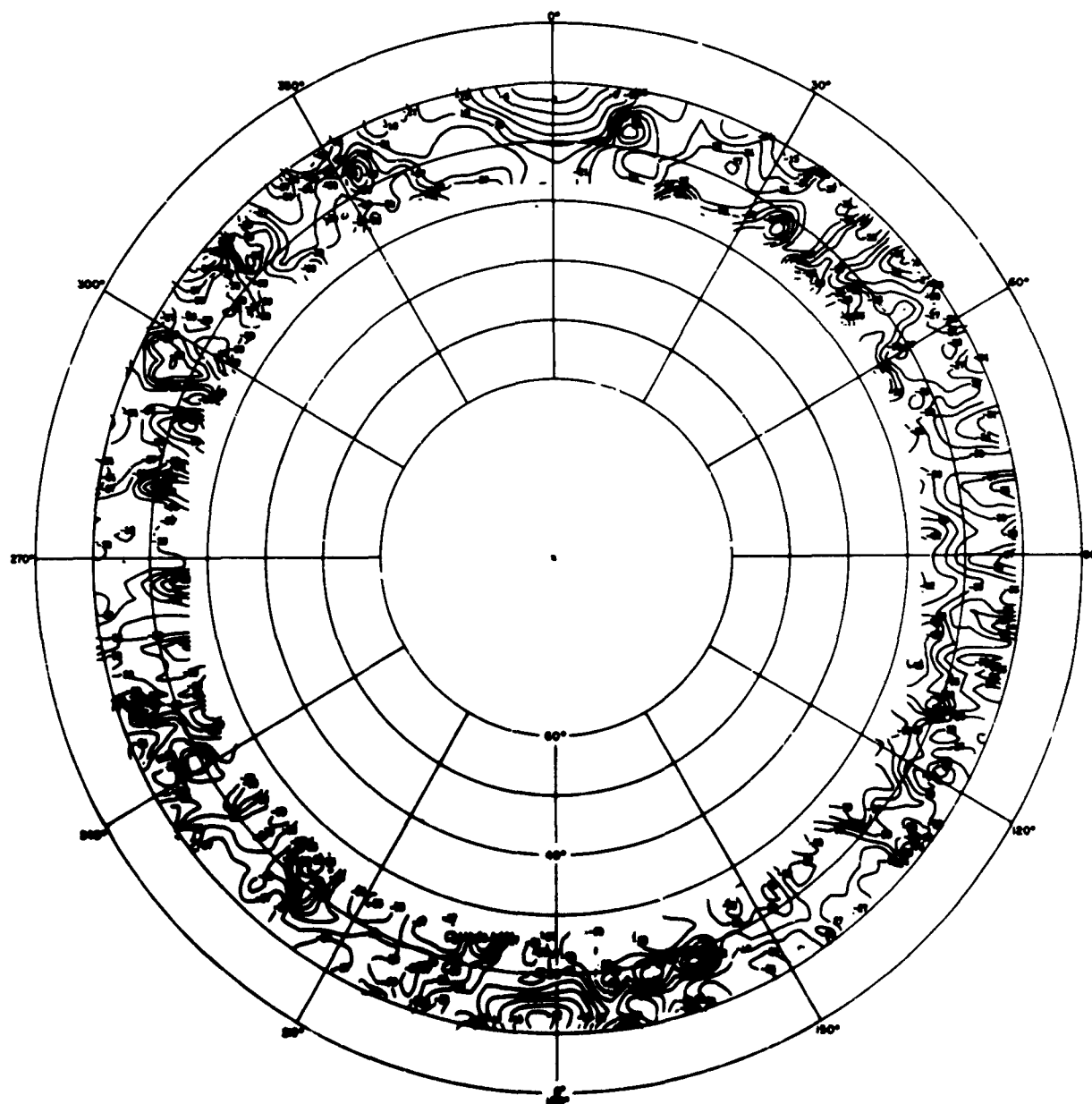


Fig. B. 60 Rhombic 4C at 25.3 Mc, E_p

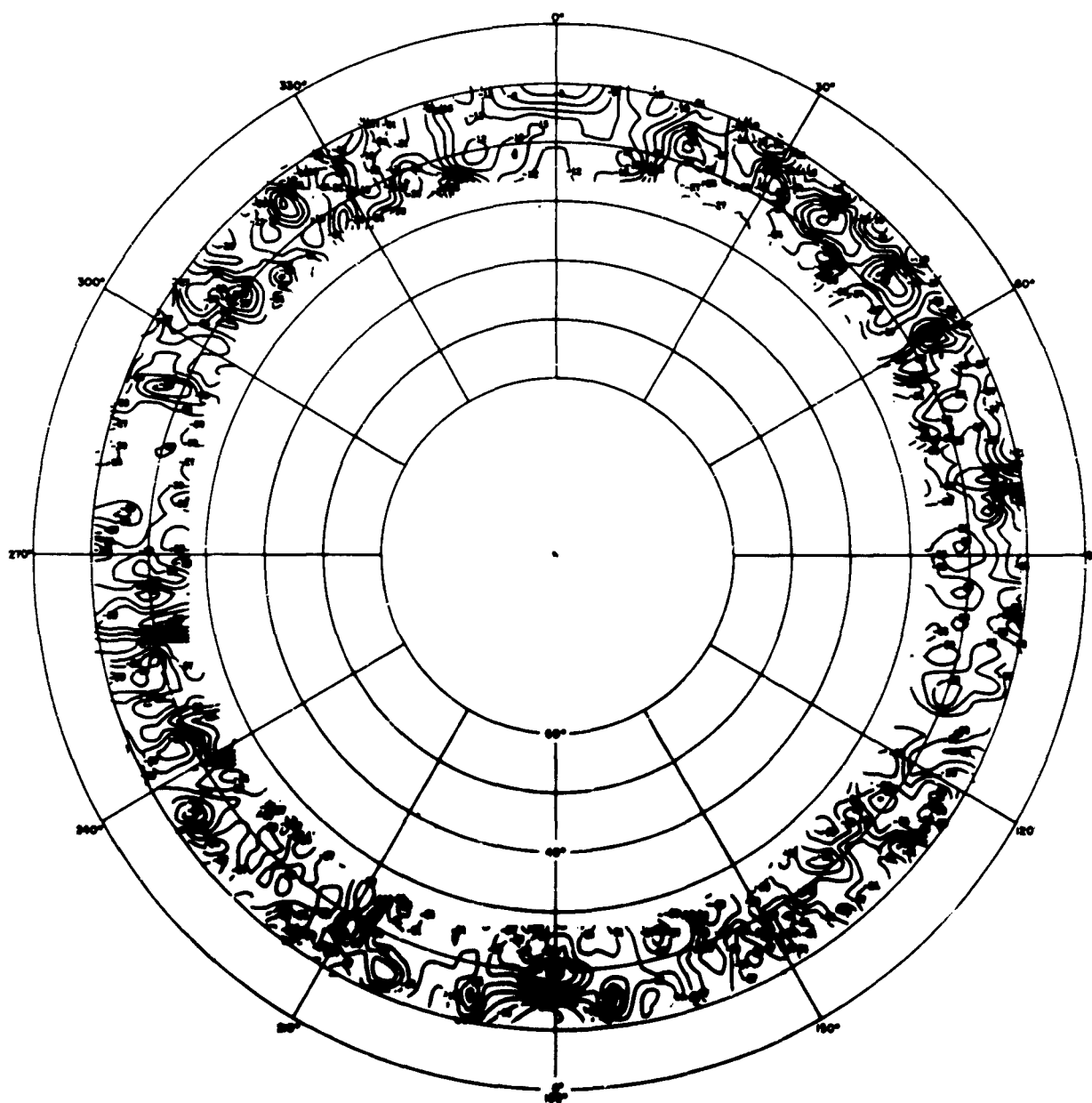


Fig. B. 61 Rhombic 4C at 30.0 Mc, E_{ϕ}

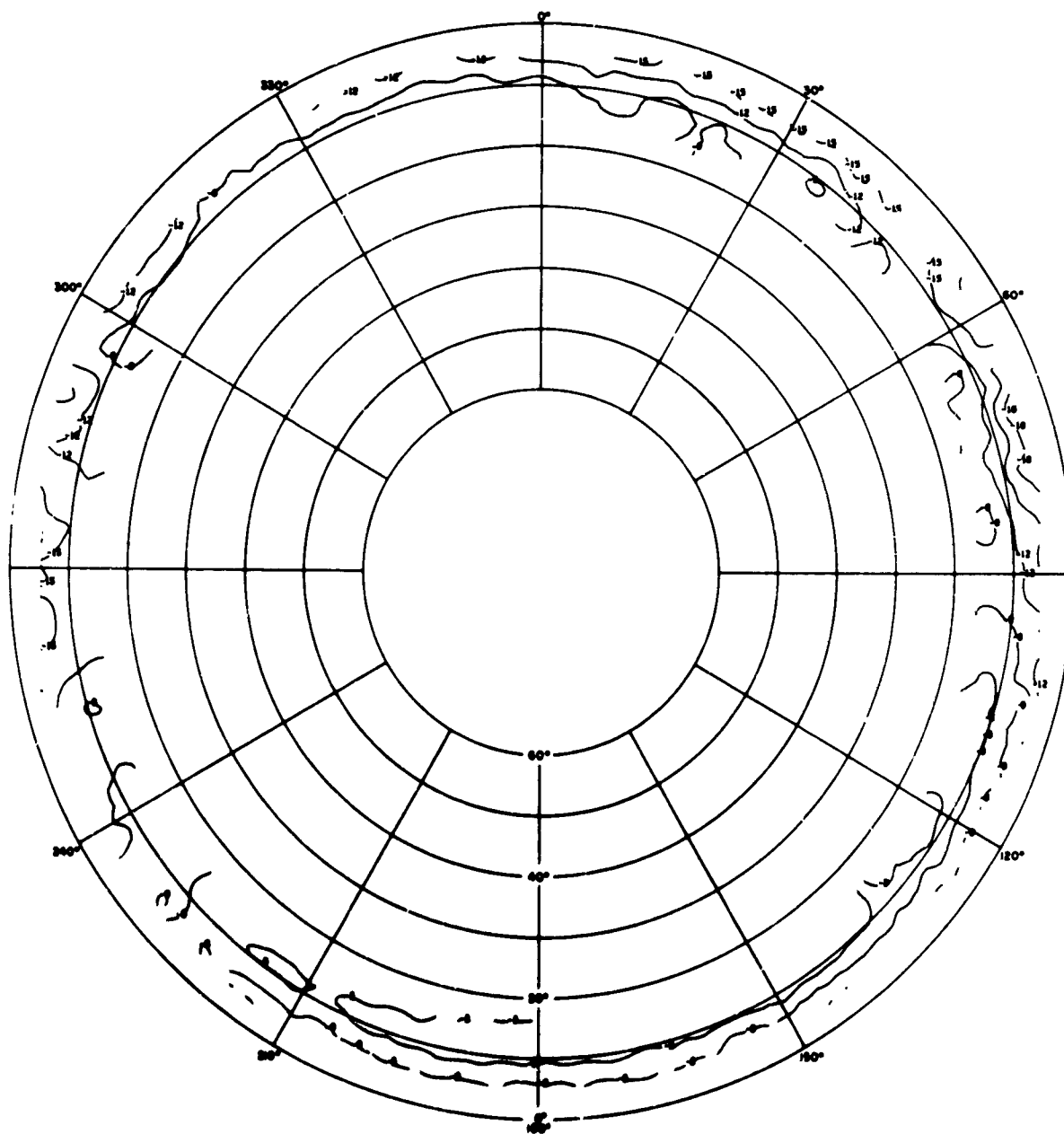


Fig. B.62 Double-Dipole Array at 5.6 Mc, E_0

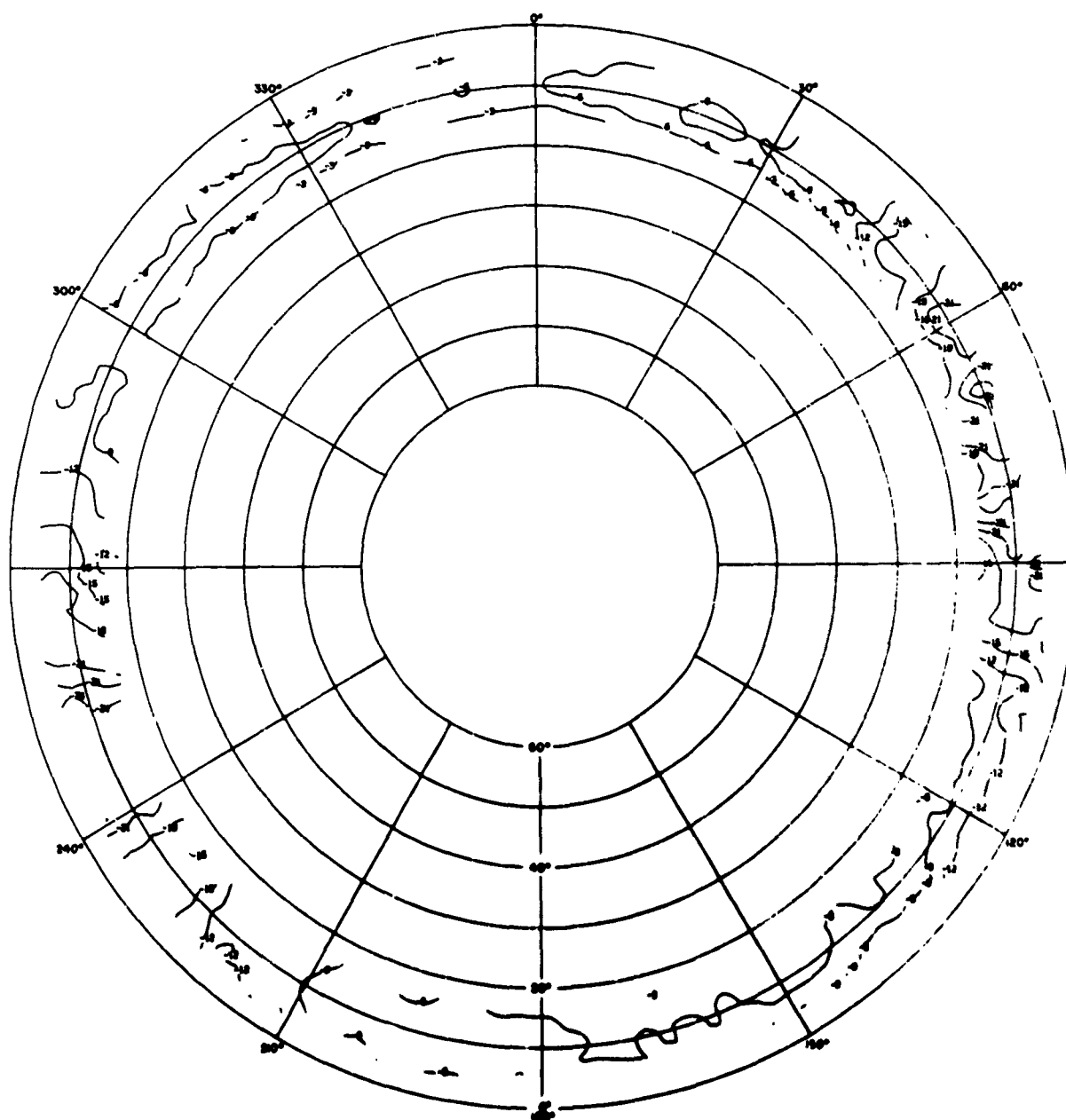


Fig. B.63 Double-Dipole Array at 9.1 Mc, E_0

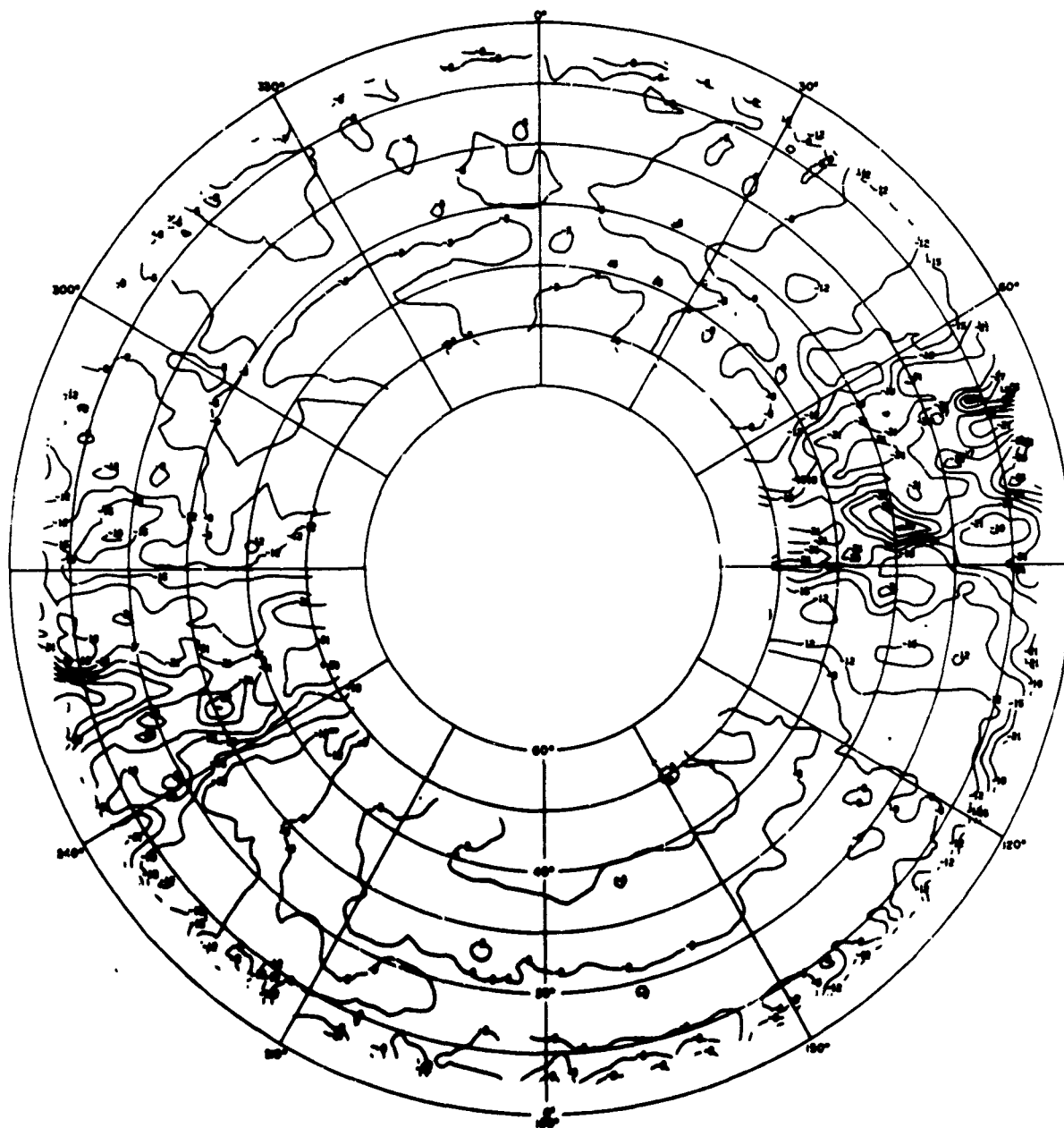


Fig. B. 64 Double-Dipole Array at 11.8 Mc, E_0

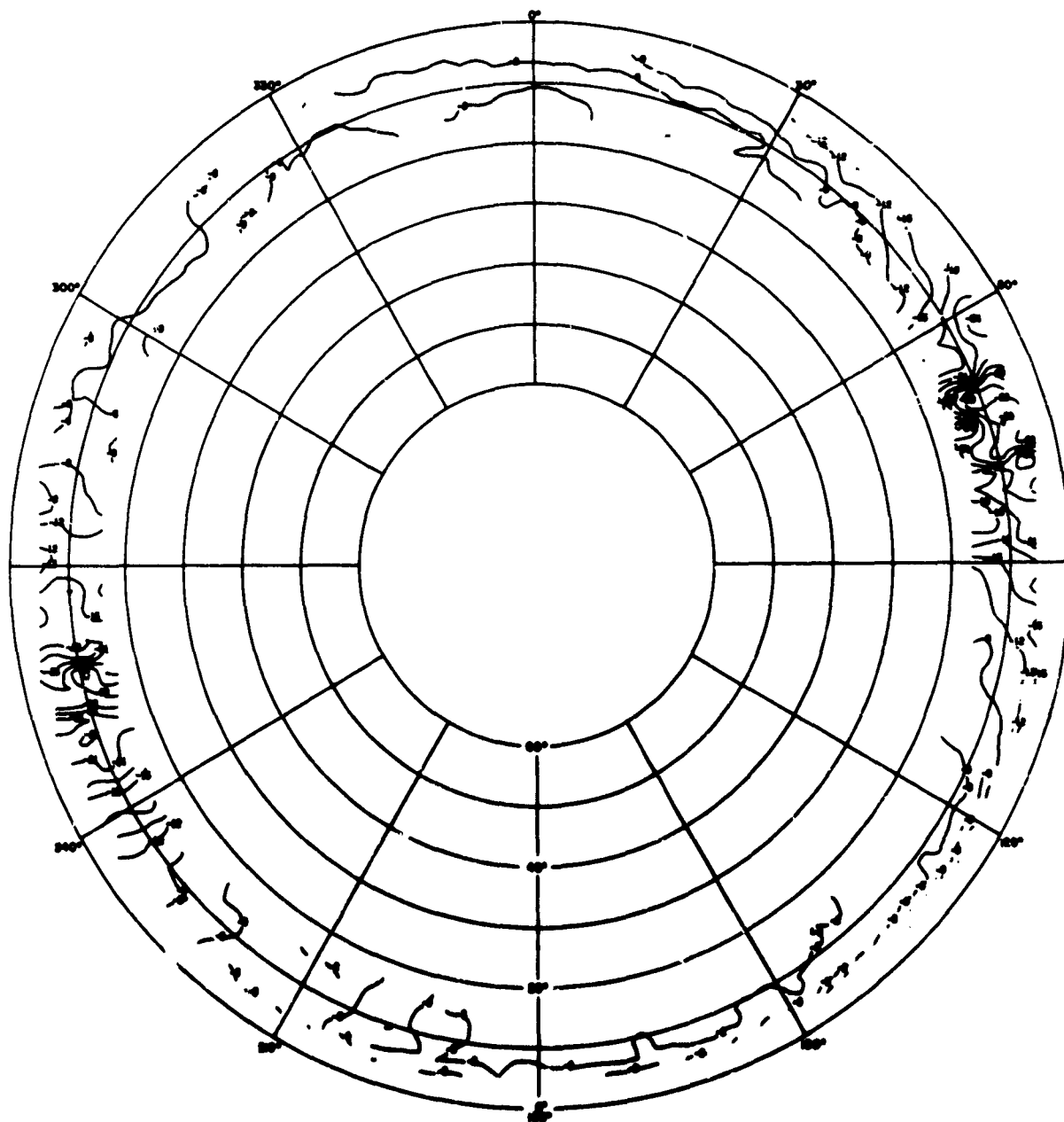


Fig. B.65 Double-Dipole Array at 15.3 Mc, E_0

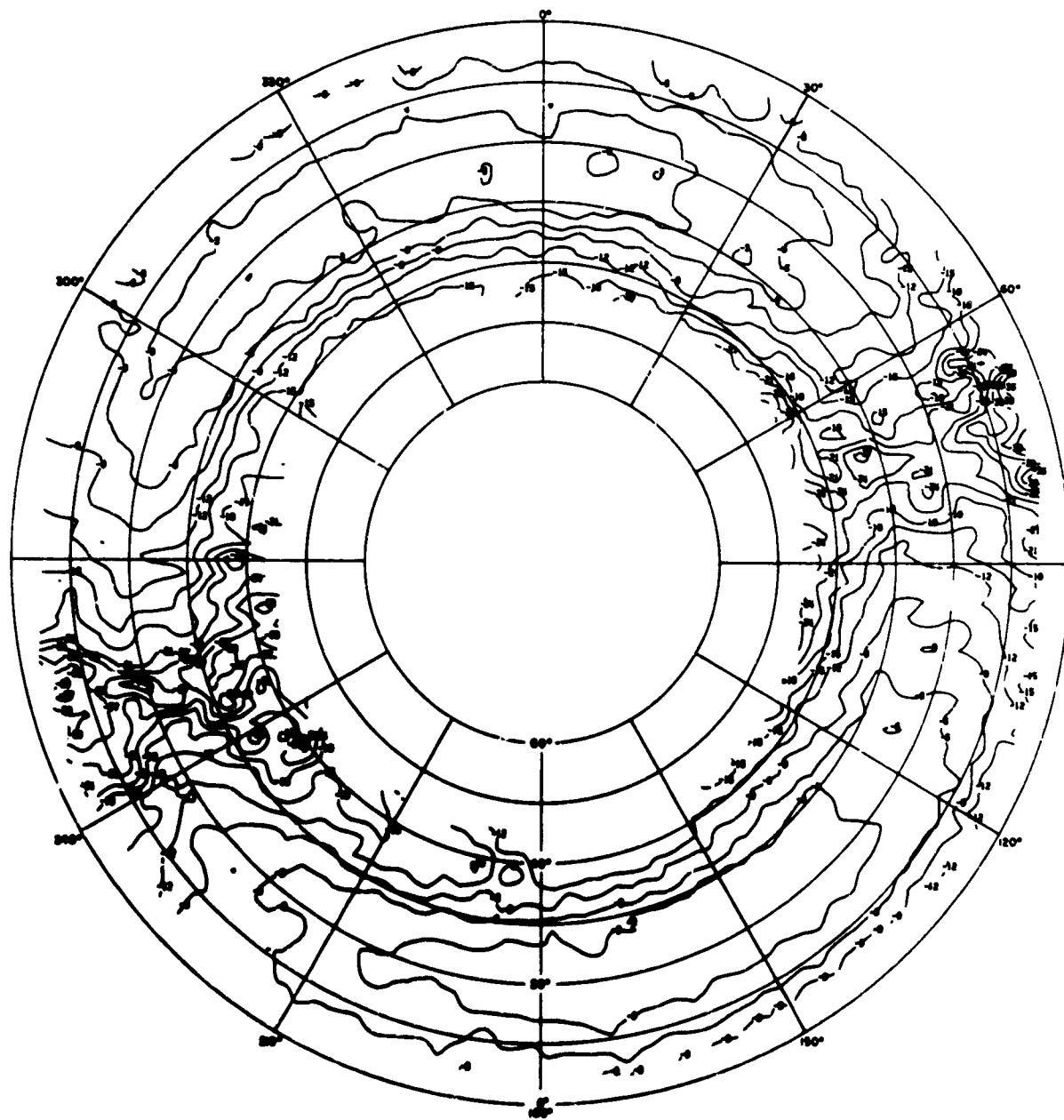


Fig. B. 66 Double-Dipole Array at 21.5 Mc, E_0

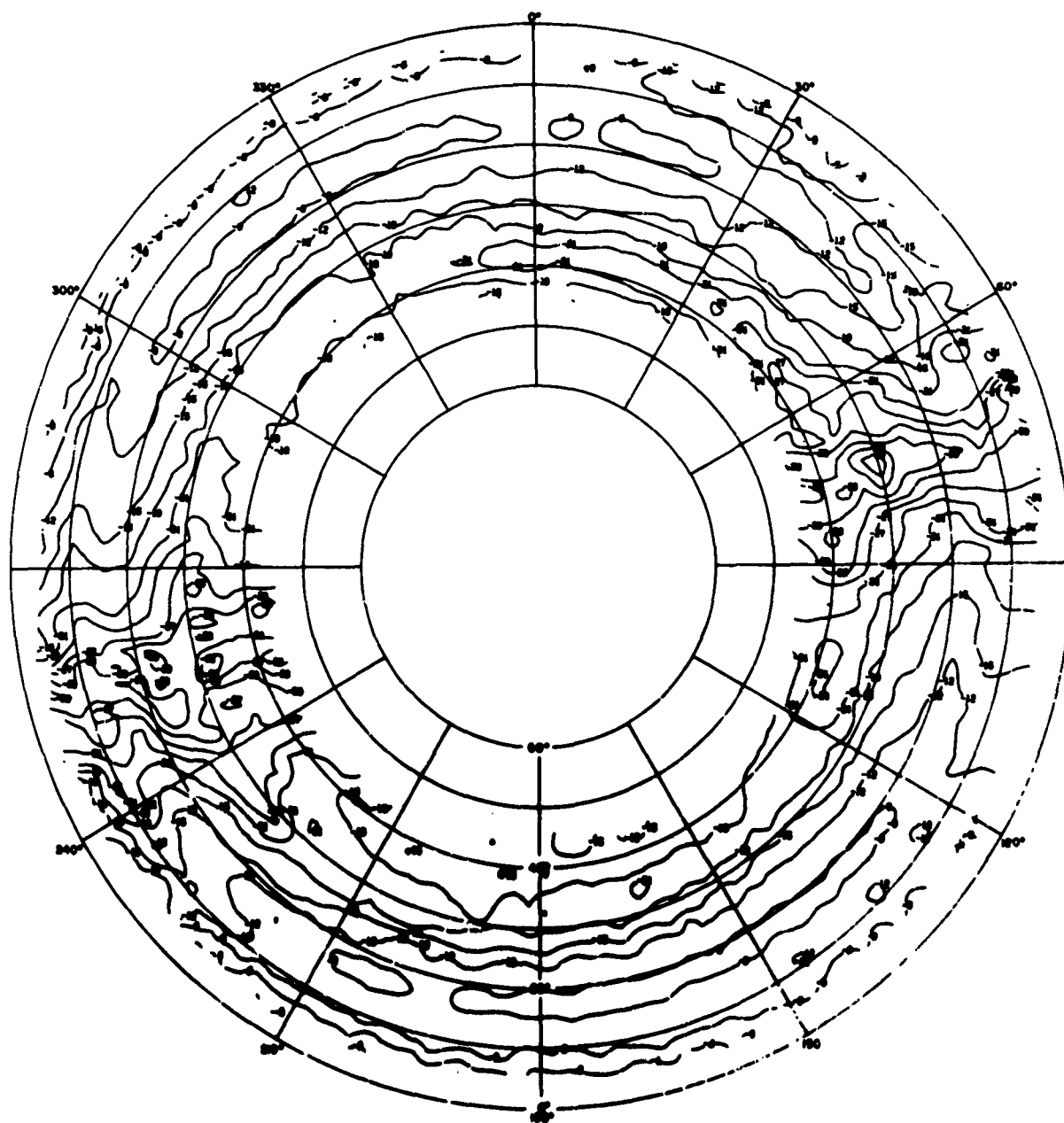


Fig. B.67 Double-Dipole Array at 25.3 Mc, E_0

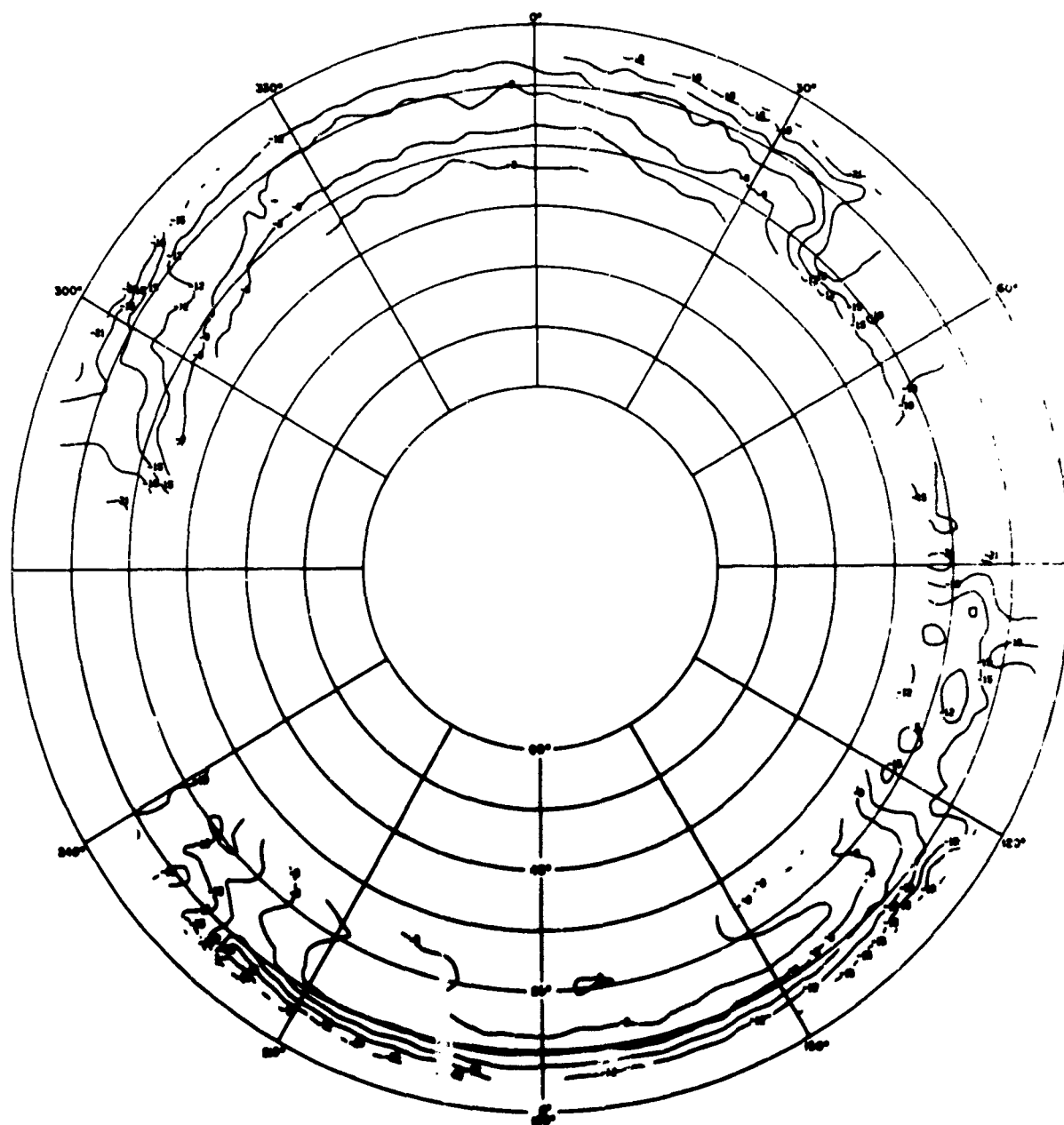


Fig. B.69 Double-Dipole Array at 5.6 Mc, E_p

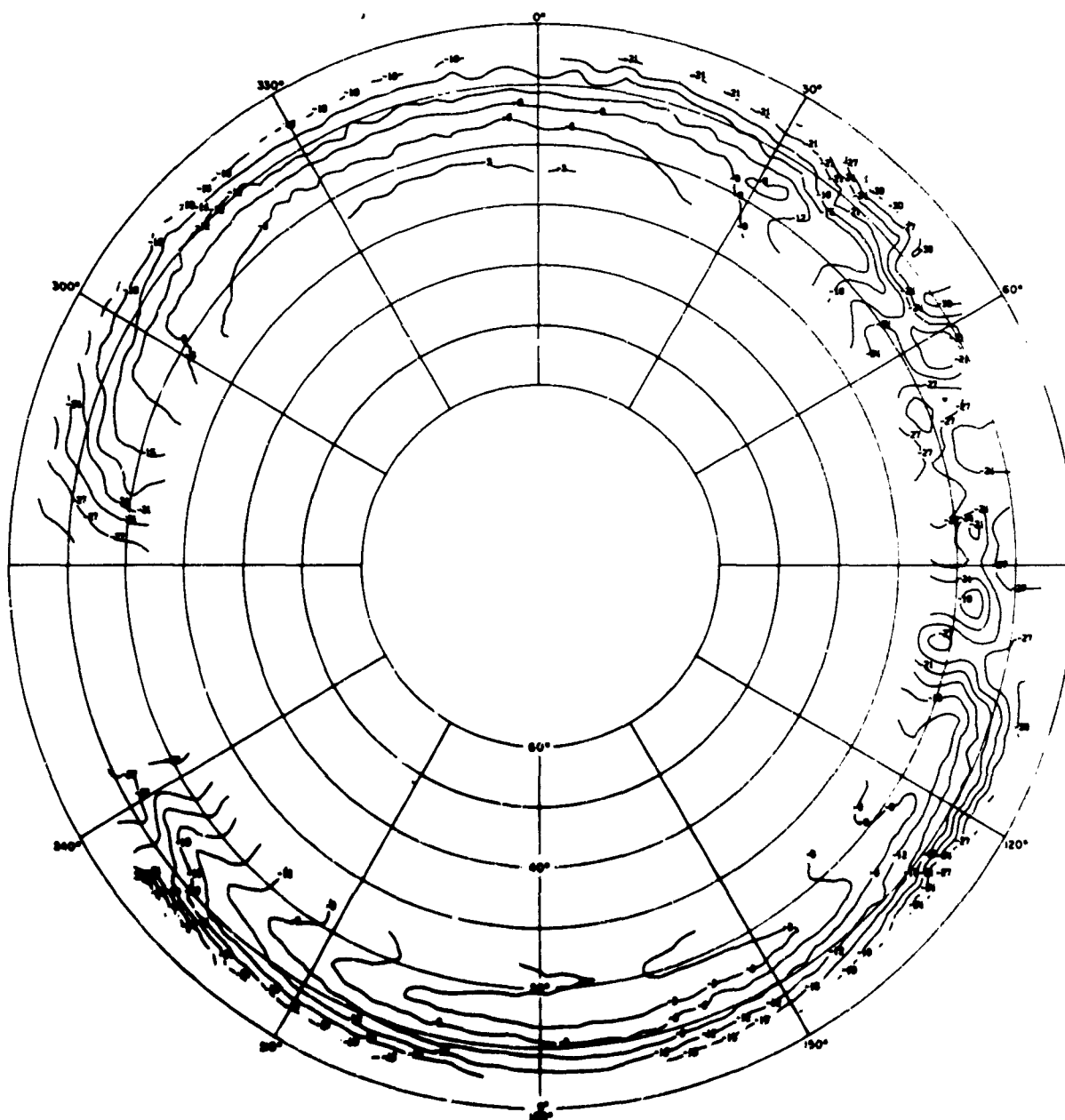


Fig. B. 70 Double-Dipole Array at 9.1 Mc, E_{ϕ}

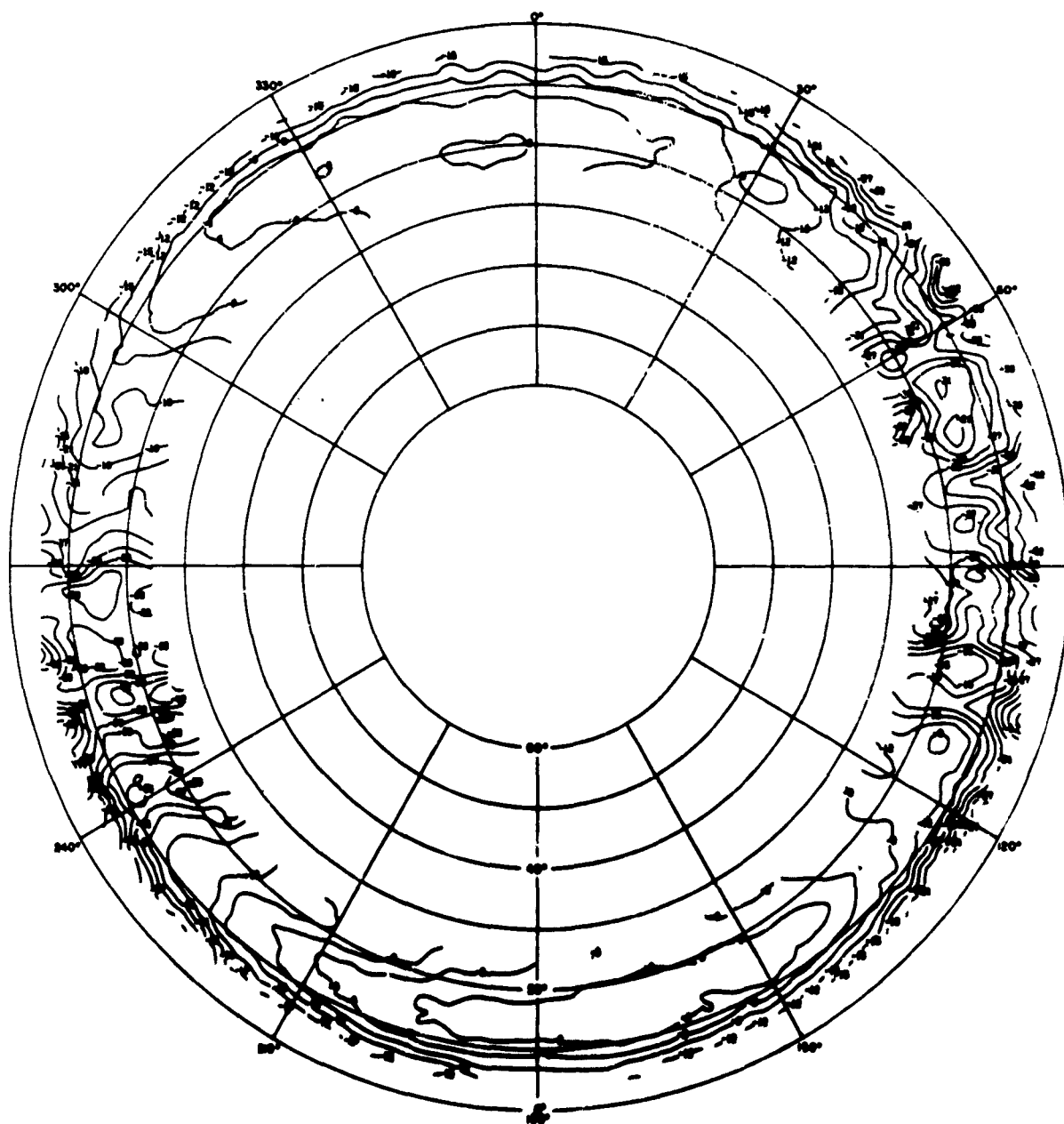


Fig. B. 71 Double-Dipole Array at 15.3 Mc, E_{ϕ}

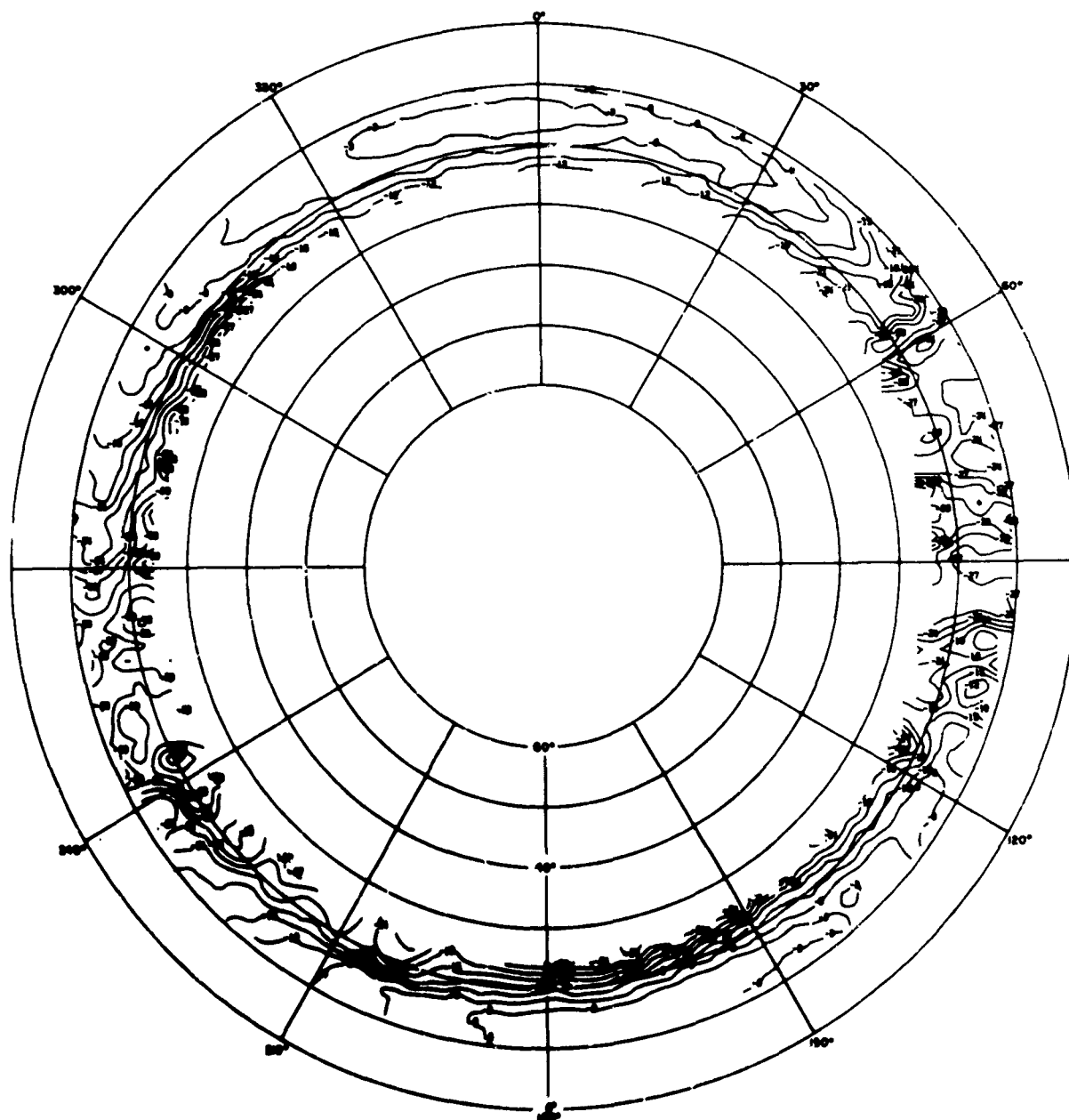


Fig. B. 72 Double-Dipole Array at 21.5 Mc, E_ϕ

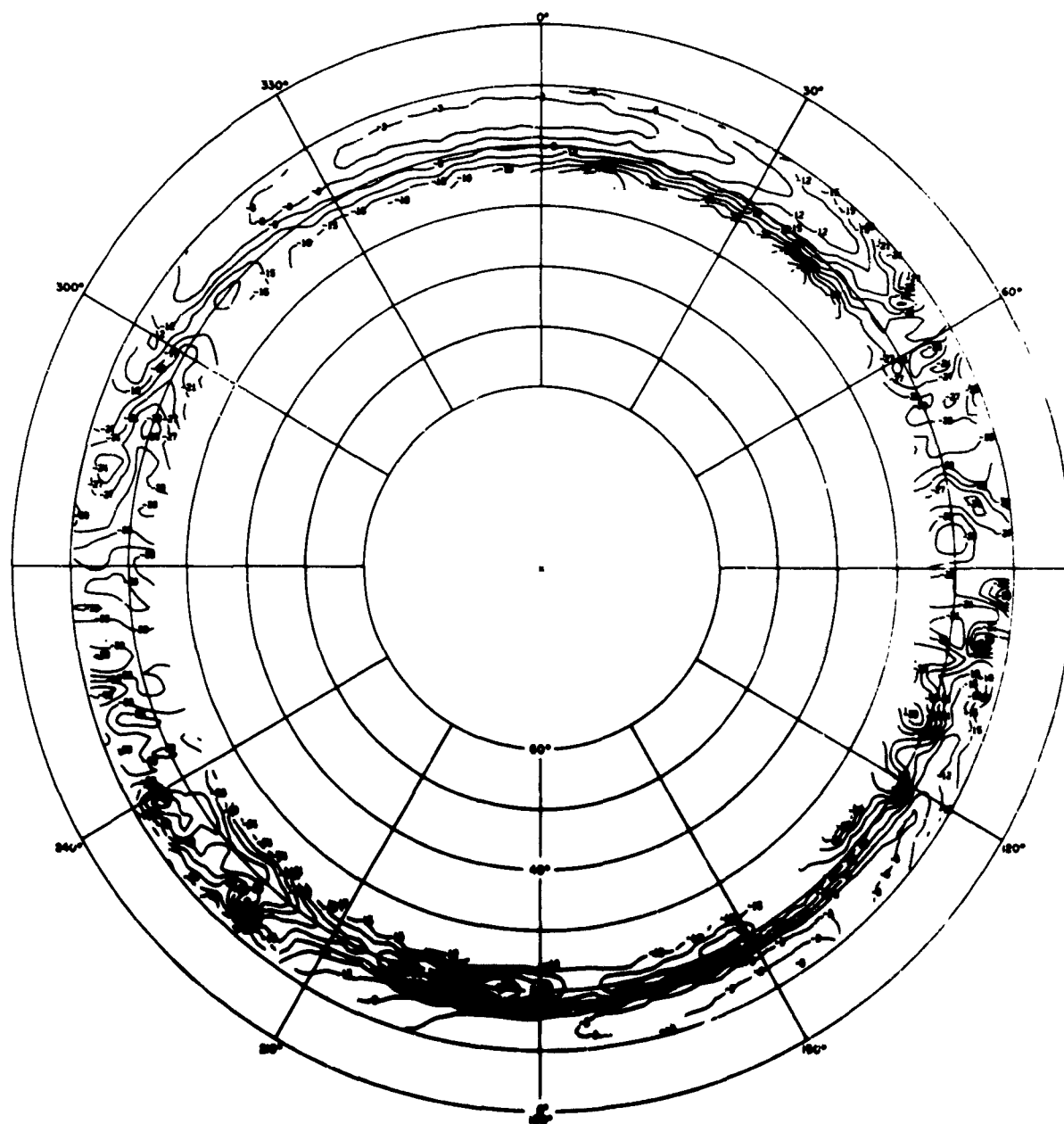


Fig. B.73 Double-Dipole Array at 25.3 Mc, E_p

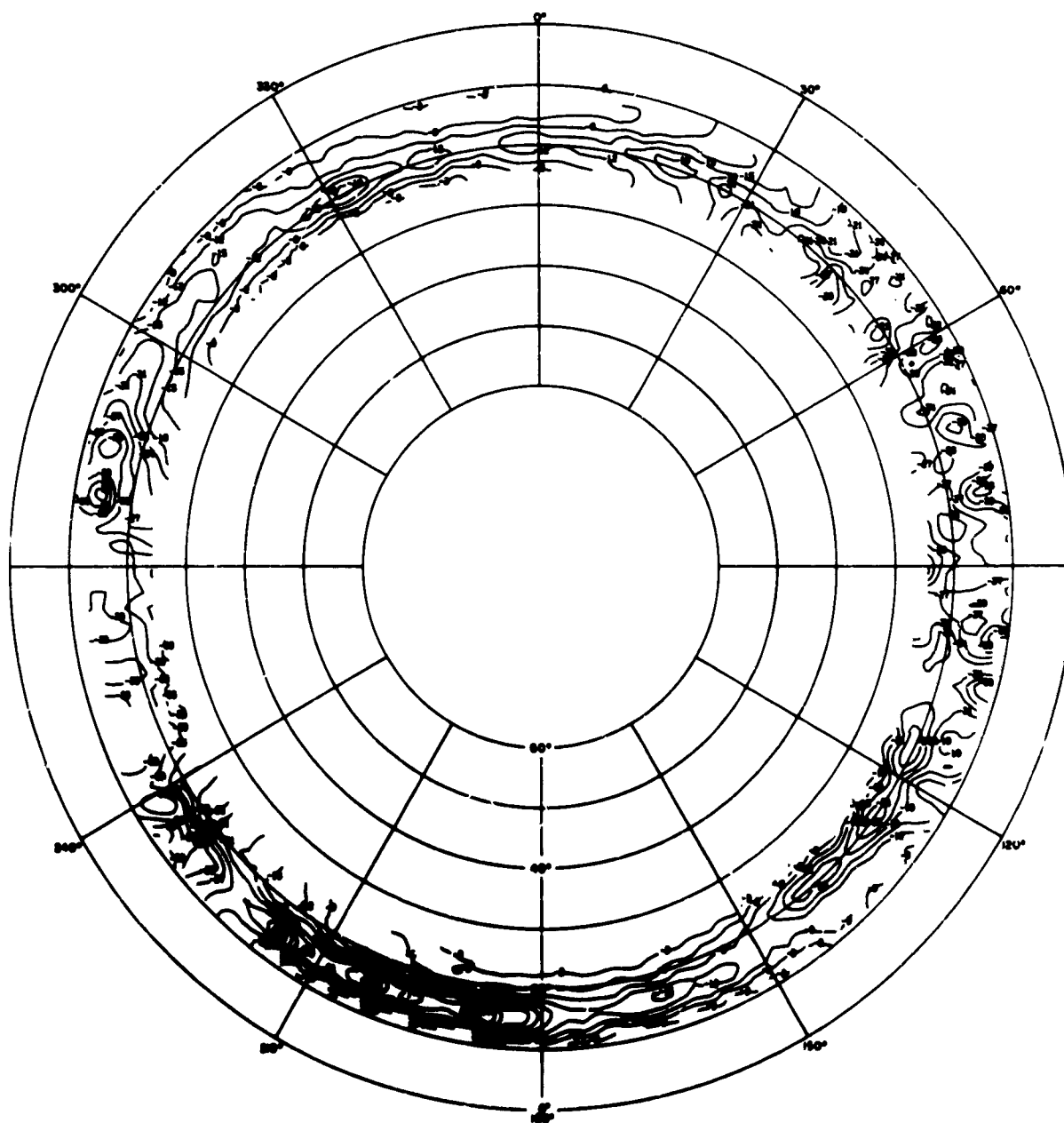


Fig. B. 74 Double-Dipole Array at 30.0 Mc, E_{ϕ}

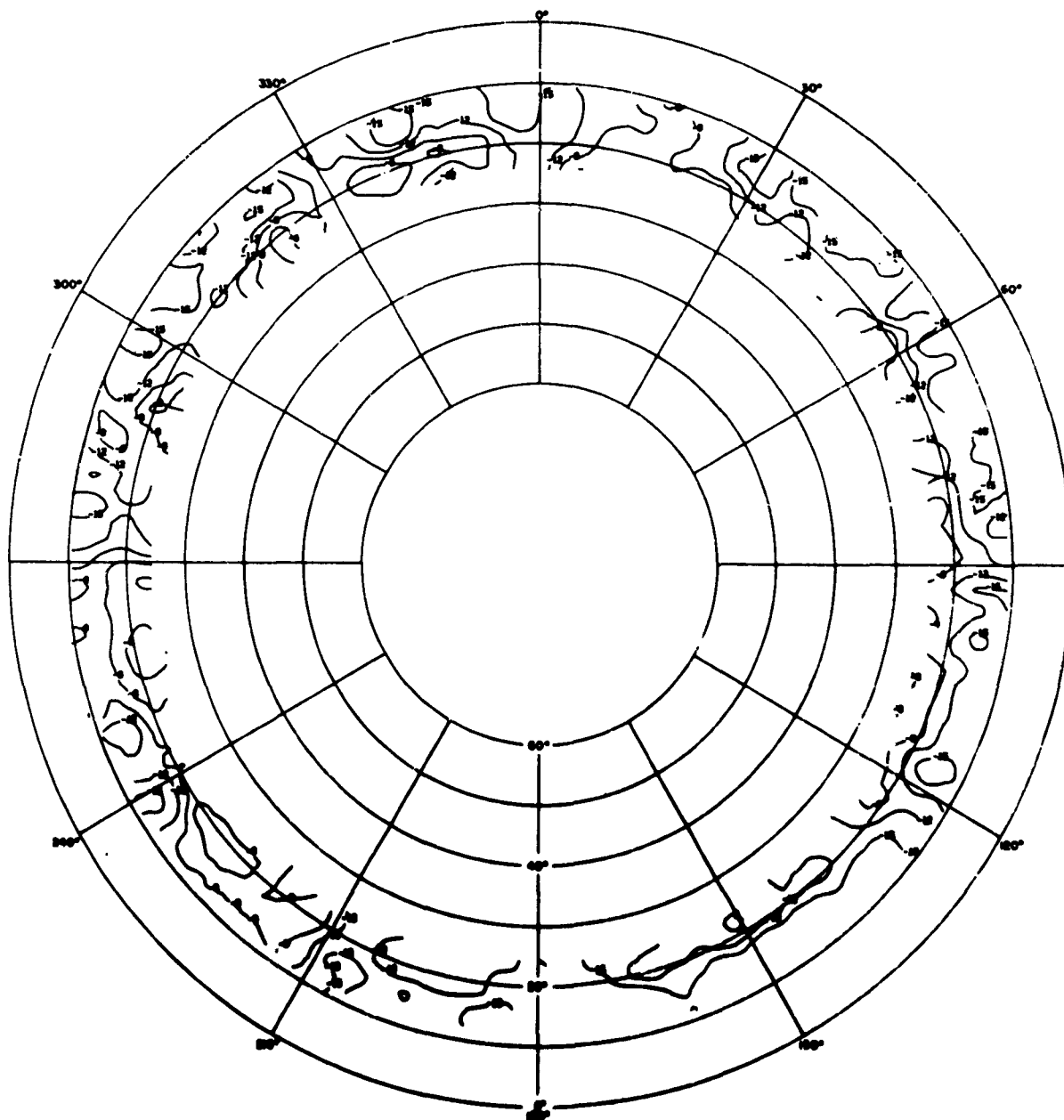


Fig. B. 75 Anchorage Feed at 3.0 Mc, E_{ϕ}
 (E_{ϕ} peak 15 db below E_{θ} peak)

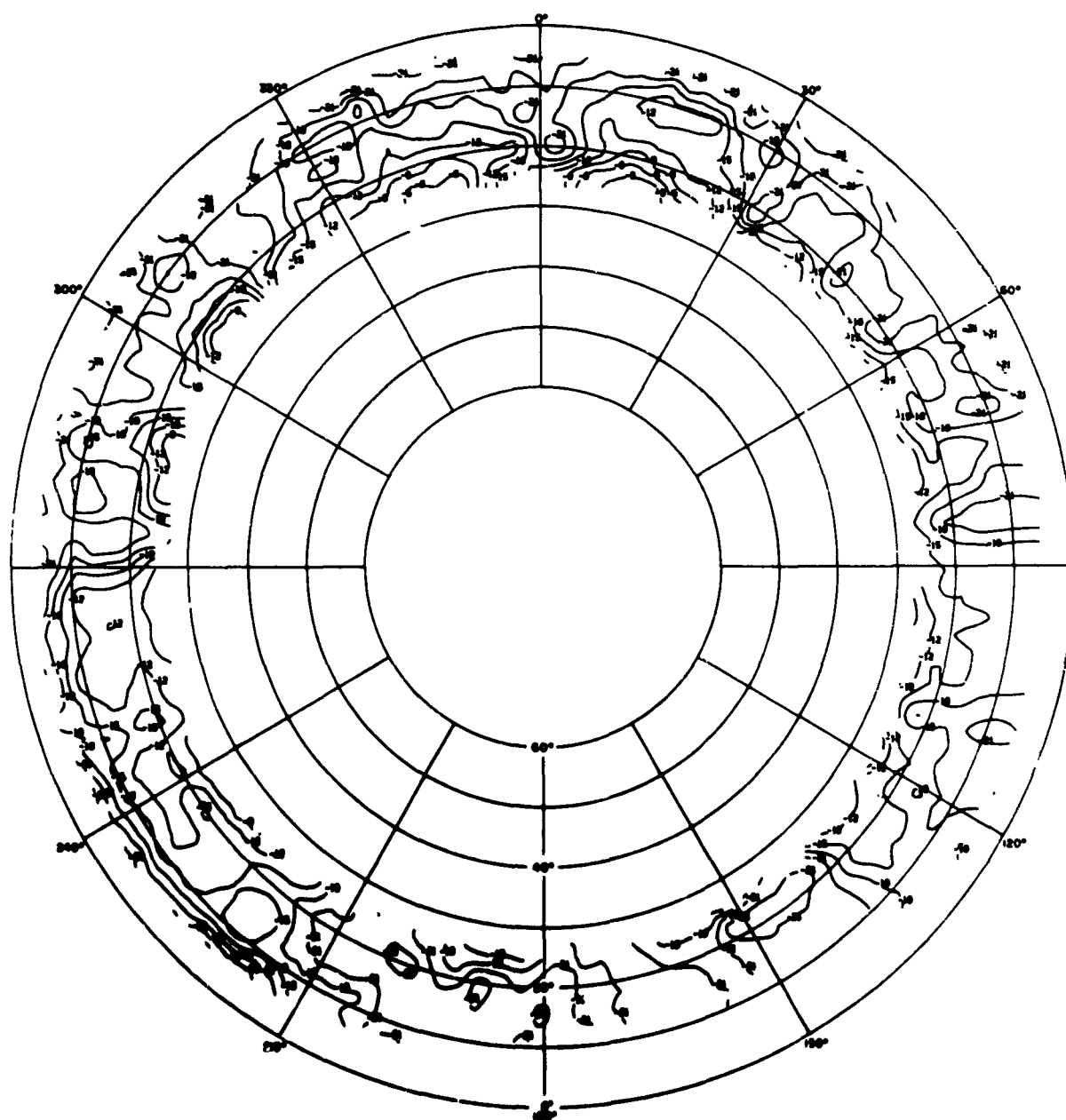


Fig. B. 76 Anchorage Feed at 4.1 Mc, E_{ϕ}
 (E_{ϕ} peak 9 db below E_{θ} peak)



Fig. B. 77 Anchorage Feed at 5.6 Mc, E_ϕ
 (E_ϕ peak 8.5 db below E_θ peak)

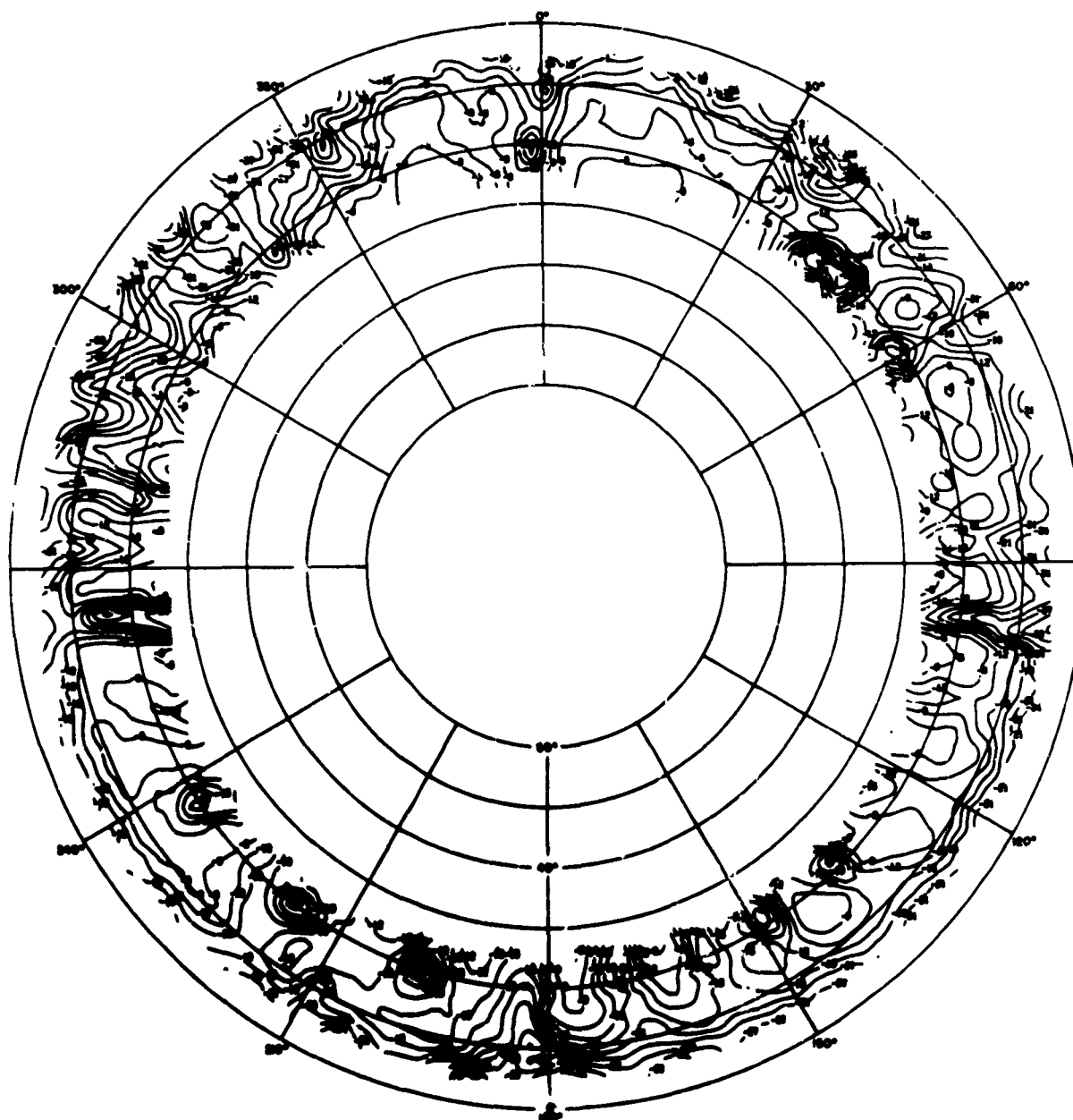


Fig. B.78 Anchorage Feed at 9.1 Mc, E_{ϕ}
(E_{ϕ} peak 11.5 db below E_{θ} peak)

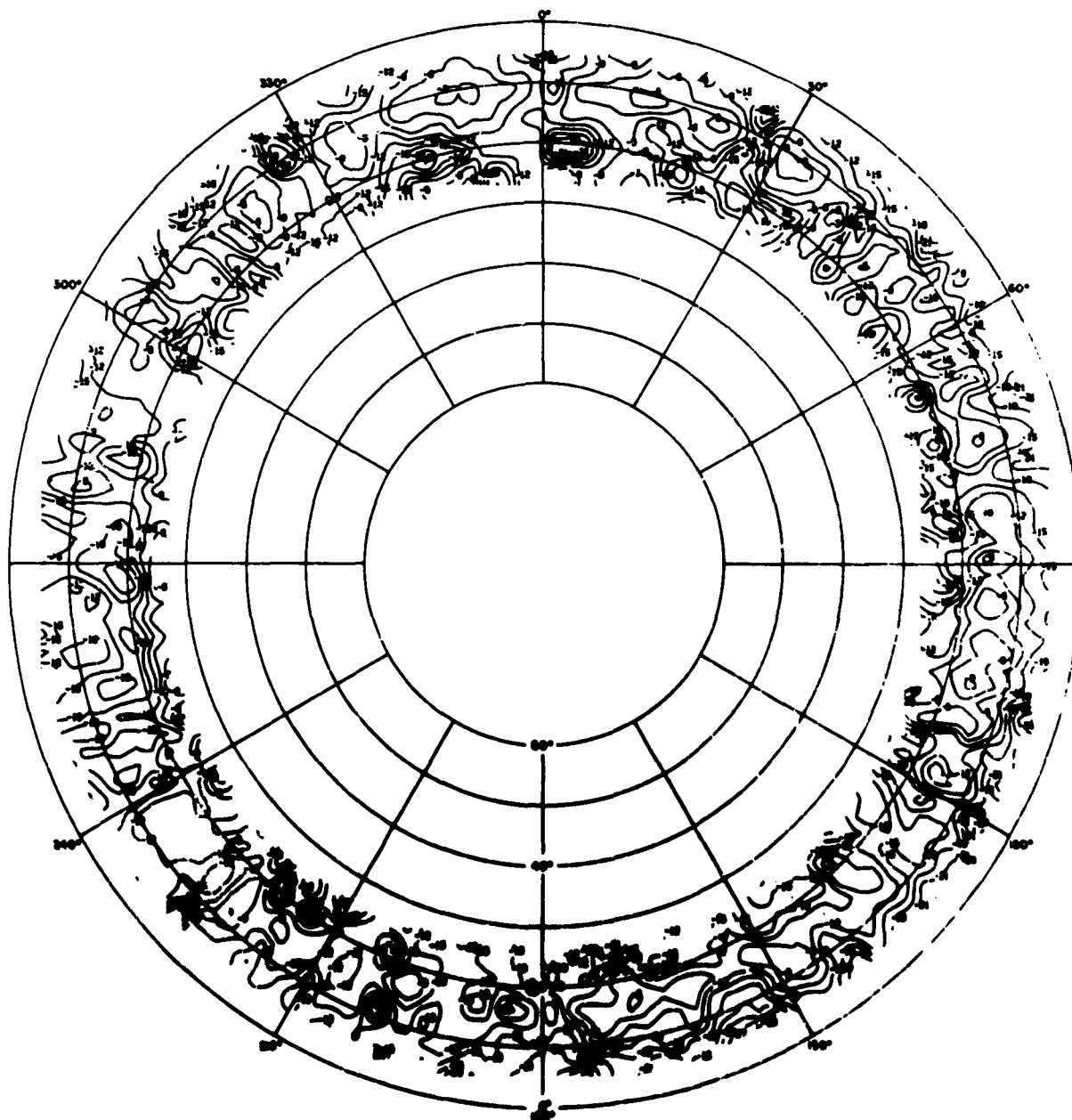


Fig. B. 79 Anchorage Feed at 15.3 Mc, E_{ϕ}
 (E_{ϕ} peak 11 db below E_{θ} peak)

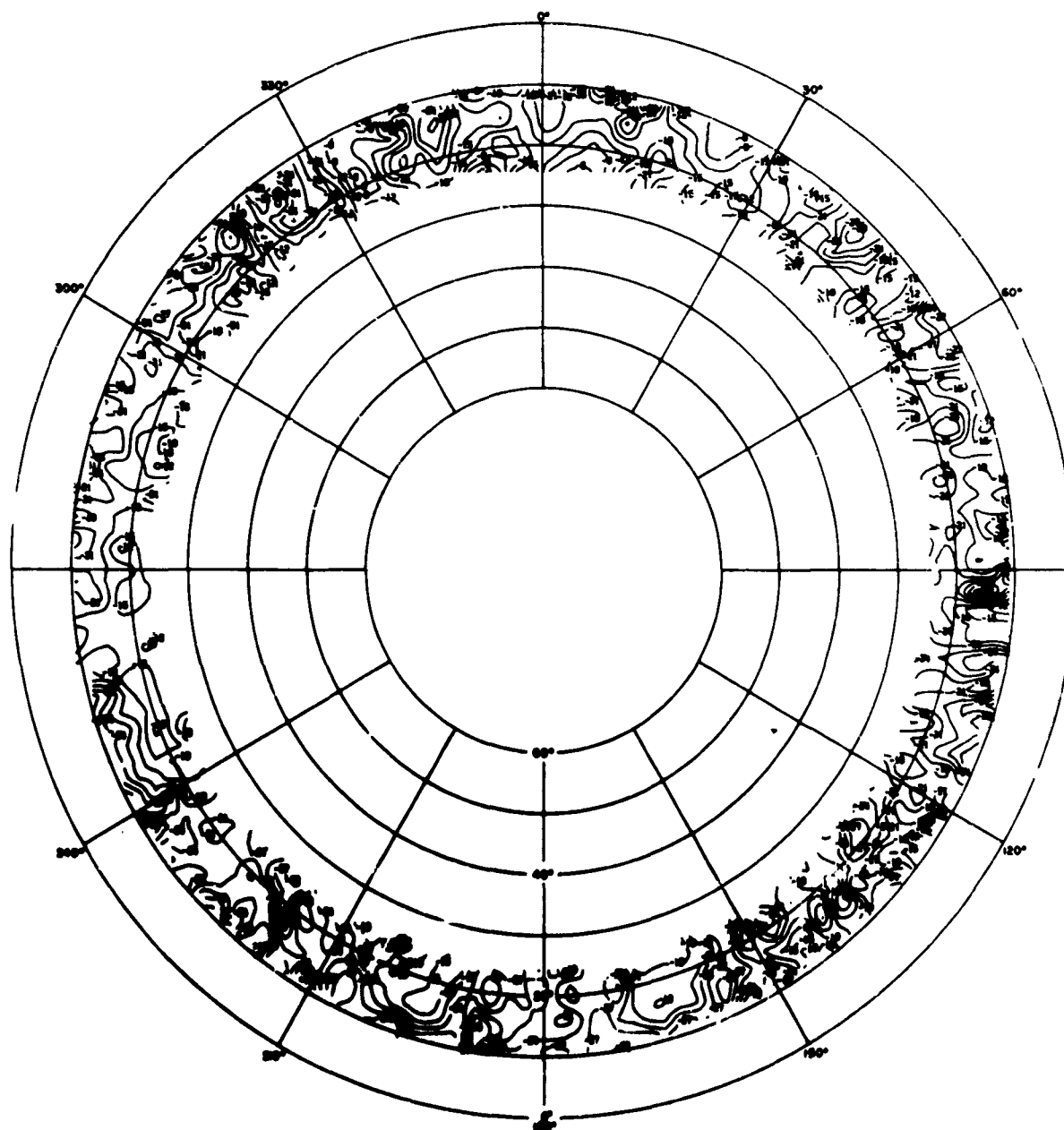


Fig. B.80 Anchorage Feed at 21.5 Mc, E_ϕ
 (E_ϕ peak 5.5 db below E_θ peak)

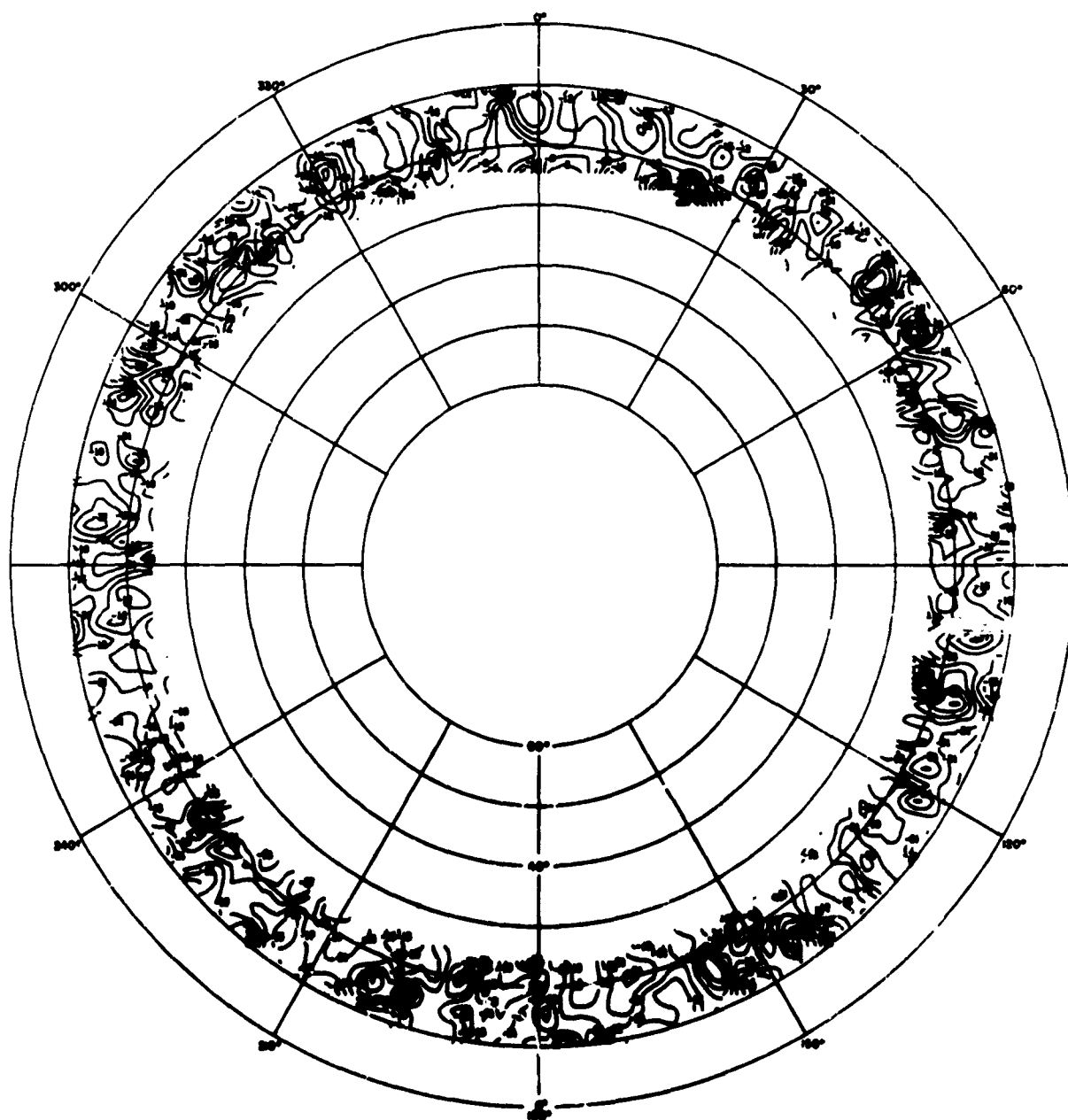


Fig. B.81 Anchorage Feed at 25.3 Mc, E_ϕ
 (E_ϕ peak 5.5 db below E_θ peak)

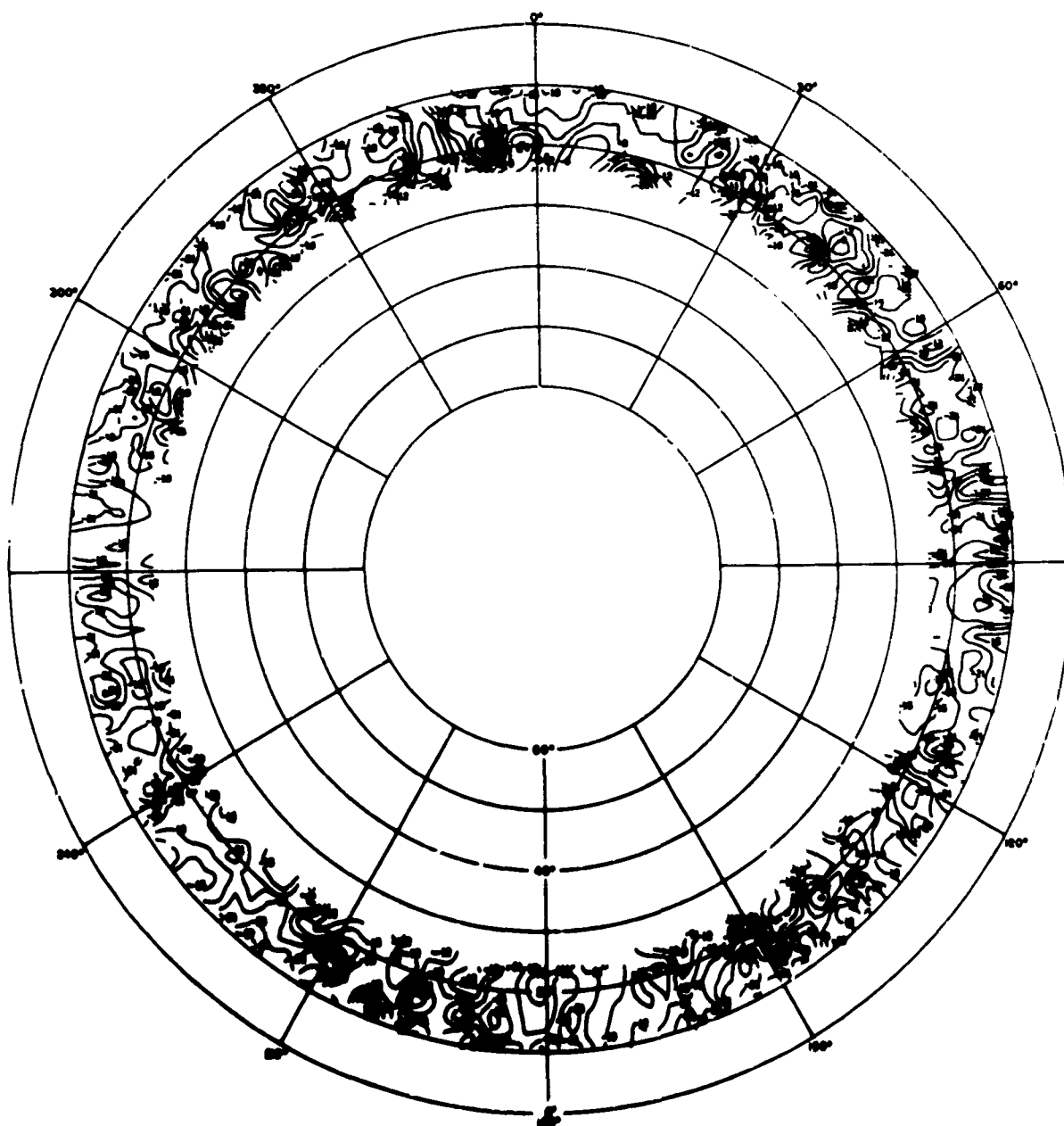


Fig. B. 82 Anchorage Feed at 30.0 Mc, E_{ϕ}
 (E_{ϕ} peak 5 db below E_{θ} peak)

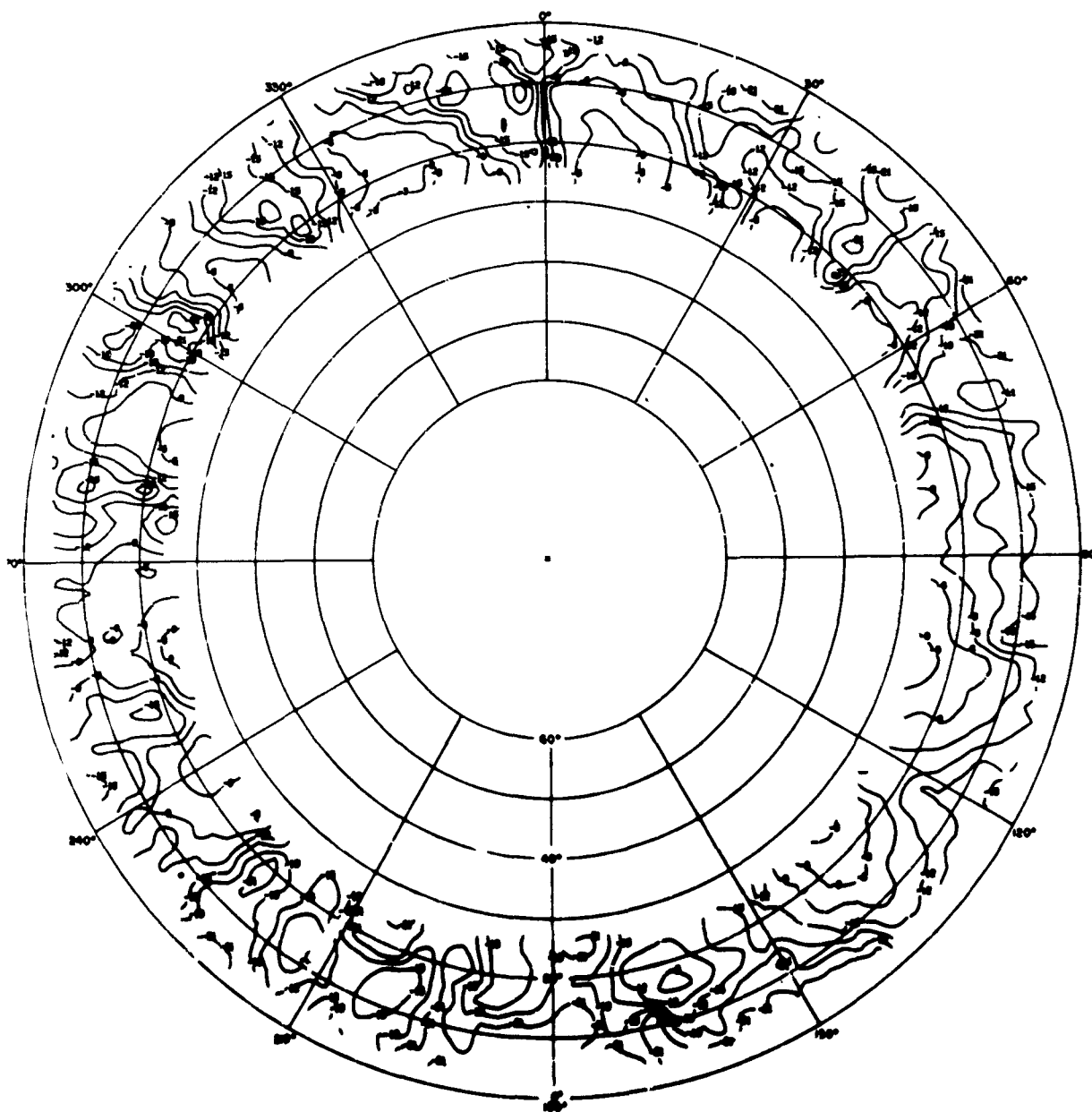


Fig. B.83 San Francisco Feed at .1 Mc, E_ϕ
 (E_ϕ peak 10 db below E_t peak)

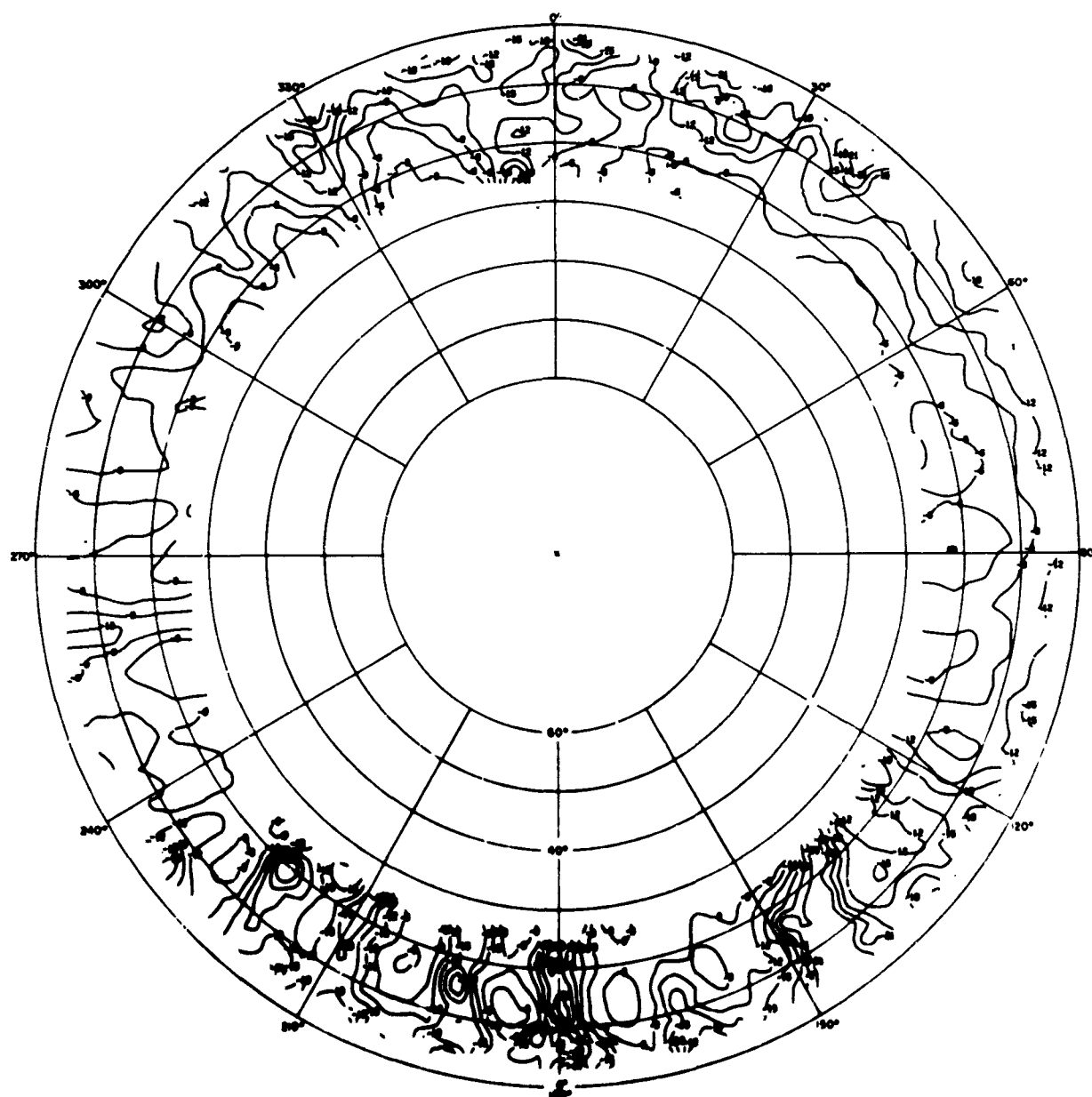


Fig. B. 84 San Francisco Feed at 5.6 Mc, E_ϕ
 (E_ϕ peak 10.5 db below E_θ peak)

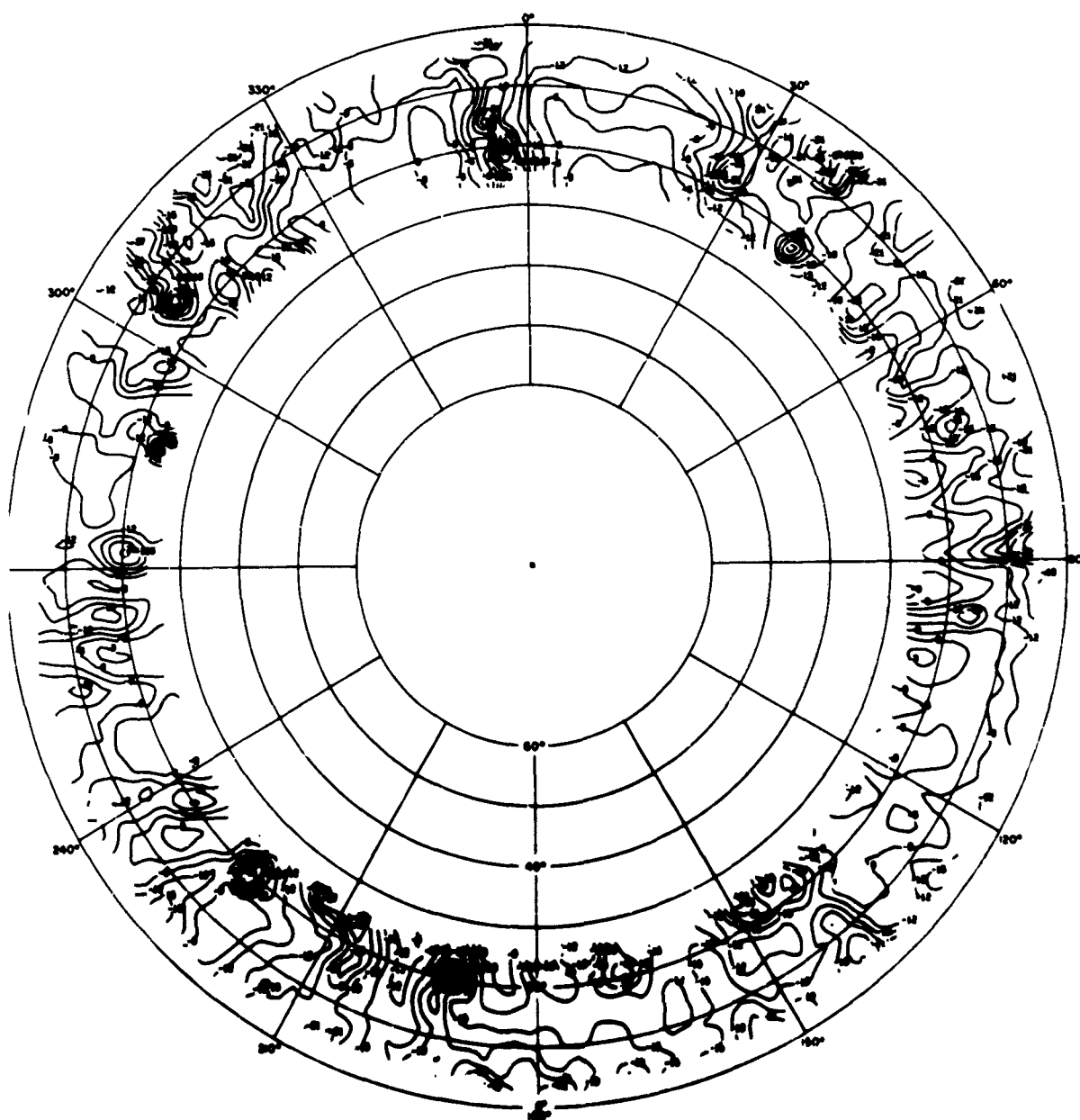


Fig. B.85 San Francisco Feed at 9.1 Mc, E_{ϕ}
 (E_{ϕ} peak 9 db below E_{θ} peak)

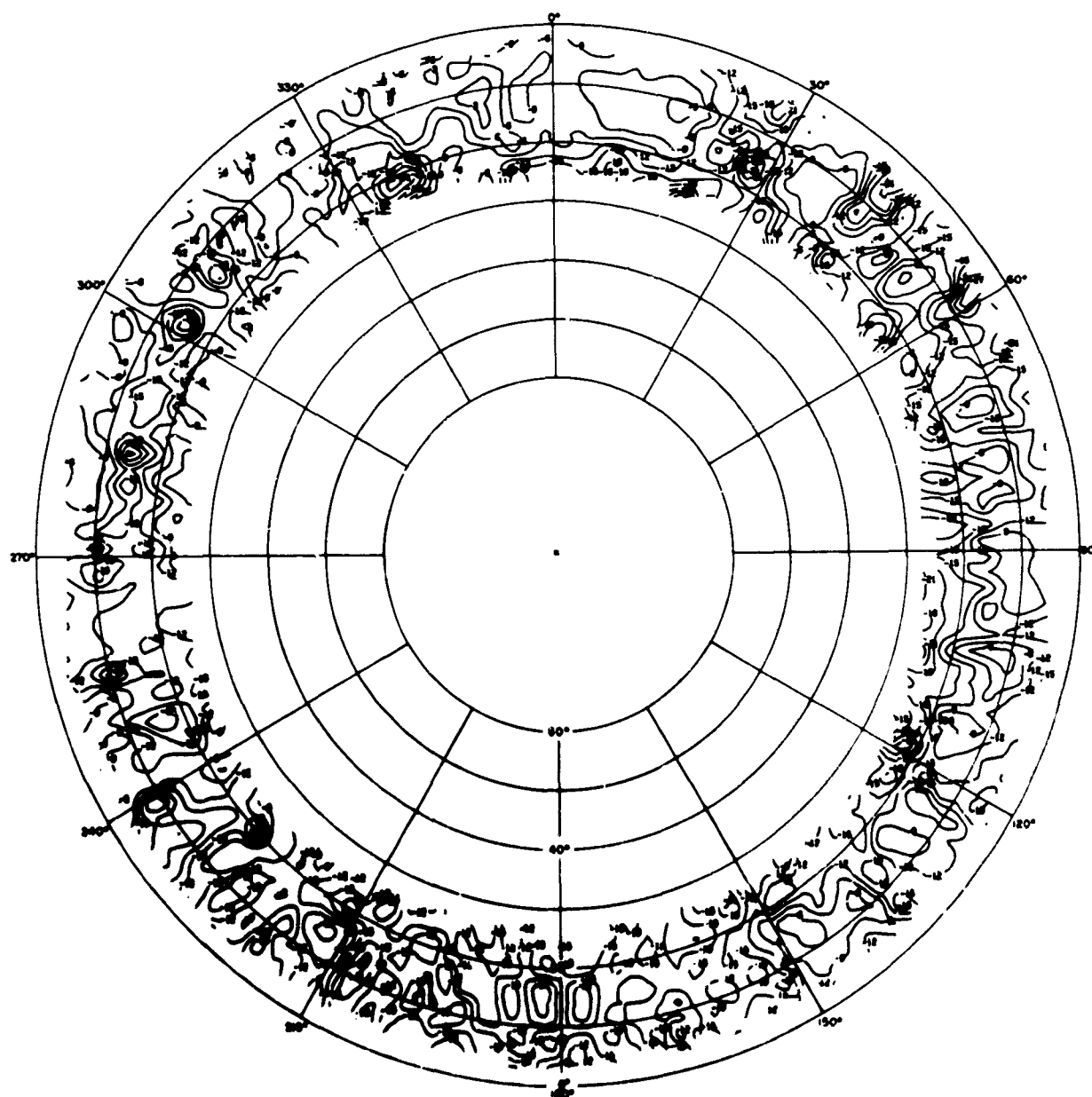


Fig. B. 86 San Francisco Feed at 15.3 Mc, E_{ϕ}
 (E_{ϕ} peak 9.5 db below E_{θ} peak)

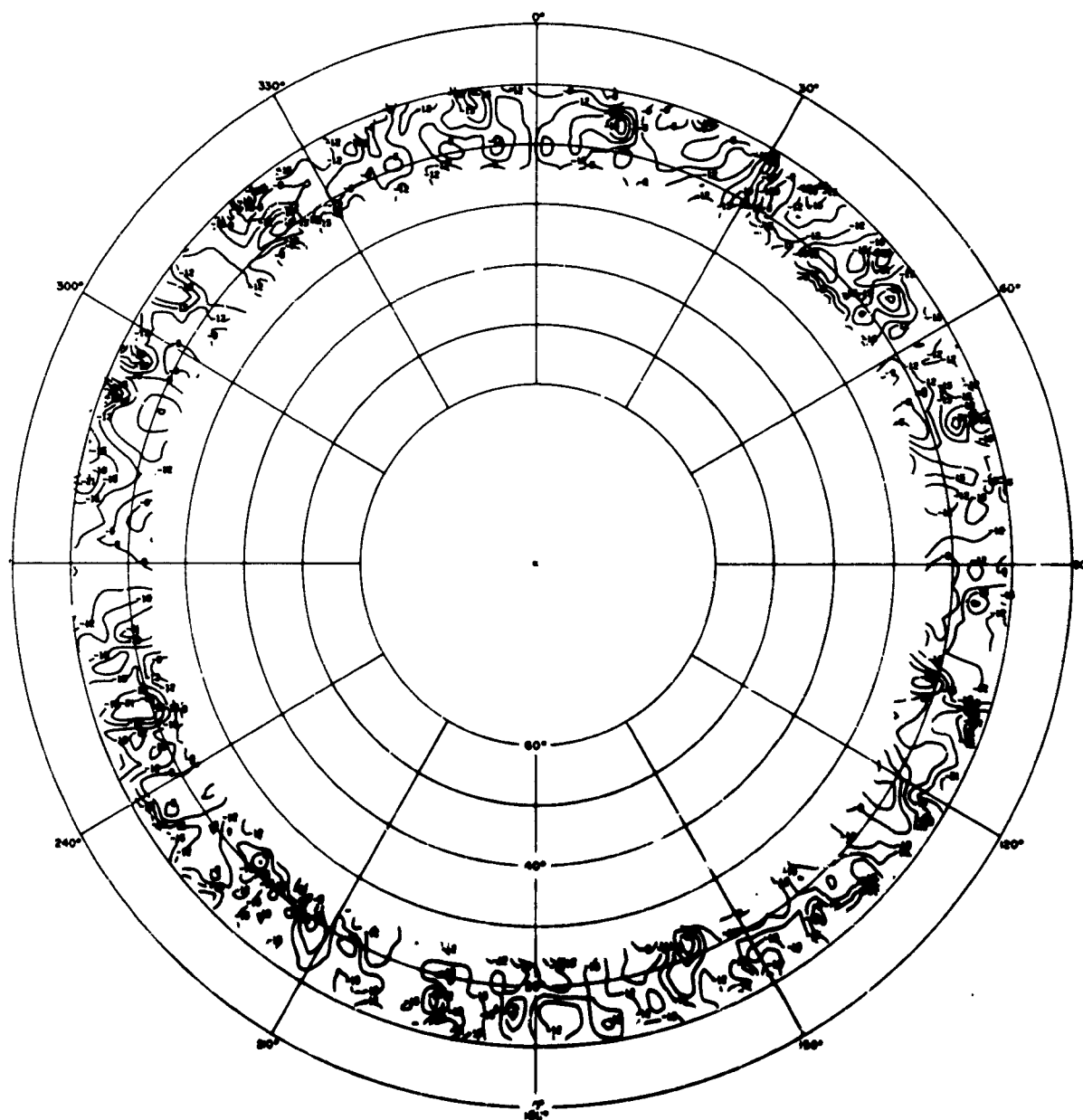


Fig. B.87 San Francisco Feed at 25.3 Mc, E_ϕ
 (E_ϕ peak 9 db below E_θ peak)

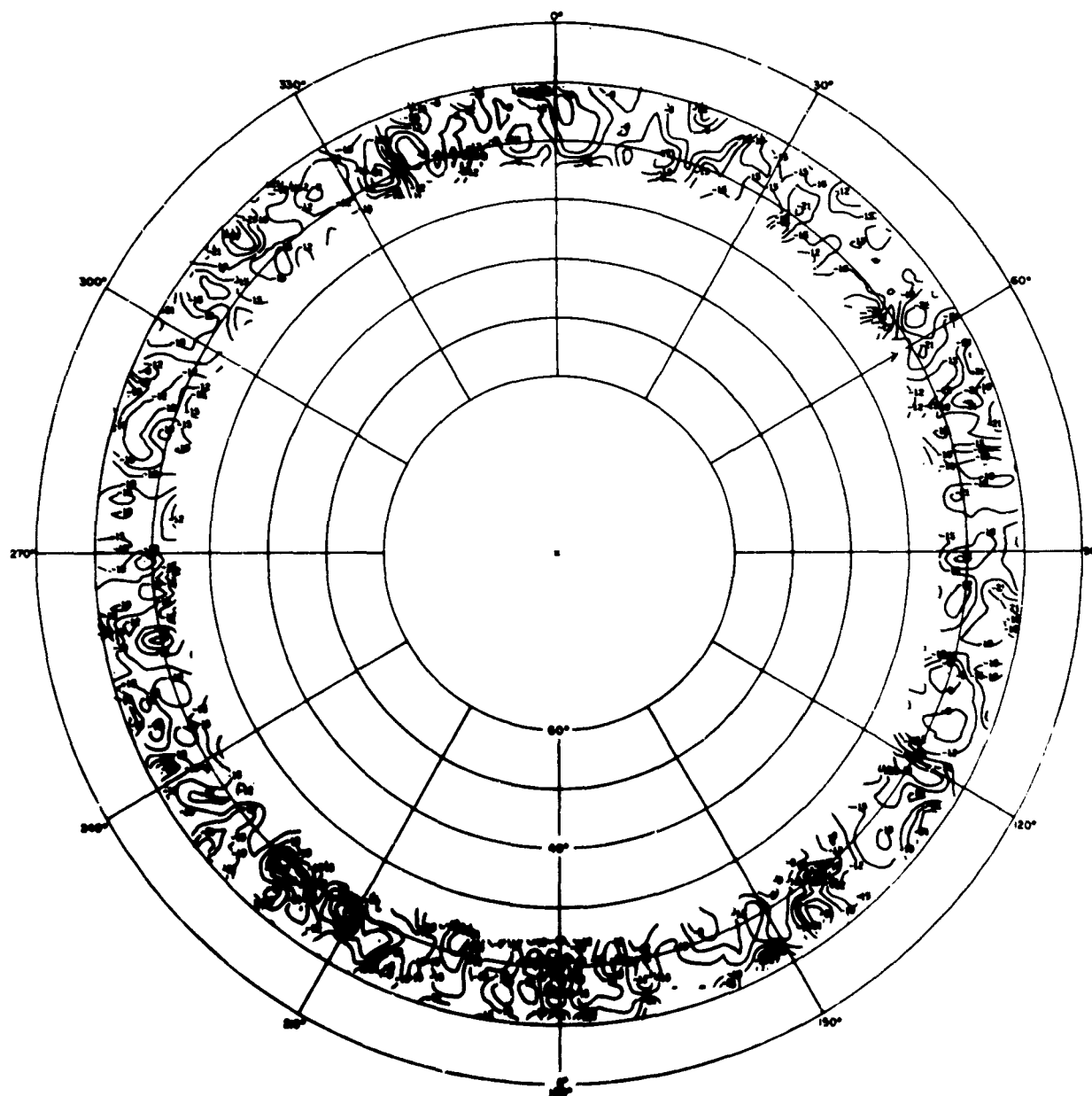


Fig. B.88 San Francisco Feed at 30.0 Mc, E_ϕ
 (E_ϕ peak 10.5 db below E_θ peak)

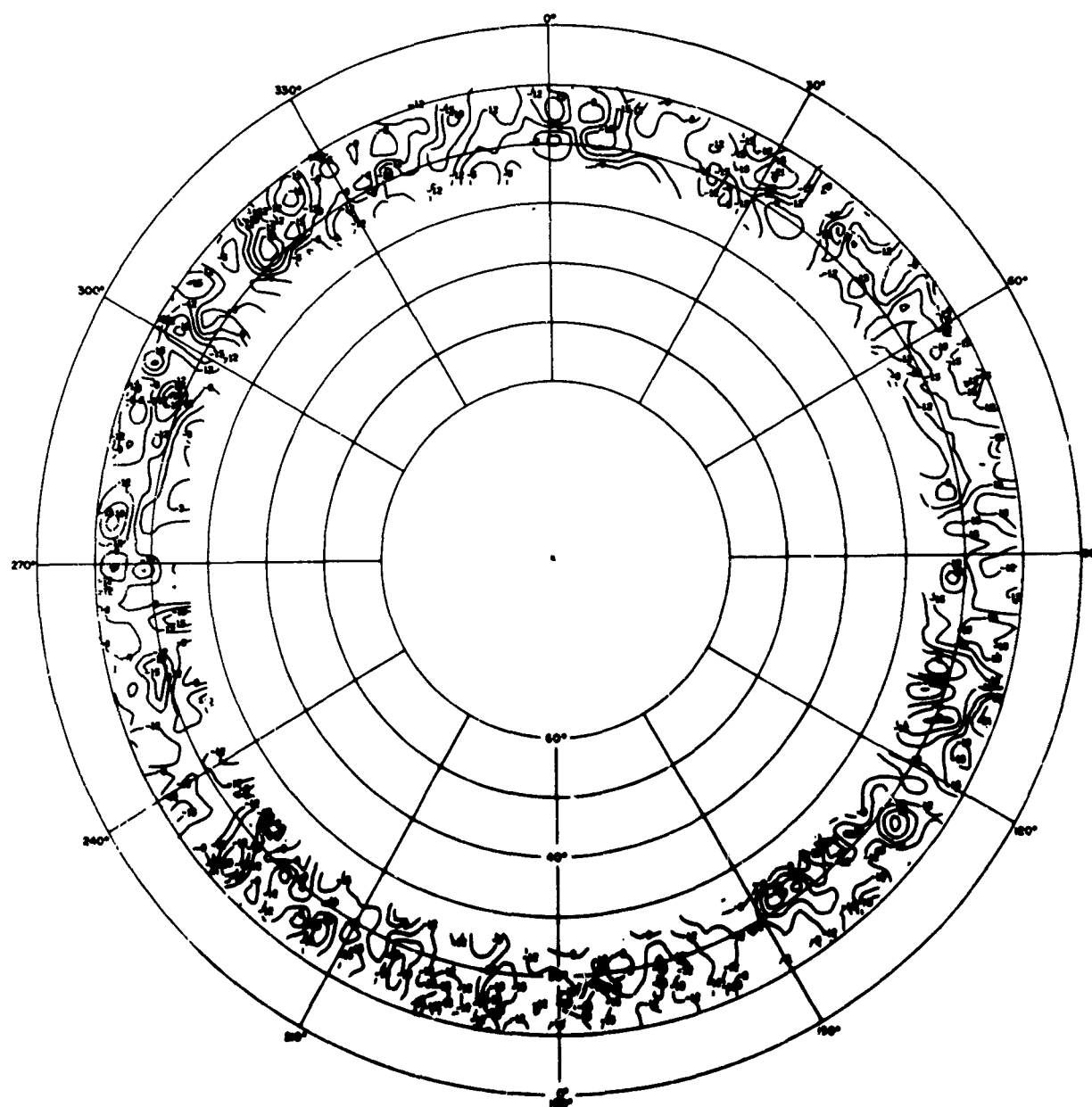
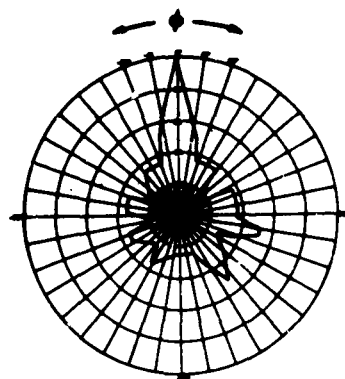


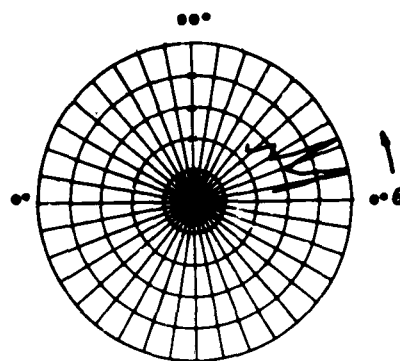
Fig. B.89 NRL Monopole at 25.3 Mc, E_ϕ

(E_ϕ peak 18 db below E_θ peak)

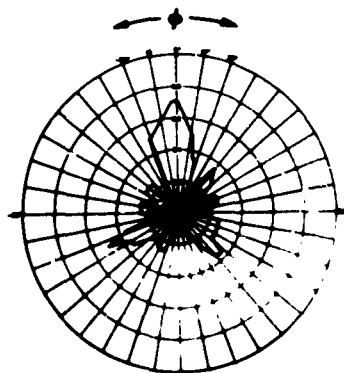
B-95



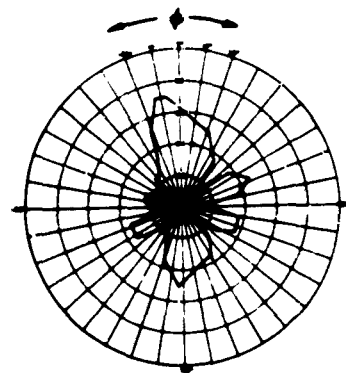
$\theta = 23^\circ$



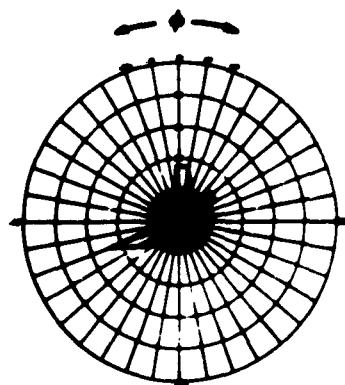
$\phi = 0^\circ$



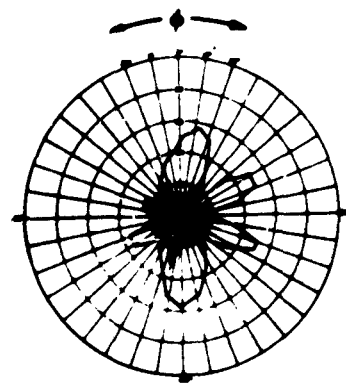
$\theta = 9^\circ$



$\theta = 36^\circ$



$\theta = 5^\circ$



$\theta = 40^\circ$

Fig. B.90 Anchorage Feed at 3 Mc, E_θ
(Voltage Plots)

B-96

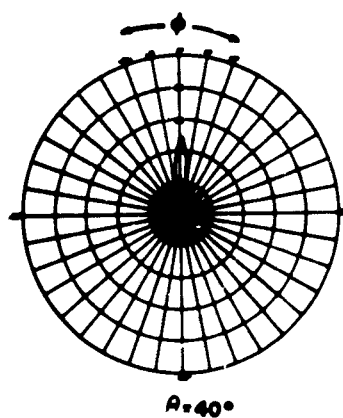
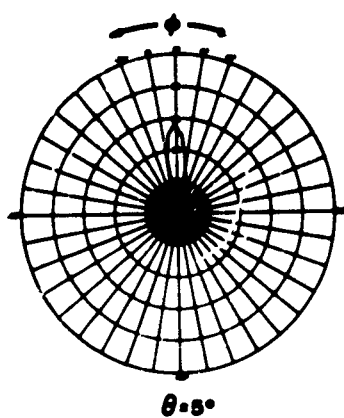
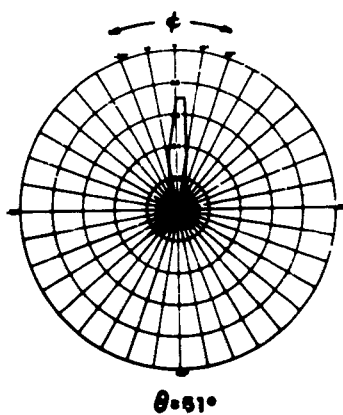
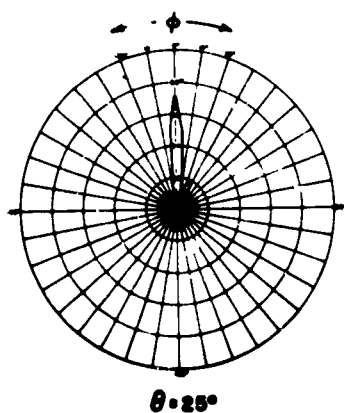
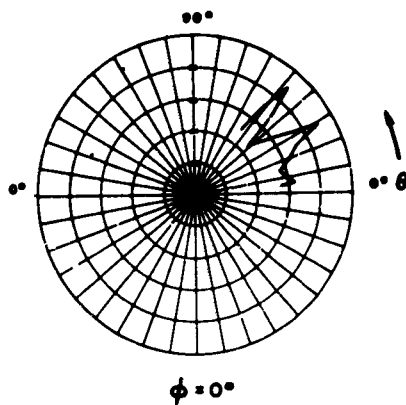
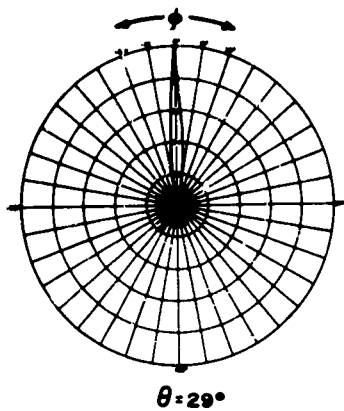


Fig. B. 91 Anchorage Feed at 11.8 Mc, E_θ
(Voltage Plots)

B-97

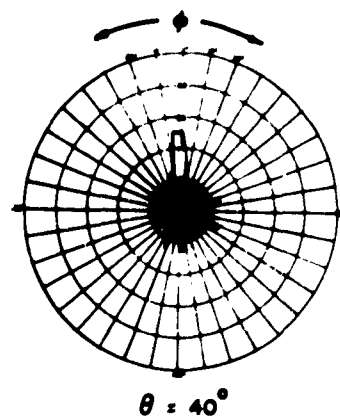
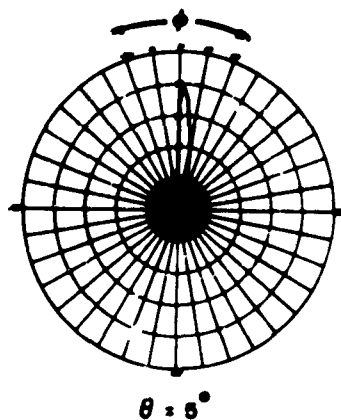
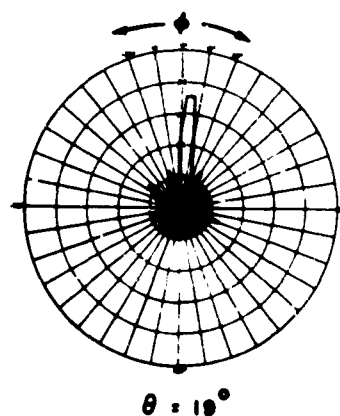
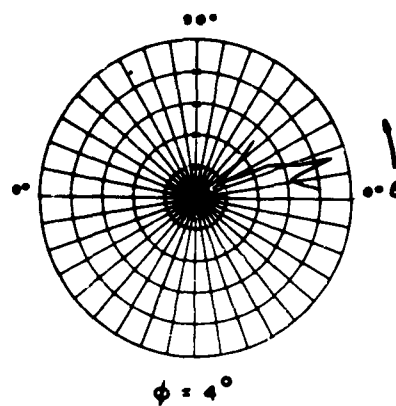
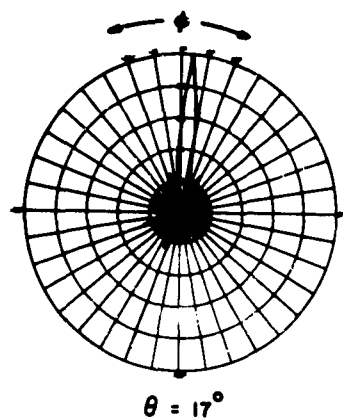
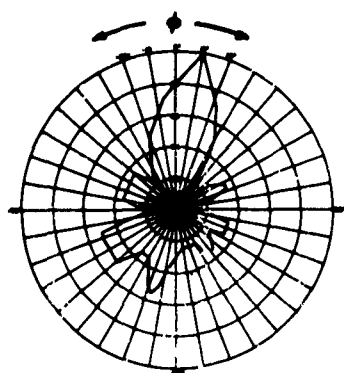
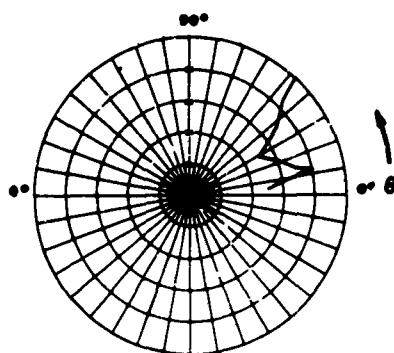


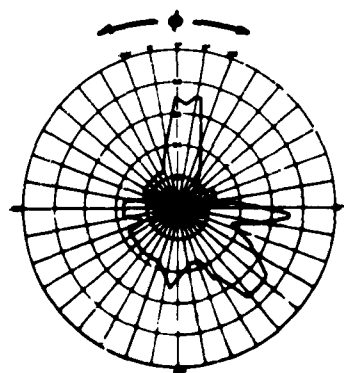
Fig. B. 92 Anchorage Feed at 30.0 Mc, E_θ
B-98 (Voltage Plots)



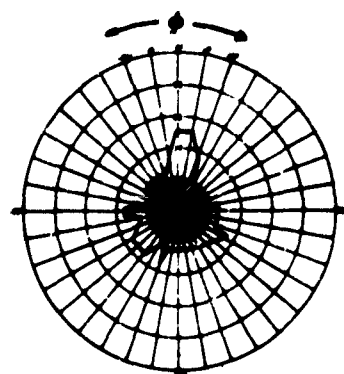
$\theta = 47^\circ$



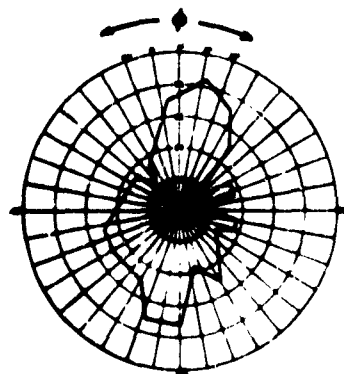
$\phi = 10^\circ$



$\theta = 10^\circ$

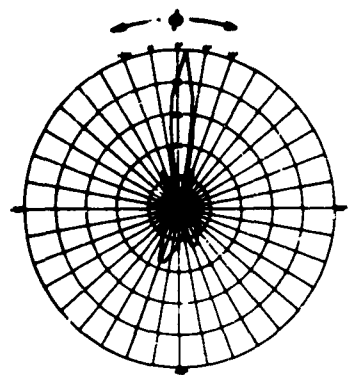


$\theta = 5^\circ$

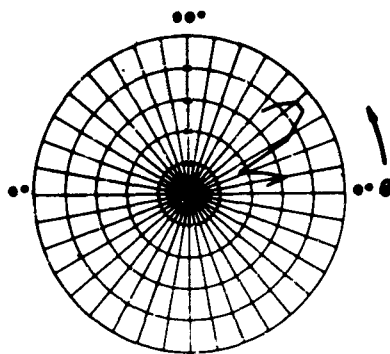


$\theta = 40^\circ$

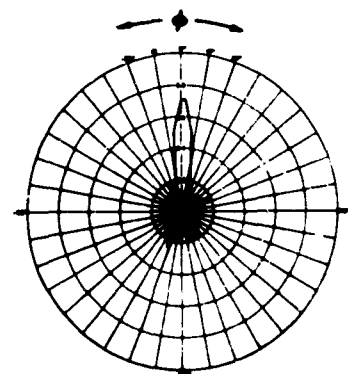
Fig. B.93 Sydney Feed at 3 Mc, E_θ
B-99 (Voltage Plots)



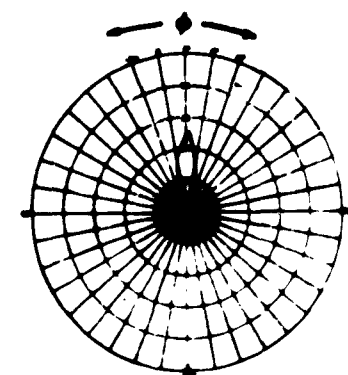
$\theta = 40^\circ$



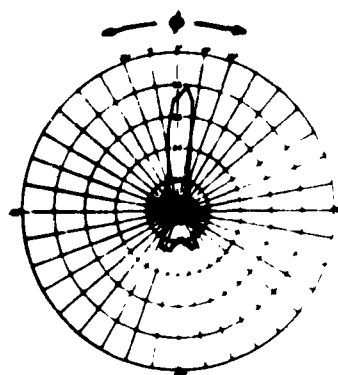
$\phi = 3^\circ$



$\theta = 20^\circ$



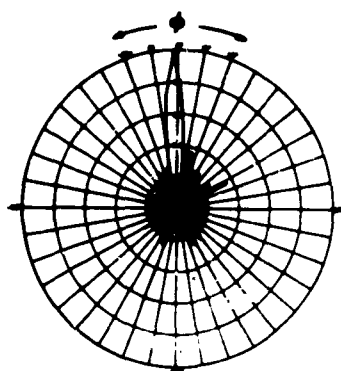
$\theta = 0^\circ$



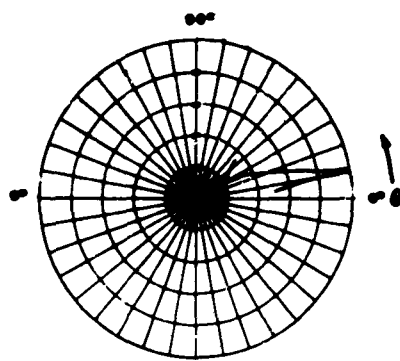
$\theta = 40^\circ$

Fig. B. 94 Sydney Feed at 11.8 Mc, E_θ
(Voltage Plots)

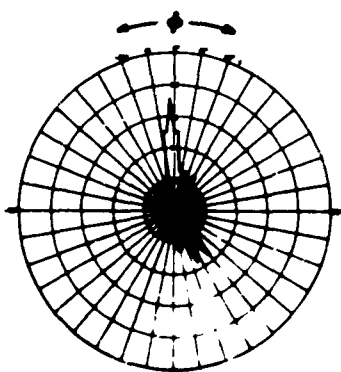
B-100



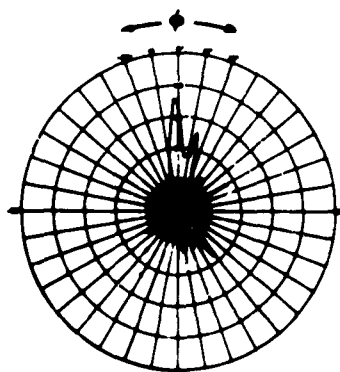
$\theta = 12^\circ$



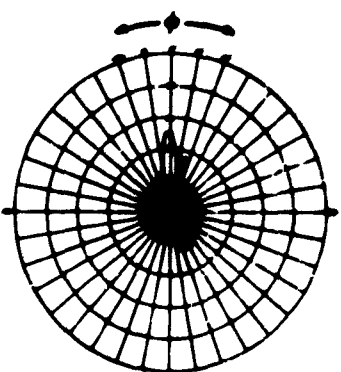
$\phi = -2^\circ$



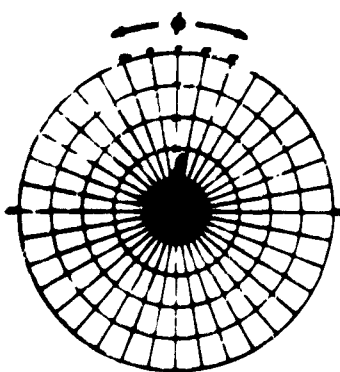
$\theta = 8^\circ$



$\theta = 18^\circ$

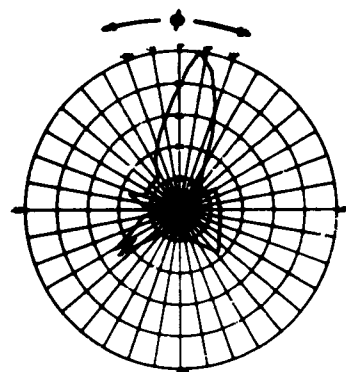


$\theta = 5^\circ$

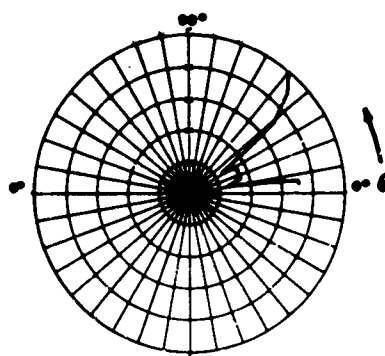


$\theta = 40^\circ$

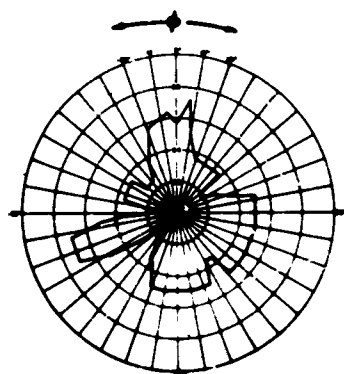
Fig. B. 95 Sydney Feed at 30.0 Mc, E_θ
B-101 (Voltage Plots)



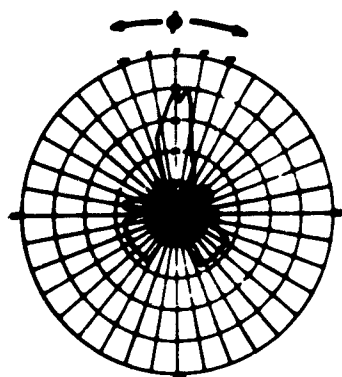
$\theta = 50^\circ$



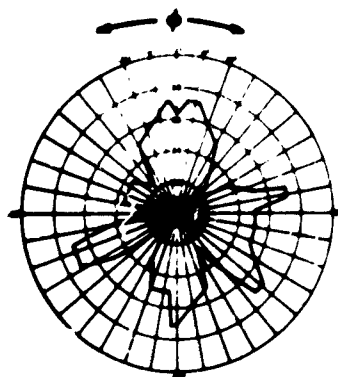
$\phi = 8^\circ$



$\theta = 38^\circ$



$\theta = 8^\circ$



$\theta = 40^\circ$

Fig. B. 96 San Francisco Feed at 3 Mc, E_θ
(Voltage Plot)

B-102

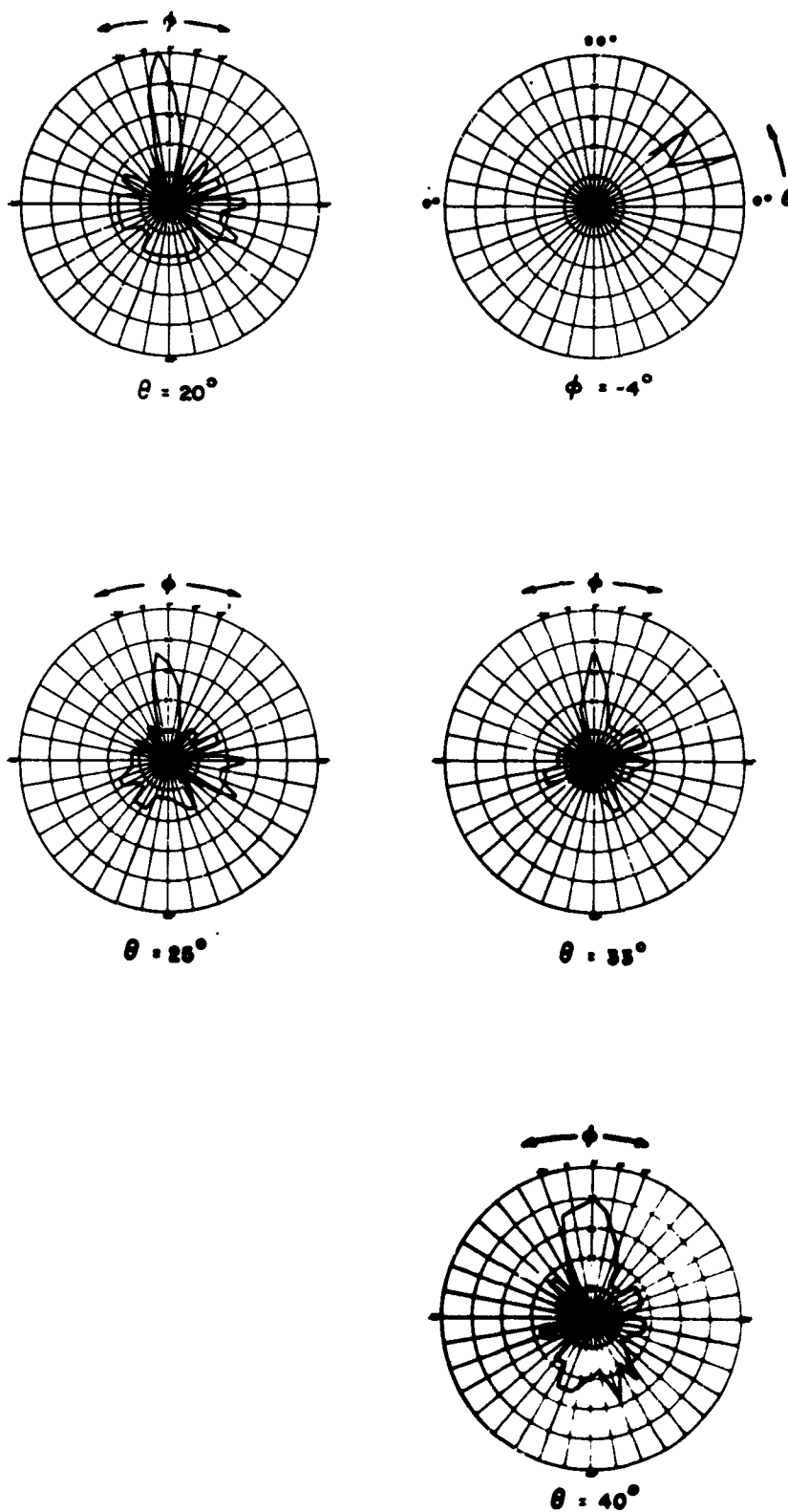


Fig. B. 97 San Francisco Feed at 4.1 Mc, E_θ
 (Voltage Plot)
 B-103

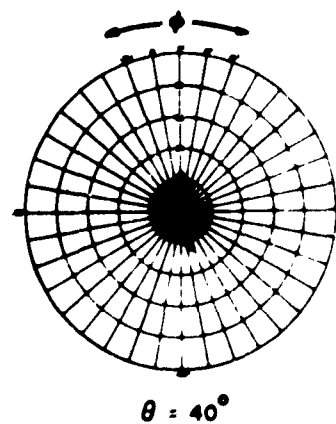
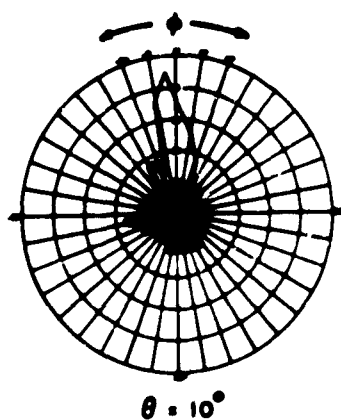
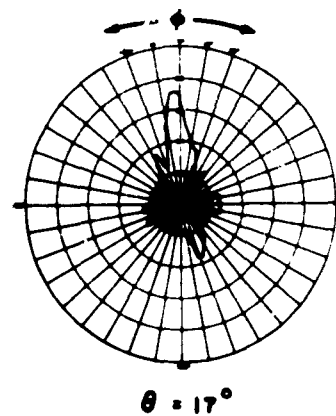
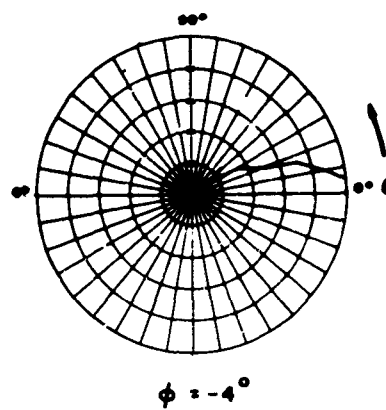
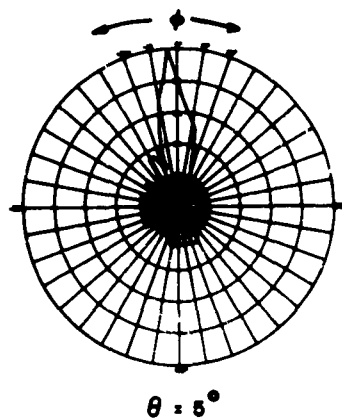


Fig. B. 98 San Francisco Feed at 5.6 Mc, E_0
(Voltage Plot)

B-104

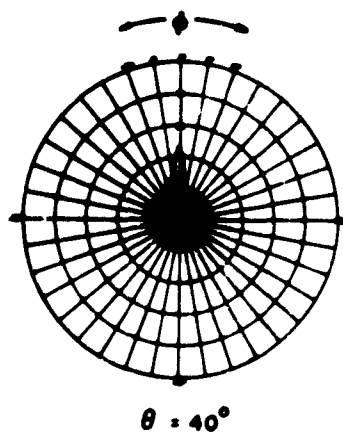
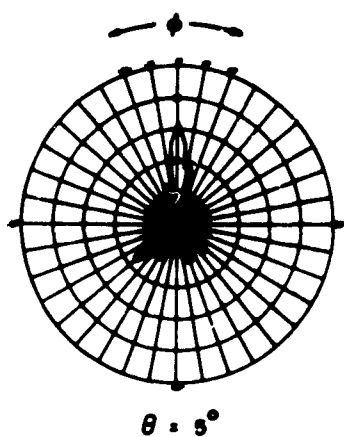
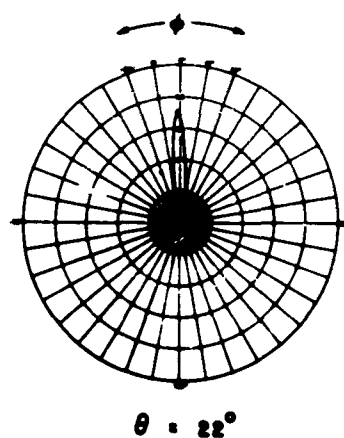
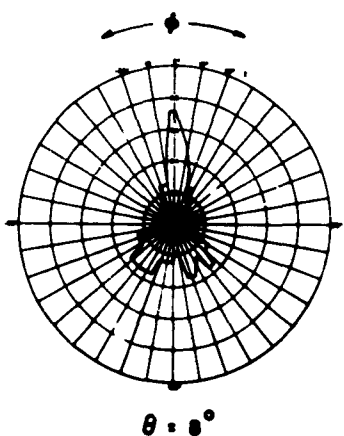
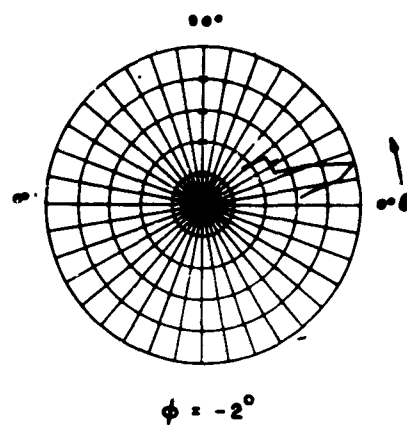
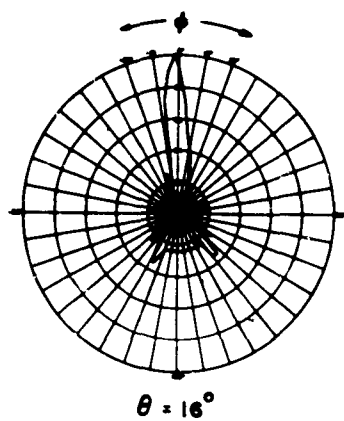
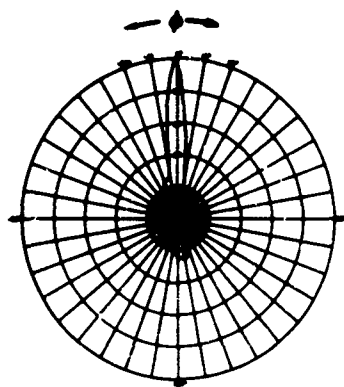
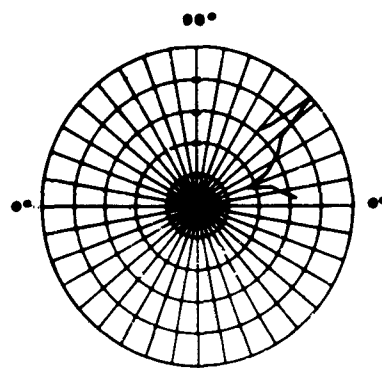


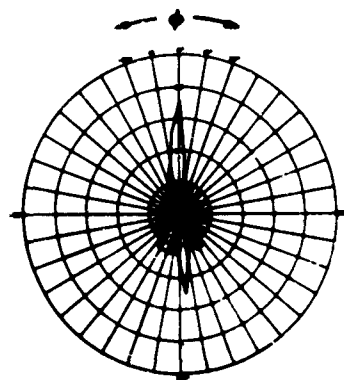
Fig. B.99 San Francisco Feed at 9.1 Mc, E_θ
(Voltage Plot)
B-105



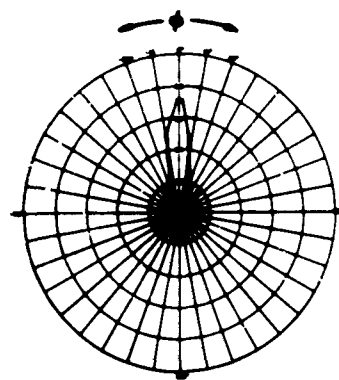
$\theta = 43^\circ$



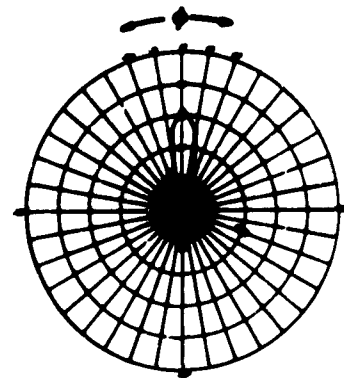
$\phi = -1^\circ$



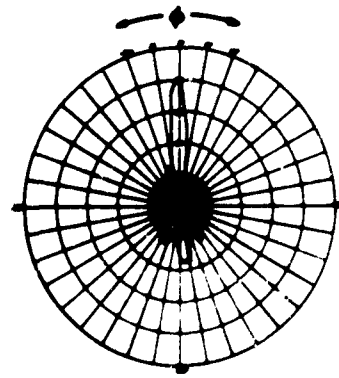
$\theta = 39^\circ$



$\theta = 47^\circ$



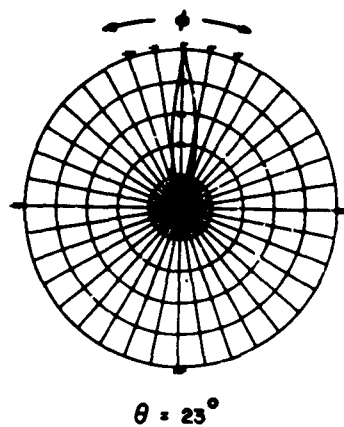
$\theta = 5^\circ$



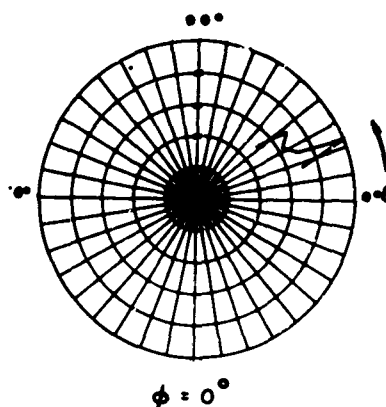
$\theta = 40^\circ$

Fig. B.100 San Francisco Feed at 11.8 Mc, E_θ
(Voltage Plot)

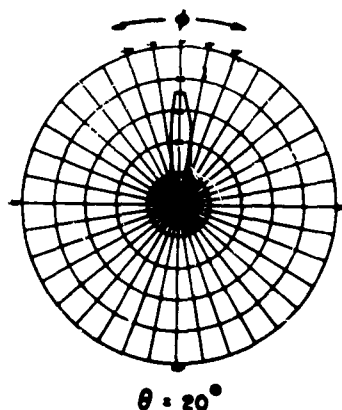
B-106



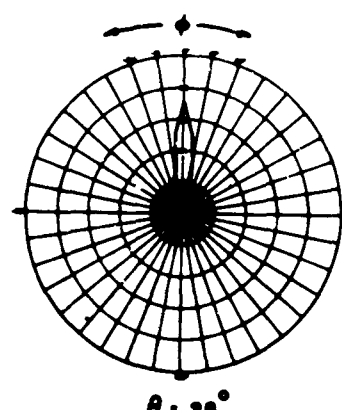
$\theta = 23^\circ$



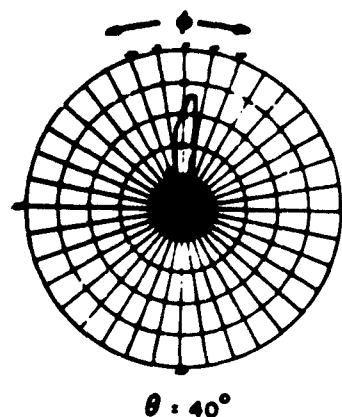
$\phi = 0^\circ$



$\theta = 20^\circ$



$\theta = 28^\circ$



$\theta = 40^\circ$

Fig. B.101 San Francisco Feed at 15.3 Mc, E_θ
(Voltage Plot)

B-107

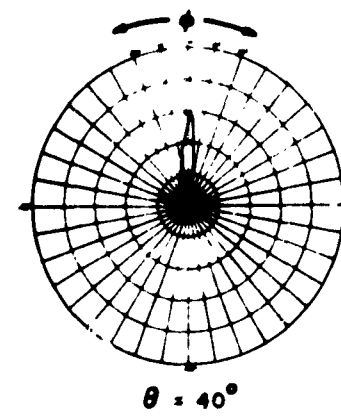
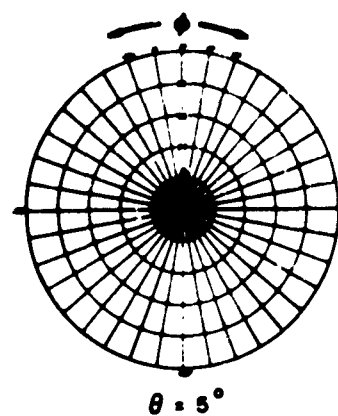
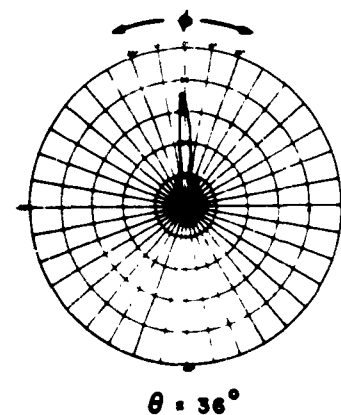
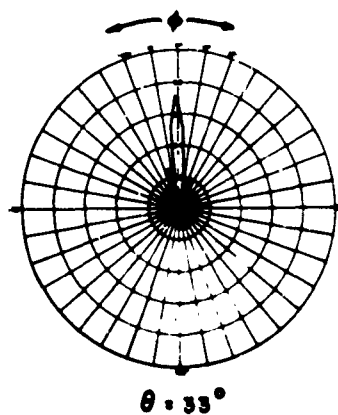
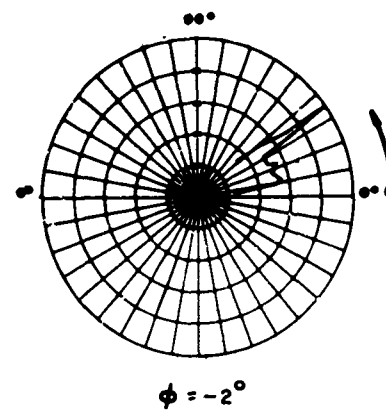
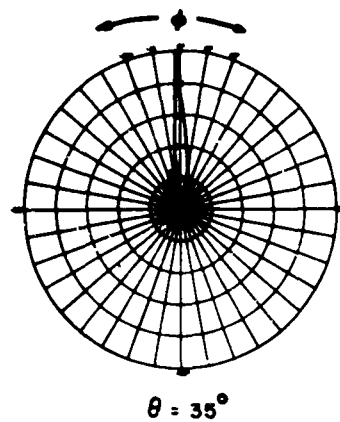


Fig. B.102 San Francisco Feed at 21.5 Mc, E_0
(Voltage Plot)

B-108

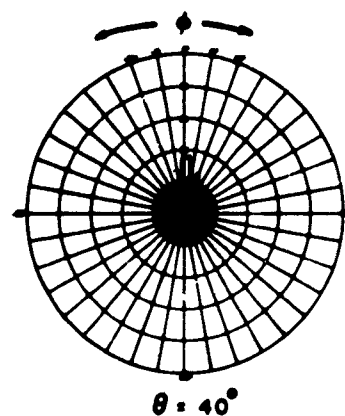
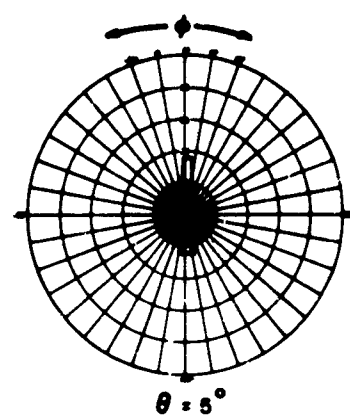
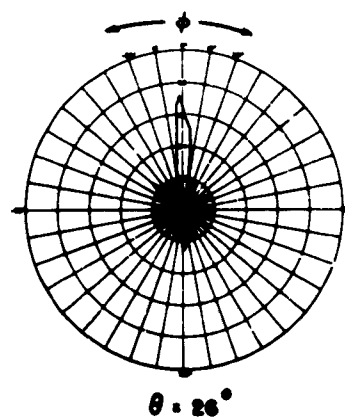
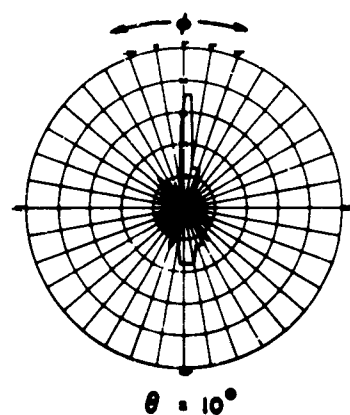
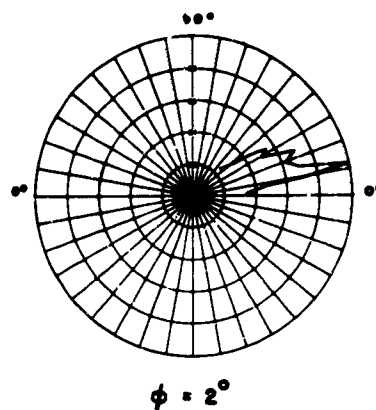
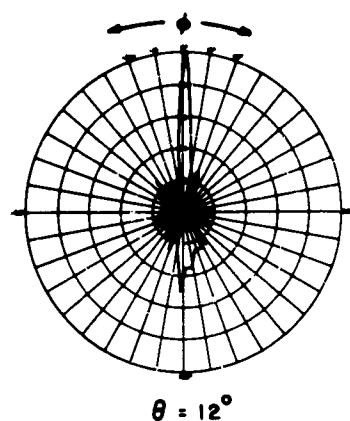
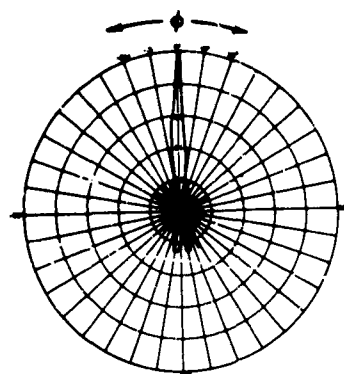
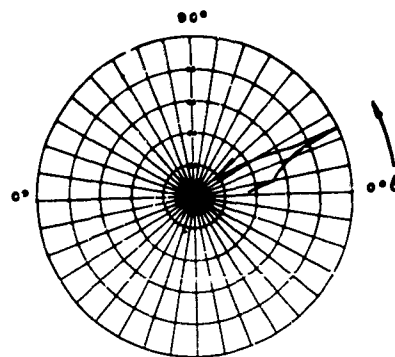


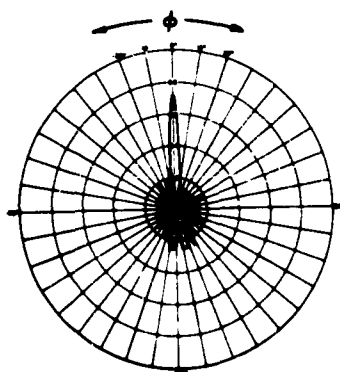
Fig. B.103 San Francisco Feed at 25.3 Mc, E_0
B-109 (Voltage Plot)



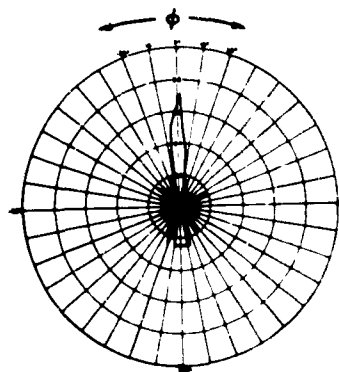
$\theta = 24^\circ$



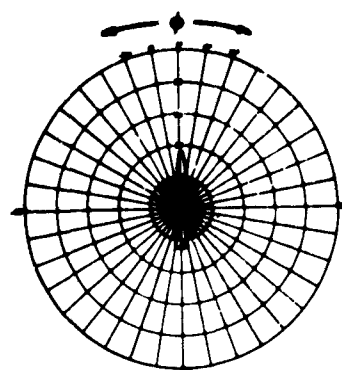
$\phi = 0^\circ$



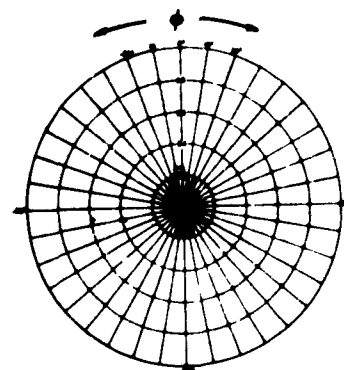
$\theta = 22^\circ$



$\theta = 26^\circ$



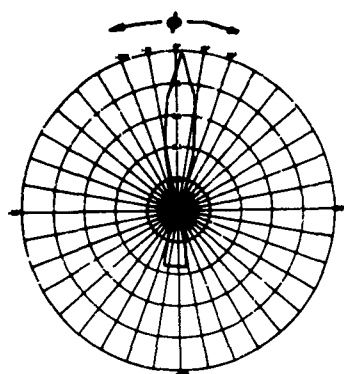
$\theta = 5^\circ$



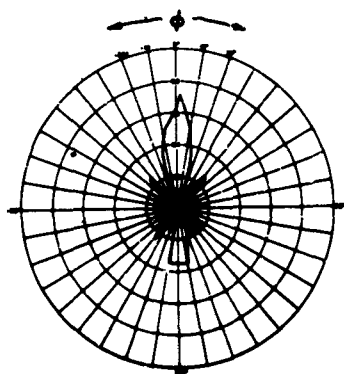
$\theta = 40^\circ$

Fig. B.104 San Francisco Feed at 30.0 Mc, E_θ
(Voltage Plot)

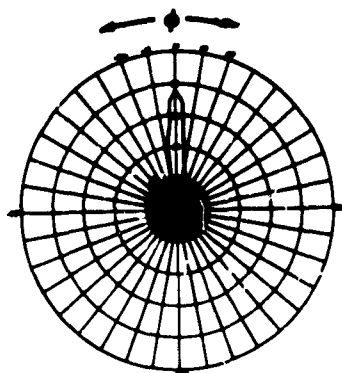
B-110



$\theta = 25^\circ$



$\theta = 18^\circ$



$\theta = 8^\circ$

Fig. B.105 Rhombic 4A at 4.1 Mc, E_ϕ
B-111 (Voltage Plot)

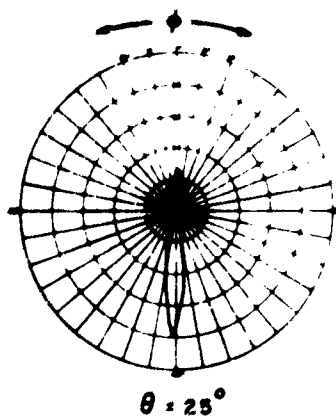
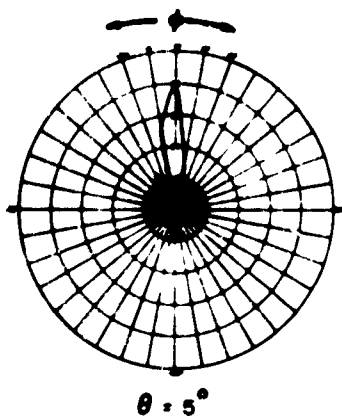
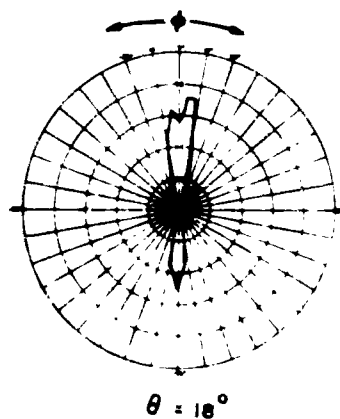
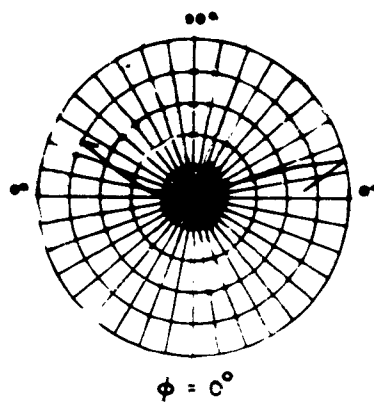
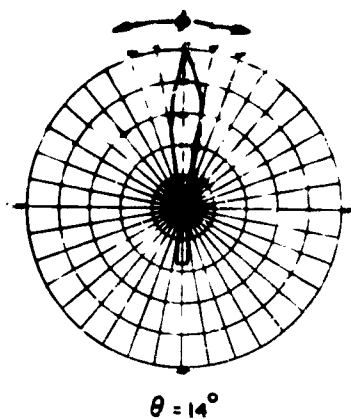


Fig. B.106 Rhombic 4A at 5.6 Mc, E_ϕ
(Voltage Plot)

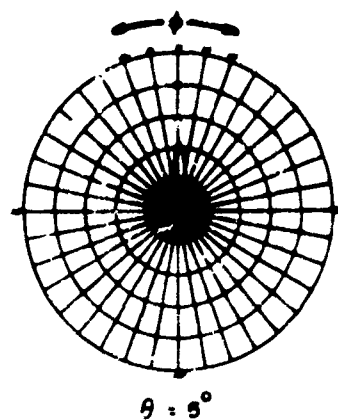
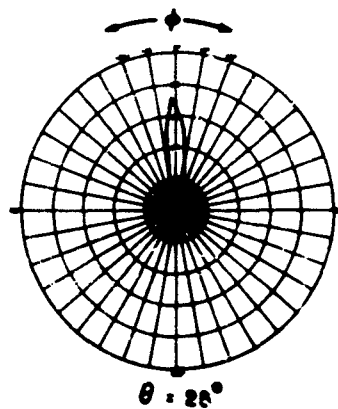
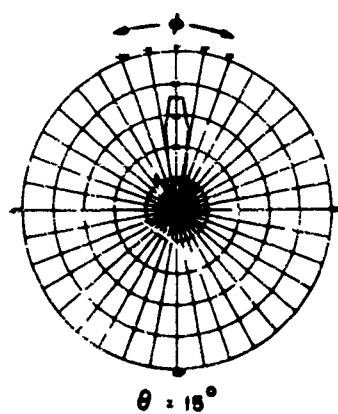
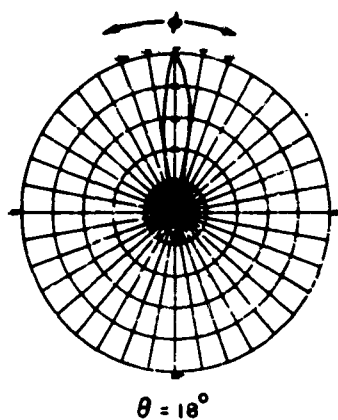


Fig. B.107 Rhombic 4E at 9.1 Mc, E.
(Voltage Plot)
B-113

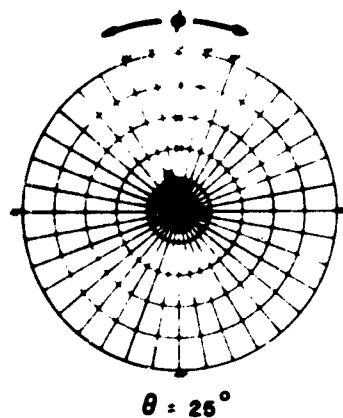
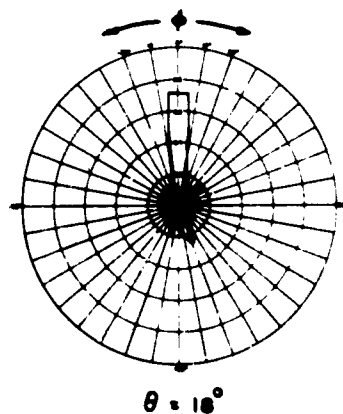
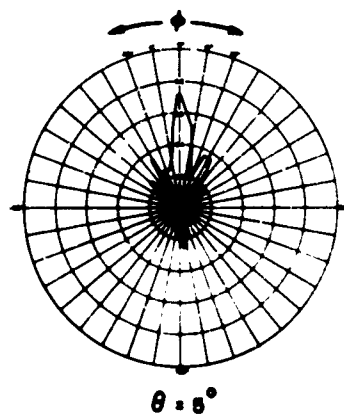
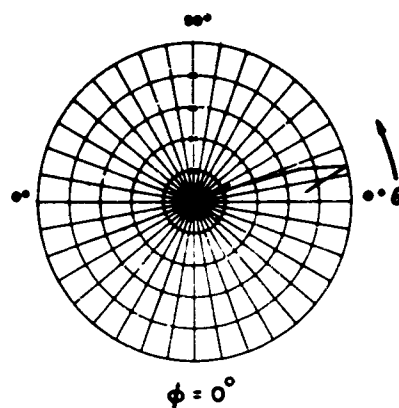
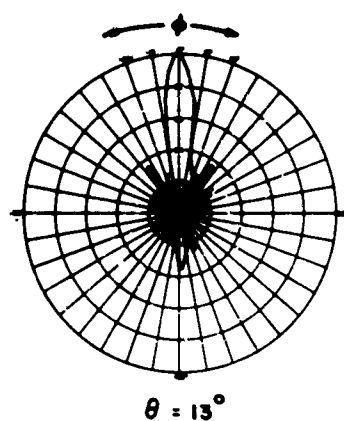


Fig. B.108 Rhombic 4B at 15.3 Mc, E_ϕ
(Voltage Plot)

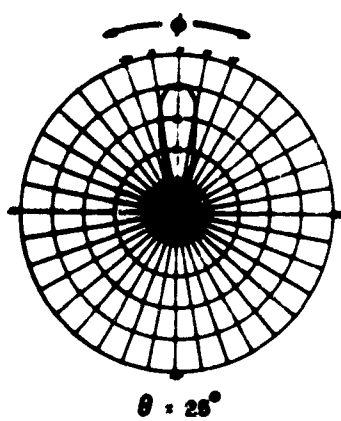
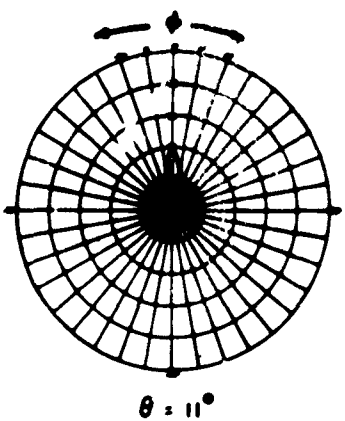
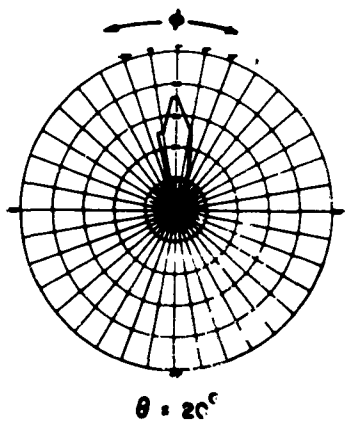
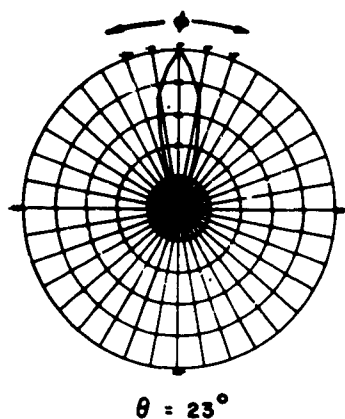


Fig. B.109 Rhombic 4C at 9.1 Mc, E_4
(Voltage Plot)

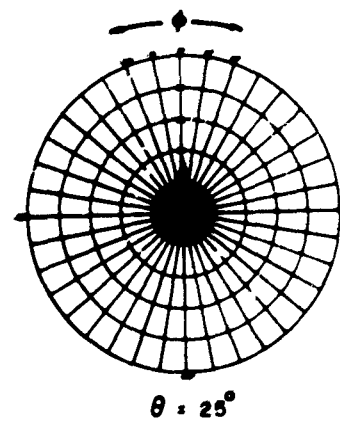
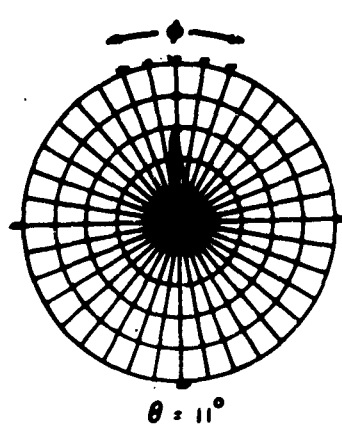
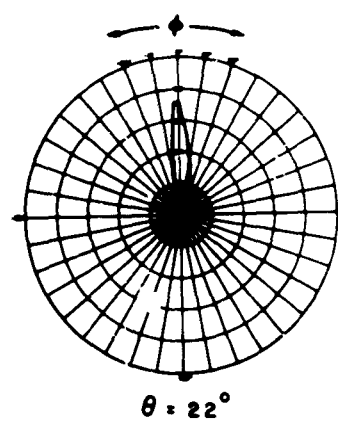
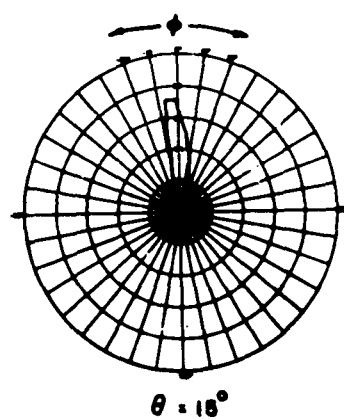
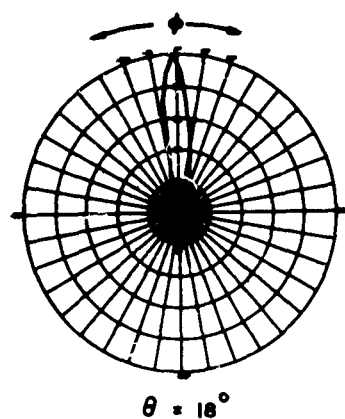


Fig. B.110 Rhombic 4C at 15.3 Mc, E_ϕ
(Voltage Plot)

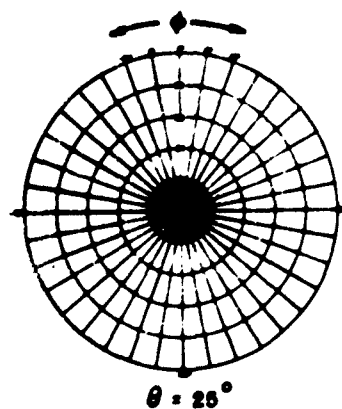
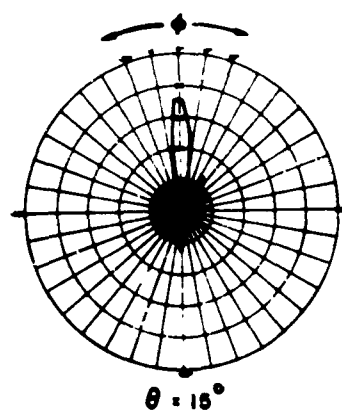
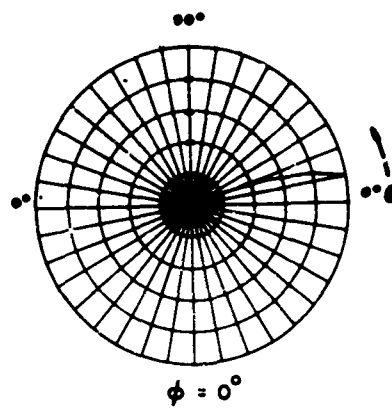
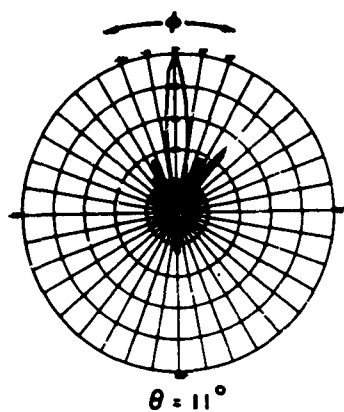


Fig. B.111 Rhombic 4C at 21.5 Mc, E_ϕ
(Voltage Plot)

B-117

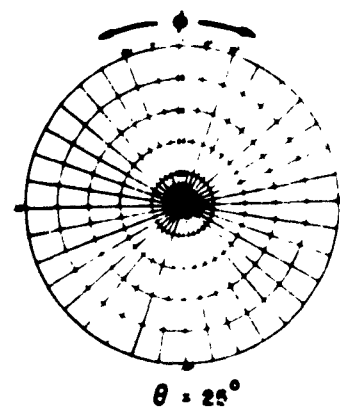
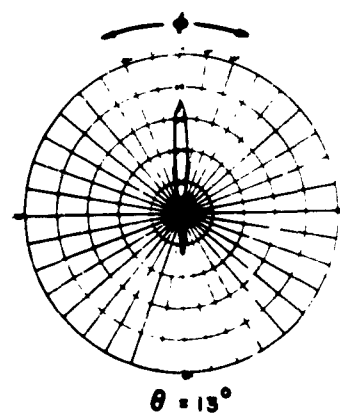
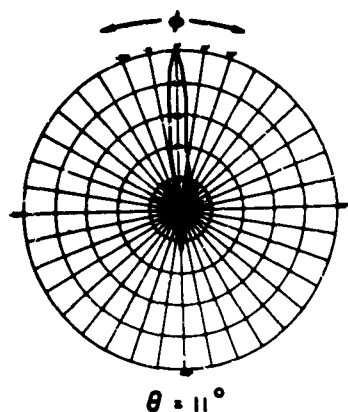


Fig. B.112 Rhombic 4C at 25.3 Mc, E_φ
B-118 (Voltage Plot)

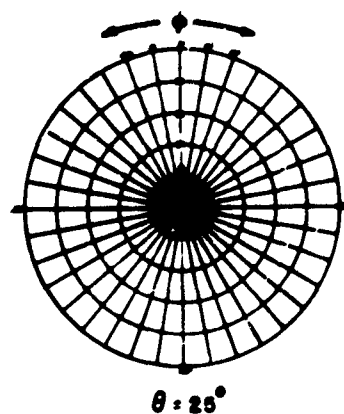
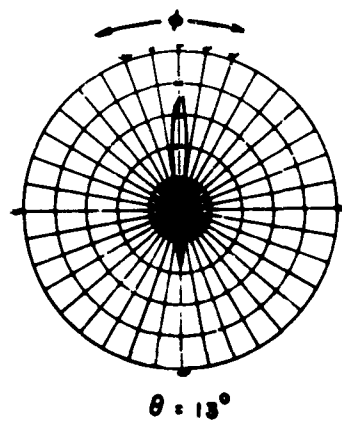
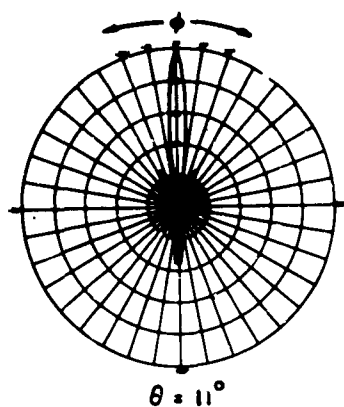


Fig. B. 113 Rhombic 4C at 30.0 Mc, E,
B-119 (Voltage Plot)

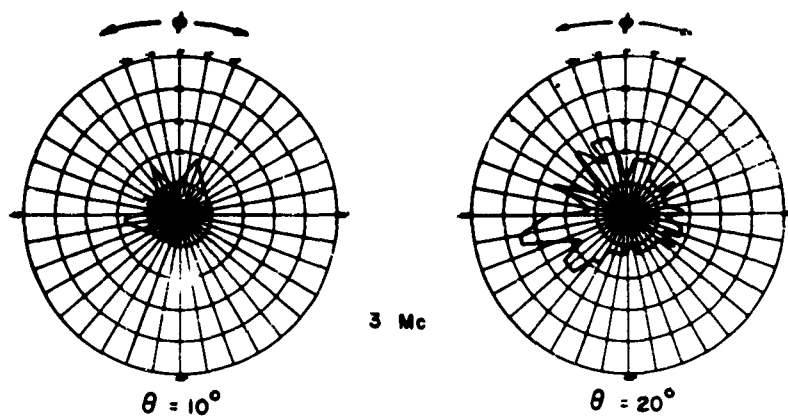


Fig. B.114a Anchorage Feed at 3 Mc, E_ϕ
(E_ϕ peak 15 db below E_θ peak)

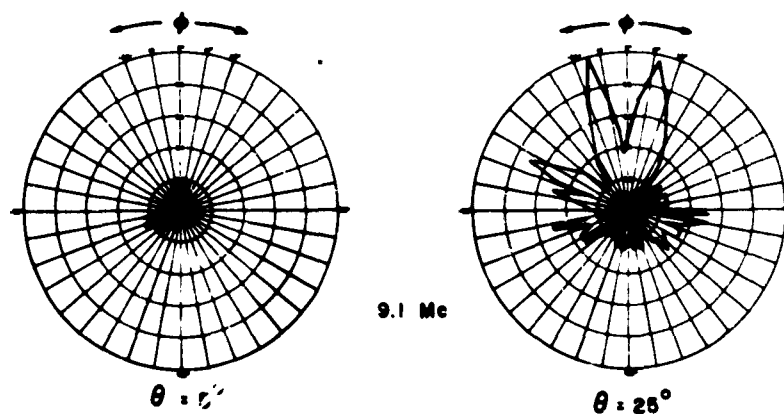


Fig. B.114b Anchorage Feed at 9.1 Mc, E_ϕ
(E_ϕ peak 12 db below E_θ peak)

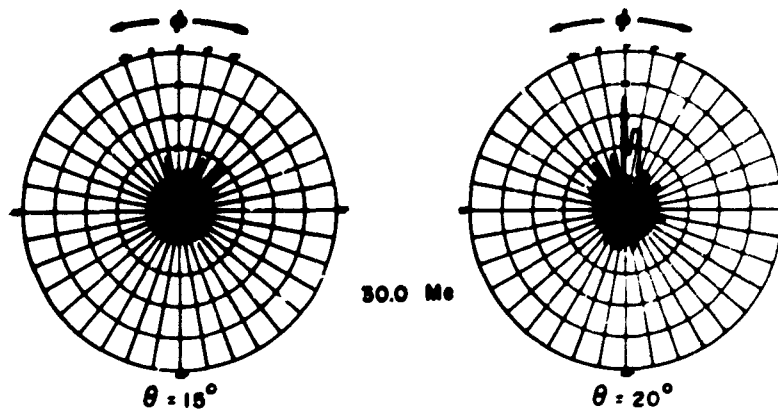
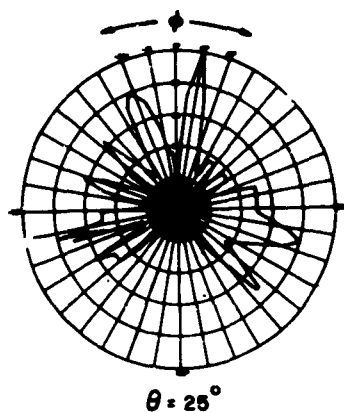
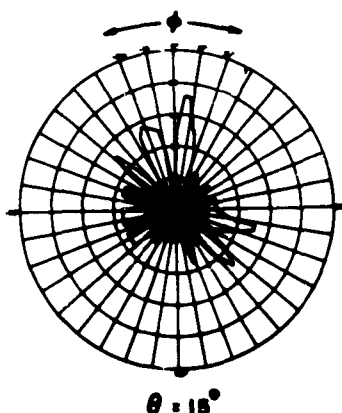


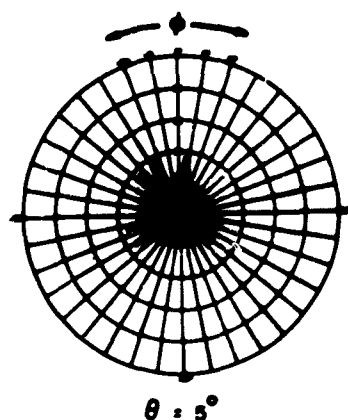
Fig. B.114c Anchorage Feed at 30.0 Mc, E_ϕ
(E_ϕ peak 5 db below E_θ peak)
Voltage Plot -



$\theta = 25^\circ$

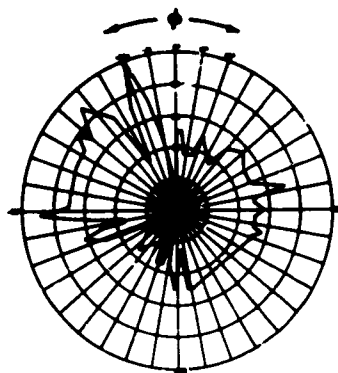


$\theta = 15^\circ$

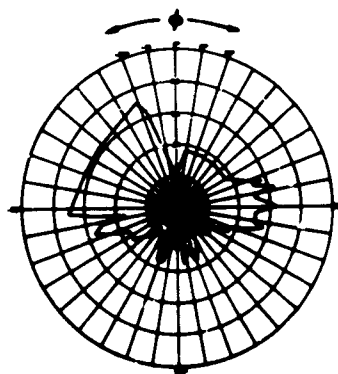


$\theta = 5^\circ$

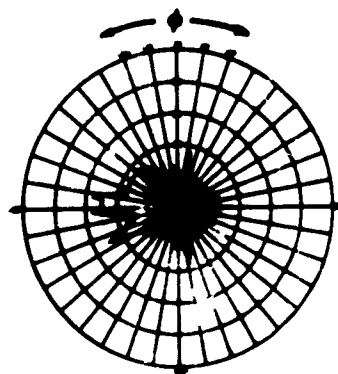
Fig. B.115 San Francisco Feed at 4.1 Mc, E_0
(E_0 peak 10 db below E_θ peak) - Voltage Plot
B-121



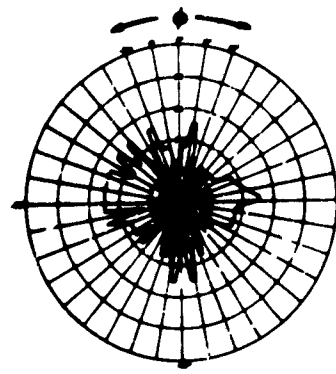
$\theta = 25^\circ$



$\theta = 19^\circ$



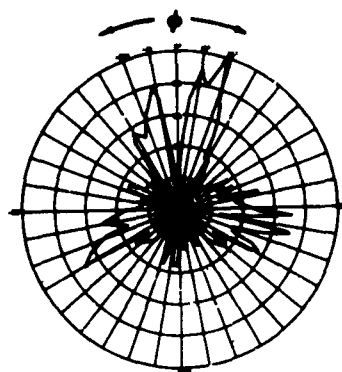
$\theta = 9^\circ$



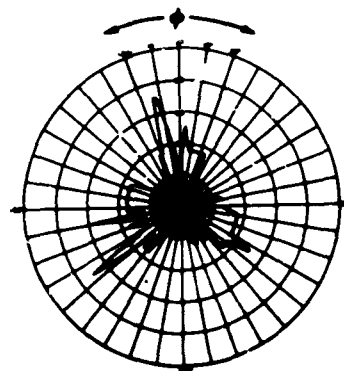
$\theta = 13^\circ$

Fig. B.116 San Francisco Feed at 5.6 Mc, E_ϕ
(E_ϕ peak 10.5 db below E_θ peak) - Voltage Plot

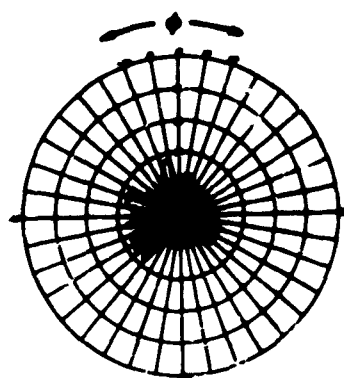
B-122



$\theta = 25^\circ$



$\theta = 12^\circ$



$\theta = 5^\circ$

Fig. 3.117 San Francisco Feed at 9.1 Mc, E_{ϕ}
(E_{ϕ} peak 9 db below E_{θ} peak)- Voltage Plot

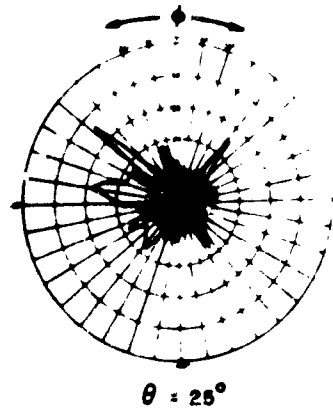
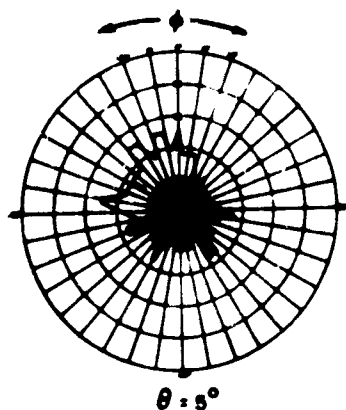
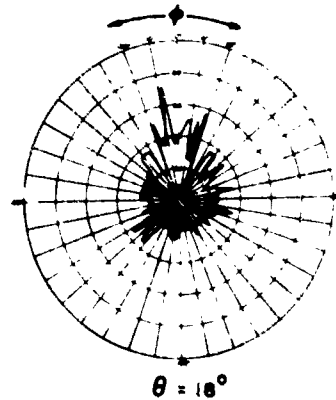
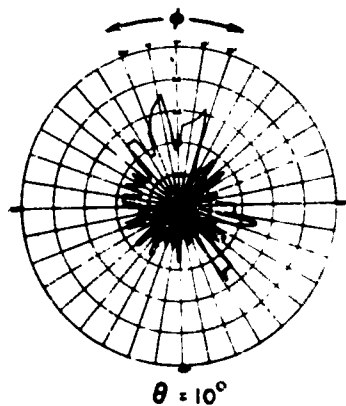
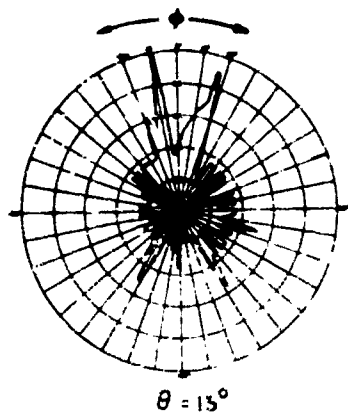


Fig. B.118 San Francisco Feed at 15.3 Mc, E_ϕ
 (E_ϕ peak 9 db below E_θ peak)-Voltage Plot
 B-124

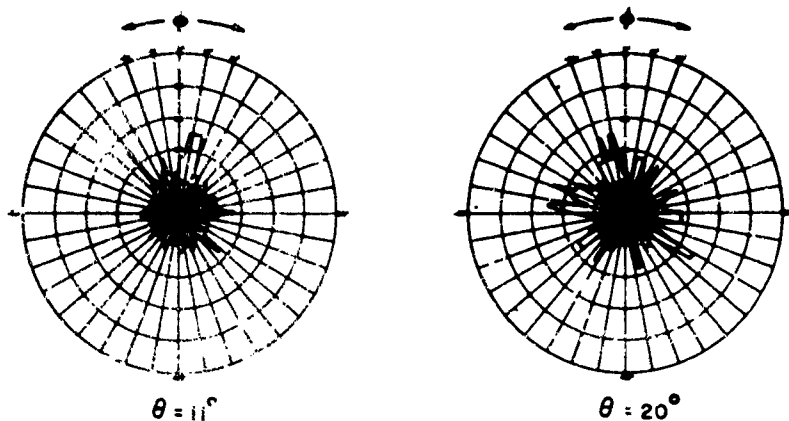


Fig. B.119a San Francisco Feed at 25.3 Mc, E_ϕ
(E_ϕ peak 9 db below E_θ peak)

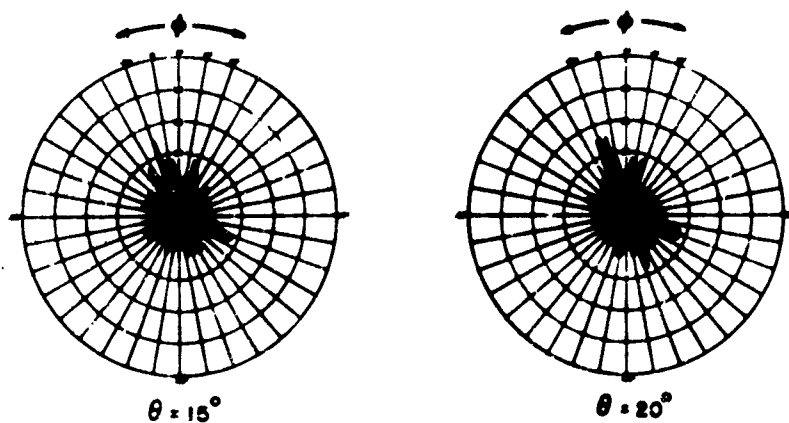


Fig. B.119b San Francisco Feed at 30.0 Mc, E_ϕ
(E_ϕ peak 11 db below E_θ peak) -Voltage Plot

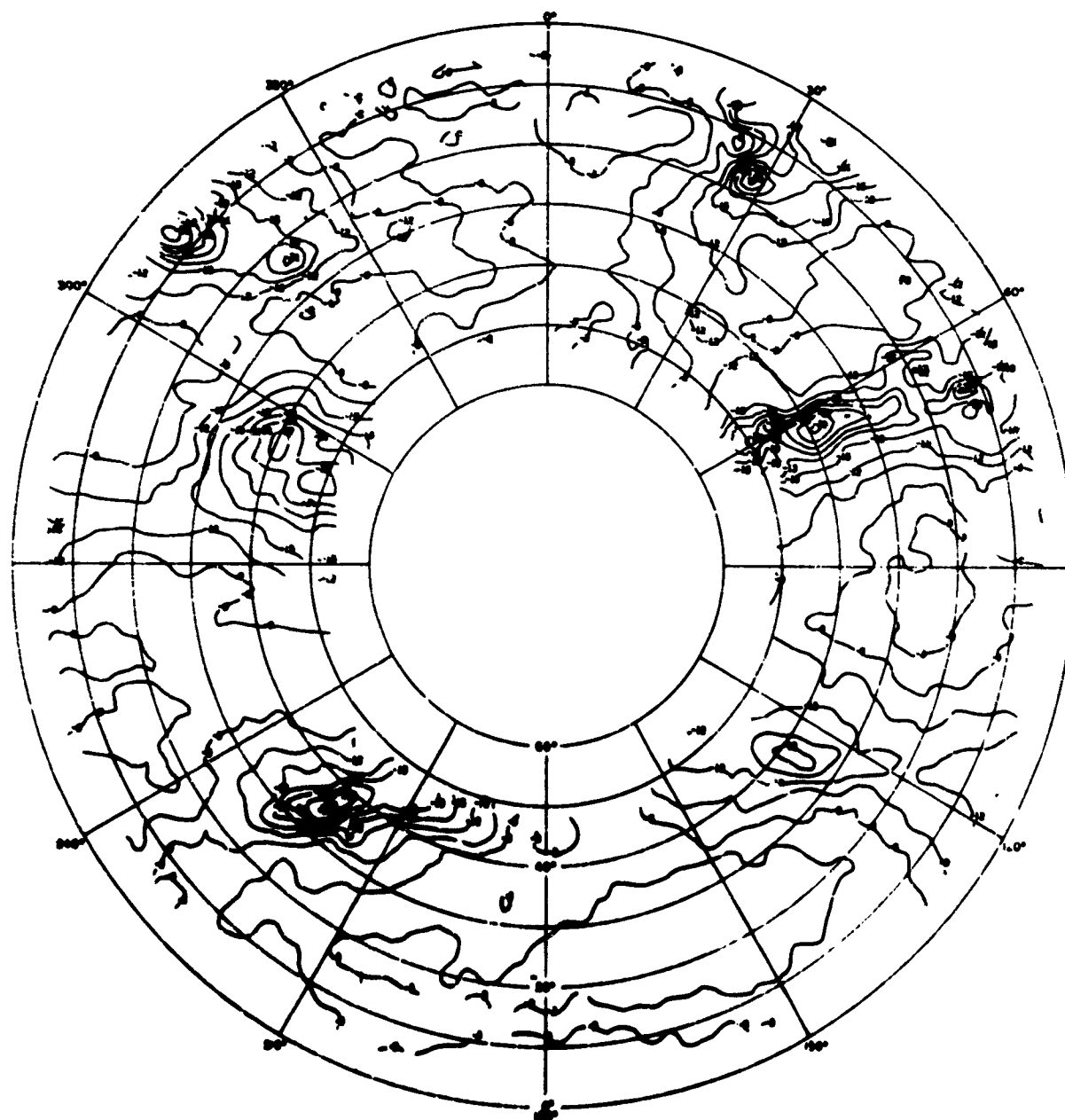


Fig. B. 120 Anchorage Feed at 2.25 Mc, E_0

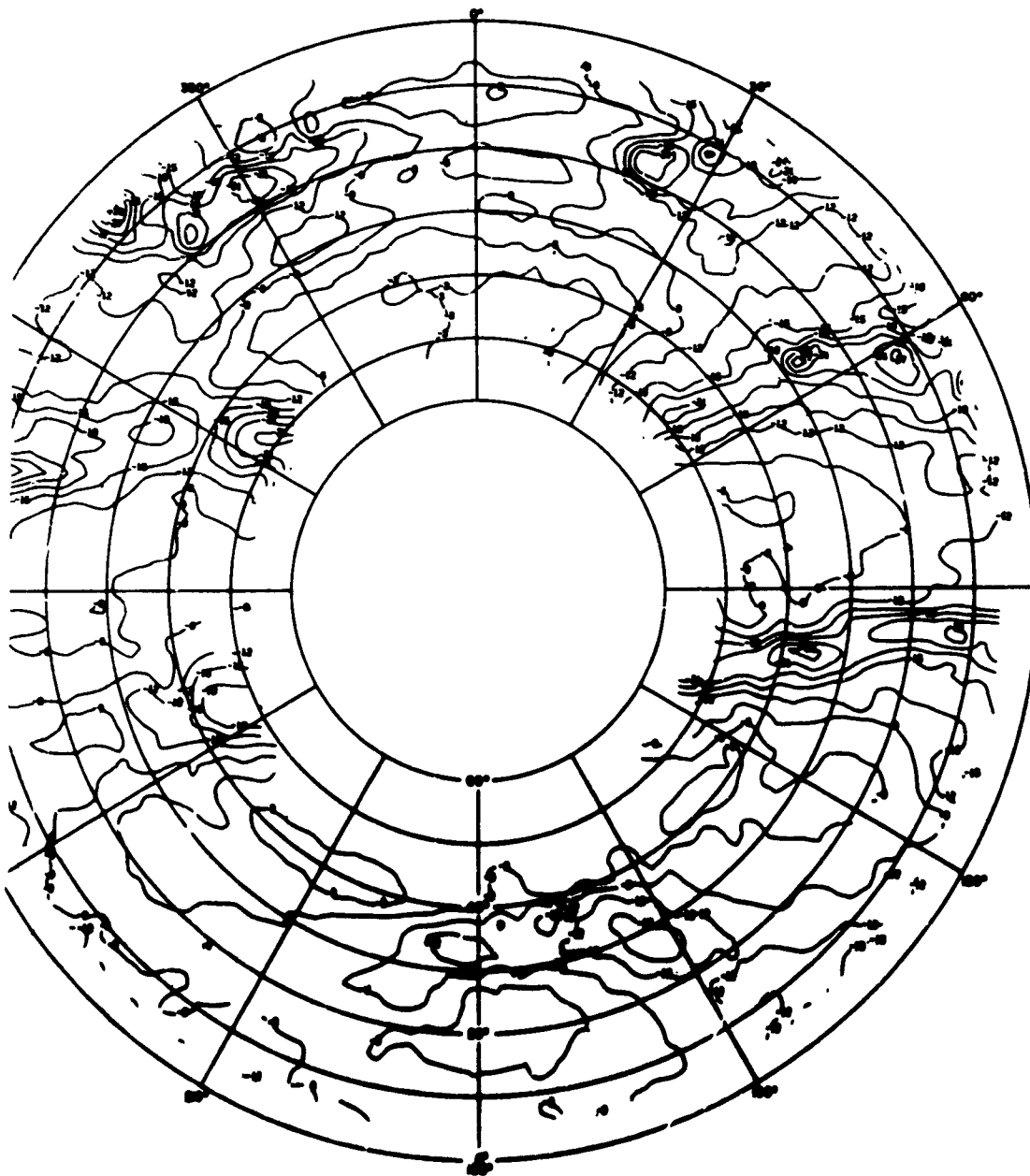


Fig. B. 121 Anchorage Feed at 2.6 Mc, E_0

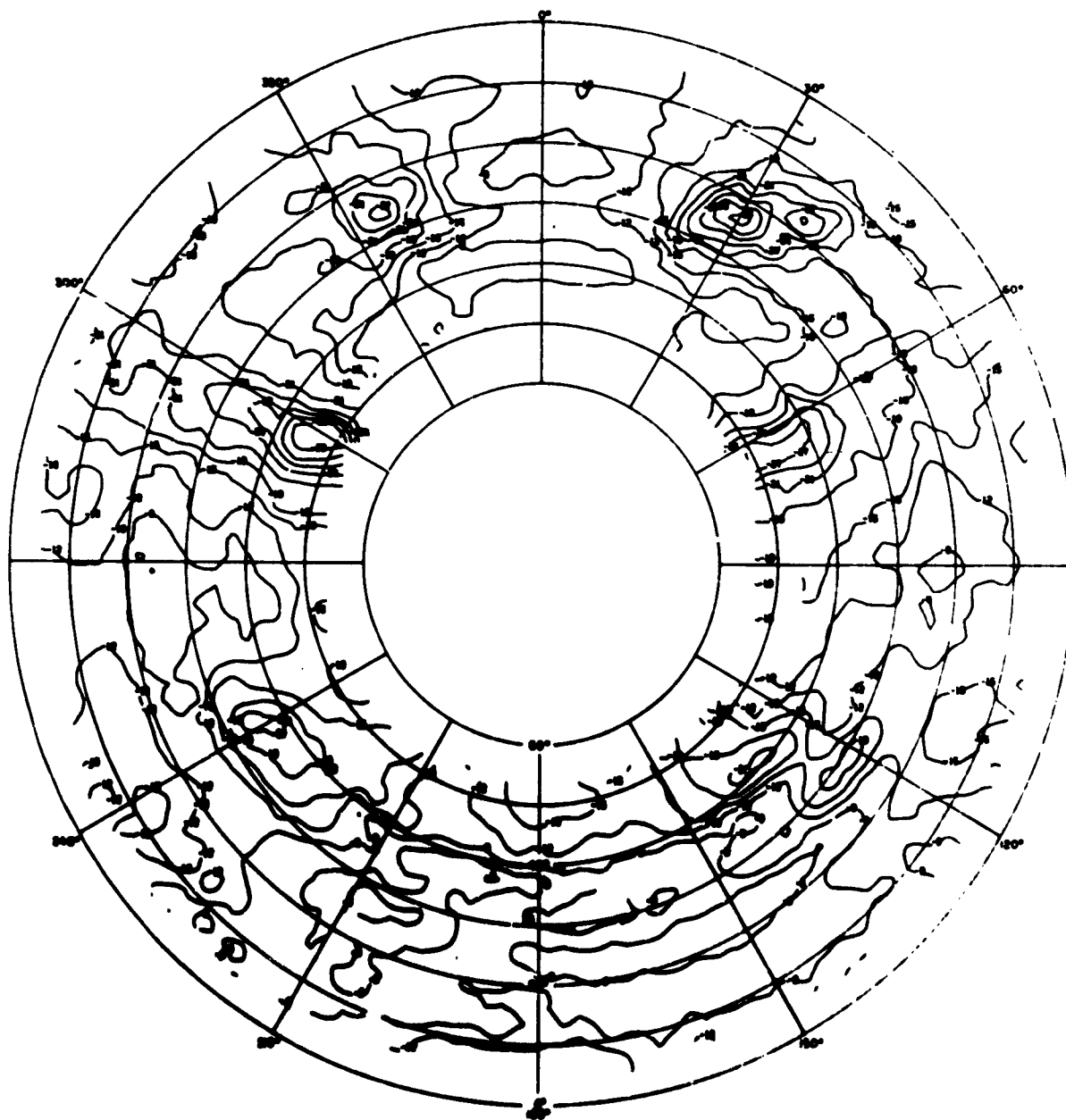


Fig. B. 122 Nandi-Canton Feed at 2.25 Mc, E_0

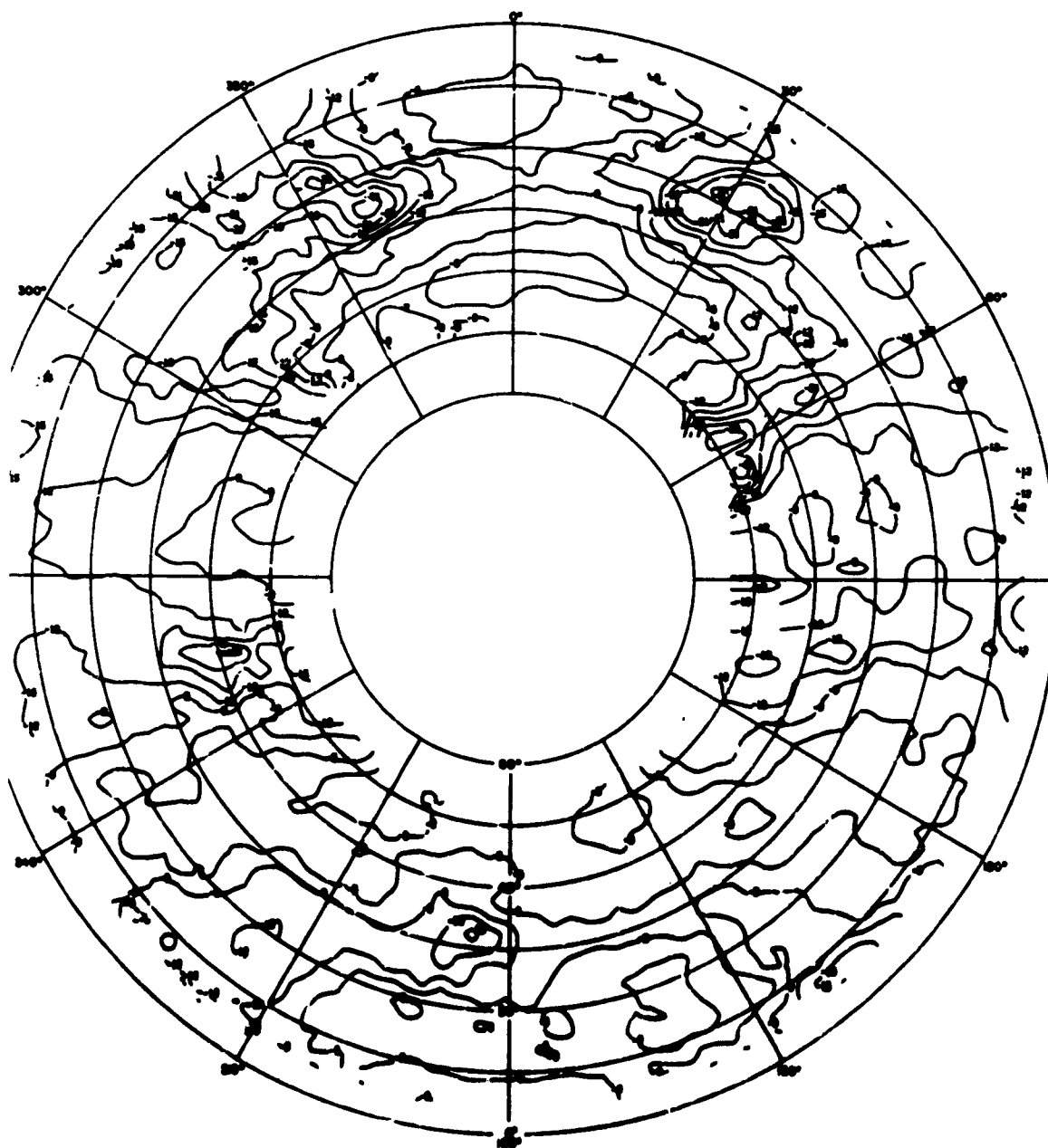


Fig. B. 123 Nandi-Canton Feed at 2.6 Mc, E_0

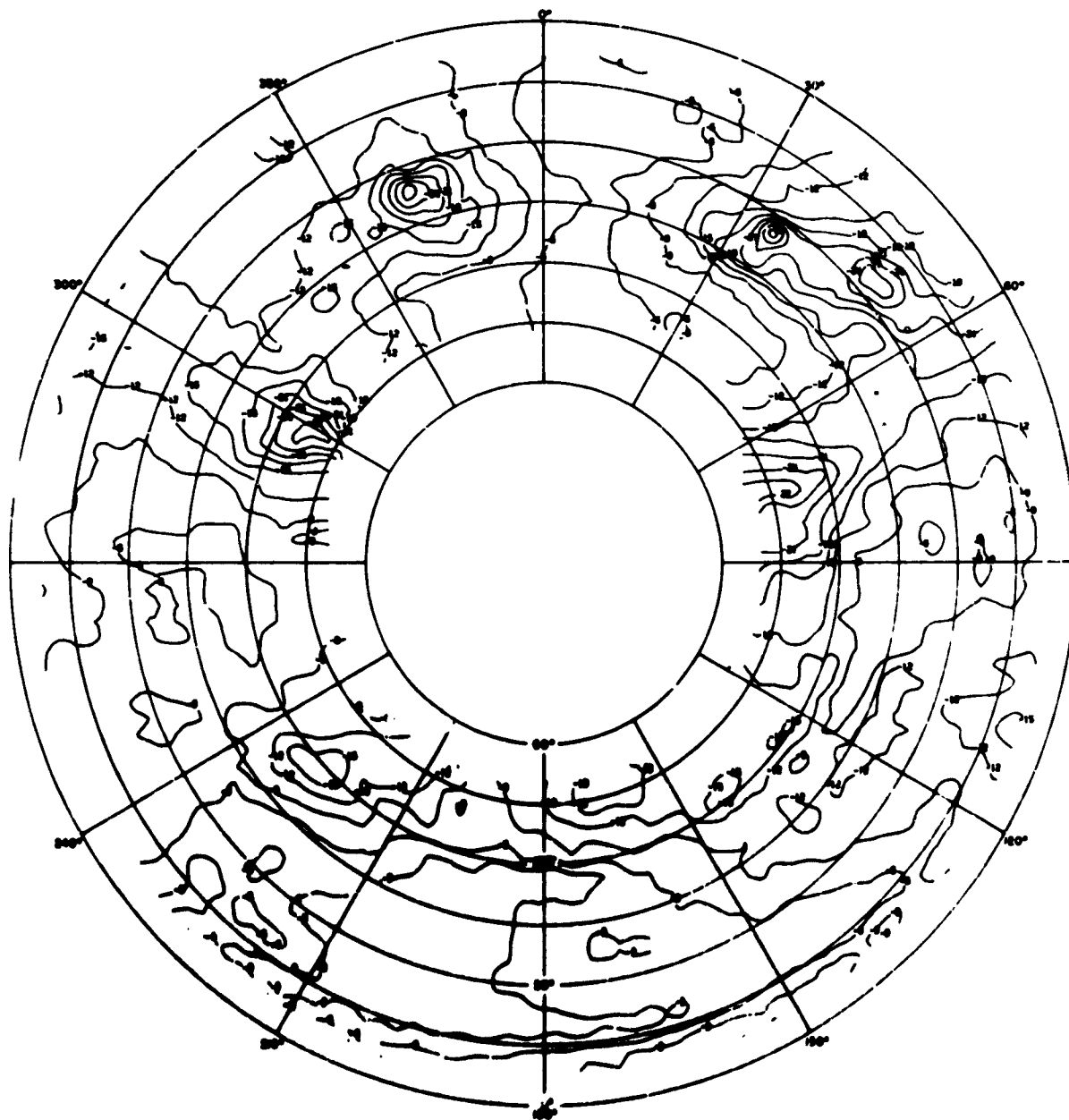


Fig. B. 124 Sydney Feed at 2.25 Mc, E_0



Fig. B.125 Sydney Feed at 2.6 Mc, E_0

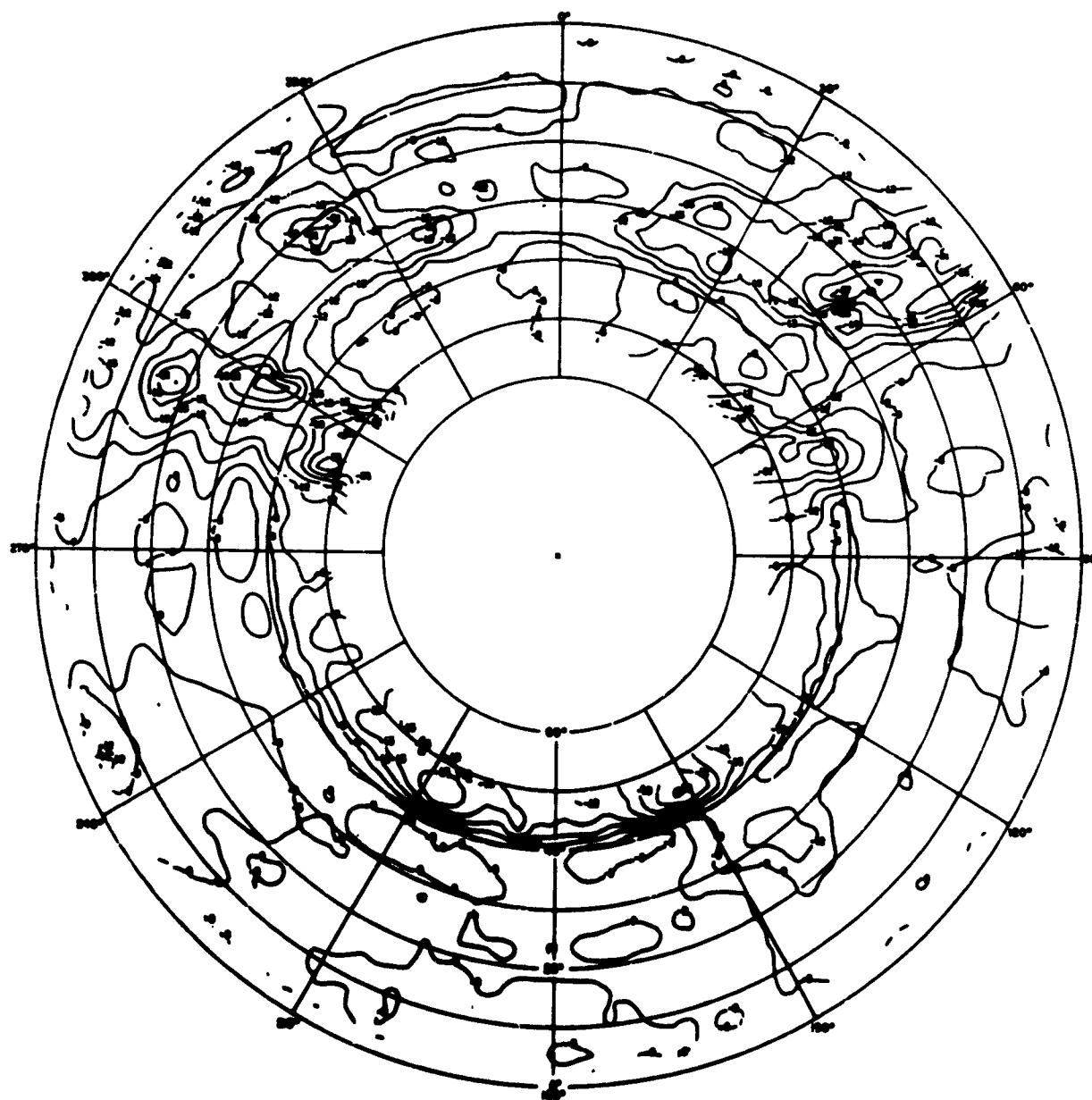


Fig. B. 126 San Francisco Feed at 2.25 Mc, E_0

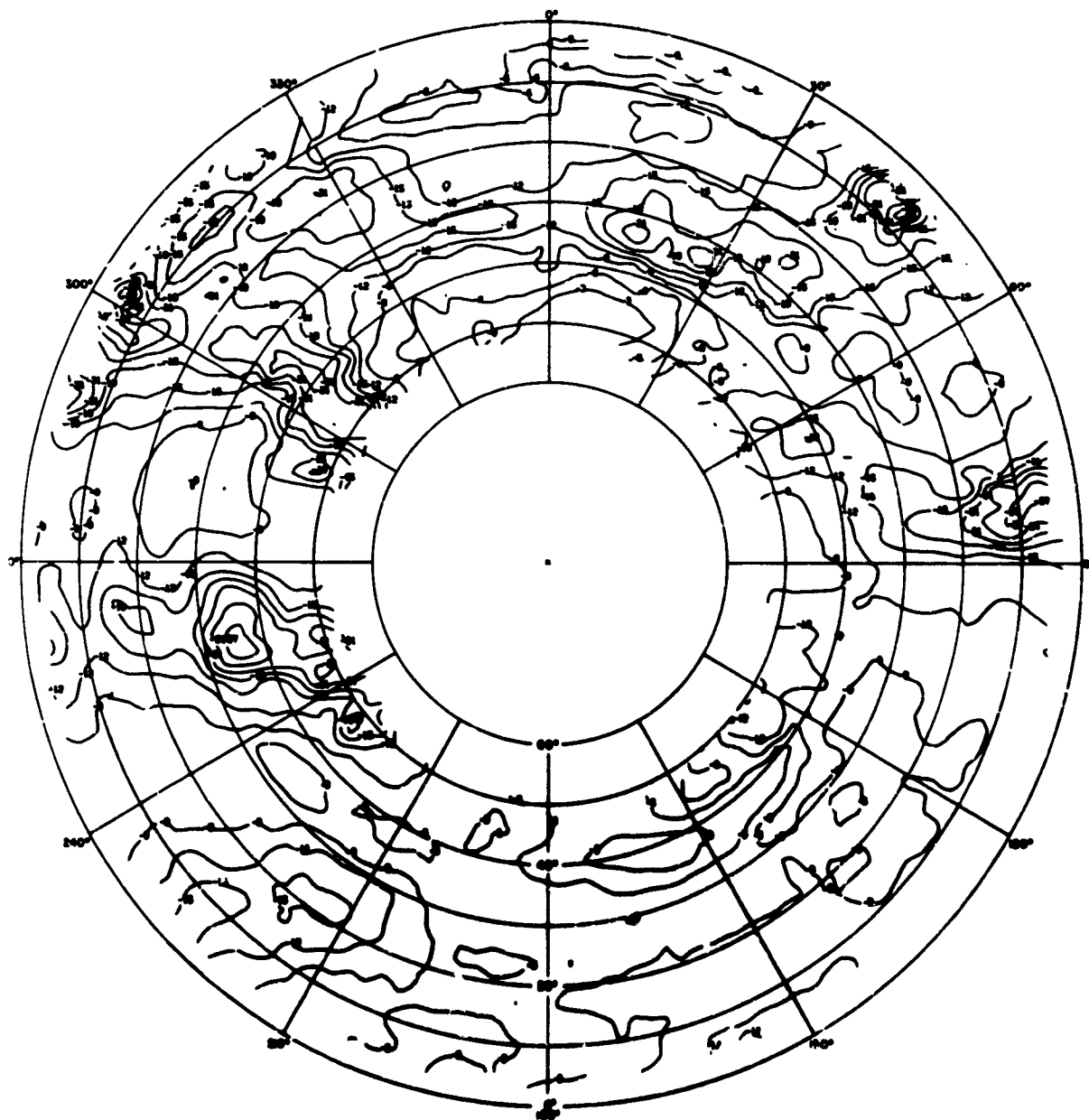


Fig. B.127 San Francisco Feed at 2.6 Mc, E_0



Fig. B. 128 San Francisco Feed at 35.0 Mc, E_0

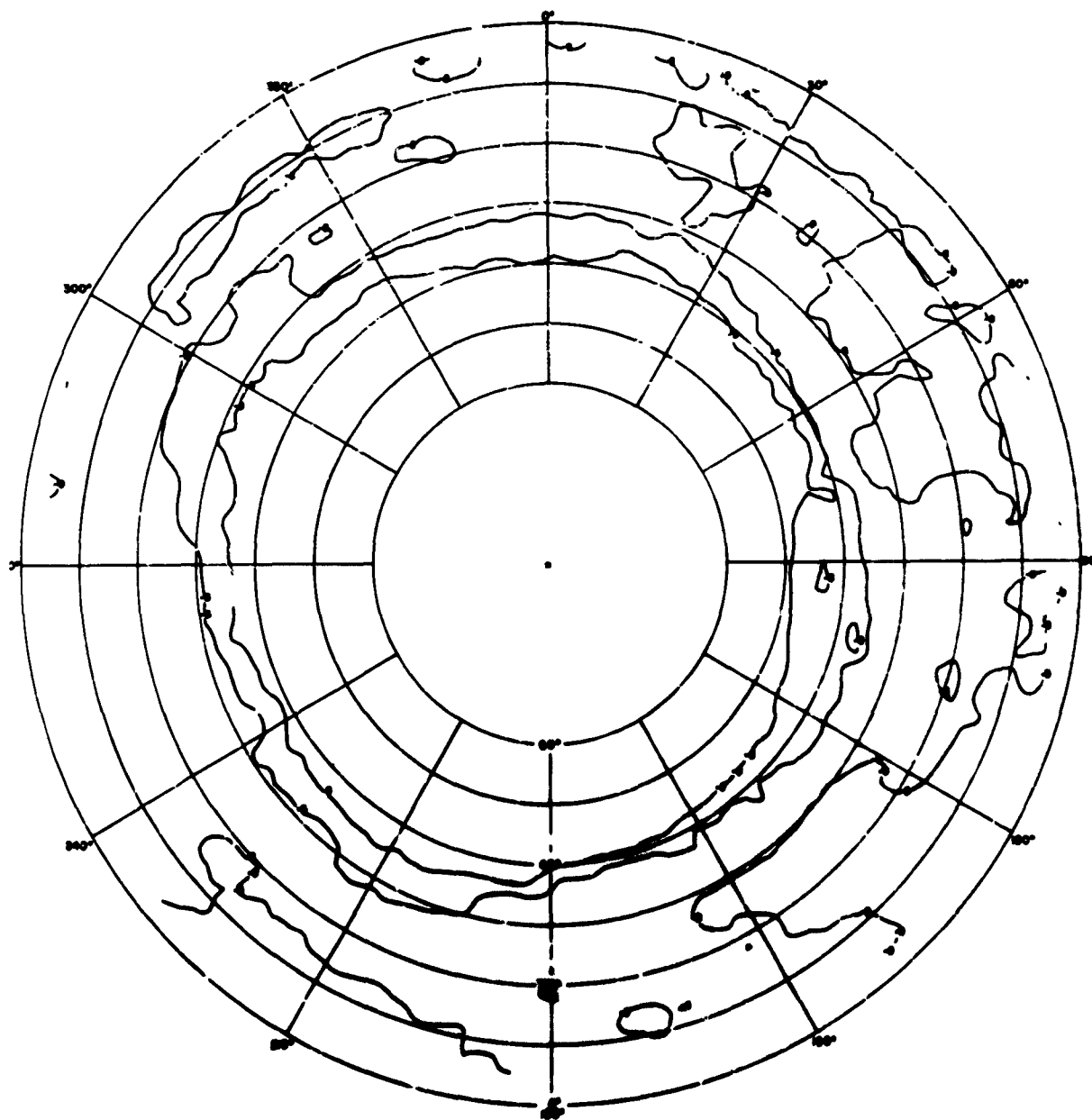


Fig. B. 129 Lens Excited as Biconical Antenna at 2.6 Mc, E_0

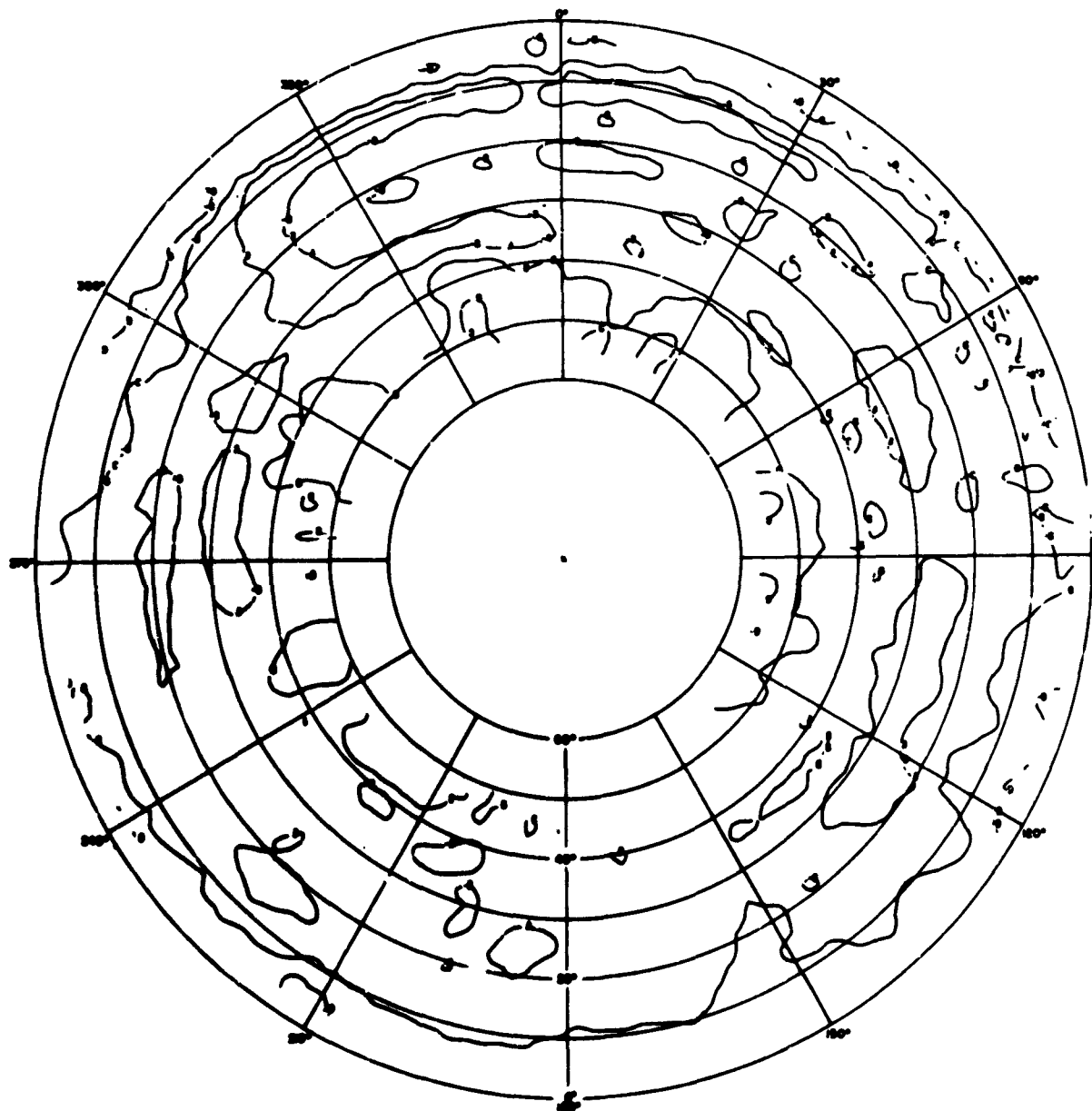


Fig. B. 130

NRL Monopole at 2.6 Mc, E_0

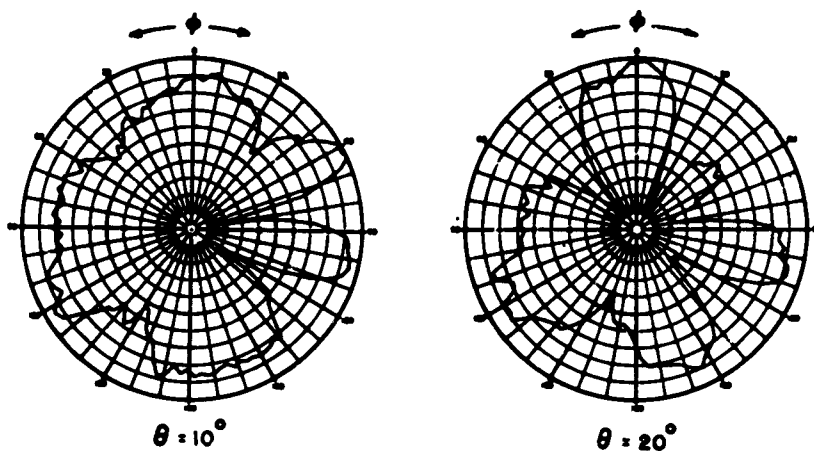


Fig. B.131 Anchorage Feed at 2.0 Mc, E_θ

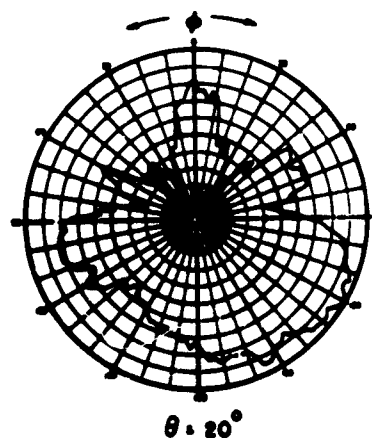


Fig. B.132 Nandi-Canton Feed at 2.0 Mc, E_θ

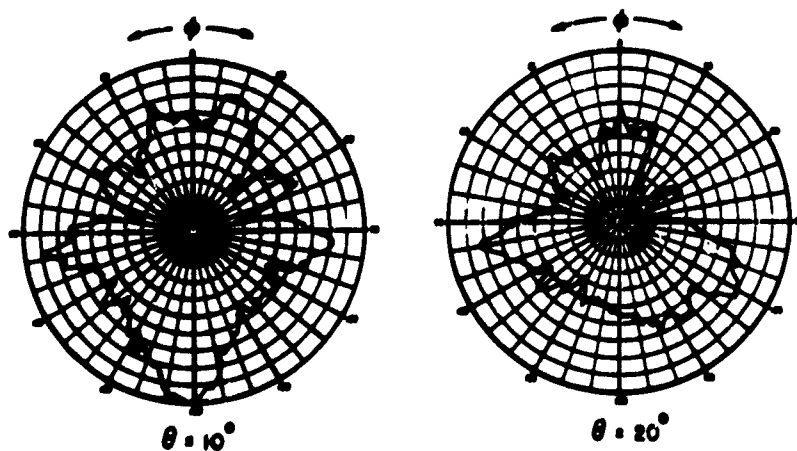


Fig. B.133 Sydney Feed at 2.0 Mc, E_θ

APPENDIX C

Optimized Feeds

INTRODUCTION AND SUMMARY*

This appendix describes the development and testing of optimized feeds for the Wire-Grid HF Lens Antenna at the FAA International Flight Service Receiver Station at Molokai, Hawaii. Utilization of these optimized feeds in the lens greatly increases its gain as well as reducing the theoretical azimuth pattern side lobes, particularly at the low-frequency end of the HF band. During the course of this program the originally installed Samoa and Nandi-Canton feeds used during the Joint Services Evaluation described in the body of this report were replaced with optimized feeds. Measurements made on these optimized feeds confirmed their predicted high efficiency of approximately 50 percent. The calculated efficiency of the optimized feeds is greater than that of the originally installed feeds by approximately 10 db at the low-frequency end of the band and 8 db at the high-frequency end of the band. Using a ground-based transmitter the measured power gain increase of the lens using the optimized feeds was approximately 7 db at the low-frequency end of the band and approximately 4 db at the upper end of the band. Measured gain increases more closely approximating the feed efficiency increases would be expected if the ground-based transmitter were replaced with an airborne transmitter located at the elevation angles corresponding to the peak of the lens elevation patterns.

* This appendix is a condensation of the Final Report, "Optimized Feeds for the Wire-Grid Lens HF Antenna at the FAA Receiver Station, Molokai, Hawaii," by F. B. Harris, Jr., R. L. Tanner, and E. M. T. Jones, Contract No. ARDS-598, Modification 14, Project 232-001-02C (formerly 113-23-1D), December 1965 (see Reference 5)

C.1 Design

The optimized feeds developed for the Molokai Wire-Grid Lens Antenna were designed using the theoretical analyses developed on a number of theoretical contracts.^{7, 8, 9} In this design, mutual coupling effects amongst all parts of a feed pair are fully accounted for. Extensive use was made of the experience gained in designing optimum feeds for the RADC Wire-Grid Lens Antenna which are described in Reference 6. The end-fire array which proved optimum for the feeds in each of these antennas is the two-hop ramp illustrated in Fig. C.1. In the Molokai antenna, two of these end-fire arrays are connected in parallel to form a single feed as illustrated in Fig. 5.1.

As is shown in the figure, the upward directed ramp starts at the outer perimeter of the lens on the lower grid and terminates at a phase reversing transformer located 25 feet in from the edge of the lens on the upper grid. The downward directed portion of the ramp inboard from the phase reversing transformer terminates in the network shown which is located 75 feet in from the edge of the lens on the lower grid. Each ramp segment is composed of two wires whose center-to-center spacing is adjusted to maintain a characteristic impedance of 210 ohms. No capacitive loading is used along the ramps so that waves travel along them at nearly free space velocity. However, because they make an appreciable angle with respect to the grids the velocity of the wave on the ramps when projected on the midplane between the grids is nearly equal to the velocity of a wave propagating between the grids of the lens.

The purpose of the phase reversing transformer is easily understood when it is remembered that it is only the vertical component of current flowing in the ramps which couples to the vertical electric field of the wave propagating between the grids. Inspection of the figure shows that the phase reversing transformer makes the vertical component of the inward traveling current on the ramp outboard from the transformer in phase with the vertical component of the inward traveling current on the ramp inboard from the transformer. Thus, both ramp segments couple in-phase to the fields in the lens and coupling efficiencies on the order of 50 percent over the 3 to 30 Mc band are obtained as is shown in Sec. C.2.1.

The terminating network at the inboard end of each ramp is a high pass filter. At the upper end of the frequency band the terminating resistance in the filter matches quite closely the characteristic impedance of the ramp so that only an inward traveling current exists on the feed. However, at the low-frequency end of the band the termination presents an appreciable mismatch to the ramp so that besides the inward traveling current on the ramp there is also a strong outward traveling current. The terminating network

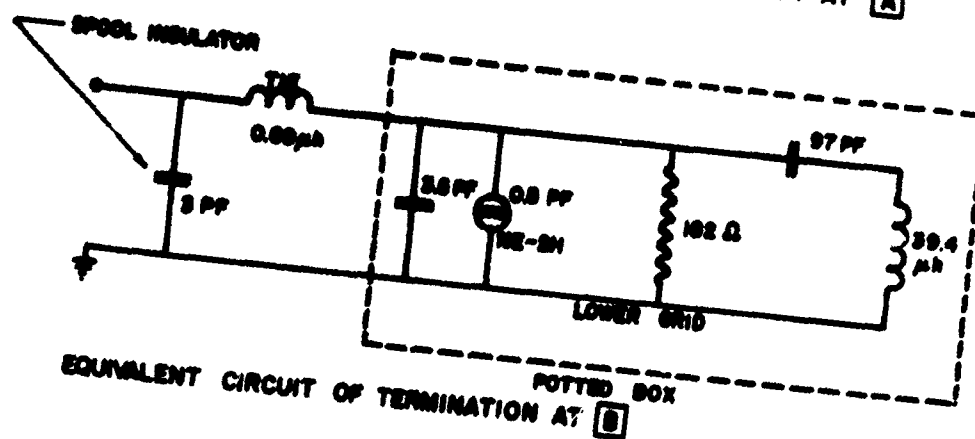
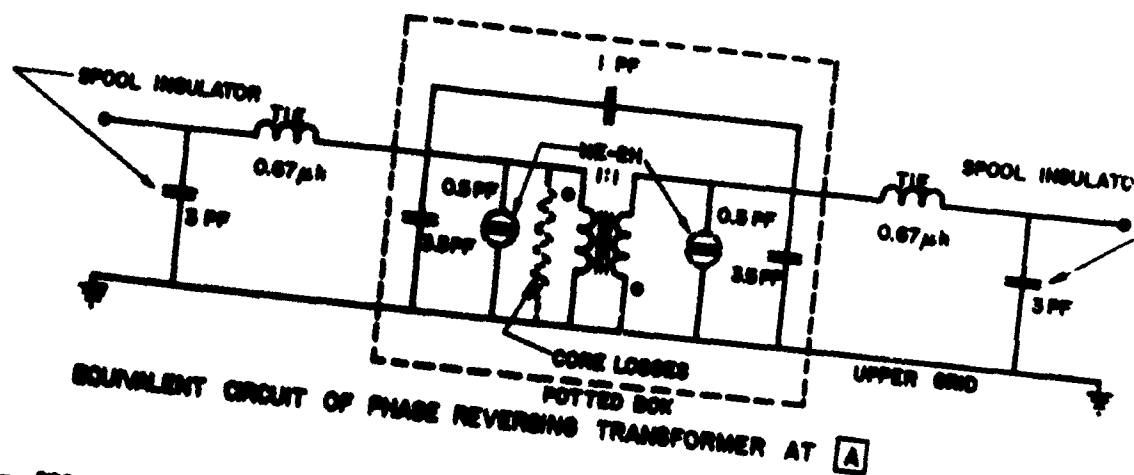
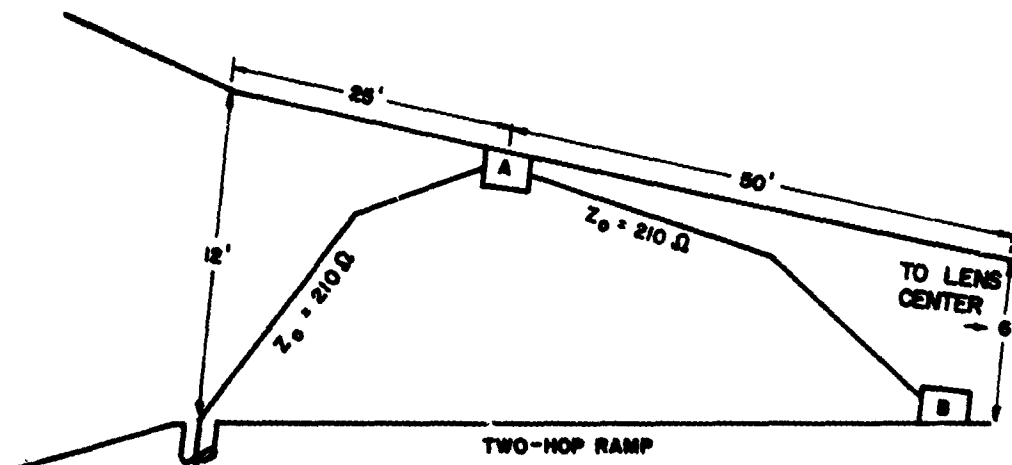


Fig. C.1 Equivalent Circuit of Optimized Two-Hop Ramps for Molokai Wire-Grid Lens Antenna

is designed so that this outward traveling current radiates a field with the proper magnitude and phase to reduce the amplitude of the minor lobes of the radiation pattern generated by the inward traveling ramp current. At the upper end of the band the inward traveling current on the ramp generates radiation patterns with acceptably low minor lobes so that no outward traveling current wave on the ramp is required

The elements used in the terminating network were chosen by the computer to optimize the antenna gain over the 3 to 30 Mc band. This was done by assigning initial values to the network elements and having the computer calculate the antenna gain at a series of frequencies across the band. Then the computer varied one of the elements in the network and again computed the antenna gain at the same test frequencies. If the gain averaged over the band were higher, it would continue to vary the element's value in the same direction until a maximum gain was achieved. If the gain were initially lower, it would change the element value in the opposite direction and proceed again until maximum gain was achieved. After the first element was optimized, each element would be optimized in turn and then the process iterated until the optimum value of each element was determined to achieve maximum gain averaged over the band.

The theoretical radiation patterns of the lens using these optimized feeds are illustrated in Fig. C. 2. Inspection of these patterns shows that they have appreciably lower minor lobes than the corresponding lens patterns using the original feeds shown in Fig. 5.5, particularly at the low-frequency end of the band. Because the measured minor lobe level of the originally installed feeds agreed quite closely with theoretical predictions, as shown in Fig. 6.21, it is expected that the theoretically predicted low minor lobe level of the optimized feeds would be realized if new airborne pattern measurements were made on the lens.

C. 2 Measured Performance

Two optimized feeds were installed in the Molokai Wire-Grid Lens to replace the original Nandi-Canton and Samoa feeds. A number of measurements were made before and after the installation to determine the improvement in lens performance obtained with the new feeds. All of these measurements were directed towards verifying the theoretically predicted improved efficiency of the new feeds as well as their impedance properties. No pattern measurements were made because of the experience during the initial evaluation of the lens described in Reference 1 when it was found that ground-based pattern measurements tended to yield irregular shaped patterns.

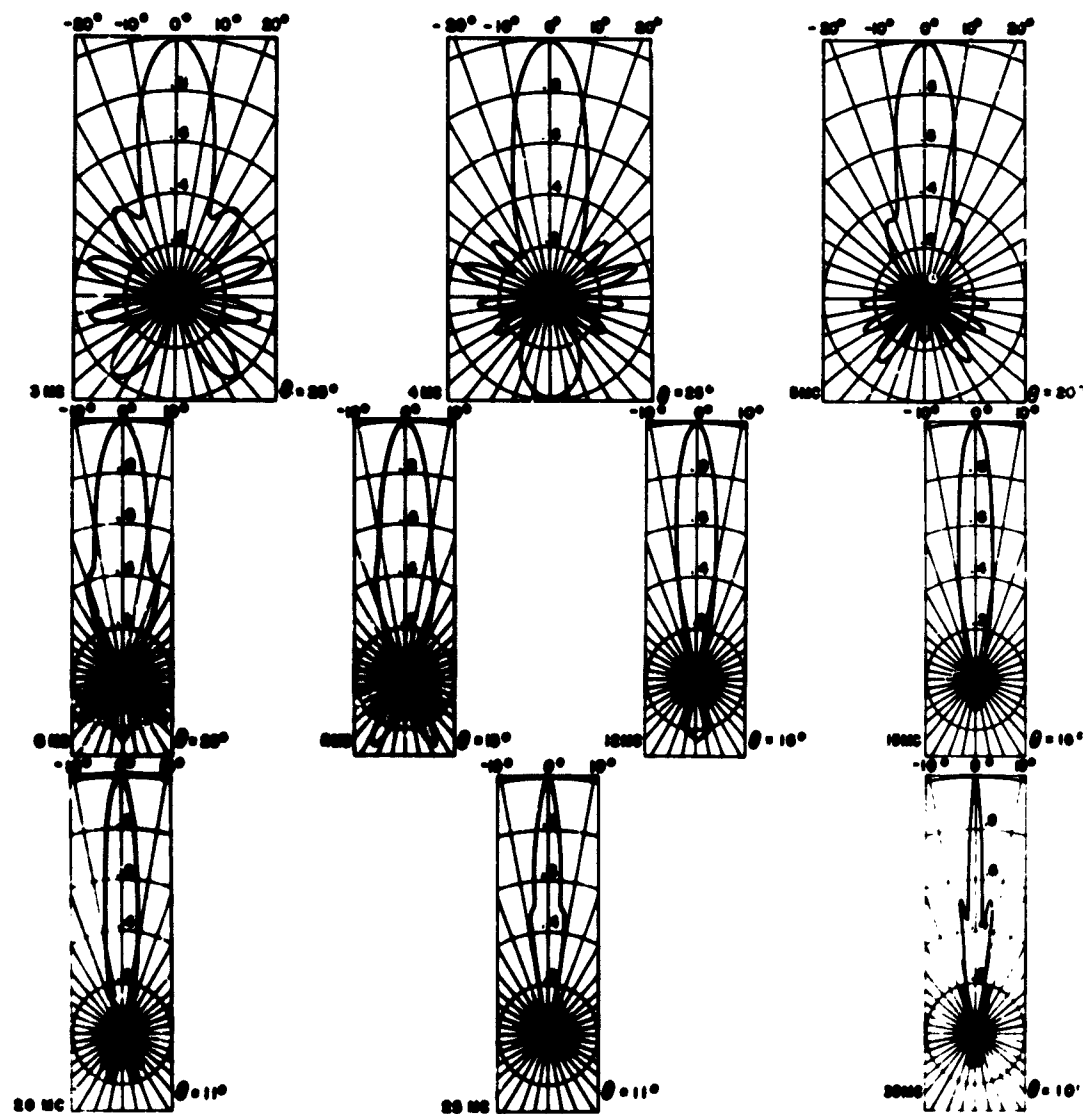


Fig. C.2

Calculated Azimuth Voltage Patterns of Wire-Grid Lens Antenna Equipped with Optimized Feeds at the Elevation Angle, θ , Corresponding to the Peak of the Main Beam

C.2.1 Absolute Feed Efficiency

One of the most accurate measurements made on the new feeds was of their absolute efficiency. The efficiency was determined by measuring the input impedance of both the Samoa and Nandi-Canton feeds at a number of frequencies with three different terminations. One termination used was the normal feed termination, another consisted of a short circuit placed across the terminating networks, while the third consisted of an open circuit obtained by removing the termination from the inboard end of each ramp. Let η_r be the fraction of the available input power that is radiated by the feed and let η_d be the fraction of the available input power that is dissipated in the core loss of the phase reversing transformer. Then it can be shown that $1 - (\eta_d + \eta_r)$, the fraction of the available input power dissipated in the terminating resistance, is given by

$$1 - \eta = 1 - (\eta_r + \eta_d) = \frac{R_t}{R_{in}} \left| \frac{(Z_{in} - Z_s)(Z_o - Z_{in})}{(Z_o - Z_s)Z_t} \right|$$

where

Z_t	=	input impedance of the terminating network,
R_t	=	input resistance of the terminating network,
R_{in}	=	feed input resistance when terminated with the normal terminating network,
Z_{in}	=	feed input impedance when terminated with the normal terminating network,
Z_s	=	feed input impedance when the inboard end of the ramp is shorted,
Z_o	=	feed input impedance when the inboard end of the ramp is open circuited.

Figure C.3 shows a comparison of the calculated and measured radiation efficiency η_r of the new feeds. The measured value of η_r was obtained from the measured value of η by subtracting the theoretical fractional power loss η_d in the phase reversing transformer which varied from 4 to 13.6 percent over the frequency band. The comparison between theory and experiment is very close and the Samoa and Nandi-Canton feeds have essentially the same measured efficiency. Furthermore, the

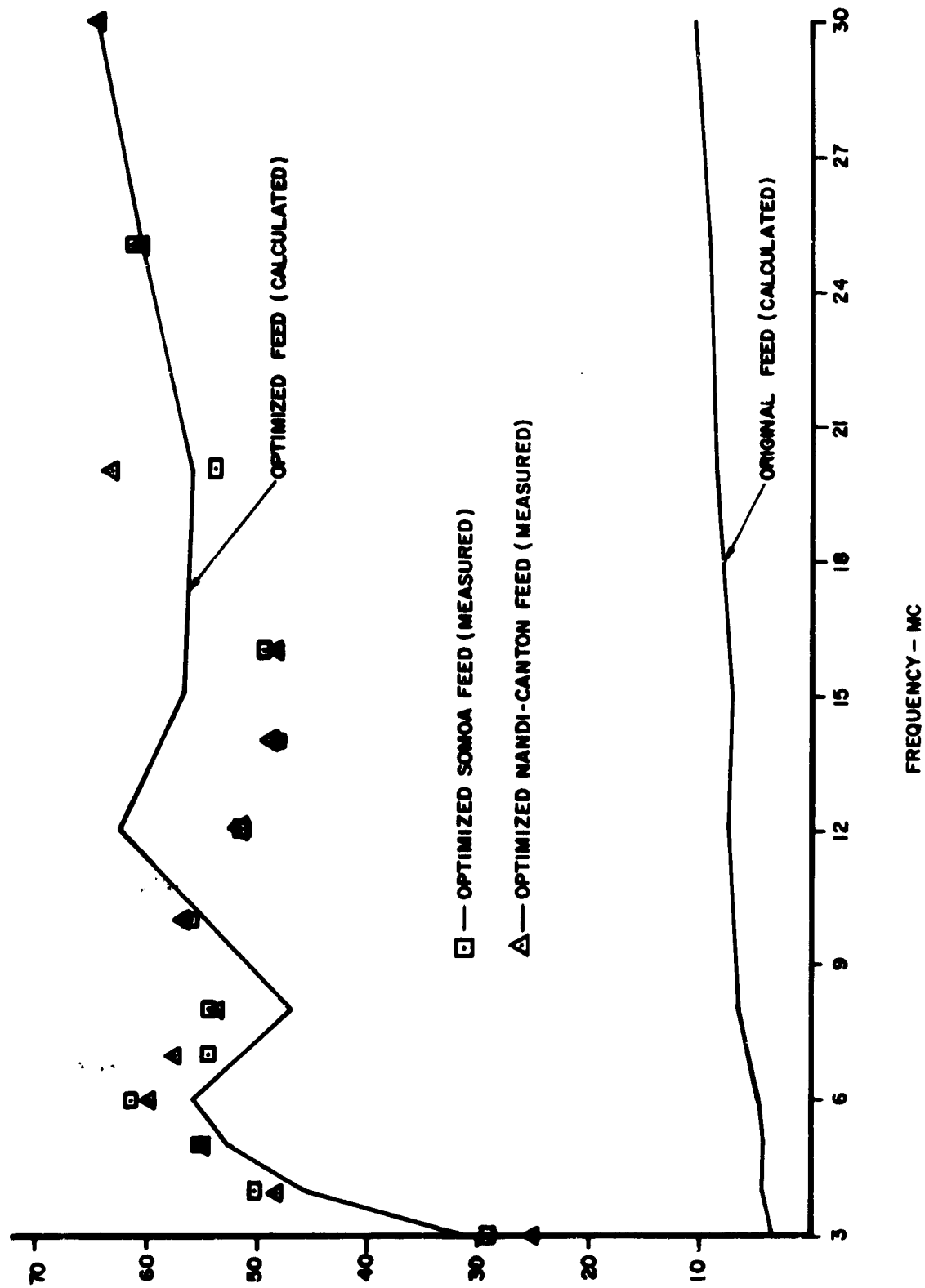


Fig. C.3 Efficiency of Optimized and Original Feeds in a 10' ai Wire-rod Lens Antenna

efficiency of the optimized feeds is gratifyingly high and is, on the average, about 8 to 10 db higher than that of the original feeds whose theoretical efficiency is also plotted in the figure for comparison.

C.2.2 Feed Response to the Zero Order Mode

Another indication of feed performance was obtained by comparing the signals received at the original and optimized Samoa and Nandi-Canton feeds when a signal was injected in the lens center. Injecting a signal in the lens center excites an outward traveling zero order mode in the lens which has an amplitude that is independent of azimuth. The signal received at the terminals of each feed is the phasor addition of the zero order mode signal incident on the feed and the scattered signals from each of the other feeds in the lens. When the feeds are non-uniformly spaced in azimuth, as is the case at Molokai, it is to be expected that the scattered signals arriving at each feed will be different and hence the signals received at the terminals of otherwise identical feeds will be somewhat different.

Figure C.4 shows the result of this experiment during which the amplitude of the signal injected in the lens center was held constant. The curves labeled Samoa and Nandi-Canton represent the ratio of the power received at a 70-ohm matched detector at the respective feed terminals with the optimized and original feeds in place. The curves labeled Sydney, Wake, Tokyo and San Francisco represent the ratio of the signals received at these feeds when the optimized Samoa and Nandi-Canton feeds are in place, to the signals received at these feeds when the original Samoa and Nandi-Canton feeds are in place. The ratio of the signals received at these unchanged feeds differs from unity (0 db) because the optimized feeds scatter to the unchanged feeds a different amount of the zero order mode signal incident upon them than do the original feeds.

The increase in signal received at the optimized Samoa and Nandi-Canton feeds is seen to average about 9 db at the low end of the band, decreasing to about 5.5 db at the high end of the band.

The oscillatory behavior of these curves is caused by several factors. One factor is the difference in the scattered signals arriving at the optimized and original feeds. Another is the different input impedances of the two feeds which causes the power delivered to the matched detector to differ from the available power by a maximum of 1 db. Still a third is the oscillatory difference in the efficiencies of the feeds illustrated in the theoretical curves of Fig. C.3. Despite these perturbations, the curves in Fig. C.4 clearly demonstrate the improved sensitivity of the optimized feeds.

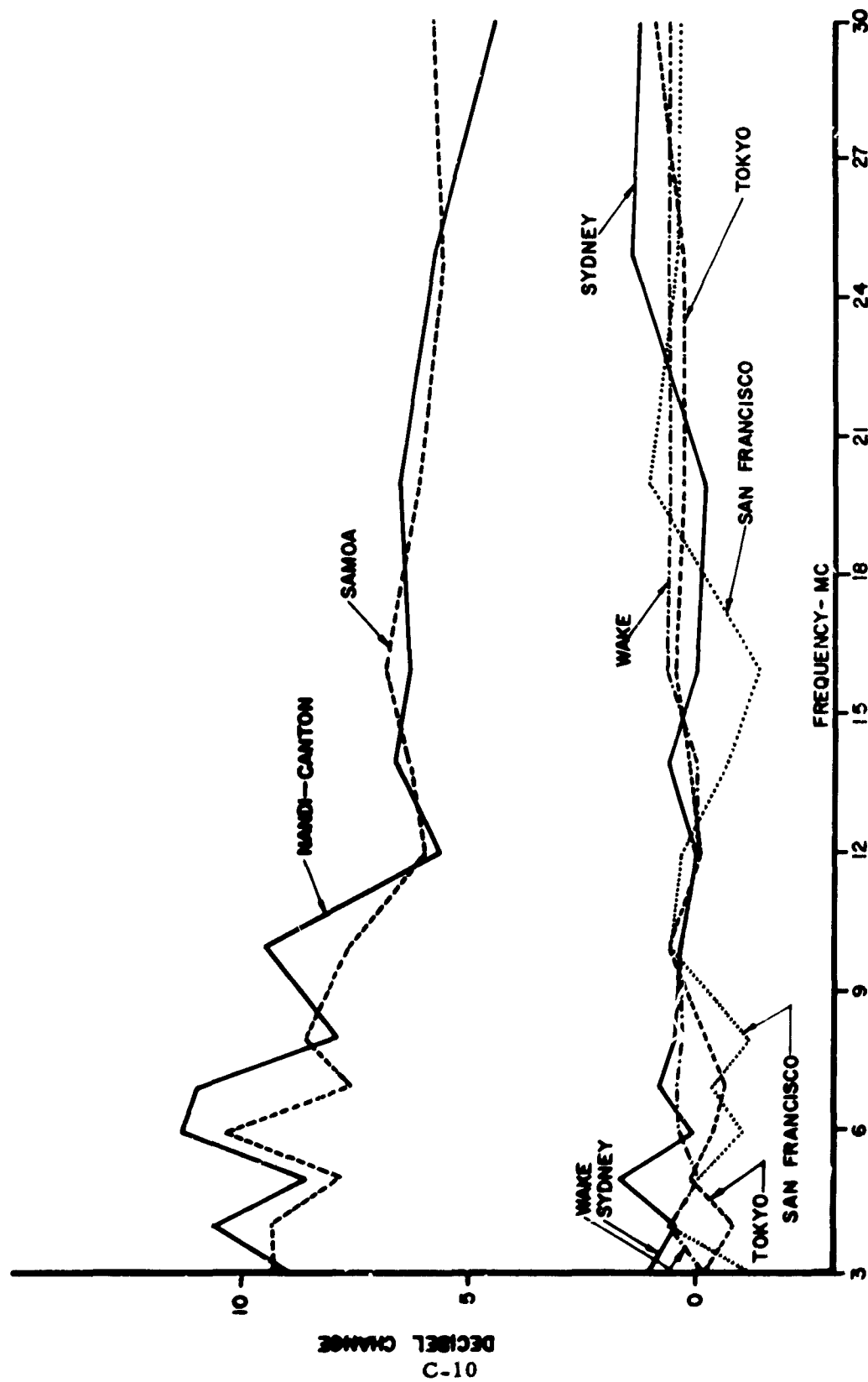


Fig. C.4 Difference in Response to the Zero Order Model of Optimized and Original Samoa and Nandi-

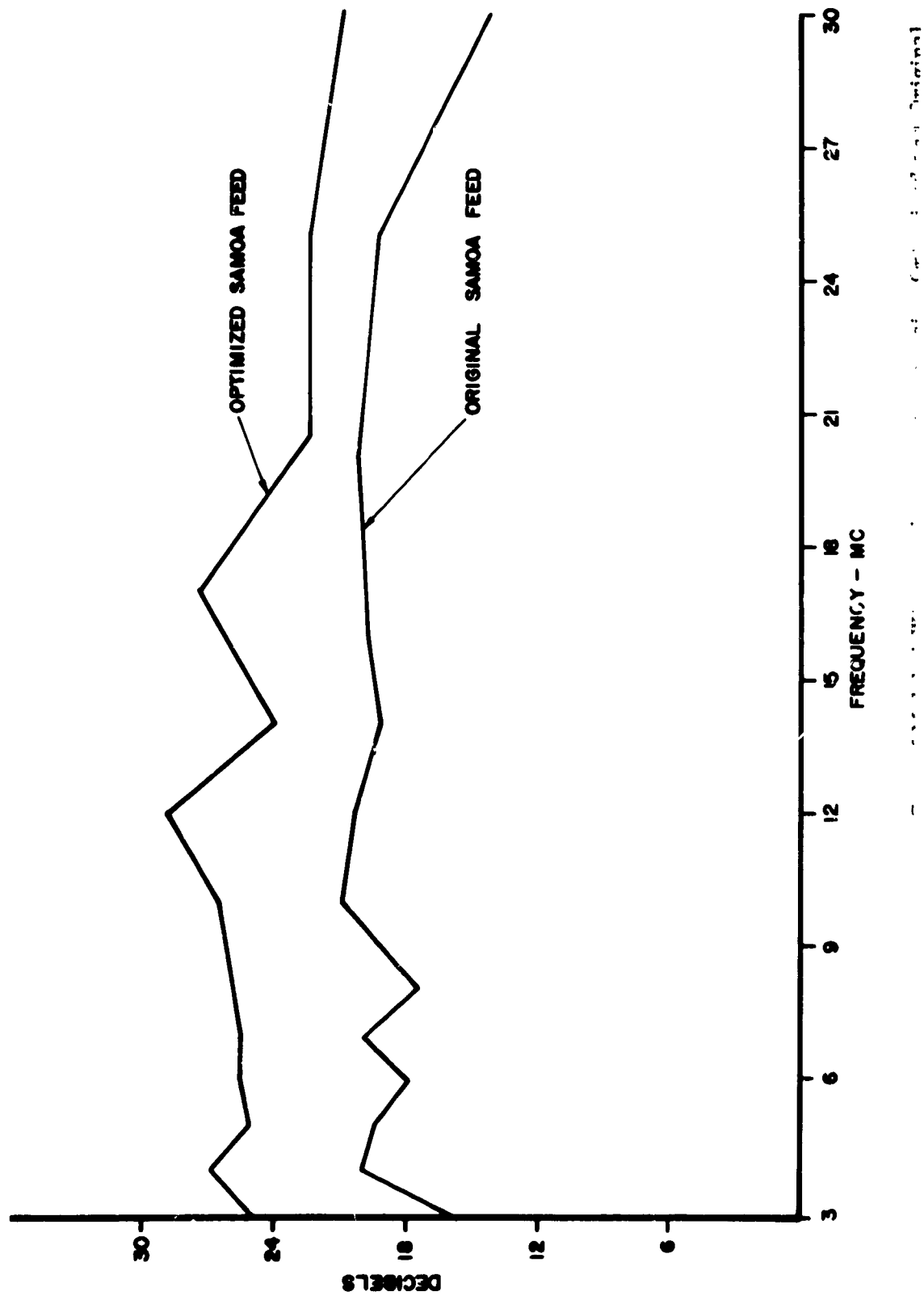
C.2.3 Measured Gain Increase of Optimized Feeds

The increase in gain of the Wire-Grid Lens HF Antenna utilizing the optimized feeds was determined directly by comparing the signals received at the Samoa and Nandi-Canton feed terminals with the optimized feeds in place with those received with the originally installed feeds in place. The signal source used for these measurements was a ground-based transmitter located in the far-zone of the lens, and placed successively at the Samoa and Nandi-Canton bearings.

To obtain the most accurate values of gain increase for the optimized feeds it would be necessary not only to locate the transmitter at the beam peak in azimuth but also at the beam peak in elevation which occurs at elevation angles shown in Fig. C.2. To locate the test transmitter in this range of elevation angles would require an airplane which was not available for these tests. Nevertheless, it is believed that the relative values of gain increase measured using the ground-based transmitter are a reasonable approximation to the values which would be obtained using an airborne transmitter.

For the tests on the Nandi-Canton feed, the ground-based transmitter was located at the bearing of Nandi-Canton on top of a 1,200-foot ridge which commanded a clear view of the lens at a range of 4.7 miles. At this location, the elevation angle of the transmitter is about 1.9 degrees with respect to the lens which is at a 400-foot elevation. It was not possible to locate the transmitter at as high an elevation for the tests on the Samoa feed because of the irregular terrain along the bearing of this feed. The site chosen for the transmitter was atop a hill called Puu o Pipika which has the same elevation as the lens and has a range of 2.9 miles. At the same time the signals received on the original and optimized Samoa and Nandi-Canton feeds were recorded, the signal received on the omnidirectional feed at the lens center was recorded. Because the signal received on the omnidirectional feed was essentially uninfluenced by the presence of the original or optimized Samoa or Nandi-Canton feeds it was used to normalize the signals received at these feeds.

The results of the measurements on the optimized and original Samoa feeds are shown in Fig. C.5. In each case the two curves were obtained by plotting the decibel difference between the signals received on the Samoa feeds and the omnidirectional feeds. The significant feature to observe from these curves is their difference which represents the increase in gain of the lens using the optimized Samoa feeds rather than the original feeds. It is seen that this gain increase is approximately 7 db at the low-frequency end of the band decreasing to a somewhat lower value at the upper end of the band.



The corresponding data for the Nandi-Canton feed is shown in Fig. C.6. Here it is observed that while the average difference between the curves is approximately the same as for the Samoa feeds, somewhat larger excursions of the signals as a function of frequency are obtained.

These larger excursions are probably associated with the more serious diffraction effects which occur when the transmitter is located up on the ridge than when it is located at the same elevation as the lens.

C.2.4 Input Impedance of Optimized Feeds

The measured input impedance of the optimized Samoa and Nandi-Canton feeds is shown in Table C.1 compared with the calculated values of input impedance. In addition, the resulting values of VSWR on the 70-ohm coaxial cable connected to the feeds are also tabulated. It is seen that the input impedances of the two feeds are almost identical and that the theoretical values compare very closely with the measured values. Inspection of the data also shows that the maximum VSWR of 3.2 would be considerably reduced if either the characteristic impedance of the cable connected to the feeds were 50 ohms rather than 70 ohms or a transformer were placed at each T-junction having a transformation ratio of 70/50.

C.3 Areas in Which Installation of Optimized Feeds Would Modify Results of the Joint Services Evaluation

If the optimized feeds, described in this appendix, had been installed in the Wire-Grid Lens Antenna during the Joint Services Evaluation, their increased coupling efficiency would have modified the results obtained in several respects. For example, Fig. 7.2, which shows the ratio of median signal levels received on the lens and the rhombics both at the antenna terminals and at the receiver terminals, would be replaced by Fig. C.7. These median signal levels are proportional to relative power gain and were derived from Fig. 7.2 using the feed efficiency data in Fig. C.3. Figure C.7(a) shows that the relative power gain of the lens would be equal to that of the rhombics at 20 Mc, somewhat lower at lower frequencies and somewhat higher at higher frequencies. When the loss in the coaxial transmission lines connecting the lens and rhombics is included, Fig. C.7(b) shows that the signal at the lens receiver will be higher than the signal at the rhombic receiver above 12 Mc because of the smaller attenuation in the lens transmission lines.

Figure 7.5, showing the calculated directive gain and power gain of the lens equipped with the originally installed feeds, would be replaced with Fig. C.8 showing the same information for the lens equipped with optimized feeds.

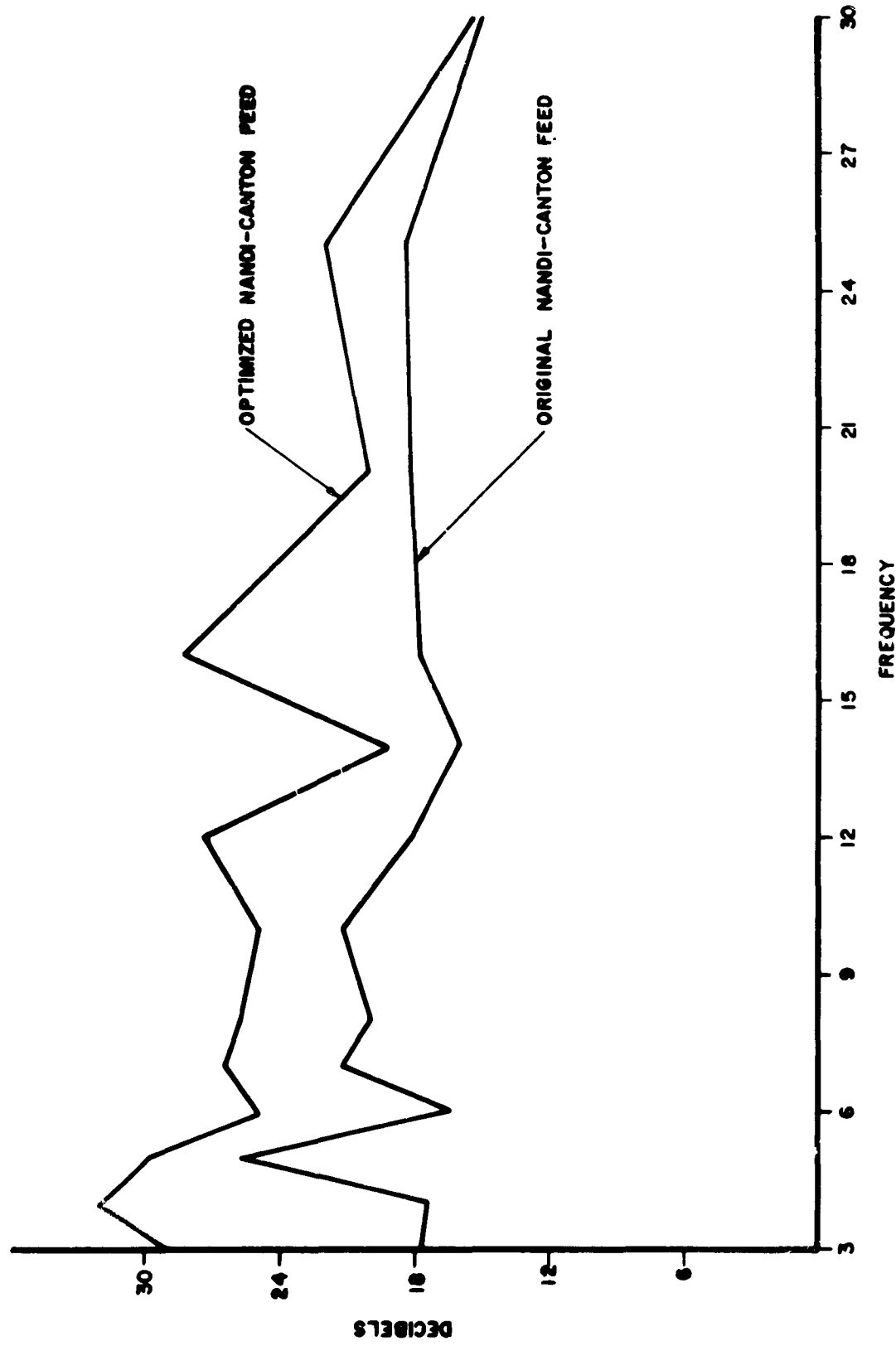
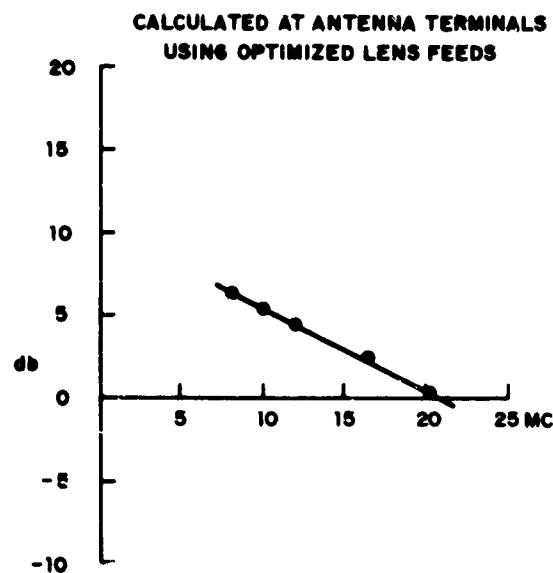


Fig. C-6. Measured Relative Gain of Molokai Wire-Gate in Antenna Feeding Order 2 and Original

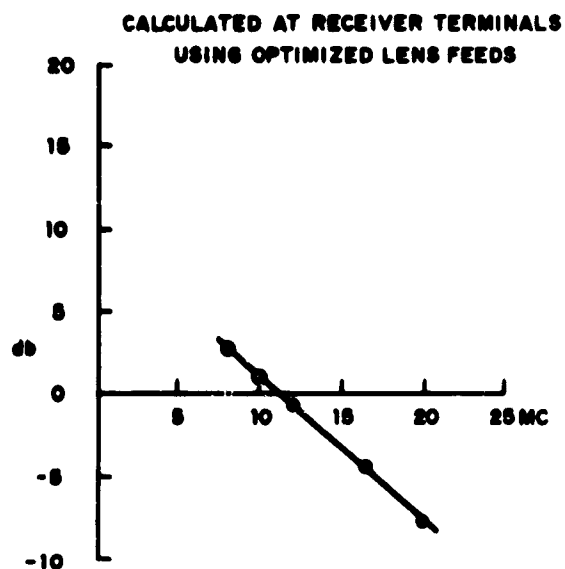
Table C.1

Input Impedance of Optimized Feeds

Frequency Mc	Samoa Feed Measured		Nandi-Canton Feed		Calculated	
	Ohms	VSWR	Ohms	VSWR	Ohms	VSWR
3	37 - j52	3.15	37 - j54	3.2	39 - j55	3.1
4	54 - j26	1.75	50 - j32	1.85	52 - j30	1.8
5	64 - j38	1.75	58 - j34	1.75	78 - j21	1.37
6	41 - j39	2.4	42 - j39	2.3	60 - j53	2.25
7	29 - j27	2.8	27 - j28	3.0		
8	23 - j 6.5	3.05	23 - j 8.3	3.1	25 - j22	3.2
10	40 + j 6.7	1.8	40 + j 6.5	1.8		
12	31 + j 1	2.25	31 + j10.5	2.3	36 - j 2.8	1.95
14	52 + j37	1.95	48 + j36	2.05		
15					47 + j23	1.75
16	68 + j32	1.6	65 + j33	1.6		
20	71 - j4.3	1.07	66 - j36	1.7	62 + j39	1.80
25	40 - j28	2.2	40 - j27	2.1	138 - j11	2.0
30	32 + j2.5	2.2	32 + j 4	2.2	77 - j 1.8	1.3



(A)



(B)

Fig. C. 7 Decibel Difference Between Median Signal Levels Received on Rhombics and on Lens (equipped with optimized feeds). Positive values correspond to stronger rhombic signals, negative values to stronger lens signals. (Calculations based on use of coaxial transmission lines to rhombics)

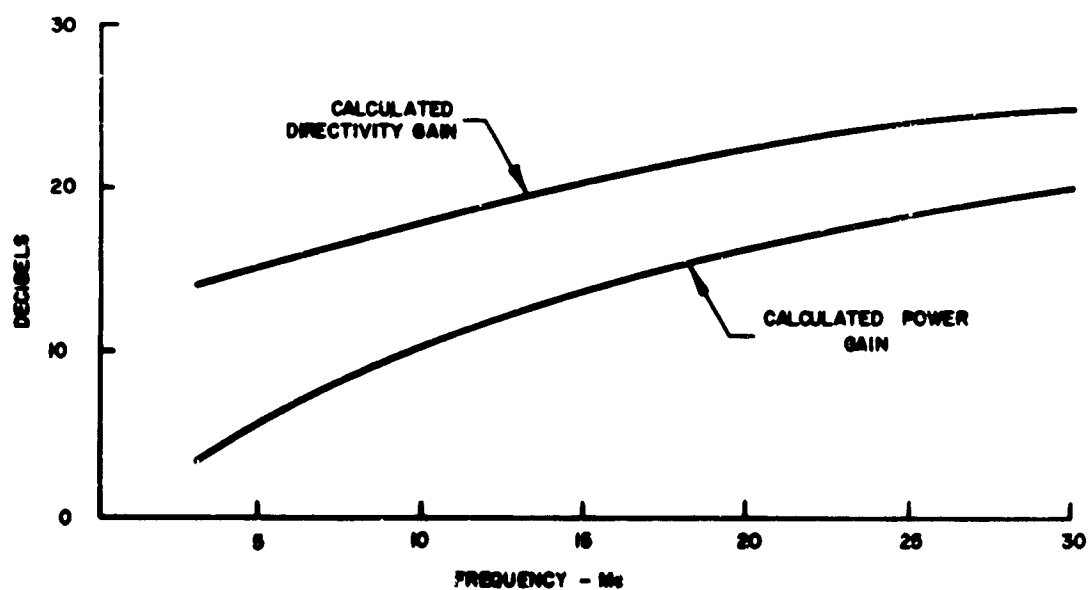


Fig. C.8 Directivity and Gain of Wire-Grid Lens Antenna Equipped With Optimized Feeds

It is seen that the directive gain of the lens equipped with the original feeds is essentially the same as that of the lens equipped with the optimized feeds. However, the power gain of the lens equipped with the optimized feeds is about 10 db greater. If the lower horn panel were extended 200 feet in radius, as has been done in another recent installation, it is expected that the lens gain using either the original or optimized feeds would be increased by about 3 db. This increase in power gain occurs because waves which formerly were incident on the ground at Brewster's angle just external to the horn would now be reflected into the lens by the extended lower horn panel.

The use of the optimized feeds should also modify somewhat the results of the error-count tests described in Sec. 8 because their improved efficiency increases its power gain of the lens. The principal effect of the increased power gain would be to reduce the noise factor of the receiving system and thereby reduce the error rate experienced when copying traffic received during the transition periods where the signal arriving at the antenna is low as was the case during a portion of the NRL tests summarized in Figs. 8.8 through 8.13.

C.4 Conclusions

The newly installed optimized feeds are superior in all respects to the originally installed feeds in the Molokai Wire-Grid Lenz HF Antenna. The theoretical radiation patterns of the lens using the optimized feeds have lower side lobes and greater directivity. Therefore, it is expected that predicted low minor lobe level of the optimized feeds would also be realized if the airborne pattern measurements were repeated.

The measured efficiency of the optimized feeds, which is approximately 50 per cent, compares very closely with the theoretically predicted values. In addition, the theoretical efficiency of the optimized feeds is greater than that of the originally installed feeds by approximately 10 db at the low-frequency end of the HF band and 8 db at the upper frequency end of the band. The measured increase in power gain of the lens using the optimized feeds is shown to be greater than that obtained using the originally installed feeds by approximately 7 db at the low-frequency end of the band, decreasing to about 4 db at the upper end of the band. These measurements were taken with a ground-based transmitter located beneath the elevation peak of the main beam. It is expected that similar relative gain measurements taken with a transmitter located at the elevation angle corresponding to the elevation peak of the main beam would show the 10 db

to 8 db increase expected from the relative feed efficiency calculations, since the estimated aperture blocking caused by the seven feeds within the lens is expected to be less than 1 db.